SECOND-ORDER DIRECT ANALYSIS FOR FIRE RESISTANCE DESIGN OF STEEL STRUCTURES

LI GUANHUA

PhD

The Hong Kong Polytechnic University

2026

The Hong Kong Polytechnic University

Department of Civil and Environmental Engineering

Second-order Direct Analysis for Fire Resistance Design of Steel Structures

Li Guanhua

A thesis submitted in partial fulfilment of the requirements for the degree of Doctor of Philosophy

December 2025

CERTIFICATE OF ORIGINALITY

I hereby declare that this thesis is my own work and that, to the best of my knowledge and belief, it reproduces no material previously published or written, nor material that has been accepted for the award of any other degree or diploma, except where due acknowledgement has been made in the text.

____________________________________ (Signed)

LI Guanhua (Name of student)

To my Family

ABSTRACT

Steel structures are sensitive to fire, as elevated temperatures can significantly reduce their strength and stiffness. When exposed to fires, the mechanical properties of steel deteriorate rapidly, potentially leading to buckling or loss of load-bearing capacity. Therefore, evaluating the performance of steel structures under fire conditions and ensuring accurate fire resistance design are of critical importance for building safety.

At present, two primary fire resistance design approaches are employed: the prescriptive method and the performance-based method. The prescriptive method, grounded in predefined codes and guidelines, is typically derived from physical fire tests and large-scale simulations. Although straightforward and convenient to implement, it is conservative and focused on member level, thereby limiting the economy and flexibility of design. In contrast, the performance-based method relies on advanced computer simulations to assess fire resistance, offering greater flexibility in optimizing fire protection measures. This approach accounts for non-uniform heating at both the member and structural levels under natural fire conditions, thereby providing a more accurate and reliable basis for fire resistance design.

Despite its advantages, the performance-based method faces three main challenges: (1) the need for sophisticated modeling and high computational demand; (2) the difficulty in capturing geometric and material nonlinearities under non-uniform fire exposure; and (3) the combination of thermal effects in nature fire scenarios. To address these issues, this thesis extends and refines the Second-Order Direct Analysis (SODA) method for fire resistance design of steel structures, using advanced line finite element methods (LFEMs) that directly account for geometric and material nonlinearities under natural fires.

This thesis first develops a refined heat transfer analysis technique for steel members protected with intumescent fire coatings (IFCs), which incorporates various thermal boundary conditions and different thermal conductivity models. The generalized Crank–Nicolson method is employed to improve the stability and convergence of the transient heat transfer analysis. Based on the computed temperature field, a novel cross-section analysis method is developed using the proposed thermal deterioration triangle (TDT) elements. The TDT element effectively captures material degradation and thermal expansion within its domain, enabling accurate cross-sectional analysis with fewer elements and improved computational efficiency. This cross-section analysis method provides essential parameters for the SODA method.

Subsequently, a stability analysis framework is proposed for steel members with arbitrary cross-sections under fire conditions. A comprehensive parametric study involving a total of 3,168 analyses is conducted to investigate global buckling capacity and to provide practical guidelines for stability design. To enable a more accurate and realistic large deflection analysis, a novel LFEM is proposed for the geometrically nonlinear analysis of steel structures subjected to non-uniform fire exposure. The derived line element formulation incorporates additional torque resulting from the non-coincidence of the shear center and the centroid of the cross-section, thereby enabling accurate analysis of large deflections with twisting effects. Moreover, the proposed LFEM accurately captures the response of steel structures under localized-fire conditions and elucidates twisting effects in steel structures subjected to non-uniform fire.

To consider the strength degradation of cross-sections under fire, a rigorous cross-section analysis method using a fiber-based numerical model capable of capturing yield surfaces and moment-curvature relationships is proposed. This approach enables a reliable evaluation of the plastic bearing capacity for arbitrary cross-sections subjected

to various fire conditions. A parametric study consisting of 162,000 analysis cases is performed, from which a simplified form of Bresler's yield surface equation is developed and validated. This approach enables evaluation of the ultimate capacity of cross-sections under various load combinations and fire scenarios, thereby laying the foundation for the next chapter.

Finally, a more efficient LFEM is proposed for analyzing steel structures exposed to non-uniform heating along both the cross-sectional and longitudinal directions. Based on the moment-curvature relationships under fire mentioned above, a strength reduction formulation is incorporated into the line element featuring zero-length plastic hinge models. This method allows frame structures to be constructed with fewer line elements, thereby achieving significantly higher computational efficiency compared with conventional methods. By simultaneously considering geometric and material nonlinearities as well as thermal effects, the proposed LFEM forms the basis for the SODA method that is applicable to fire resistance design for steel structures.

This thesis aims to provide an efficient and accurate second-order analysis framework for fire resistance design of steel structures. By simultaneously accounting for the coupled effects of material degradation, thermal strains and geometric nonlinearity, the proposed approach enhances the efficiency and reliability of structural performance assessments under fire, thereby facilitating the adoption of the SODA method in fire resistance design.

Keywords: Second-order direct analysis; Steel structures; Fire resistance design; Structural fire design; Line element; Finite element method

PUBLICATIONS & AWARDS

Journal Paper:

J1. **Li, G. H.**, Gu, Z. Z., Chen, L., & Liu, S. W. (2025). Geometrically nonlinear analysis of steel members under non-uniform fire considering twisting effects. ***Journal of Constructional Steel Research***, *231*, 109596. ***(Published)***

J2. **Li, G. H.**, Gu, Z. Z., Du, E., Liu, S. W., Liu, Y. P., & Chan, S. L. (2025). Global buckling analysis of IFC-protected steel members with irregular sections under fire. ***Journal of Constructional Steel Research***, *224*, 109158. ***(Published)***

J3. **Li, G. H.**, Ouyang, W., Ouyang, W., & Liu, S. W. (2024). Static analysis of two-side supported 2-ply laminated glass panes through physics-informed neural networks. ***Engineering Structures***, *309*, 118038. ***(Published)***

J4. **Li, G. H.**, Gu, Z., Zhang, H., Ouyang, W., & Liu, S. W. (2024). Line Finite Element Method for Geometrically Nonlinear Analysis of Functionally Graded Members Accounting for Twisting Effects. ***Composite Structures***, *343*, 118268. ***(Published)***

J5. **Li, G. H.**, Gu, Z., Ouyang, W., Liu, S. W., & Abdelrahman, A.H.A. (2024). Finite-Element-Based Cross-Section Analysis Method for Functionally Graded Sandwich Members with Arbitrary Shapes and Gradients. ***Journal of Sandwich Structures and Materials***, 10996362241275557. ***(Published)***

J6. **Li, G. H.**, Liang, A. R., Du, E. F., & Liu, S. W. (2025). Improved Line-Element-Based Method for Performance-Based Analysis of Steel Structures under Localized Fires. ***Journal of Constructional Steel Research*** (***Submitted***).

J7. **Li, G. H.**, Pan, J. L., Cai, J. M., & Liu, S. W. (2025). Strength Interaction Diagrams of Composite Columns after Fire Exposure: Analysis Method, Validation and Design. ***Fire Technology*** (***Submitted***).

J8. Gu, Z. Z., **Li, G. H.**, Zhang, M., Looi, D. T. W., & Liu, S. W. (2025). Experimental study on tensile and compressive properties of neosinocalamus affinis-based bamboo scrimber. ***Construction and Building Materials***, *492*, 143059. ***(Published)***

J9. Zeng, Z. Y., **Li, G. H.**, Liu, S. W., Huang, D. H., Liu, Y. P., & Chan, S. L. (2026). Low-cycle fatigue of laser-arc hybrid welded S960 high-strength steel joints. ***Journal of Constructional Steel Research***, *236*, 110040. ***(Published)***

J10. Ouyang, W., **Li, G. H.**, Chen, L., & Liu, S. W. (2024). Machine learning-based soil–structure interaction analysis of laterally loaded piles through physics-informed neural networks. ***Acta Geotechnica***, 1-26. ***(Published)***

J11. Ouyang, W., **Li, G. H.**, Chen, L., & Liu, S. W. (2024). Physics-informed neural networks for large deflection analysis of slender piles incorporating non-differentiable soil-structure interaction. ***International Journal for Numerical and Analytical Methods in Geomechanics***, 48(5), 1278-1308. ***(Published)***

J12. Liang, A. R., **Li, G. H.**, Bai, R., Chen, L., & Liu, S. W. (2025). Efficient Beam-Column Finite-Element Method for Second-Order Analysis of Members with Arbitrary Geometry. ***Structures*** (***Submitted***).

J13. Liang, A. R., Chen, L., **Li, G. H.**, Chan, J., Chan, S-L., & Liu, S. W. (2025). Influence of Heat Treatment on the Flexural Buckling of WAAM Austenitic Stainless Steel Circular Hollow Section Columns. ***Engineering Structures*** (***Submitted***).

J14. Pan, J., Sun, Y., **Li, G. H.**, Wang, Y., Elchalakani, M., & Cai, J. (2026). Nonlinear Analysis of Engineered Cementitious Composite-Encased Concrete Filled Steel Tube Columns Under Eccentric Loading After Fire Exposure. ***Fire Technology***, 62(2), 42. (***Published***)

J15. Liu, Y. P., Zeng, Z. Y., **Li, G. H.**, Su, A. D., Chan S-L., & Liu, S. W. (2025). Low-Cycle Fatigue Performance of High-Power Laser-Arc Hybrid Welded S690 High-Strength Steel Joints. ***Structures*** (***Submitted***).

Conference Paper:

C1. **Li, G. H.**, Chen, L., Ouyang, W., & Liu, S. W. (2023). Emerging Machine-learning Techniques for Second-order Analysis of Steel Members through Physics-informed Neural Networks. Eleventh International Conference on Advances in

Steel Structures (ICASS’2023).

C2. **Li, G. H.** & Liu, S. W. (2024) Second-order Direct Analysis for the fire resistance design of steel structures. 2nd International Smart Firefighting Workshop, Hong Kong SAR, China.

C3. Zhang, H., Chen, L., **Li, G. H.**, & Liu, S. W. (2022) Second-order analysis of steel members using nonsymmetric sections with moderately thick-walled steel plates, Tenth International Conference on Advances in Steel Structures, Chengdu, China, August 21-23.

Award:

A1. International Collaborative Research Fellowship by *Hong Kong Polytechnic University* 2024

ACKNOWLEDGEMENTS

First of all, I would like to express my sincere gratitude to my supervisor, Dr. Liu Si-Wei. His guidance helped me find the key research direction and gave me guidance during my doctoral studies. During this period, he guided me to the cutting-edge research on second-order direct analysis and gave me patient guidance.

I also would like to extend my appreciation to my co-supervisors, Prof. Liu Yao-Peng and Prof. Chan Tak-Ming, for their invaluable advice and warm encouragement.

Then, my gratitude goes to the Department of Civil and Environmental Engineering at The Hong Kong Polytechnic University for providing me abundant research resources and a free academic environment.

Furthermore, I would like to acknowledge all members of the NIDA team. The time we spent together solving practical engineering problems in the projects enriched my doctoral career.

I am also grateful to my fellow disciples in ZS912 for their companionship, selfless support, and the meaningful research experiences we shared. Additionally, I highly value the opportunity to collaborate academically with them.

Finally, I wish to convey my deepest gratitude to my family. Their unconditional love, understanding, and unwavering support are always my greatest source of strength and motivation to pursue my doctoral degree.

CONTENTS

LIST OF FIGURES

LIST OF TABLES

CHAPTER 1.

INTRODUCTION

Steel is one of the most widely used materials in model structures due to its excellent strength, ductility, strength-to-weight ratio and ease of fabrication. These advantages make it a preferred choice for tall buildings, long-span bridges, space grid structures and modular integrated construction. However, steel is sensitive to high temperatures. Once exposed to fire, its mechanical properties degrade rapidly, leading to large deflection, buckling, and even progressive collapse. Therefore, fire resistance design is essential for ensuring the safety of steel structures.

Traditional fire resistance design methods are typically prescriptive and rely on set rules and guidelines derived from standard fire tests to ensure safety. It is straightforward but cannot obtain the most accurate and cost-effective design for steel structures. In contrast, performance-based design employs advanced computational simulations to evaluate the fire resistance of buildings. This approach offers greater flexibility and design freedom but requires substantial computational resources and precise simulation techniques. However, the requirement for sophisticated modeling, high computational costs, and the challenge of capturing thermally induced nonlinear effects have impeded the advancement of performance-based design. Therefore, this study aims to develop a Second-Order Direct Analysis (SODA) method to efficiently and accurately simulate the mechanical behavior of steel structures under fire conditions.

This chapter presents the research background, the research objectives, and the outlines of this thesis.

1.1 Background

With the promotion of the "carbon neutrality" goal and the acceleration of new urbanization construction, the use of steel in high-rise buildings, large-span structures, and energy infrastructure continues to expand. However, steel is sensitive to high temperatures. When the temperature exceeds 400 °C, the yield strength of steel rapidly decreases. Under fire conditions, steel members may develop plastic hinges and undergo global buckling, potentially leading to progressive collapse, as shown in Figure 1-1(a). Due to the temperature sensitivity of steel (Figure 1-1(b)), fire safety has become a core concern in ensuring resilience of steel structures.

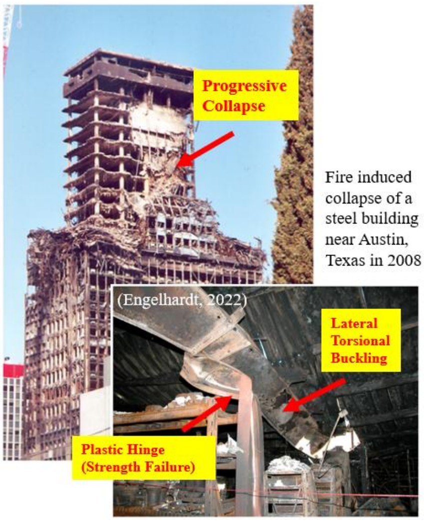

TABLE A-4.2.1
Properties of Steel at Elevated Temperatures
(ANSI/AISC 360-22)

Steel Temperature, °F (°C)	$k_E = E(T)/E = G(T)/G$	$k_p = F_p(T)/F_y$	$k_y = F_y(T)/F_y$
68 (20)	1.00	1.00	1.00
200 (93)	1.00	1.00	1.00
400 (200)	0.90	0.80	1.00
600 (320)	0.78	0.58	1.00
750 (400)	0.70	0.42	1.00
800 (430)	0.67	0.40	0.94
1000 (540)	0.49	0.29	0.66
1200 (650)	0.22	0.13	0.35
1400 (760)	0.11	0.06	0.16
1600 (870)	0.07	0.04	0.07
1800 (980)	0.05	0.03	0.04
2000 (1100)	0.02	0.01	0.02
2200 (1200)	0.00	0.00	0.00

(a) Typical failure under fire [1]　　(b) Material degradation factors

Figure 1-1 Fire induced damage and material degradation.

Approaches for fire resistance design generally are divided into two categories, as depicted in Figure 1-2: (1) prescriptive design, and (2) performance-based design. Traditional prescriptive methods presented in current design routines, such as

Eurocode-3 (2005), ANSI/AISC 360 (2022) and Hong Kong steel codes (2011), highly rely on the standard fire scenarios and prescriptive analysis procedures. These methods follow a set of rules prescribed in the codes, requiring the structural elements to satisfy specified hourly fire resistance ratings without accurately predicting the response of steel structures in real fire scenarios. As an element-level approach based on standard fire tests and many assumptions, the prescriptive method may result in excessive design conservatism, less flexibility and increased risk of local failures.

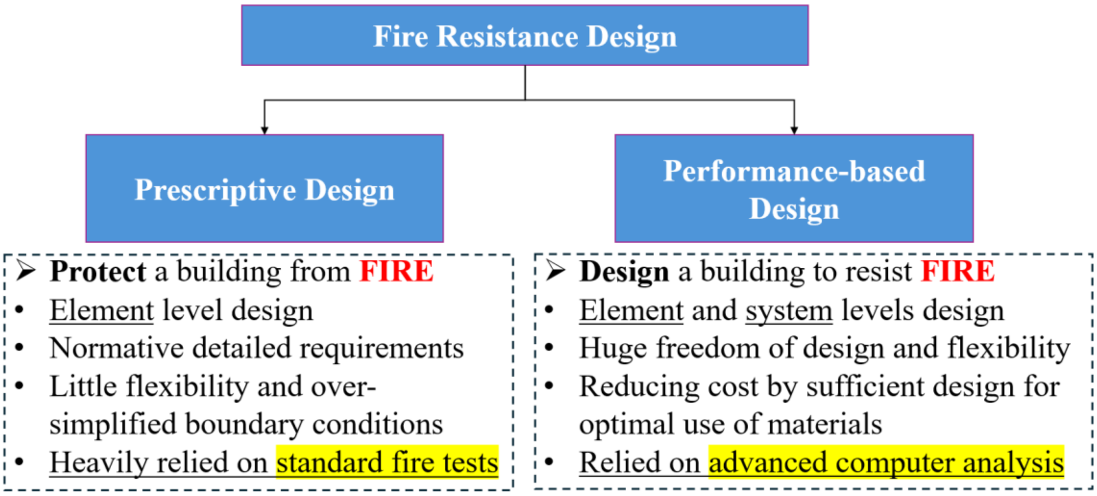

Figure 1-2 Categories of fire resistance design.

To address these limitations, the design strategy has shifted towards the paradigm of performance-based fire resistance design (Figure 1-3), which achieves a dynamic balance between safety and economy through heat transfer simulation, structural damage evolution prediction, and multi-objective optimization. The performance-based fire design requires accurately predicting the response of steel structures under real fire scenarios.

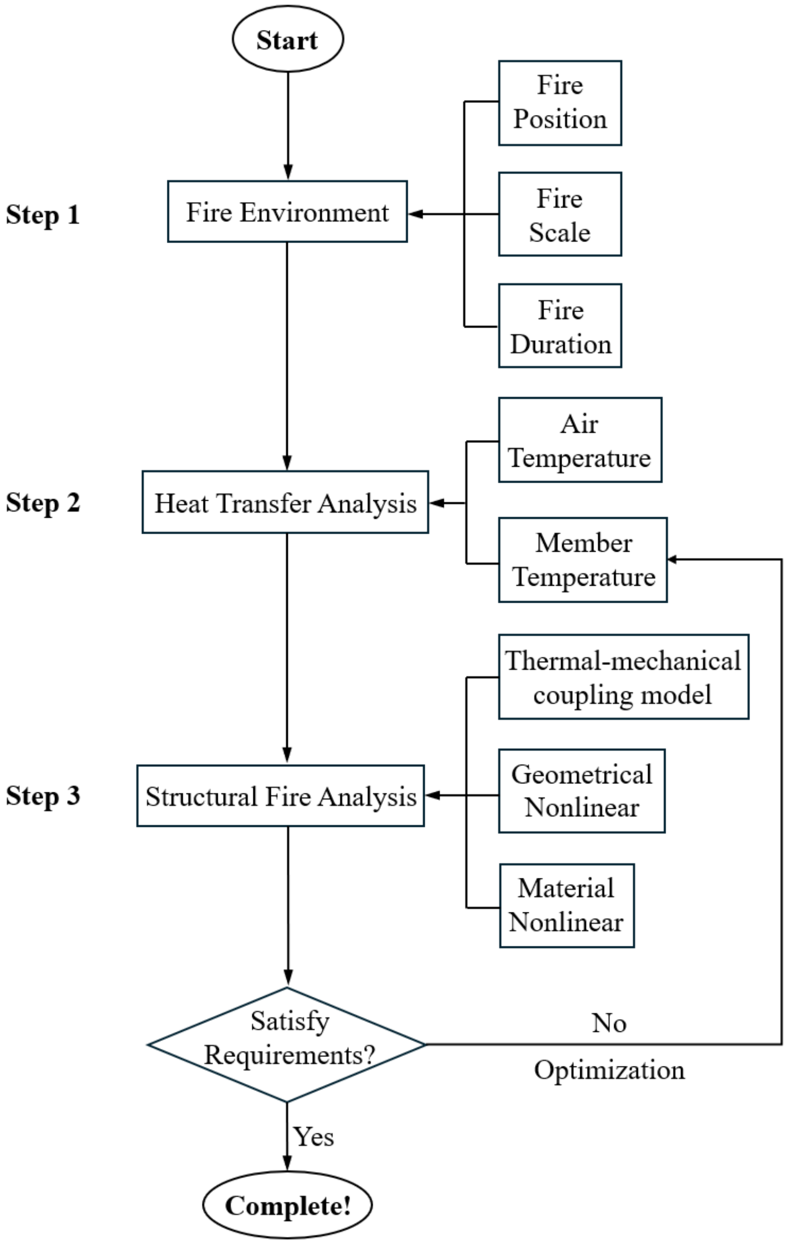

Figure 1-3 Flowchart of typical performance-based fire resistance design approach.

This design method typically involves three steps. The first step is to characterize the fire conditions, including fire position, fire scale and fire duration. Guidelines for determining the fire conditions have been provided in several design codes, such as EN1991-1-2 and SFPE S.01-2011. The second step aims at calculating the temperature field within the members through heat transfer analysis, taking into account the influence of air temperature due to the fire environment. Two primary heat fluxes, convection and radiation, are typically considered in the heat transfer model. Once the temperature field is computed, the final step is to analyze the structural response, accounting for material and geometric nonlinearities under actions of high temperatures and other applied loads. The design scheme is adjusted until the structural response meets the requirements. The three steps outlined above can be calculated using various methods and tools and can be analyzed at either member or system levels.

However, the performance-based fire resistance design method still faces three major technological bottlenecks. Firstly, the calculation cost of nonlinear thermal-mechanical coupling analysis is quite high, and traditional finite element methods are difficult to support engineering level optimization. Secondly, the modeling efficiency of random fire scenarios is low, making it difficult for existing methods to cover the spatiotemporal heterogeneity of fire loads. Thirdly, the combination of thermal effects in nature fire scenarios renders structural analysis considerably more complex. Hence, there is a critical need to develop an accurate and efficient analysis method to support the broader use of the performance-based fire resistance design approach.

Current performance-based fire resistance design methods generally consist of fire dynamics simulation (DFS) and structural response analysis done by advanced finite element software. The former provides the fire load acting on the structure, while the latter requires heat transfer and structural mechanics analyses of the steel structures. This study focuses on the latter, the structural fire resistance design, aiming to provide a more efficient and accurate analysis method. Although traditional finite element software such as ANSYS, Abaqus, and SAFIR can provide promising results for structural response, developing advanced nonlinear temperature-dependent finite element models requires significant expertise and experience. These models must account for complex factors that have a substantial impact under fire conditions, including initial imperfections, second-order effects, material nonlinearity, thermal strain, etc.

To address the challenges in fire resistance design, this research extends Second-Order Direct Analysis (SODA) method to fire conditions. The SODA method is an advanced and efficient nonlinear analysis approach for steel structures at ambient temperature and has been endorsed by several major steel design codes, including Hong Kong Steel Code (2011), GB 50017 (2017), AISC 360 (2016) and Eurocode-3 (2005), as shown in Figure 1-4. Instead of using linear analysis with separate stability checks, SODA method performs a second-order analysis that directly accounts for both the global P–Δ effects (frame sway) and local P–δ effects (member curvature) in the structural model. This direct simulation makes SODA a truly direct and accurate design approach, as the analysis itself confirms whether the structure can carry the design loads without failure. Given its strengths at ambient temperature, the SODA method is well-suited for extension to structural fire engineering. In a fire, steel members experience degraded material properties and thermal expansion, which can introduce additional forces and deformations. By integrating temperature-dependent material models and thermally induced effects into the SODA framework, the SODA method can successfully give accurate predictions of structural response, thus efficiently achieve more accurate fire resistance design.

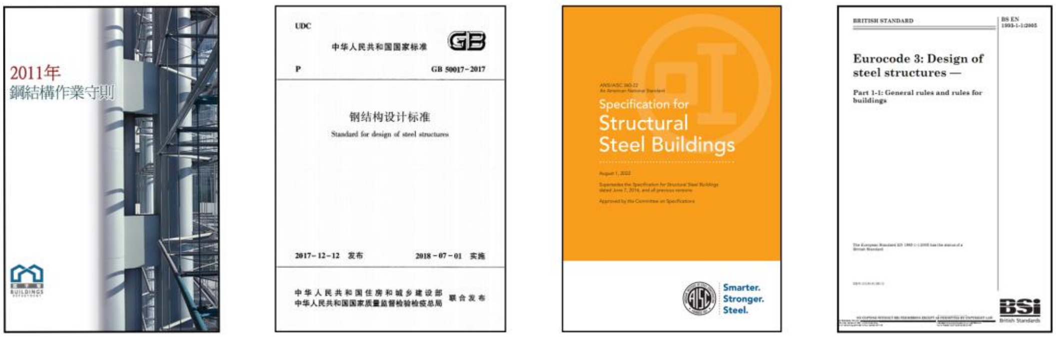

Figure 1-4 The SODA method is available in several design codes.

In general, the SODA method employs the Line Finite Element Method (LFEM) to evaluate the nonlinear behavior of structural systems. LFEM refers to the finite element method using beam-column elements, which offer enhanced computational efficiency and compatibility with large-scale frame structures. It takes into account initial imperfections at both the local member and global frame structure levels to assess member instability and structural buckling. Although typical line elements provide valuable insights into the geometrically nonlinear analysis of steel members, they assume a simplified distribution of temperature and thermal expansion and lack the ability to accommodate arbitrary cross-sections subjected to non-uniform fire conditions. Additionally, some thermal-induced second-order effects are neglected. Therefore, there remains a gap in applying the SODA method to fire resistance design.

This thesis proposes a new numerical analysis framework that extends the SODA method to fire resistance design, utilizing the LFEM, which is more efficient and practical for design. First, a refined heat transfer analysis method and cross-section analysis approach are proposed to derive key fire parameters for the LFEM implementation. The method calculates non-uniformly degraded cross-sectional properties, warping and torsion properties, and Wagner effects influenced by non-uniform fire conditions. Next, an advanced LFEM is applied to analyze steel structures under fire, accounting for initial imperfections, second-order effects, thermal strain, localized fire, and material nonlinearity. A rigorous strength capacity analysis method is then derived to support the structural resistance check and assess the interaction diagram for members. Finally, a novel LFEM is developed to account for the thermal gradient along both the axial and cross-sectional directions, fulfilling the need for more precise and efficient simulations in fire resistance design.

1.2 Objectives

The primary objective of this thesis is to develop a Second-Order Direct Analysis (SODA) method for a more accurate fire resistance design method of steel frames. The LFEM-based SODA framework is established based on the refined cross-section analysis, which provides essential parameters for structural analysis. The line finite element formulation is derived by simultaneously considering initial imperfections, second-order effects, thermal strain, localized fire, and material nonlinearity, which are factors that are critical to structural behavior under fire. Within the SODA framework, section capacity checks are performed using a proposed yield surface algorithm. Finally, by incorporating a refined line element capable of capturing thermal gradients along both axial and cross-sectional directions, the method achieves enhanced efficiency and accuracy.

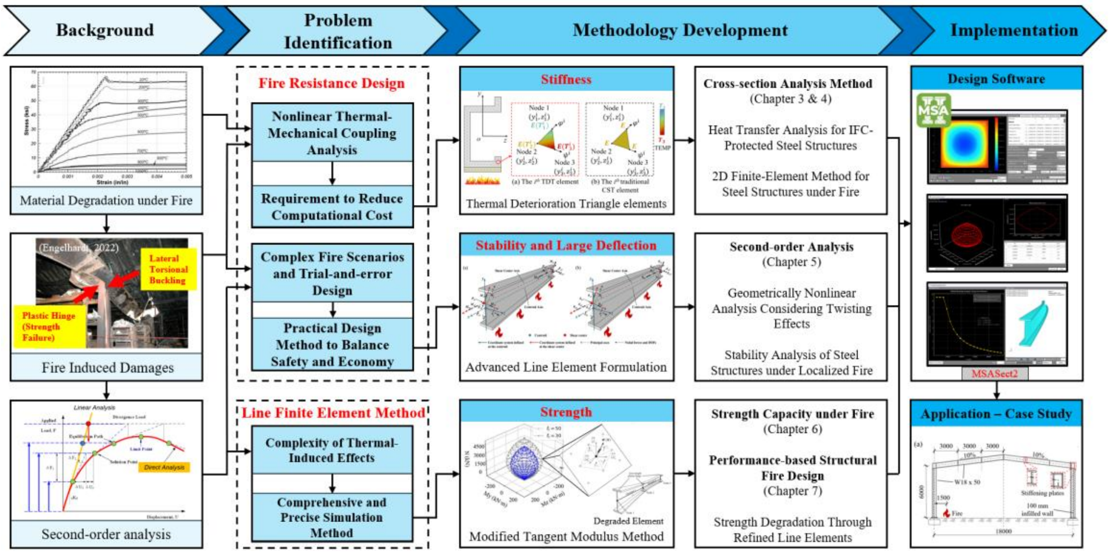

Figure 1-5 Research roadmap of the thesis.

The research roadmap is illustrated in Figure 1-5. To facilitate efficient and accurate fire resistance design, the key research objectives are summarized as follows:

- To propose a SODA framework for the fire resistance design of steel structures. This framework includes refined heat transfer analysis, cross-section analysis, and line elements to conduct robust structural fire analysis.
- To develop a cross-section analysis method that accounts for factors under fire conditions, including material degradation, nonuniform fire exposure, fire-resistant materials, and the computation of cross-sectional properties essential for line element formulations and stability analysis.
- To develop a geometrically nonlinear analysis framework using the advanced line finite element method, which considers thermal-induced effects under fire, such as twisting, thermal expansion, and thermal strain.
- To integrate a rigorous cross-sectional yield surface to evaluate the strength capacity of steel structures under fire conditions and provide the moment-curvature relationship for inelastic second-order analysis.
- To develop a thermal-degraded line element for sequentially coupled thermal-structural analysis. The element formulations are derived based on the localized fire assumption and offer superior efficiency for fire resistance design.
- To integrate the algorithm into novel software, MSASsect2, which provides a user-friendly tool and facilitates the application of the proposed method in fire resistance design.

1.3 Outline of the Thesis

There are seven main chapters in this thesis, and the outline is presented as follows:

Chapter 1 introduces the present research, highlighting the concept of fire resistance design for steel structures and the urgent gaps for its implementation. The objectives and structure of the thesis are also presented in this chapter.

Chapter 2 provides a literature review of previous studies on structural fire design for steel structures. The chapter first reviews fire resistance design and then offers a detailed examination of the Second-Order Direct Analysis (SODA) method and its potential for fire resistance design.

Chapter 3 presents a finite element formulation for heat transfer analysis. The governing equations for transient heat transfer are derived and discretized for finite element implementation. Several benchmark problems are solved to verify the accuracy of the approach. Finally, the method is implemented in software for practical applications.

Chapter 4 proposes a novel cross-section analysis method using nonhomogeneous planar elements. The effects of nonuniform material degradation under localized fire are considered, and essential parameters for line element implementation are calculated. A global buckling design method is introduced based on parametric study.

Chapter 5 presents the second-order direct analysis of steel members under fire conditions, accounting for critical phenomena such as twisting effects, thermal expansion, and nonuniform fire exposure. This approach provides an accurate evaluation of the deformation and stability of steel members under fire.

Chapter 6 develops a rigorous cross-sectional yield surface to evaluate the strength capacity of steel structures under fire conditions and provides the moment-curvature relationship for inelastic second-order analysis under fire. A design method is summarized for calculating the yield surface of steel structures under fire conditions.

Chapter 7 proposes a more accurate and efficient fire resistance design framework based on the SODA method. The modified tangent modulus is integrated into the line element, and the method can handle localized fire conditions. The eccentricity of the cross-sectional centroids and the cross-section varying factors are calculated and incorporated into the element formulation.

Chapter 8 concludes the thesis, highlighting the significance of the research and proposing directions for future work to further improve the present study.

CHAPTER 2.

LITERATURE REVIEW

2.1 Introduction

This chapter provides a literature review on fire resistance design and the Second-Order Direct Analysis (SODA) method. Section 2.2 presents the development of fire resistance design, followed by an introduction to the SODA method and its potential application to fire resistance design. The literature review on SODA method is divided into four parts: heat transfer analysis, cross-section analysis, line finite element analysis, and strength capacity analysis.

2.2 Fire Resistance Design

Fire resistance design is generally categorized into two approaches: traditional specification-based prescriptive design method and performance-based design method. The prescriptive design method has long been well-established, whereas the performance-based design method has undergone gradual development and widespread adoption over the past few decades. Accordingly, the focus of this section's literature review is placed on the performance-based design method.

Performance-based fire resistance design is recognized as an engineered approach to fire protection design. The implementation of this approach is based on several key factors: (1) the goal of design for fire safety; (2) analysis of the designated fire scenario or conducting uncertainty analysis; (3) quantitative analysis and evaluation based on safety objectives for design purposes [2]. According to difference performances of the building, Nelson [3] categorized the performance-based fire design into four types, including environment performance, component performance, threat potential performance and risk potential performance, as shown in Figure 2-1.

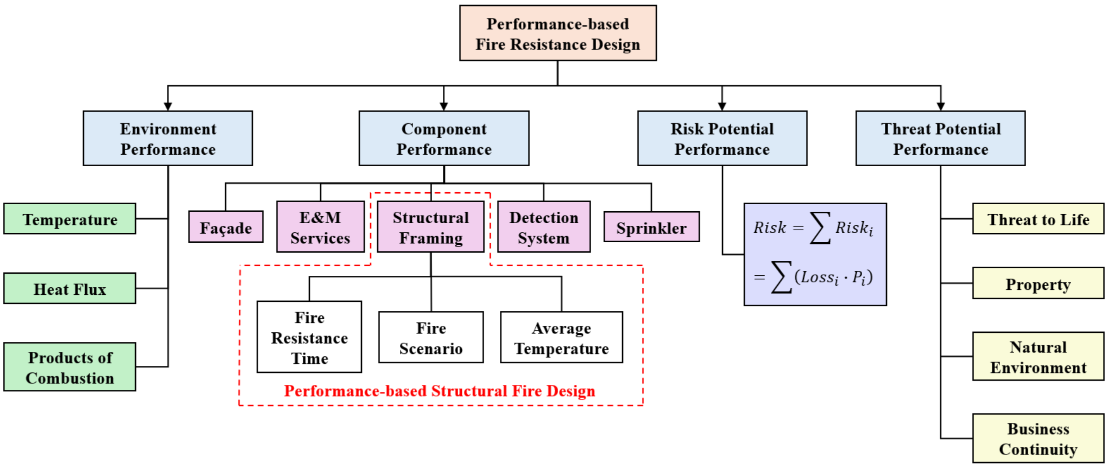

Figure 2-1 Different types of performance-based fire resistance design.

Among these four performances, component performance focuses on the individual component system of the building in fire. Typical components, such as façade, E&M service system, structural framing, detection system, and sprinklers, can be designed in isolation to meet the performance requirements, without accounting for the influence of other components [4]. For instance, an example of a component performance-based approach is designing a steel structure framework that achieves a 1-hour rated value in a specified fire scenario. The requirements include the highest average temperature of the framework, the maximum displacement under fire, and the maximum acceptable plastic deformation area.

The component-performance-based fire design focusing on the structural framing mentioned above is also identified as performance-based structural fire design (PBSFD) [5]. Through this design method, structural engineers can create optimal solutions for valuable structures by applying science-driven methods and demonstrating expected performance. This approach offers numerous benefits, including enhanced confidence through safety quantification, integration of sustainability and resilience goals alongside life protection, and fostering innovation and architecture design [6].

The concept of performance-based structural fire design can be traced back to at least since the 1980s [7], with design tools available to support this method. In 1992, New Zealand introduced a code for performance-based building design, which included specifications for fire design proposed by Buchanan in 1994 [8]. The U.S. Electric Power Research Institute also released guidance on quantitative fire hazard analysis, built on a robust fire safety assessment method [9]. In 1994, Australia incorporated performance-based design into housing design standards [10]. In 1995, the Canadian commission on building and fire codes announced plans to transition design specifications from a prescriptive to a performance-based approach [11]. In 1998, the society of fire protection engineers formally initiated projects in the U.S. to develop a framework for performance-based fire design [12].

By the early 2000s, the concept of PBSFD had matured, accompanied by an increasing number of emerging guidelines. Notable milestones include the publication of key documents: the performance option in the National Fire Protection Association (NFPA) *Life Safety Code* [13], *Engineering Guide to Performance-Based Fire Protection Analysis and Design of Buildings* from the Society of Fire Protection Engineers (SFPE) [14], *Performance Code for Buildings and Facilities* from the International Code Council (ICC) [15], and the performance option in the NFPA Building Code [16]. These guidelines permit the use of advanced approaches or materials to facilitate performance-based design, as long as they can be shown to provide at least an equivalent level of safety.

In the past two decades, PBSFD has continuously developed and improved, and many scholars have conducted in-depth and extensive research on PBSFD during this period. For instance, Saab et al. [17] proposed a nonlinear analysis method for the analysis of 2D steel frame under fire, considering material degradation and geometrically nonlinear. EI-Rimawi et al. [18] developed a secant stiffness method for steel beams under fire and analyzed the influence of thermal distribution. Bailey et al. [19] studied the compartment fire in a full scale steel structure through fire tests and evaluated the fire-resistance performance of the steel structure. Tang et al. [20] investigated the performance of a large-span arched structure subjected to localized fire through numerical simulation. Huang et al. [21] studied composite steel structures in fire through 3D nonlinear finite element method, which showed good accuracy in predicting the structural response. Liew et al. [22] introduced an advanced plastic hinge method for the performance-based design of various steel structure, including a multistory car park, an arched framed, and a steel dome. Usmani et al. [23] carried out a case study on Twin-Towers of the World Trade Center using a finite-element model and developed a robust and practical method for PBSFD. Lamont and Lane [24] also conducted a case study on an 11-storey office building to demonstrate the fire resistance performance and give an optimized structural fire design. Block and Yu [25] gave a design case on a multi-story building using the finite element software Vulcan involving optimal response different fire scenarios. These studies established a robust foundation for future developments by introducing a series of reliable methods for performance-based analysis.

In recent years, aligned with the value proposition of PBSFD, there has been a renewed interest in risk-based design, enabling design, and failure assessment design. For example, risk-based design focuses on the risk sensitivity and tolerability of the structures. Tonicello, Desanghere et al. [26] studied the risk sensitivity of the structure to a high temperature exposure. Mohan et al. [27] introduced risk tolerability for fire safety design and proposed a risk perception and acceptance framework. Guo et al. [28] proposed a quantitative risk analysis of reinforced concrete structures, which facilitates the performance-based design for severe fire hazards. Enabling design focuses on accommodating architectural preferences, such as the use of timber and the integration of innovative structural systems. Hopkin et al. [29] conducted a study on Four Pancras

Square in London, where the implementation of PBSFD was required to allow the use of weathering steel, enabling the development of its protective patina and achieving the intended aesthetic. Meacham et al. [30] introduced regulatory considerations with performance-based fire design for modern methods of construction like modular integrated construction (MiC). For failure assessment design, Molkens et al. [31] proposed a method for evaluating the post-fire behavior of concrete slabs, accounting for uncertainties in residual capacity.

In summary, PBSFD offers a goal-oriented approach based on fire dynamics and structural engineering principles to develop tailored solutions that address specific stakeholder requirements. Over recent decades, this methodology has been increasingly standardized and widely recognized. Numerous research efforts and case studies have validated its feasibility. However, challenges remain, including high computational costs, modeling complexity, applicability to new structural system and the limited investigation of several complex fire-induced phenomena. In summary, there still exists a need for efficient and precise analysis approaches, while the coupling of multiple thermal effects continues to pose a key technical challenge in the fire resistance design.

2.3 Second-Order Direct Analysis (SODA) Method for Fire Resistance Design

The implementation of Second-Order Direct Analysis (SODA) Method for fire resistance design typically involves the following steps. First, the functional requirements, risk assessment, or performance criteria for structural fire safety are established based on fire scenarios, build-environment characteristics, and fuel types. Subsequently, the fire dynamics simulator is employed to determine the heat flux input to the structure, including thermal radiation and convection effects. The SODA method is then applied to perform a thermal-structural coupled analysis, yielding both the thermal and mechanical responses of the structure. These responses are evaluated against the predefined performance criteria to assess compliance. If the criteria are not satisfied, the design process is iteratively refined until all objectives and performance requirements are achieved.

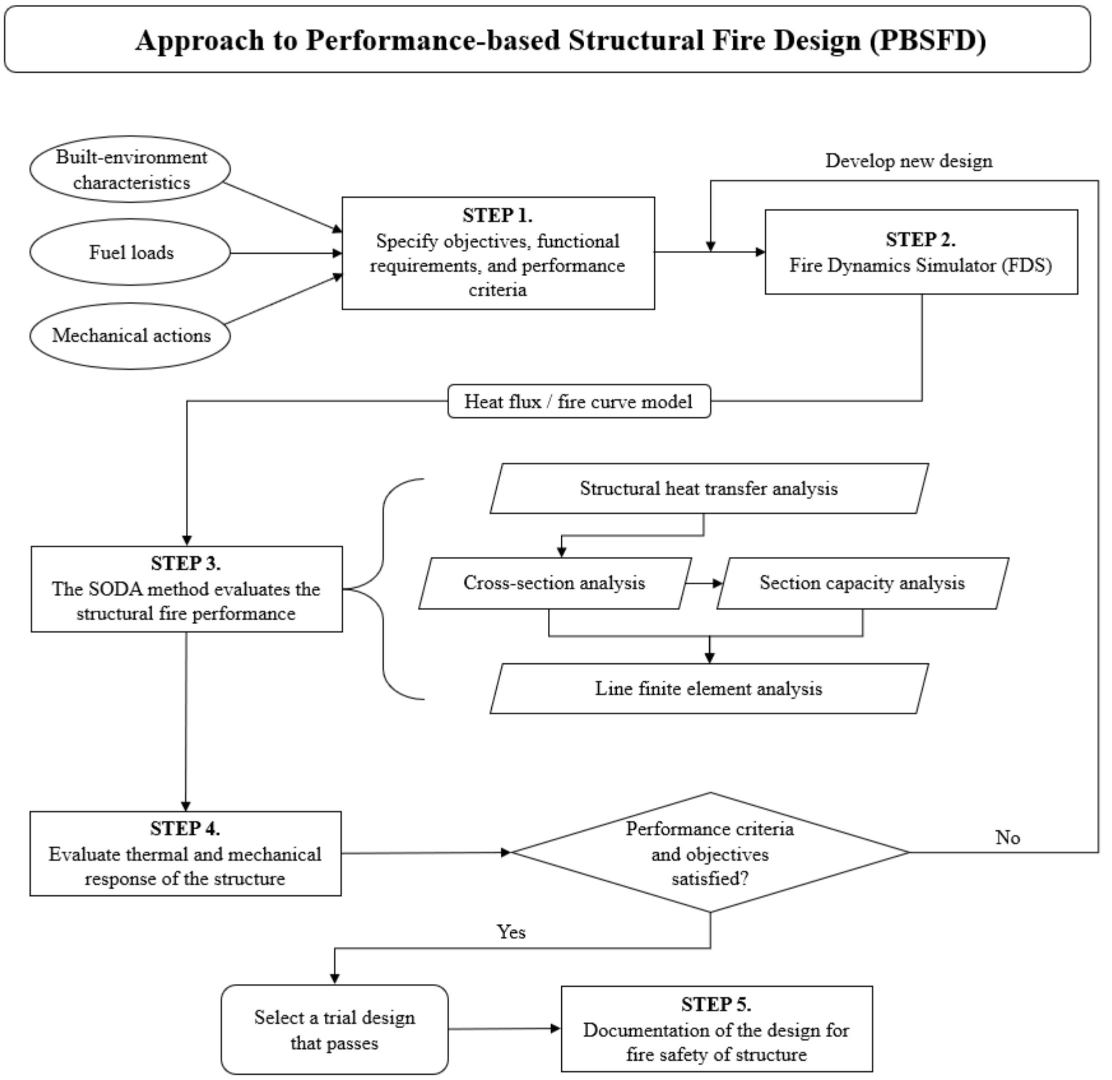

Figure 2-2 Workflow of the SODA method within a PBSFD framework.

As illustrated in Figure 2-2, the SODA method is primarily situated within Step 3 of the PBSFD framework and is utilized for thermal-structural coupling analysis. As a nonlinear analysis approach, the SODA method eliminates the need for equivalent length assumptions, with the final structural evaluation based on cross-sectional inspection. Accordingly, the literature review begins with cross-sectional heat transfer analysis of structures, as the cross-sectional properties are derived from the structural geometry and the temperature-induced material degradation. These properties, combined with the inelastic sectional strength capacity, form the basis for constructing the line finite element formulation used to predict the structural mechanical response. Based on this workflow, the literature review is structured into the following key areas: heat transfer analysis, cross-section analysis, strength capacity evaluation, and the line finite element method.

2.3.1 Heat transfer analysis of structures

The problem of heat transfer in solids is usually typically described by partial differential equations derived from Fourier's law [32]. These governing equations often involve complex boundary conditions in practical engineering applications, making them difficult to solve directly [33]. Irregular boundaries and complex geometries frequently prevent the derivation of analytical solutions [34]. Consequently, various numerical methods have emerged alongside advances in computational technology. These methods (see Figure 2-3) include finite element method (FEM) [35, 36], finite difference method (FDM) [37], and finite volume method (FVM) [38]. Among these, FEM is particularly advantageous due to its ease of implementation and compatibility with irregular and complex boundary conditions. This study primarily employs FEM, and the literature review is accordingly focused on its development and applications.

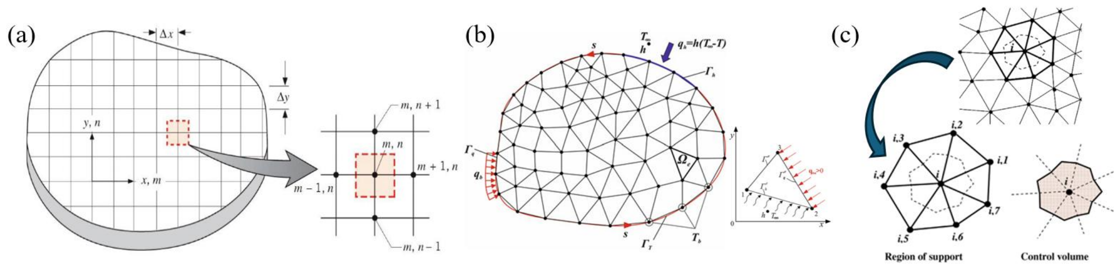

Figure 2-3 Various numerical methods for heat transfer: (a) finite difference method [39]; (b) finite element method [34]; (c) finite volume method [38].

Numerous studies have been conducted on heat transfer analysis under fire conditions. The accurate calculation of the temperature field forms the foundation for subsequent mechanical analysis or thermo-mechanical coupling analysis. Based on the mode of heat flux input in heat transfer analysis using FEM, three primary approaches are commonly used. The first approach involves directly applying heat flux to the structural surface, typically derived from experimental measurements or computational fluid dynamics (CFD) simulations. The second approach utilizes the time-temperature relationships defined by fire curves to model thermal radiation and convection on the structure's surface, followed by internal heat transfer analysis. The third method is the equivalent boundary via adiabatic surface temperature (AST), simplify the thermal environment obtained from CFD or experiments into a single temperature boundary and an equivalent heat transfer coefficient.

The first analysis method more closely reflects real fire scenarios, enabling a comprehensive assessment of fire sources and environmental conditions. For example, Xue et al. [40] simulated fires in enclosed spaces and identified limitations in existing fire models for accurately predicting structural temperatures. Yu et al. [41] investigated the temperature filed of a steel reticulated shell and found that, compared with the standard heating curve, the temperature distribution at the measuring points exhibited localized high-temperature zones. Fan et al. [42] introduced a computational method to attain temperature filed of large-scale steel structure, considering the effects of burning duration and smoke plume behavior. Jiang et al. [43] explored the feasibility of applying dimensionality reduction techniques to heat transfer analysis of structural components under localized fire exposure, demonstrating that such approaches are accurate and effective in reducing computational cost.

The second method employs a fire curve for heat flux input, significantly reducing the analytical workload and enhancing its practical applicability. For instance, Wang et al. [44] investigated the performance of a steel frame subjected to a single-story fire using a parabolic fire curve. Liew et al. [22] adopted the car fire curves reported in ECCS [45] to compute the temperature field and conduct structural fire analysis of a multi-story car park. Liew et al. [46] also introduced the design fire models, radiation models and a “multi-zone” fire model for constructing fire curves specific to each structural element. Parkinson and Kodur [47] summarized fire curves for a range of fire scenarios, based on over 20 years of empirical data, to facilitate their practical application in performance-based design methods. Hamilton et al. [48] developed a probabilistic method for the fire engineering method based on parametric fire curve model to calculate the temperature field. Gernay and Khorasani [49] carried out structural fire design for a steel frame and calculated the temperature filed using design fire curves generated by the software *Ozone*. These heat transfer analysis methods based on real fire curves enable more practical and convenient design while providing relatively accurate predictions of the temperature field.

The last method is proposed by Wickström et al. [50]. To balance realism and computational efficiency, many structural fire design workflows [51, 52] adopt the AST (also called the equivalent-temperature) boundary. By enforcing conservation of net heat flux, the complex thermal environment obtained from CFD or experiments is represented by a single temperature boundary paired with an equivalent heat-transfer coefficient. In practice, the AST method enables the import of CFD- or experimentally derived thermal fields into structural finite-element models without strong coupling, while preserving spatial non-uniformity with modest modelling effort [53].

Nowadays, with the development of structural systems and fire-resistant coating materials of modern structures, heat transfer analysis under fire conditions has become increasingly challenging. In modern steel buildings, composite floor slabs provide effective insulation for steel beams, resulting in highly non-uniform temperature distributions and delayed temperature rise effects [54]. Regarding fire-resistant coating materials, intumescent fire coatings (IFCs) offer excellent protection for steel structures. However, their thickness and thermal conductivity vary during fire exposure [55], complicating the heat transfer analysis using FEM [56]. Therefore, it is necessary to develop refined finite-element-based heat transfer analysis methods to meet these new demands.

2.3.2 Cross-section analysis

Cross-sectional properties are critical to the SODA method employing LFEM, as they play a fundamental role in constructing the line finite element formulation [57]. The total potential energy formulation and the element stiffness matrix strongly depend on bending stiffness, axial stiffness, torsional stiffness, and warping stiffness, all of which are determined by key cross-sectional properties [58, 59]. Currently, various design specifications [60, 61] provide databases containing the basic properties of standard steel sections. However, these databases are often insufficient for line element formulation, as they typically lack advanced cross-sectional properties such as Wagner coefficients, warping constants, and shear center locations. These properties significantly influence the buckling modes and large deflection behavior of structural members [62, 63].

To obtain these cross-sectional properties, efforts have been made to cross-section analysis techniques. For example, Chen et al. [64] proposed an advanced design method applicable to arbitrary sections. Pilkey [65] introduced a finite element method capable of analyzing sections with arbitrary geometries, incorporating torsional and shear properties. Anwar and Najam [66] introduced a practical design method for various cross-sections, accounting for the flexural, shear, and torsional responses of the sections. Liu et al. [62] developed a cross-section analysis algorithm for general steel open sections based on a representation of the geometry using discrete points and segments. Li et al. [67] proposed a novel finite element-based method for calculating the cross-sectional properties of functionally graded sections with arbitrary shapes. These studies have provided valuable insights into cross-section analysis; however, challenges remain under fire scenarios, as these methods are not capable of addressing complex thermal boundary conditions and non-uniform cross-sectional degradation.

Temperature-induced degradation of material properties within steel members is often uneven due to thermal gradients, as illustrated in Figure 2-4(a). Such non-uniformity conditions typically arise when only one face of a column is subjected to fire [68] or when protective coatings are applied asymmetrically [69]. When thermal degradation varies across the section, key parameters such as the shear center, torsional constant, and warping constant become difficult to determine with existing methods. While prior studies [68-70] have made progress in evaluating cross-sectional properties under elevated temperatures, their focus is generally restricted to simple properties (position of stiffness center, flexural stiffness, and axial stiffness) and does not extend to complex parameters such as Wagner coefficients or warping-related characteristics.

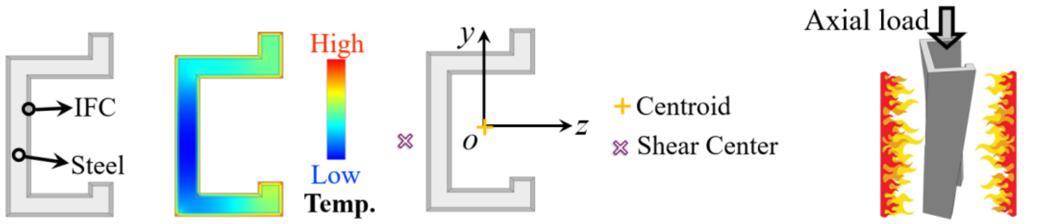

(a) Temperature gradient across the cross-section (b) Shear center offsets from the centroid (c) Complex buckling behavior

Figure 2-4 Challenges in cross-section analysis under fire.

Modern structural applications increasingly employ non-standard or asymmetric cross-sections [62], further complicating stability analysis. For these sections, the shear center often does not align with the centroid (see Figure 2-4(b)), making the member prone to coupled instabilities, such as lateral-torsional buckling under bending and axial-torsional buckling under compressive forces or eccentric loads (see Figure 2-4(c)). To accurately capture such responses, a detailed understanding of advanced sectional properties, including the shear center and Wagner coefficients, is essential [57, 71]. However, under fire exposure where material properties degrade non-uniformly, conventional techniques [59, 70] become inadequate due to their limited flexibility and computational inefficiency. This highlights the need for an advanced cross-section analysis framework capable of accommodating temperature-induced heterogeneity to ensure reliable prediction of structural behavior under fire conditions.

2.3.3 Strength capacity analysis

In SODA method, a structural resistance check is required, which is based on the section strength capacity [72]. The internal forces obtained from the SODA method are used to calculate the section utilization, where a value of less than 1 indicates safety. The section strength capacity is typically defined by the yield surface, which describes a load domain involving two bending moments and an axial load, as shown in Figure 2-5(a). The yield surface effectively represents the ultimate axial-bending capacity within the loading domain. A column's strength is considered safe if the moment-axial load point lies within the yield surface. When the structure is exposed to fire, the material properties degrade, causing a shrinkage of the yield surface. The design load, previously considered safe, is now unsafe, as depicted in Figure 2-5(b).

Several studies have contributed to the development of practical methods for calculating yield surfaces under fires. Caldas, Sousa [73] introduced a procedure for deriving axial force-moment interaction curves for short columns, which was later extended to composite columns with various cross-sections. Law and Gillie [74] proposed a numerical approach to generate 2D yield surfaces at high temperatures using the tangent stiffness matrix of cross-sections. Liu et al. [75] introduced an algorithm to calculate the 3D yield surfaces of steel structures using an elaborated integration method. Li et al. [76] proposed a rigorous cross-section analysis technique to obtain 3D yield surfaces of steel members considering residual stress. Pham et al. [77] presented a yield design method for directly calculating 2D yield surfaces for sections exposed to fire. Albero et al. [78] addressed temperature variations across components by assigning equivalent uniform temperatures, leading to a simplified design approach.

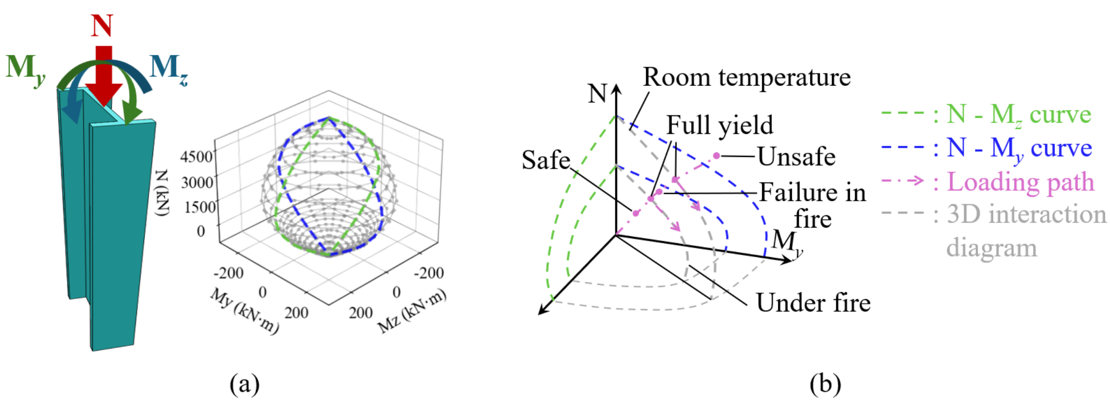

Figure 2-5 Strength capacity of steel structure: (a) Yield surface; (b) Section capacity check under fire.

While these studies provide useful insights into analysis of yield surfaces, they either mainly focus on ambient behavior or neglect biaxial bending and compression. Additionally, simplifications such as assuming uniform temperature distribution in parts and modeling the yield surface as polylines may result in overly inaccurate estimates. Therefore, an accurate design method is needed to calculate the 3D yield surfaces of steel columns under fire exposure, enabling section capacity checks for practical design using the SODA method in fire conditions.

2.3.4 Line finite element method

Morden structural design approaches for steel members and frames, such as the SODA method in the Hong Kong Steel Code [79], Direct Analysis Method (DAM) in AISC-360 [60] and the second-order design approach in Eurocode 3 [61], demand accurate nonlinear analysis of steel structures that directly accounts for buckling behaviors. To fulfill such requirements, several numerical methods have been developed and widely used in current design routines, including sophisticated finite-element method (SFEM) [80-82], finite-strip element (FSM) [83-85] and line finite element method (LFEM) [59, 86, 87].

SFEM and FSM are widely used, employing numerous shell elements, solid elements, or strips to develop detailed finite element models without relying on simplified assumptions. These approaches account for all factors influencing structural behavior, including initial imperfections, second-order effects, and residual stresses. While they provide precise predictions, they are computationally intensive and typically applied to isolated members [56, 88], limiting their practicality for steel frame structural design. Consequently, researchers have shifted focus to more efficient and reliable computational methods.

LEFM, which utilizes beam-column elements, is a more practical and efficient design method for steel structures. By employing nonlinear beam-column elements, such as Euler beam or Timoshenko beam elements, each member requires only one element [89, 90] to several dozen elements [62, 63] to fully capture the instability and geometric nonlinear deformation of the structure. In contrast to SFEM or FSM, which often require hundreds or thousands of elements per member, the reduction in element count with LFEM significantly decreases the size of the global stiffness matrix, enhancing computational efficiency and enabling the practical design of large-scale frame structures. Additionally, LFEM, which is also suitable for analyzing steel structures under fire, continues to evolve, providing a foundation for the development of SODA design methods under fire conditions.

Literature review of LFEM considering fire conditions are summarized as below. Chan and Chan [91] proposed a second-order elastic-plastic beam-column element for the analysis of 2D steel frames under fire, based on the refined plastic hinge method, offering engineers a practical means for design. El-Tawil and Deierlein [92] developed a beam-column element for analyzing 3D composite frames, accounting for the inelastic behavior of line elements. Liew et al. [22] introduced an LFEM method for the performance-based fire design of steel frames, considering plastic deformation, thermal expansion, and natural fire scenarios. Iu and Chan [93] presented a beam-column element to address the geometric and material nonlinearities of steel structures under fire, which has been shown to exhibit good convergence rates and require less computational effort. Landesmann et al. [94] proposed a beam-column element that accounts for the nonlinear parabolic model of inelastic stiffness reduction in steel. Li et al. [95] proposed an Euler-Bernoulli beam element to analyze 2D restrained steel beams under fire. Heidarpour and Bradford [96] developed a semi-analytical non-discretization method based on line element formulation for steel members under fire and explosion. Sun et al. [97] conducted progressive collapse analysis of steel structures via 3-nodes beam-column elements. Jiang and Usmani [98] extended the beam-column elements in OpenSees to analyze steel beams under localized fire. Possidente, Tondini [99] introduced a 3D beam element that accounts for the degradation of torsional strength and stiffness in steel members under fire, and demonstrated its accuracy through validation. Chen et al. [100] proposed an advanced line element for analyzing steel structures with non-symmetric cross-sections under elevated temperatures.

These studies have significantly advanced the nonlinear analysis of steel structures under fire conditions. However, fiber-based theories and semi-analytical or semi-empirical methods developed for beam-column elements often remain impractical for engineering design, as they typically incur high computational costs, rely on subjective judgment, or require the use of SFEM to determine temperature distributions and plastic hinge stiffness across cross-sections. Looking ahead, efficient modelling approaches, more comprehensive consideration of fire-induced effects, and the development of direct and efficient LFEM are expected to facilitate fire resistance design of steel structures.

CHAPTER 3.

REFINED HEAT TRANSFER ANALYSIS USING FINITE ELEMENT METHOD

3.1 Introduction

Fire resistance design is a complex multi-physics problem that spans fire dynamics, heat transfer, and structural mechanics. In practice, most engineers are trained in either fire or structural engineering, with limited cross-disciplinary integration [7]. Therefore, the absence of an integrated capability framework necessitates pragmatic, reliable simplifications of fire–structure interaction for design purposes [101].

Fortunately, heat-transfer analysis serves as an essential bridge between fire dynamics and structural mechanics and as a basis for structural fire design. Once the thermal boundary conditions are determined, the internal temperature field of the structure can be derived. In finite-element-based heat transfer modelling, thermal boundaries are typically prescribed using three strategies, distinguished by how the incident heat flux is defined:

The first approach is the direct heat-flux specification. Incident heat flux is applied to the exposed surfaces, with inputs taken from experiments or from computational fluid dynamics (CFD). This route more closely represents actual fire environments and allows explicit treatment of fire sources and enclosure effects. For example, Salminen and Hietaniemi [102] employed SAFIR for the CFD simulation to demonstrate a fire resistance design for a stadium's steel structure. Khan et al. [103] reviewed the evolution of fire models for fire-resistance design and noted that CFD provides higher-resolution thermal boundary conditions. However, due to the fire and structural domains differ in spatial and temporal resolution, tightly coupling CFD with FEMs to simulate fire and structural responses concurrently remains challenging.

The second method is the fire-curve-based boundary conditions. Here, time–temperature relationships (fire curves) prescribe surface radiation and convection, after which internal conduction is solved. This approach markedly reduces modelling effort and is well suited to design practice. Using this framework, Kuehnen et al. [104] employed an equivalent standard fire curve to conduct fire resistance design of RC beams. Hurley and Rosenbaum [2] introduced a five-stage fire curve for use in performance-based fire protection design. Gernay and Khorasani [49] used software Ozone to obtain the gas temperature-time curves of Fire spread and conducted fire resistance design of composite buildings. In practice, such fire-curve-driven analyses offer a convenient workflow while delivering temperature predictions of sufficient fidelity for design.

The last approach is the equivalent boundary via adiabatic surface temperature (AST), which is proposed by Wickström et al. [50]. To balance realism and computational efficiency, many fire resistance design workflows adopt the AST (also called the equivalent-temperature) boundary. By enforcing conservation of net heat flux, the complex thermal environment obtained from CFD or experiments is reduced to a single temperature boundary paired with an equivalent heat-transfer coefficient. In practice, the AST method enables the import of CFD or experimentally derived thermal fields into FEMs without strong coupling, while preserving spatial non-uniformity with modest modelling effort. Although reliance on AST measurements and fire tests incurs computational and experimental costs, existing studies [105-108] have demonstrated the robustness of this approach for fire resistance design.

Therefore, this study employs the latter two methods described above as thermal-boundary inputs for the heat transfer analysis of steel structures exposed to fire. Given their advantages, ease of implementation, and suitability for irregular or complex boundaries (see Section 2.3.1), the FEM is used in this study for the heat transfer analysis of fire resistance design. Given the adoption of line elements in fire resistance design with SODA, the cross-sectional temperature distribution is of critical importance for subsequent cross-sectional analysis. Therefore, this chapter focuses on presenting the two-dimensional transient heat conduction method based on the FEM, thereby laying a theoretical foundation for the subsequent mechanical analysis of cross-sectional fibers.

A primary challenge lies in the complexity of determining the temperature field in steel structures protected by intumescent fire coatings (IFCs) when applying the FEM [109, 110]. By swelling to form a low-density, foamed char with low thermal conductivity, IFC can significantly prevent degradation of steel, thereby IFC has become one of the most widely used passive fire protection materials for steel structures [111]. As shown in Figure 3-1, the foaming reaction of the IFC involves complex chemical processes, including melting, reaction, and charring of the coating, with each stage exhibiting distinct thermal properties [112]. The variations in thermal conductivity and volume of IFC complicate the resolution of temperature field in steel members during transient heat transfer analysis [113].

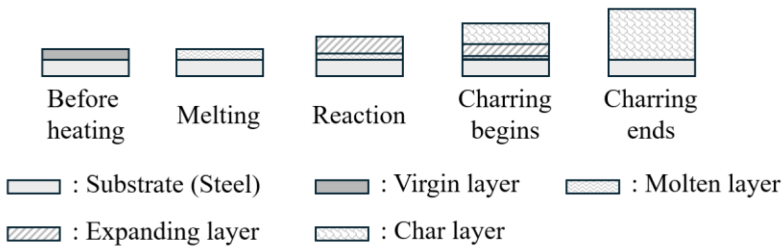

Figure 3-1 Foaming reaction of the IFC.

Currently, BS EN 13381–8 [114] offers a practical approach by considering IFC with a constant equivalent thickness, while the effective thermal conductivity varies with temperature. This method, which uses temperature-dependent thermal conductivities, has been validated by many scholars [55, 109, 115]. Nevertheless, the variation in thermal conductivity, especially discontinuous changes in some simplified models [116], increases the difficulty of achieving convergency results and reduces computational efficiency in transient heat transfer analysis [35, 117]. To address this, the generalized Crank-Nicolson method [118, 119] is introduced in this chapter to enhance the heat transfer analysis using FEM, making it more suitable for these thermal conductivity models.

This chapter first introduces the governing equations for heat transfer analysis, followed by the finite element assembly procedure. A refined heat transfer method is developed, incorporating the equivalent thermal conductivity of IFC. The stability of the generalized Crank–Nicolson method is evaluated, and the optimal coefficients are identified through parametric analysis. The proposed approach is validated using multiple examples and integrated into a new structural analysis software, MSASect2. This software is developed and released by the authors to provide a user-friendly tool and to enhance the reproducibility of this study.

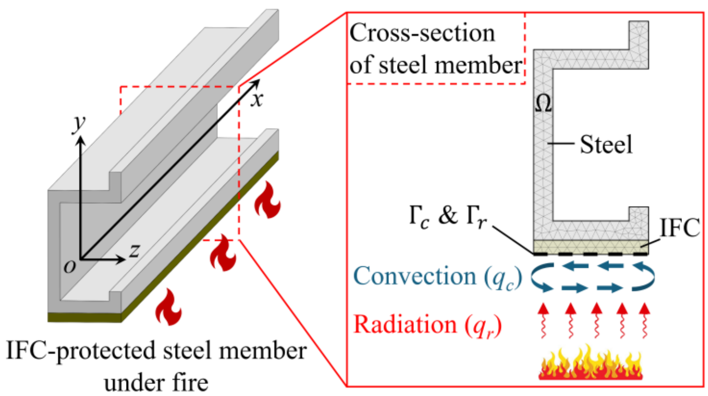

Figure 3-2 Finite element-based heat transfer analysis.

3.2 Governing Equations

This section illustrates the governing equations for the transient heat transfer analysis. Because the SODA method assumes that members are slender, heat transfer within the cross-section plays a dominant role compared with conduction along the longitudinal direction. Therefore, this study primarily focuses on the analysis of cross-sectional heat transfer. The formulas for transient heat transfer analysis are presented as follows.

Heat transfer within the cross-section (as shown in Figure 3-2) is described by the following equation [120, 121]:

$$\frac{\partial}{\partial y}\left(k\frac{\partial T}{\partial y}\right)+\frac{\partial}{\partial z}\left(k\frac{\partial T}{\partial z}\right)+q_{bc}=\rho c\frac{\partial T}{\partial t} \tag{3.1}$$

where T denotes the temperature within the cross-section at time t; k is the thermal conductivity; c and ρ are the specific heat and density of steel, respectively; q_{bc} represents the direct boundary flux of the cross-section. The temperature field in the e^{th} element is calculated as below:

$$T^e(y,z)=\sum_{i=1}^{n}T_i^e\cdot N_i^e(y,z)=\mathbf{N}^e\mathbf{T}^e \tag{3.2}$$

in which, n refers to the number of the triangular element nodes; T_i^e is the nodal temperature; $N_i^e(y,z)$ represents the shape function of linear triangular element, which is a practical and efficient triangular 2D element for heat transfer analysis and has a high adaptability to mesh sections with irregular shapes [117]. With Galerkin method, Eq. (3.1) can be discretized within the element domain Ω^e by nodal temperatures and shape functions:

$$\int_{\Omega^e}\left\{\rho c\frac{\partial T^e}{\partial t}-q_{bc}-\left[\frac{\partial}{\partial y}\left(k\frac{\partial T^e}{\partial y}\right)+\frac{\partial}{\partial z}\left(k\frac{\partial T^e}{\partial z}\right)\right]\right\}N_i^e(y,z)dydz=0 \qquad (3.3)$$

Using the Green's theorem, the third and fourth terms of above equation are transformed into:

$$\int_{\Omega^e}\left[\frac{\partial}{\partial y}\left(k\frac{\partial T^e}{\partial y}\right)+\frac{\partial}{\partial z}\left(k\frac{\partial T^e}{\partial z}\right)\right]N_i^e dydz=\int_{\Gamma^e}\left(-k\frac{\partial T^e}{\partial z}dy+k\frac{\partial T^e}{\partial y}dz\right)N_i^e \qquad (3.4)$$

where Γ^e is boundary of the element. The left side of Eq. (3.4) is the integration over element domain Ω^e and the right-hand side denotes the integration over element boundary Γ^e. Perform partial integration on the left side of Eq. (3.4):

$$\begin{aligned}&\int_{\Omega^e}\left[\frac{\partial}{\partial y}\left(k\frac{\partial T^e}{\partial y}\right)+\frac{\partial}{\partial z}\left(k\frac{\partial T^e}{\partial z}\right)\right]N_i^e dydz=\\&-\int_{\Omega^e}\left(k\frac{\partial T^e}{\partial y}\frac{\partial N_i^e}{\partial y}+k\frac{\partial T^e}{\partial z}\frac{\partial N_i^e}{\partial z}\right)dydz+\int_{\Gamma^e}\left(-k\frac{\partial T^e}{\partial z}dy+k\frac{\partial T^e}{\partial y}dz\right)N_i^e\end{aligned} \qquad (3.5)$$

Substitute the result into Eq. (3.3), the following equation is obtained:

$$\begin{aligned}&\int_{\Omega^e}\rho c N_i^e N_j^e dydz\frac{\partial T_j^e}{\partial t}\\&+\int_{\Omega^e}\left(k\frac{\partial T^e}{\partial y}\frac{\partial N_i^e}{\partial y}+k\frac{\partial T^e}{\partial z}\frac{\partial N_i^e}{\partial z}\right)dydz-\int_{\Omega^e}N_i^e q_{bc}dydz\\&=\int_{\Gamma^e}\left(-k\frac{\partial T^e}{\partial z}dy+k\frac{\partial T^e}{\partial y}dz\right)N_i^e\end{aligned} \qquad (3.6)$$

The second term of this equation denotes the thermal conduction within the element domain Ω^e, while the term on the other side represents the thermal conduction at the element boundary Γ^e. The right side of Eq. (3.6) is rewritten as below:

$$\begin{aligned}&\int_{\Gamma^e}\left(-k\frac{\partial T^e}{\partial z}dy+k\frac{\partial T^e}{\partial y}dz\right)N_i^e=\int_{\Gamma^e}\left(k\frac{\partial T^e}{\partial z}n_z ds+k\frac{\partial T^e}{\partial y}n_y ds\right)N_i^e\\&=\int_{\Gamma^e}q_n N_i^e ds\end{aligned} \tag{3.7}$$

where n_y and n_z are the components of a unit vector directed outward from the section boundary; q_n denotes the heat flow resulting from boundary conditions other than the direct heat flux q_{bc}. In most heat transfer simulation models [115, 122, 123], thermal convection and radiation are considered for q_n. The CFD results and experimental data are also compatible with this boundary. q_n in this study consists of two components: convection (q_c) and radiation (q_r), as shown in Figure 3-2. The convective heat flux at the boundary Γ^c can be computed by

$$\left.\left(k\frac{\partial T}{\partial z}n_z+k\frac{\partial T}{\partial y}n_y\right)\right|_{\Gamma^c}=h\left(T_\infty-T|_{\Gamma^c}\right) \tag{3.8}$$

where T_∞ represents the environment temperature; h is the convective heat transfer coefficient, taken as 25 W/(m^2·°C) [124]. The radiation heat transfer between the cross-section and environment can be expressed as

$$\left.\left(k\frac{\partial T}{\partial z}n_z+k\frac{\partial T}{\partial y}n_y\right)\right|_{\Gamma^c}=\sigma\varepsilon\left(T_\infty{}^4-T|_{\Gamma^c}{}^4\right) \tag{3.9}$$

in which, σ is the Stefan-Boltzmann constant; ε denotes the emissivity coefficient, and taken as 0.92 [125] in this study. The radiation heat transfer can also be expressed by

$$\sigma\varepsilon\left(T_\infty{}^4-T|_{\Gamma^c}{}^4\right)=\sigma\varepsilon\left(T_\infty{}^2+T|_{\Gamma^c}{}^2\right)\left(T_\infty+T|_{\Gamma^c}\right)\left(T_\infty-T|_{\Gamma^c}\right) \tag{3.10}$$

Considering the difference between T_∞ and the temperature of boundary Γ^c is not significant, the radiation is linearized as [126]

$$\left.\left(k\frac{\partial T}{\partial z}n_z+k\frac{\partial T}{\partial y}n_y\right)\right|_{\Gamma^c}=4\sigma\varepsilon T_\infty^{\ 3}\left(T_\infty-T|_{\Gamma^c}\right) \tag{3.11}$$

Providing the boundary conditions of Eqs. (3.8) and (3.11), Eq. (3.7) becomes:

$$\int_{\Gamma^e}\left(-k\frac{\partial T^e}{\partial z}dy+k\frac{\partial T^e}{\partial y}dz\right)N_i^e=\int_{\Gamma^e}h\left(T_\infty-T^e\right)N_i^e ds+\int_{\Gamma^e}4\sigma\varepsilon T_\infty^{\ 3}\left(T_\infty-T^e\right)N_i^e ds \tag{3.12}$$

Since direct heat flux q_{bc} is not commonly used in simulation, after discarding q_{bc} and considering thermal convection and radiation, Eq. (3.6) can be rewritten as

$$\begin{aligned}&\int_{\Omega^e}\rho c N_i^e N_j^e dydz\frac{\partial T_j^e}{\partial t}+\int_{\Omega^e}\left(k\frac{\partial T^e}{\partial y}\frac{\partial N_i^e}{\partial y}+k\frac{\partial T^e}{\partial z}\frac{\partial N_i^e}{\partial z}\right)dydz\\&=\int_{\Gamma^e}h\left(T_\infty-T^e\right)N_i^e ds+\int_{\Gamma^e}4\sigma\varepsilon T_\infty^{\ 3}\left(T_\infty-T^e\right)N_i^e ds\end{aligned} \tag{3.13}$$

For realistic fire scenarios, the thermal boundary conditions of convection and radiation (Eqs. (3.8)and (3.11)) in this study can be integrated with computational fluid dynamics (CFD) results to address actual fire conditions. This governing equation can be expressed by matrix form as shown below:

$$\mathbf{M}^e\frac{d\mathbf{T}^e}{dt}+\mathbf{K}^e\mathbf{T}^e=\mathbf{f}^e \tag{3.14}$$

The matrices and vectors are defined as

$$\mathbf{M}^e=\int_{\Omega^e}\rho c\left[\mathbf{N}^e\right]^{\mathrm{T}}\mathbf{N}^e dydz \tag{3.15}$$

$$\mathbf{K}^e=\int_{\Omega^e}\left[\mathbf{B}^e\right]^{\mathrm{T}}\mathbf{D}^e\mathbf{B}^e dydz+\int_{\Gamma^e}h\left[\mathbf{N}^e\right]^{\mathrm{T}}\mathbf{N}^e ds+\int_{\Gamma^e}4\sigma\varepsilon T_\infty^{\ 3}\left[\mathbf{N}^e\right]^{\mathrm{T}}\mathbf{N}^e ds \tag{3.16}$$

where $\mathbf{B}^e$ is the spatial derivatives matrix; $\mathbf{D}^e$ is the thermal conductivity matrix and expressed as

$$\mathbf{D}^e = \begin{bmatrix} k & 0 \\ 0 & k \end{bmatrix} \tag{3.17}$$

The nodal load vector is defined as

$$\mathbf{f}^e = \int_{\Gamma^e} hT_\infty \left[\mathbf{N}^e\right]^{\mathrm{T}} \mathbf{N}^e ds + \int_{\Gamma^e} 4\sigma\varepsilon T_\infty{}^4 \left[\mathbf{N}^e\right]^{\mathrm{T}} \mathbf{N}^e ds \tag{3.18}$$

in which, the left term represents the boundary convective flux vector, and the right term represents the radiative flux vector.

3.3 Finite Element Assembly Procedure

3.3.1 Generalized Crank-Nicolson approach

The generalized Crank-Nicolson method [118, 119] is introduced to improve the transient heat transfer analysis. According to this method, the temperature at $(s+1)^{th}$ time step is expressed by

$$\left\{\mathbf{T}^e\right\}^{s+1} = \Delta t\left[\tau\left\{\dot{\mathbf{T}}^e\right\}^{s+1} + \left(1-\tau\right)\left\{\dot{\mathbf{T}}^e\right\}^{s}\right] + \left\{\mathbf{T}^e\right\}^{s} \tag{3.19}$$

where τ ($0 \le \tau \le 1$) is the parameter controlling the stability of solutions. Providing Eq. (3.14), the governing equation is rewritten as

$$\left(\frac{1}{\Delta t}\mathbf{M}^e + \tau\mathbf{K}^e\right)\left\{\mathbf{T}^e\right\}^{s+1} = \left[\frac{1}{\Delta t}\mathbf{M}^e - (1-\tau)\mathbf{K}^e\right]\left\{\mathbf{T}^e\right\}^{s} + (1-\tau)\left\{\mathbf{f}^e\right\}^{s} + \tau\left\{\mathbf{f}^e\right\}^{s+1} \tag{3.20}$$

For better stability and convergence, the optimal value of τ is investigated to ensure accuracy and stability results. As demonstrated by Section 3.3.3, $\tau = 0.9$ is selected. When $\tau = 1$, Eq. (3.20) is fully implicit and expressed as follows:

$$\left(\frac{1}{\Delta t}\mathbf{M}^e + \mathbf{K}^e\right)\left\{\mathbf{T}^e\right\}^{s+1} = \frac{1}{\Delta t}\mathbf{M}^e\left\{\mathbf{T}^e\right\}^{s} + \left\{\mathbf{f}^e\right\}^{s+1} \tag{3.21}$$

The temperature at each time step is obtained by solving the equation using the Gauss-Seidel method, which can provide a stable solution when the thermal conductivity coefficient is updated with temperature.

3.3.2 Equivalent thermal conductivity model for IFC

IFC material undergoes complex chemical reactions and changes in physical properties at high temperatures. Once the temperature exceeds 200 °C, thermal decomposition occurs, and the components gradually react, leading to changes in thickness and thermal conductivity [112]. This characteristic makes it difficult to accurately predict the performance of IFC. A practical method introduced by BS EN 13381–8 [114], estimates the equivalent thermal conductivity of IFC by assuming that the IFC maintains a fixed thickness, equal to the dry film thickness (DFT), while its equivalent thermal conductivity continuously varies with temperature. This approach is convenient for engineering design and has been proven accurate [55, 115].

With this in mind, some scholars have proposed various equivalent thermal conductivity models for IFC. For instance, Li et al. [113] proposed a constant model that considers the equivalent thermal conductivity as a constant, which is defined as

$$k_e(T) = \frac{1}{200}\int_{400}^{600} k(T)dT \tag{3.22}$$

in which, k_e(T) denotes the effective thermal conductivity. Another model is the temperature-dependent three-stage model [116], given by

$$k_e(T)=\begin{cases}\dfrac{1}{200}\displaystyle\int_{100}^{300}k(T)dT, T\le 300\\ \dfrac{1}{100}\displaystyle\int_{300}^{400}k(T)dT, 300<T<400\\ \dfrac{1}{200}\displaystyle\int_{400}^{600}k(T)dT, 400\le T\end{cases} \tag{3.23}$$

According to Eq.(3.21), by updating k of the s^{th} step based on $k_e(T)$, the updated $\mathbf{K}^e$ can be calculated for the $(s+1)^{th}$ step. Therefore, the heat transfer analysis method can be applied to various thermal conductivity models.

3.3.3 Stabilization of the iteration method

The stability of the generalized Crank-Nicolson method is evaluated in this section. The parameter τ ($0\le \tau \le 1$) in Eq. (3.19) controls the stability of the solutions [127]. When $\tau = 0$, the equation is fully explicit. The cross-section in Figure 3-3 is investigated, with the thickness t_w set to 15 mm in this example. The DFT is set to 2 mm and the equivalent constant thermal conductivity follows the discontinue three-stage model in Eq.(3.23). Under the influence of ISO 834 standard fire on one side, the temperatures at two key points (as depicted in Figure 3-4) are calculated using the Crank-Nicolson method and compared with the benchmark solutions obtained through SFEM. Different values of τ are investigated to find the optimal parameter. The number of time steps is the same for each method.

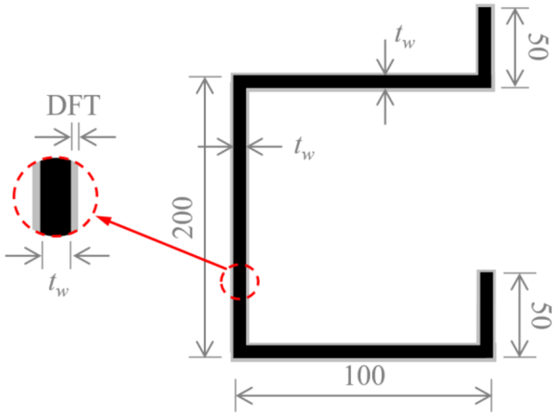

Figure 3-3 Dimensions (mm) of the cross-section.

The results are summarized in Figure 3-4. It is notable that when the equivalent thermal conductivity of IFC varies discontinuously with temperature, the traditional explicit method cannot achieve a convergent solution, therefore, the results for $0 \leq \tau < 0.30$ are not shown in the figure. As τ gradually increases, the temperatures obtained by the Crank-Nicolson method approach benchmark solutions, demonstrating improved stability and accuracy. When τ is equal to 0.9, the result is most accurate, with a maximum error of 4.6%. However, when τ is 1, that is, when the governing equation (3.21) becomes fully implicit, the error actually increases. It can be concluded that $\tau = 0.9$ can be used as the optimal value to address discontinuous changes in thermal conductivity. Compared to explicit methods, this approach demonstrates higher stability and accuracy. Therefore, $\tau = 0.9$ is adopted in the following examples.

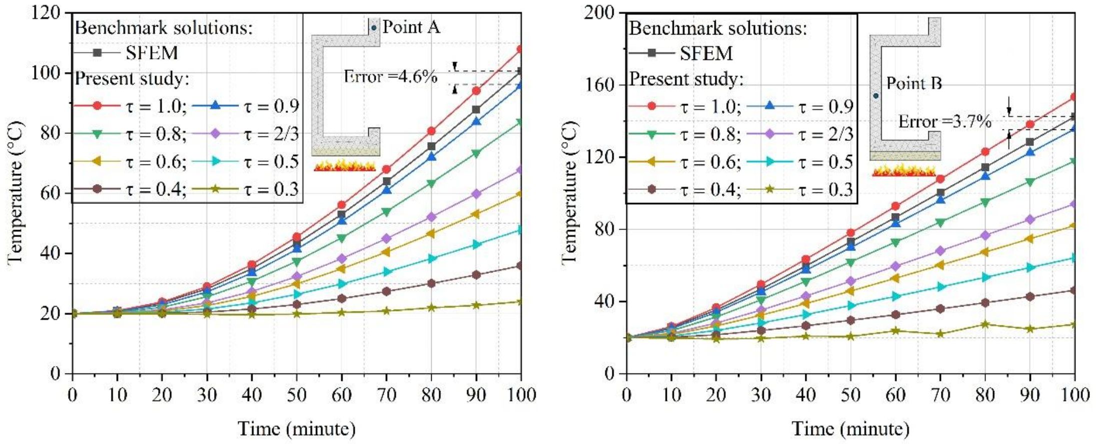

(a) Temperature of point A (b) Temperature of point B

Figure 3-4 Temperature obtained by SFEM and generalized Crank-Nicolson method.

3.4 Validation Examples

Three examples are provided in this chapter to validate the proposed heat transfer analysis method. The examples include the analysis of temperature filed of IFC-protected steel members under fire, steel beams under localized fire and concrete-encased steel columns under standard fire tests. These examples cover different fire conditions and protection conditions, which can fully verify the proposed heat transfer analysis method.

3.4.1 Temperature field of IFC-protected steel members under fire

The temperature field obtained using the proposed approach is compared with experimental results to verify the accuracy of the heat transfer analysis method. According to the experiment reported by Li et al. [113], the temperatures at key points of four different IFC-protected specimen types are calculated and compared with the fire test results. The dimensions of the specimens are depicted in Figure 3-5. The target dry film thicknesses (DFTs) of IFC are indicated by their specimen ID. For example, “A07T1” denotes a specimen type of “A”, a DFT of 7 mm, and “T1” refers to the sample number. Additionally, "E09T1" and "E15T3" correspond to hot-rolled I-shaped steel sections (138×360×12×15.8 mm). These specimens were exposed to the ISO 834 standard fire condition [128], and their temperatures were recorded using thermocouples.

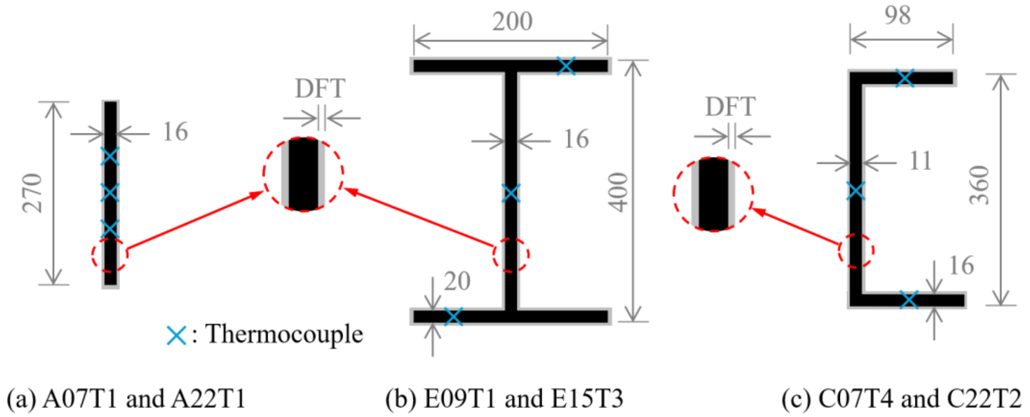

Figure 3-5 Dimensions of the test specimens in Ref. [113].

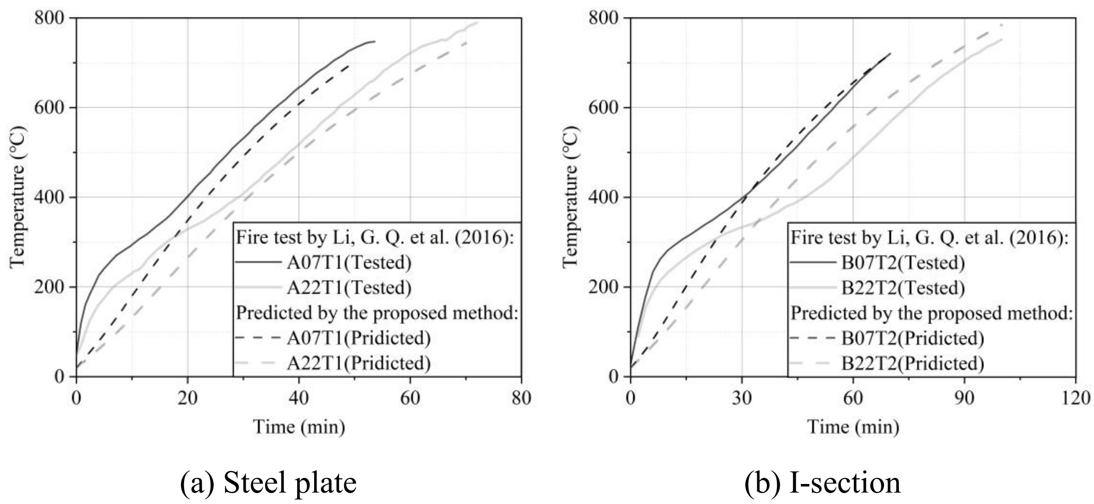

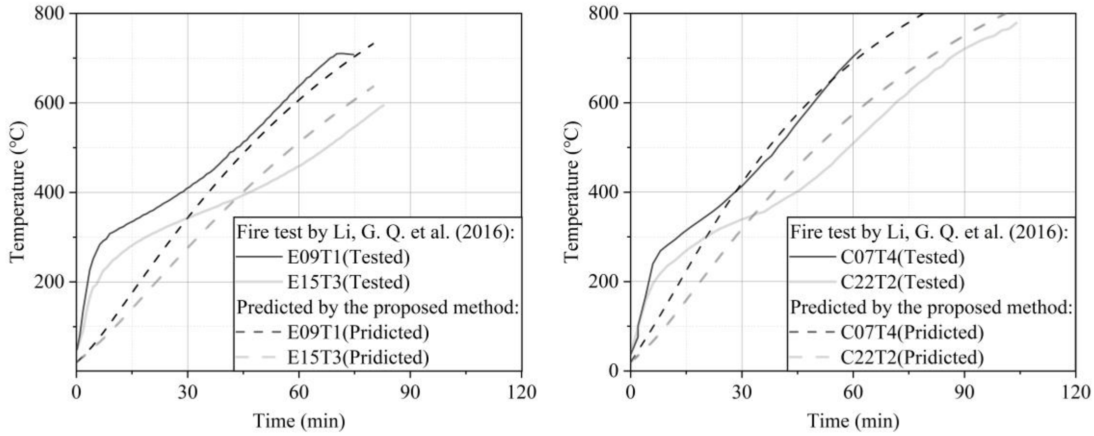

(c) H-section (d) C-section

Figure 3-6 Comparison of experimental and calculated temperature.

The temperature of each specimen was measured by averaging the measurements from three thermocouples. The experimental results and calculations obtained via the method proposed in this study are presented in the Figure 3-6. The constant thermal conductivity model, as illustrated by Li et al. [113], is utilized for the calculations, as constant model is more suitable for water based coatings. The model proposed by Lie [129] is adopted to characterize the thermal parameters of steel at elevated temperatures. The thermal conductivity k [W/(m×°C)], specific heat capacity c [J/(kg×°C)] and density ρ (kg/m^3) of steel at high temperatures are calculated as

$$k = \begin{cases} -0.022T + 48, 0 \le T \le 900 \\ 28.2, T > 900 \end{cases} \tag{3.24}$$

$$\rho c = \begin{cases} (0.004T + 3.3) \times 10^6, 0 \le T \le 650 \\ (0.068T - 38.3) \times 10^6, 650 < T \le 725 \\ (-0.086T + 73.35) \times 10^6, 725 < T \le 800 \\ 4.55 \times 10^6, T > 800 \end{cases} \tag{3.25}$$

The agreement between the measured and calculated results is satisfactory for all specimens. The temperature from the fire test rises more quickly than that predicted by the proposed method. This discrepancy is due to the unstable heating of the fire furnace, where the actual temperature significantly exceeded the standard fire curve at the start of the test [113]. Additionally, this discrepancy can also be due to the use of the average values of several thermocouples in the measurement, uneven heating of the fire furnace leading to uneven temperature rise. Overall, the proposed heat transfer analysis method is validated.

3.4.2 Steel beams subjected to localized fire

This example employs the heat transfer analysis method presented in this study to replicate the fire test conducted by Li et al. [130]. The setup of the fire test is depicted in Figure 3-7, where an H250×250×8×12 steel beam is exposed to non-uniform fire conditions. The top flange of the beam was wrapped with a ceramic fiber blanket to provide approximate adiabatic conditions. Several thermocouples were positioned at mid-span to monitor the temperature distribution within the cross-section.

The beam underwent a heating and cooling fire test, and the average furnace temperature was recorded, as shown by the black dashed line in Figure 3-8. The comparison between the calculated and experimental results is presented in Figure 3-8, demonstrating good agreement. The primary source of error may stem from the blanket's imperfect adiabatic properties. Despite this, the comparison validates the accuracy of the heat transfer method.

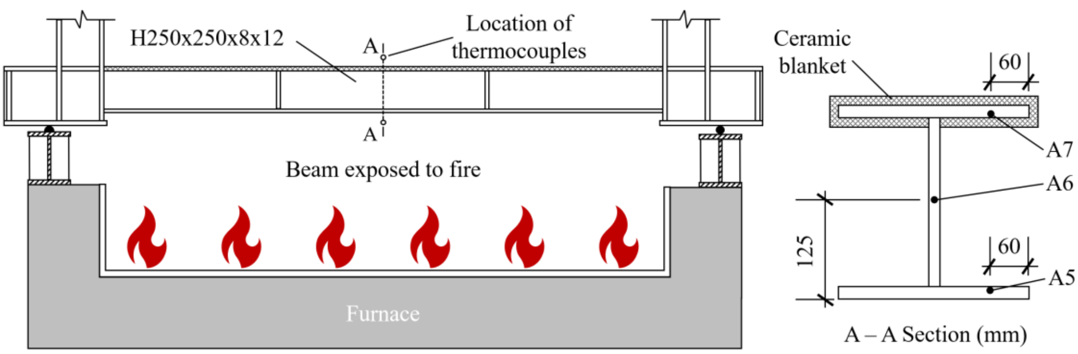

Figure 3-7 Fire test setup and locations of thermal couples.

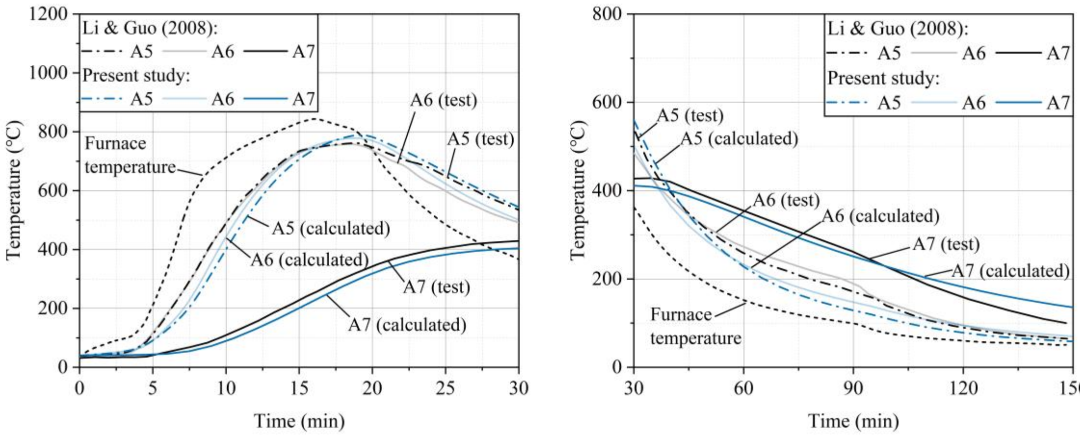

(a) Temperature - time curves before 30 min

(b) Temperature - time curves after 30 min

Figure 3-8 Comparison between the fire test and the proposed method.

3.4.3 Concrete-encased steel columns under standard fire tests

This example calculates the temperature filed of a concrete-encased steel column reported by Pan et al. [131]. The geometric dimensions of the column and the arrangement of thermocouples are shown in Figure 3-9. The column underwent an ISO 834 standard fire test in the fire furnace. Concrete undergoes water evaporation at 100 °C, an endothermic process that influences temperature field distribution. Lie's thermal parameter model [129] for concrete incorporates this factor and has been employed in several studies [131-133], yielding accurate calculation results. Therefore, this model is also adopted in the present study.

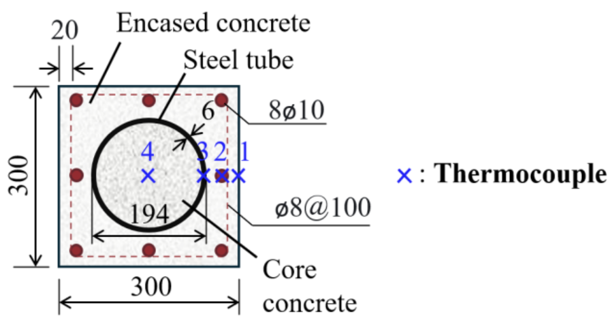

Figure 3-9 Dimensions arrangement of thermocouples (Unit: mm).

The average temperature of the furnace is calculated by

$$\text{Ascending stage:} \quad T = T_0 + 345\log_{10}\left(8t+1\right) \tag{3.26}$$

$$\text{Descending stage:} \quad T = \begin{cases} T_h - 10.417\left(t-t_h\right), t_h \le 30 \\ T_h - 4.167\left(3-t_h/60\right)\left(t-t_h\right), 30 < t_h < 120 \\ T_h - 4.167\left(t-t_h\right), t_h \ge 120 \end{cases} \tag{3.27}$$

where T denotes the fire temperature (in °C, above T_0); T_0 and T_h represent the room temperature and the maximum fire temperature, respectively; t (min) is the elapsed time from the start of the fire; t_h (min) is the duration of the ascending stage.

The fire-temperature curves for EC-45-100-4 and CC-45-100-4 are calculated using the proposed numerical method and compared with those recorded by the thermocouples. The results are depicted in Figure 3-10, where the scatter points represent the thermocouple measurements, and the lines represent the predicted curves. Based on the comparison, it can be concluded that the proposed approach is capable of accurately predicting the temperature evolution over time.

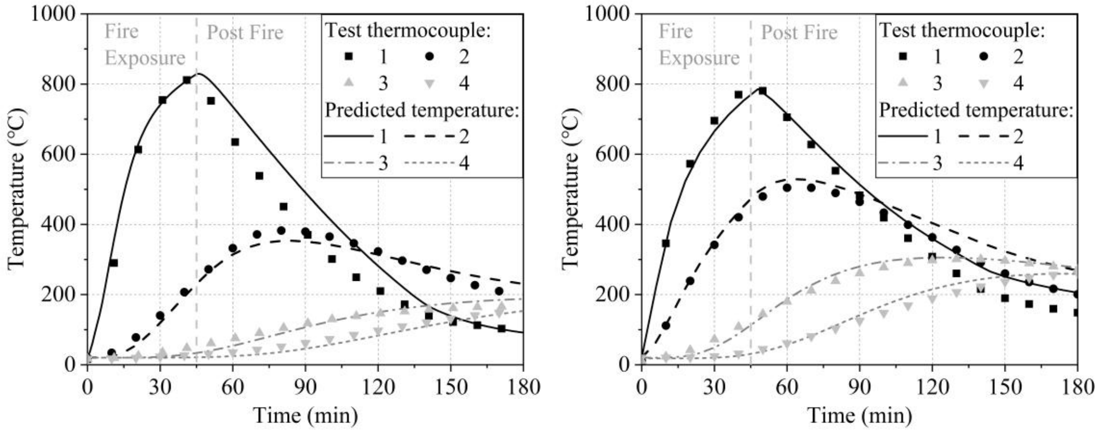

(a) EC-45-100-4 (b) CC-45-100-4

Figure 3-10 Comparison between predicted values and thermocouple measurements.

3.5 Software Implementation

To provide engineers with more accessible and efficient methods for heat transfer analysis and enhance the reproducibility of this study, the proposed heat conduction method has been integrated into the cross-sectional analysis software MSASect2 [134], which is a cross-platform cross-section analysis and design software enabling the analysis of mechanical properties and thermal conductivity for arbitrary cross-section.

The graphical user interface of MSASect2 is shown in Figure 3-11. Heat transfer analysis in this software consists of two modules: preprocessing and postprocessing. The software's analysis workflow is as follows:

Step 1: Input cross-sectional information on the software's main interface either via a template or manually, including the cross-section's nodal coordinates, outlines, and material properties.

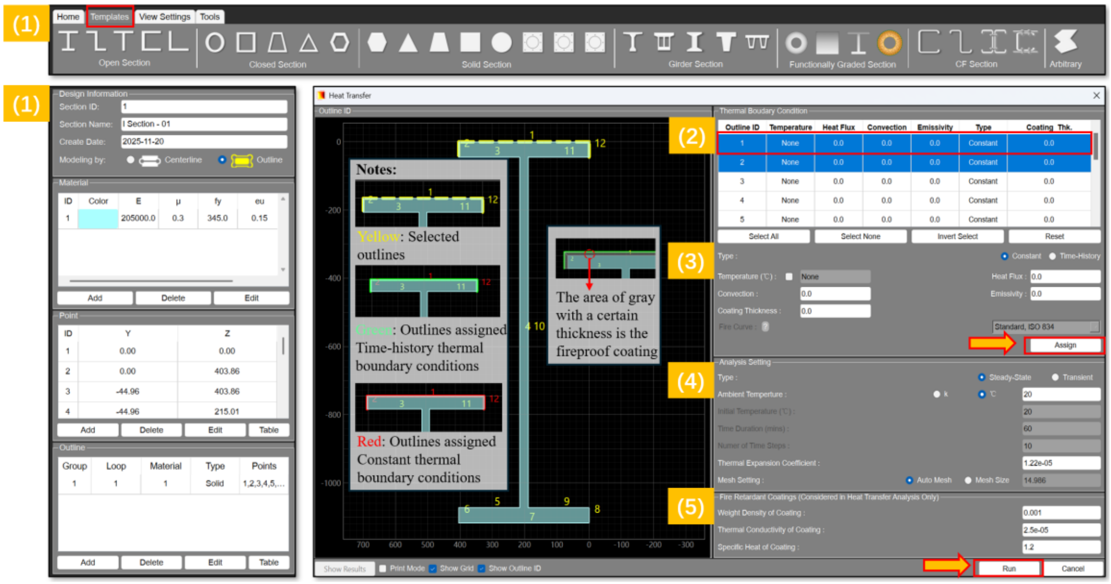

(a) Preprocessing module

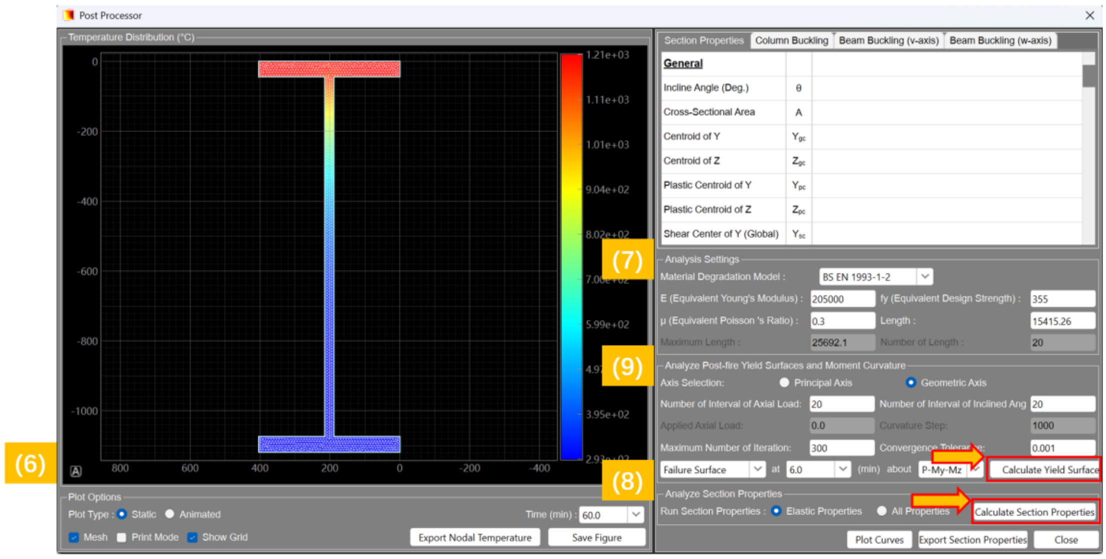

(b) Postprocessing module

Figure 3-11 The graphical user interface of MSASect2.

Step 2: Launch the preprocessing module for heat transfer analysis and select the outlines in the outline list that require the assignment of thermal boundary conditions.

Step 3: Input the required parameters (e.g. Temperature, heat flux, convection, emissivity and coating thickness) in the corresponding input fields. Click "Assign" to assign the thermal conditions. Diverse thermal boundary conditions are supported in the heat transfer analysis.

Step 4: Configure the “Analysis Settings” and adjust the required analysis parameters. Notably, a reasonable number of time steps and an appropriate mesh size are essential for accurate analysis.

Step 5: Input the parameters for the fire proof coatings if necessary. Click “Run” to start the analysis.

Step 6: Upon completion of the analysis, launch the postprocessing module and select appropriate plotting options to generate temperature cloud maps.

Step 7: Input material properties for the following calculation of cross-sectional properties, yield surfaces and moment curvatures.

Step 8: Select the analysis type and click “Calculate Cross-Sectional Properties” to compute the cross-sectional properties under fire.

Step 9: Input the analysis parameters for the yield surface and click “Calculate Yield Surface” to compute the yield surface under fire.

The software supports both fire curve and heat flux input methods, as well as transient and steady-state heat transfer calculations. To obtain more accurate results, it is recommended that the mesh size be 1/3 the width of the narrowest edge, and the number of time steps be no less than 20. The calculation of cross-sectional properties, yield surfaces and moment curvatures under fire are based on the results of the heat transfer analysis. These functions will be introduced in the following chapters.

CHAPTER 4.

COUPLED THERMAL-STRUCTURAL CROSS-SECTION ANALYSIS BY IMPROVED PLANAR FINITE ELEMENT FORMULATIONS

4.1 Introduction

Modern fire resistance design methods are evolving toward the adoption of more realistic fire scenarios and more precise structural analysis. Fire resistance design approaches based on the line finite element method (LFEM) also relay on more accurate cross-sectional properties. In this study, LFEM plays a central role in the second-order structural fire analysis, and the cross-sectional properties are essential parameters for the LFEM. However, the assessment of the influence of intumescent fire coatings (IFCs) on the fire-resistant performance of steel members, especially their cross-sectional properties and the associated global buckling response under fire, remains challenging. A significant challenge in the cross-section analysis arises from the complexity of obtaining the temperature field in IFC-protected steel structures under fire conditions [109, 110]. As shown in Figure 4-1(b), the foaming reaction of the IFC involves complex chemical processes, including melting, reaction, and charring of the coating, with each stage exhibiting distinct thermal properties [112]. The variations in thermal conductivity and volume of IFC complicate the resolution of temperature field in steel members during transient heat transfer analysis [113]. This issue has been addressed by the refined heat transfer analysis method illustrated in Chapter 3.

The non-uniform deteriorated material properties induced by the temperature gradient, as shown in Figure 4-1(c), introduces additional complexities in cross-section analysis. Most prescriptive design methods assume that the members are uniformly heated [60, 135] across the cross-sections. However, this assumption can lead to unsafe conditions when temperature gradients develop within the cross-sections [70]. Such gradients can occur when only one side of a column is exposed to fire [136] or when fireproof coatings are applied [69]. While fire tests and sophisticated finite element method (SFEM, typically employing shell or solid elements to provide a comprehensive and detailed model), can robustly capture the buckling behavior of steel members with thermal gradients [69, 137], their application in design practice is limited due to high costs and intensive computational demands. Some cross-sectional properties, such as the shear center, torsion constant, and warping constant, are quite challenging to determine when the material deterioration is non-uniform within the cross-section. Although several studies [69, 70, 136] have investigated the cross-sectional properties of these members, their scope is limited to specific, simple cross-sectional geometries, and they cannot account for properties related to torsion constant, shear center, warping constant, and Wagner coefficients. Therefore, a comprehensive cross-section analysis method that accounts for non-uniform material deterioration induced by the temperature filed is necessary.

Furthermore, irregular cross-sections, which have become increasingly common in modern steel structures [62, 138], lead to more complex buckling modes, thereby adding further challenges to the calculation of buckling capacity. Steel member with irregular cross-section, particularly non-symmetric section, has shear center that does not coincide with the centroid, as shown in Figure 4-1(d). Consequently, they are susceptible to lateral-torsional buckling under bending, axial-torsional buckling under compression (as depicted in Figure 4-1(e)), or other coupled buckling modes under eccentric axial load [139]. To analyze these buckling behavior, some key cross-sectional properties related to irregular sections, such as the shear center and Wagner coefficients [71, 140], are essential prerequisites. However, determining these parameters can be challenging due to material deterioration caused by the temperature gradient under fire, which makes traditional methods [59, 70] complex and inefficient.

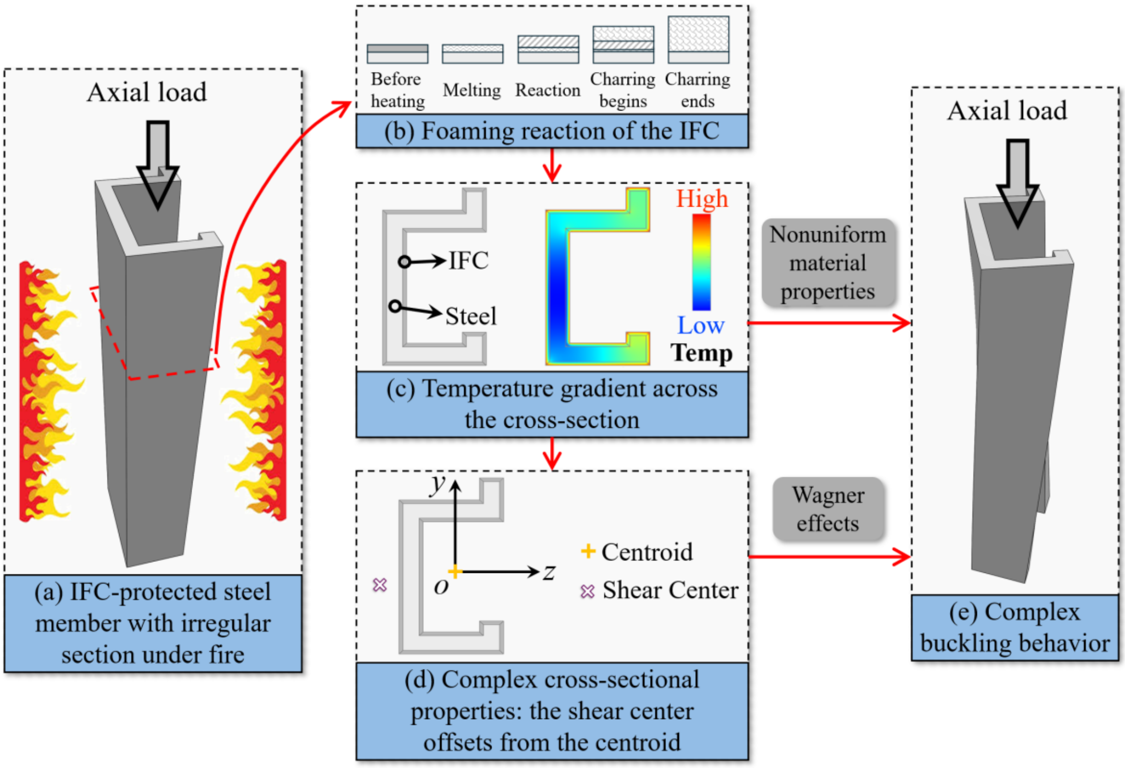

Figure 4-1 Challenges in the cross-section and global buckling analysis of IFC-protected steel member under fire.

To address these challenges, this study proposes an improved cross-section analysis framework for IFC-protected steel members with irregular cross-sections under fire. Based on the calculated temperature field, an improved cross-section analysis method employing the proposed thermal deterioration triangle (TDT) element is introduced, demonstrating both high accuracy and efficiency. With the derived cross-sectional properties, flexural buckling, axial-torsional buckling and lateral-torsional buckling are taken into consideration in the global buckling analysis. The proposed approach is validated through multiple examples and integrated into a new structural analysis software, MSASect2. The software is developed and released by the authors to provide a user-friendly tool and enhance the reproducibility of this study. Irregular sections with arbitrary IFCs and fire conditions can be easily modeled and rapidly analyzed to determine the global buckling capacity. Parametric studies are conducted to investigate the influence of fire exposure time, cross-sectional shape, load condition, dry film thickness (DFT) of IFC, slenderness ratio, and section factor. Finally, an approximate evaluation method is provided to estimate the fire exposure time corresponding to the initial and near-total loss of buckling capacity.

4.2 Assumptions and Limitations

The cross-section analysis in this study is based on the following assumptions:

1) The thickness of the IFC equals its DFT and is assumed to remain unchanged during heat transfer analysis, with a temperature-dependent equivalent thermal conductivity applied.
2) The cross-section remains planar after deformation, ensuring that the deteriorated cross-sectional properties of slender members can be determined through integration over the finite element mesh, as detailed in the cross-section analysis in Section 4.3.
3) The cross-sectional properties are represented by a series of products, such as bending stiffness $E_r\overline{I}$, compression stiffness $E_r\overline{A}$ and torsional rigidity $G_r\overline{J}$. This assumption is employed because modulus-weighted integrations are used to calculate the cross-sectional properties with thermal gradients, as discussed in Section 4.3.
4) The stress-strain relationship of steel is treated as elastic perfectly-plastic.
5) The proposed global buckling analysis primarily focuses on global buckling under fire, without accounting for the influence of local buckling or cross-sectional distortion. Additionally, the steel member is considered to be uniformly exposed to fire along its length, as this is a common scenario in

standard fire resistance tests [141-143].

4.3 Cross-section Analysis Using Improved Planar Finite Element Formulations

Accurate cross-sectional properties are fundamental to the LFEM. When a fire affects only three sides of a steel member [144], or when the steel member is a corner column or a beam supporting a floor slab [69], a significant temperature gradient will develop within the cross-section. The use of IFC can also result in a temperature gradient [55], leading to non-uniform deterioration of material properties, which complicates the cross-section analysis. Some typical fire resistance design methods account for thermal gradients within the cross-section by assuming mean temperatures [145] or dividing the cross-section into multiple regions with approximately equal temperatures [98, 146], providing a simplified model for cross-sections with thermal gradients. To address this limitation and enhance accuracy, this study proposes a thermal deterioration triangle (TDT) element that captures non-uniform thermal gradients, as shown in Figure 4-2.

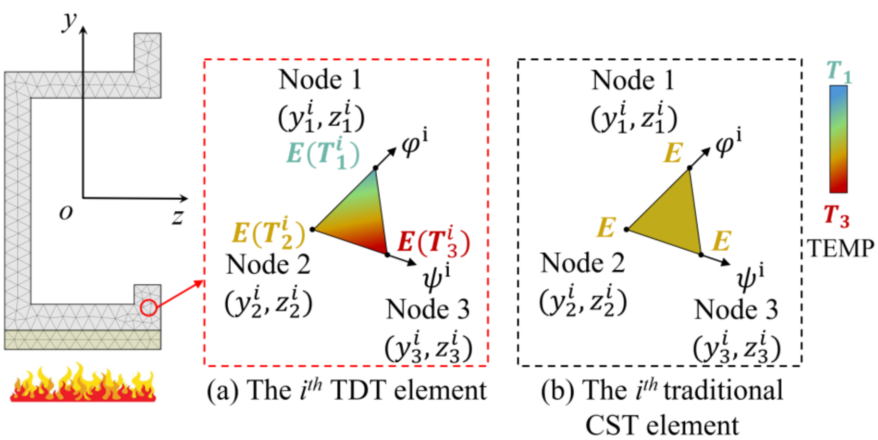

Figure 4-2 Cross-section analysis of a steel member under fire using: (a) TDT element and (b) CST element.

4.3.1 Derivation of the TDT element

The TDT element is developed from the traditional three-node constant strain triangle (CST) element, which exhibits good accuracy and stability in cross-section analysis [147]. As shown in Figure 4-2(b), the material properties, such as Young's modulus *E*, are constant within the CST element domain, thus requiring a fine-meshed cross-section to ensure accuracy. The TDT element can accurately capture material deterioration within the element domain, as depicted in Figure 4-2(a), allowing for cross-section analysis with fewer elements and thereby improving calculation efficiency. In addition to steel structures exposed to fire, the TDT element can be further developed for analyzing other structures with material gradients, such as timber, bamboo, WAAM steel, and composite stainless steel structures. The material properties and displacements within the TDT element can be extracted by linearly interpolating. The shape function for the i^{th} TDT element is defined as

$$N^i(\psi^i,\varphi^i)=\begin{bmatrix}\psi^i & \varphi^i & 1-\psi^i-\varphi^i\end{bmatrix} \tag{4.1}$$

where ψ^i and φ^i are the local coordinates for the i^{th} element, as shown in Figure 4-2(a). The values of ψ^i and φ^i range from zero to one. Then, the Jacobian matrix for each element is calculated as follows:

$$\mathbf{J}^i=\begin{bmatrix}\dfrac{\partial z}{\partial\psi^i} & \dfrac{\partial y}{\partial\psi^i}\\ \dfrac{\partial z}{\partial\varphi^i} & \dfrac{\partial y}{\partial\varphi^i}\end{bmatrix}=\begin{bmatrix}\dfrac{\partial\mathbf{N}^i}{\partial\psi^i}\\ \dfrac{\partial\mathbf{N}^i}{\partial\varphi^i}\end{bmatrix}\begin{bmatrix}\boldsymbol{z}^i & \boldsymbol{y}^i\end{bmatrix}=\begin{bmatrix}z_1^{\,i}-z_3^{\,i} & y_1^{\,i}-y_3^{\,i}\\ z_2^{\,i}-z_3^{\,i} & y_2^{\,i}-y_3^{\,i}\end{bmatrix} \tag{4.2}$$

in which, $\boldsymbol{y}^i=\left[y_1^{\,i},y_2^{\,i},y_3^{\,i}\right]^{\mathrm{T}}$ and $\boldsymbol{z}^i=\left[z_1^{\,i},z_2^{\,i},z_3^{\,i}\right]^{\mathrm{T}}$ are the nodal coordinate vectors for the i^{th} element in the global *y-o-z* coordinate system. Since the material matrix can be eliminated during the variational process, the stiffness matrix for calculating the warping function of the TDT element can similarly be derived using the principle of virtual work [65]:

$$\mathbf{R}^i = \int_{A^e} \left(\frac{\partial \left[\mathbf{N}^i \right]^T}{\partial y} \frac{\partial \mathbf{N}^i}{\partial y} + \frac{\partial \left[\mathbf{N}^i \right]^T}{\partial z} \frac{\partial \mathbf{N}^i}{\partial z} \right) d\tilde{A} \tag{4.3}$$

where $d\tilde{A}$ denotes the modulus-weighted differential law illustrated in the following section.

4.3.2 Degraded cross-sectional properties

According to assumption (3), a reference Young's modulus E_r is introduced for the analysis of deteriorated cross-sectional properties, and a modulus-weighted differential law for the i^{th} element is given by

$$d\tilde{A} = \frac{1}{E_r} \mathbf{N}^i \mathbf{E}^i dA \tag{4.4}$$

where $E_r > 0$ is a constant that does not affect the results; $\mathbf{E}^i$ represents the Young's modulus vector, demonstrating the deteriorated material properties under fire, and is expressed as

$$\mathbf{E}^i = \left[E(T_1^i), E(T_2^i), E(T_3^i) \right]^{\mathrm{T}} \tag{4.5}$$

in which, T_1^i, T_2^i and T_3^i are the nodal temperatures; $E(T)$ demonstrates the Young's modulus of steel at high temperatures, as recommended by ASCE 29-05 [148]. Based on the modulus-weighted differential law, the deteriorated cross-section area is given by

$$\bar{A} = \sum_{i=1}^{n_t} A^i = \sum_{i=1}^{n_t} \int d\tilde{A} = \sum_{i=1}^{n_t} \int_{-1}^{1} \int_{-1}^{1} \left| \mathbf{J}^i \right| \mathbf{N}^i \mathbf{E}^i / E_r d\psi^i d\varphi^i \tag{4.6}$$

where nt is the number of the TDT elements; A^i denotes the deteriorated cross-section area for the i^{th} element. Then, the deteriorated first moments of area are obtained by

$$\bar{Q}_y = \sum_{i=1}^{n_t} Q_y^i = \sum_{i=1}^{n_t} \int z d\tilde{A} = \sum_{i=1}^{n_t} \int_{-1}^{1} \int_{-1}^{1} \left|\mathbf{J}^i\right| \mathbf{N}^i \mathbf{E}^i \left(\mathbf{N}^i \boldsymbol{z}^i\right) / E_r d\psi^i d\varphi^i \tag{4.7}$$

$$\bar{Q}_z = \sum_{i=1}^{n_t} Q_z^i = \sum_{i=1}^{n_t} \int y d\tilde{A} = \sum_{i=1}^{n_t} \int_{-1}^{1} \int_{-1}^{1} \left|\mathbf{J}^i\right| \mathbf{N}^i \mathbf{E}^i \left(\mathbf{N}^i \boldsymbol{y}^i\right) / E_r d\psi^i d\varphi^i \tag{4.8}$$

Based on the above results, the coordinates of the centroid (y_c, z_c) can be calculated by

$$y_c = \frac{E_r \bar{Q}_z}{E_r \bar{A}} = \frac{\bar{Q}_z}{\bar{A}} \tag{4.9}$$

$$z_c = \frac{E_r \bar{Q}_y}{E_r \bar{A}} = \frac{\bar{Q}_y}{\bar{A}} \tag{4.10}$$

The deteriorated moments of inertia and product of inertia are

$$\bar{I}_y = \sum_{i=1}^{n_t} I_z^i = \sum_{i=1}^{n_t} \int z^2 d\tilde{A} = \sum_{i=1}^{n_t} \int_{-1}^{1} \int_{-1}^{1} \left|\mathbf{J}^i\right| \mathbf{N}^i \mathbf{E}^i \left(\boldsymbol{N}\boldsymbol{z}^i\right)^2 / E_r d\psi^i d\varphi^i \tag{4.11}$$

$$\bar{I}_z = \sum_{i=1}^{n_t} I_y^i = \sum_{i=1}^{n_t} \int y^2 d\tilde{A} = \sum_{i=1}^{n_t} \int_{-1}^{1} \int_{-1}^{1} \left|\mathbf{J}^i\right| \mathbf{N}^i \mathbf{E}^i \left(\boldsymbol{N}\boldsymbol{y}^i\right)^2 / E_r d\psi^i d\varphi^i \tag{4.12}$$

$$\bar{I}_{yz} = \sum_{i=1}^{n_t} I_{yz}^i = \sum_{i=1}^{n_t} \int yz d\tilde{A} = \sum_{i=1}^{n_t} \int_{-1}^{1} \int_{-1}^{1} \left|\mathbf{J}^i\right| \mathbf{N}^i \mathbf{E}^i \left(\boldsymbol{N}\boldsymbol{y}^i\right)\left(\boldsymbol{N}\boldsymbol{z}^i\right) / E_r d\psi^i d\varphi^i \tag{4.13}$$

For most irregular cross-sections under fire, the principal *w*-*v* axes usually deviate from the global *x*-*y* axes [58]. The angle θ between the principal and global axes can be calculated by

$$\theta = \frac{1}{2}\arctan\left(\frac{2\overline{I}_{yz}}{\overline{I}_y - \overline{I}_z}\right) \tag{4.14}$$

The coordinate transformation relationship between w-v axes and x-y axes is

$$\begin{bmatrix} \cos\theta & -\sin\theta \\ \sin\theta & \cos\theta \end{bmatrix} \begin{Bmatrix} y \\ z \end{Bmatrix} = \begin{Bmatrix} v \\ w \end{Bmatrix} \tag{4.15}$$

4.3.3 Degraded torsion and warping properties

Torsion and warping properties are vital for determining the global buckling load, as illustrated in Section 5. Obtaining the warping value and shear center is a prerequisite for the calculation of torsion constant [65]. The nodal warping values $\boldsymbol{\omega}$ are calculated by solving:

$$\mathbf{R}\boldsymbol{\omega} = \mathbf{P}_w \tag{4.16}$$

in which, $\mathbf{R}$ denotes the total stiffness matrix for the section, assembled from $\mathbf{R}^i$; $\mathbf{P}_w$ is the total load vector. $\mathbf{R}^i$ has been given by Eq.(4.3), $\mathbf{P}_w^i$ is calculated by the following equation:

$$\mathbf{P}_w^i = \int_0^1\int_0^{1-\varphi^i}\left(\mathbf{N}^i\boldsymbol{y}^i\frac{\partial\left[\mathbf{N}^i\right]^T}{\partial z} - \mathbf{N}^i\boldsymbol{z}^i\frac{\partial\left[\mathbf{N}^i\right]^T}{\partial y}\right)\det\left|\mathbf{J}^i\right|\mathbf{N}^i\mathbf{E}^i / E_r d\psi^i d\varphi^i \tag{4.17}$$

The coordinates of shear center (v_s, w_s) in the principal axes are given by

$$v_s = \sum_{i=1}^{n_t} v_s^i = \frac{1}{E_r}\frac{1}{\overline{I}_v}\sum_{i=1}^{n_t}\int_{-1}^{1}\int_{-1}^{1}\mathbf{N}^i\boldsymbol{w}^i\mathbf{N}^i\boldsymbol{\omega}^i\mathbf{N}^i\mathbf{E}^i\det\left|\mathbf{J}^i\right|d\psi^i d\varphi^i \tag{4.18}$$

$$w_s = \sum_{i=1}^{n_t} w_s^i = \frac{1}{E_r}\frac{1}{\overline{I}_w}\sum_{i=1}^{n_t}\int_{-1}^{1}\int_{-1}^{1}\mathbf{N}^i\boldsymbol{v}^i\mathbf{N}^i\boldsymbol{\omega}^i\mathbf{N}^i\mathbf{E}^i\det\left|\mathbf{J}^i\right|d\psi^i d\varphi^i \tag{4.19}$$

where $\boldsymbol{w}^i = \left[w_1, w_2, w_3\right]^T$, $\boldsymbol{v}^i = \left[v_1, v_2, v_3\right]^T$ and $\boldsymbol{\omega}^i = \left[\omega_1, \omega_2, \omega_3\right]^T$ are the nodal coordinate vectors along the w-axis, v-axis, and the nodal warping value vector, respectively; $\bar{I}_v$ and $\bar{I}_w$ represent the deteriorated moments of inertia about the v- and w- axes. The torsion constant can be calculated after the nodal warping values are standardized by:

$$\boldsymbol{\omega}_s{}^i = \boldsymbol{\omega}^i - \frac{1}{A^i}\int_A \boldsymbol{\omega}^i dA + w_s{}^i \boldsymbol{v}^i - v_s{}^i \boldsymbol{w}^i \tag{4.20}$$

The deteriorated torsion constant $\bar{J}$ can be calculated by

$$\begin{aligned}\bar{J} = &\sum_{i=1}^{n_t}\int_{-1}^{1}\int_{-1}^{1}\left\{\left[\frac{\partial \mathbf{N}^i}{\partial y}\boldsymbol{\omega}_s{}^i\left(\mathbf{N}^i\boldsymbol{z}^i - z_s\right) + \left(\mathbf{N}^i\boldsymbol{z}^i - z_s\right)^2\right]\right\}\det\left|\mathbf{J}^i\right|\mathbf{N}^i\mathbf{G}^i / G_r d\psi^i d\varphi^i \\ &-\sum_{i=1}^{n_t}\int_{-1}^{1}\int_{-1}^{1}\left\{\left[\frac{\partial \mathbf{N}^i}{\partial z}\boldsymbol{\omega}_s{}^i\left(\mathbf{N}^i\boldsymbol{y}^i - y_s\right) - \left(\mathbf{N}^i\boldsymbol{y}^i - y_s\right)^2\right]\right\}\det\left|\mathbf{J}^i\right|\mathbf{N}^i\mathbf{G}^i / G_r d\psi^i d\varphi^i\end{aligned} \tag{4.21}$$

where y_s and z_s are the coordinates of the cross-section; $\mathbf{G}^i = \mathbf{E}^i / \left[2\left(1+\mu\right)\right]$ denotes the shear modulus vector. Providing the warping values in Eq.(4.20), the warping constant $\bar{I}_\omega$ is expressed as follows:

$$\bar{I}_\omega = \sum_{i=1}^{n_t} I_\omega^i = \frac{1}{E_r}\sum_{i=1}^{n_t}\int_0^1\int_0^{1-\varphi^i}\left(\mathbf{N}^i\boldsymbol{\omega}_s{}^i\right)^2 \det\left|\mathbf{J}^i\right|\mathbf{N}^i\mathbf{E}^i d\psi^i d\varphi^i \tag{4.22}$$

The Wagner coefficients [62, 71] , which significantly influence the stability of steel members, are derived from the following equations based on the proposed deteriorated cross-sectional properties:

$$\beta_y = \frac{1}{I_y}\int_A \bar{z}^3 + \overline{zy}^2 dA - 2z_s dA, \beta_z = \frac{1}{I_z}\int_A \bar{y}^3 + \overline{yz}^2 dA - 2y_s dA,$$
$$\beta_\omega = \frac{1}{I_\omega}\int_A \omega_s\left(\bar{y}^2 + \bar{z}^2\right) dA \tag{4.23}$$

in which, $\bar{y}$ and $\bar{z}$ are the coordinates with the centroid as the origin in the global coordinate system.

4.3.4 Plastic section modulus

The section modulus of steel members rapidly decreases under fire, which can cause significant strength failure rather than stability failure [70]. Therefore, the proposed method considers the plastic section modulus of the steel members. Assuming that under bending conditions, all elements within the cross-section reach the yield strength and have sufficient plastic deformation capacity. The position of the plastic neutral axis is calculated by determining the axis in the yielding section where the total axial load is zero, considering the appropriate sign for compression or tension:

$$\int_A f_y(T) dA = \sum_{i=1}^{n_t}\int_{-1}^{1}\int_{-1}^{1}\mathbf{N}^i \boldsymbol{f}_y^{\,i} \det\left|\mathbf{J}^i\right| d\psi^i d\varphi^i \tag{4.24}$$

where $f_y(T)$ is the function for determining yield strength of steel at elevated temperatures, as recommended by ASCE 29-05 [148]; $\boldsymbol{f}_y^{\,i}$ is the nodal yield strength vector, demonstrating the deteriorated yield strength under fire, and is expressed as

$$\boldsymbol{f}_y^{\,i} = \left[f_y(T_1^i), f_y(T_2^i), f_y(T_3^i)\right]^{\mathrm{T}} \tag{4.25}$$

The plastic moment can be calculated by integrating the yield strength of each element multiplied by the area and the distance to the plastic neutral axis:

$$M_{p,y} = \sum_{i=1}^{n_t} y_p^i \int_{-1}^{1}\int_{-1}^{1}\mathbf{N}^i \boldsymbol{f}_y^{\,i} \det\left|\mathbf{J}^i\right| d\psi^i d\varphi^i \tag{4.26}$$

$$M_{p,z} = \sum_{i=1}^{n_t} z_p^i \int_{-1}^{1}\int_{-1}^{1} \mathbf{N}^i \boldsymbol{f}_y^{\,i} \det\left|\mathbf{J}^i\right| d\psi^i d\varphi^i \tag{4.27}$$

in which, y_p^i and z_p^i are the distances between the centroid of the i^{th} element and the two plastic neutral axes, respectively.

4.4 Global Buckling Analysis Based on the Cross-sectional Properties

4.4.1 Global buckling analysis

After obtaining the temperature-dependent cross-sectional properties of steel members exposed to fire, this chapter further analyzes the global buckling behavior of such members. Global buckling is a core consideration in the fire resistance design of steel structures, as it directly often governs the ultimate load-carrying capacity and stability of slender members when subjected to elevated temperatures. Given that high temperatures non-uniformly degrade the elastic modulus and yield strength of steel, the cross-sectional stiffness and strength (which have derived in Section 4.3) undergo substantial changes, which in turn alter the global buckling modes, critical buckling temperature, and buckling load of members.

Understanding the behavior of single members under fire is essential for developing appropriate design criteria. Three different global buckling modes: flexural buckling, axial-torsional buckling, and lateral-torsional buckling are considered. For columns with axial loads, the bearing capacity is primarily controlled by flexural buckling and axial-torsional buckling. For beams under bending, lateral-torsional buckling is more likely to occur. Lateral-torsional buckling is sensitive to parameters such as the shear center, torsion constant, and Wagner coefficients, which describe the asymmetrical properties arising from irregular cross-sections and thermal gradients. The global buckling load of a centrally loaded column can be calculated using the closed-form solution provided by Ziemian [71], where the theoretical buckling load N_{cr}

can be determined through solving the equation:

$$
\begin{aligned}
&(r^2 - v_s^2 - w_s^2)N_{cr}^3 - \left[\left(N_v + N_w + N_r\right)r^2 - N_w v_s^2 - N_v w_s^2\right]N_{cr}^2 + \\
&r^2\left(N_v N_w + N_w N_r + N_r N_v\right)N_{cr} - N_v N_w N_r r^2 = 0
\end{aligned}
\tag{4.28}
$$

where N_v and N_w are the flexural buckling loads about v- and w- axes of the cross-section, respectively; N_r denotes the axial-torsional buckling load; r is the radius of gyration.

The flexural buckling loads are obtained from

$$N_v = \frac{\pi^2 E_r \bar{I}_v}{(\lambda L)^2} \tag{4.29}$$

$$N_w = \frac{\pi^2 E_r \bar{I}_w}{(\lambda L)^2} \tag{4.30}$$

in which, λ is a coefficient related to the boundary conditions, ranging from 0.5 to 1.0. The axial-torsional buckling load is expressed by

$$N_r = \frac{G_r \bar{J} + \pi^2 E_r \bar{I}_\omega / L^2}{v_s^2 + w_s^2 + \left(\bar{I}_v + \bar{I}_w\right) / \bar{A}} \tag{4.31}$$

The closed-form solutions provided by Galambos [149] for lateral-torsional buckling loads of steel beams under pure bending are given by

$$M_{cr,z} = \frac{\pi^2 E_r \bar{I}_y}{L^2}\left\{\frac{\beta_z}{2} + \sqrt{\left(\frac{\beta_z}{2}\right)^2 + \left[\frac{\bar{I}_\omega}{\bar{I}_y} + \frac{G_r \bar{J} L^2}{E_r \bar{I}_y \pi^2}\right]}\right\} \tag{4.32}$$

$$M_{cr,y} = \frac{\pi^2 E_r \bar{I}_z}{L^2}\left\{\frac{\beta_y}{2} + \sqrt{\left(\frac{\beta_y}{2}\right)^2 + \left[\frac{\bar{I}_\omega}{\bar{I}_z} + \frac{G_r \bar{J} L^2}{E_r \bar{I}_z \pi^2}\right]}\right\} \tag{4.33}$$

where $M_{cr,z}$ and $M_{cr,y}$ are the buckling loads when the steel member is under pure bending moments about *z*- and *y*- axes, respectively. These analytical solutions provide a limiting point in the mathematical space for buckling analysis [71].

For buckling analysis under other loads and boundary conditions with thermal expansion, the buckling mode is complex, potentially involving a combination of multiple modes, making it difficult to determine the buckling load through analytical solutions. The buckling loads can be obtained by applying the cross-sectional properties provided in this study to LFEMs [98, 100, 150, 151] for eigen-buckling analysis. In extremely slender members, deformations due to uneven thermal expansion become more pronounced than the effects of uneven degradation of material properties [69]. For these cases, LFEMs are recommended to calculate the buckling loads, as thermal bowing and thermal buckling are well accounted for. These methods rely on accurate cross-sectional properties, which are challenging to determine when the cross-section is irregular and affected by thermal gradients.

The degradation of the yield strength at high temperatures is significant. It is essential to conduct strength checks for buckling loads. The buckling load must be lower than the capacity when the entire section undergoes plastic deformation:

$$N_r \le f_y \overline{A} \tag{4.34}$$

$$M_{cr,z} \le M_{p,z}, M_{cr,y} \le M_{p,y} \tag{4.35}$$

4.4.2 Numerical implementation

The proposed numerical framework for cross-section and global buckling analysis of IFC-protected steel members under fire is summarized in Figure 4-3. Three parts are included in this framework: (1) Heat transfer analysis; (2) Cross-section analysis; and (3) Global buckling analysis. The first part generates the mesh model and temperature field for cross-section analysis in the second part, while the second part provides accurate cross-sectional properties for the global buckling analysis in the third part. It should be noted that the IFC in step 6 needs to be removed from the mesh as it does not participate in the global buckling analysis.

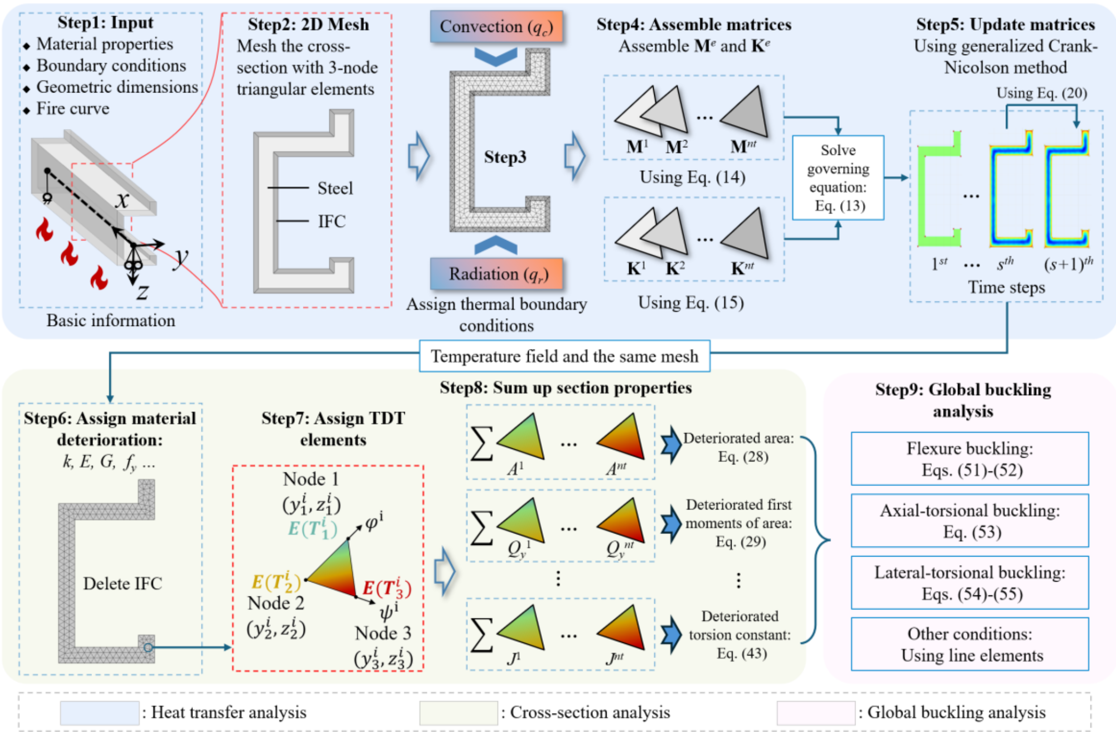

Figure 4-3 The proposed numerical framework for the global buckling analysis of IFC-protected steel members under fire.

The authors have integrated the proposed cross-section and global buckling analysis method into the new educational structural analysis software, MSAsect2 [134], to provide a user-friendly tool and enhance the reproducibility of the present study. The graphical user interface of MSASect2 is shown in Figure 4-4, where the software primarily consists of two modules: one is the preprocessor for inputting model information, and the other is the postprocessor for displaying results.

In the preprocessor module, cross-sections are constructed by defining nodes and assigning IFC. After specifying material properties, fire, and load conditions, the input model is analyzed by the proposed method. The postprocessor module displays the temperature field, cross-sectional properties, and global buckling capacity over time. To extend practical applications, a local buckling analysis module for IFC-protected members is under development.

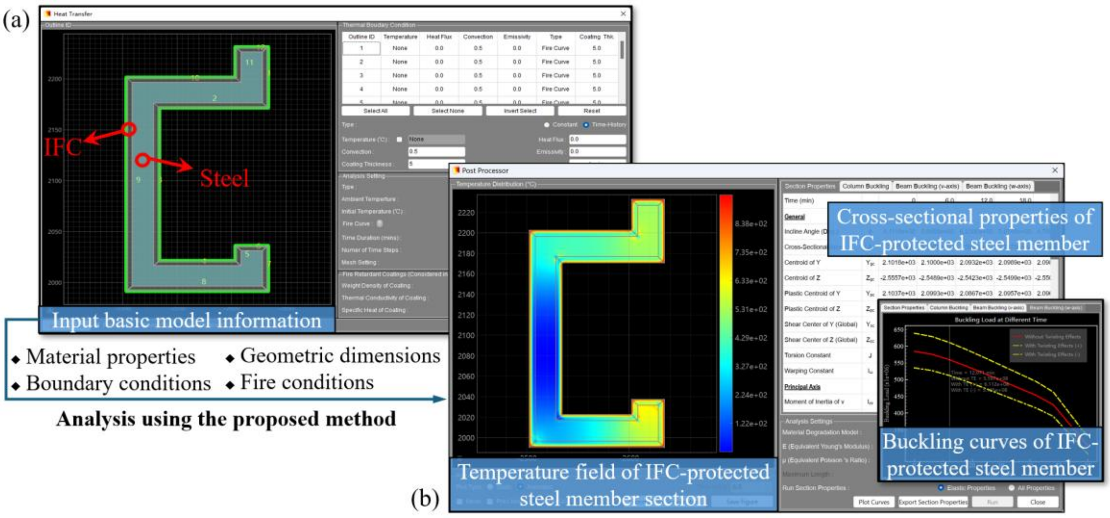

Figure 4-4 The graphical user interface of MSASect2: (a) Preprocessor; (b) Postprocessor.

4.5 Validation Examples

Two examples verify the accuracy of the proposed method, including cross-section analysis and global buckling analysis.

4.5.1 Cross-sectional properties of IFC-protected steel members under fire

The cross-sectional properties calculated using SFEM and the traditional method with CST elements are compared with those obtained from the proposed method to demonstrate the accuracy and efficiency of TDT element, respectively. Figure 4-5 illustrates the dimensions of typical irregular cross-sections, where the thickness t_w is set to 15 mm. The dry film thickness and equivalent constant thermal conductivity of the IFC are taken as 5 mm and $0.0216\ \mathrm{W/(m \cdot K)}$ [115], respectively.

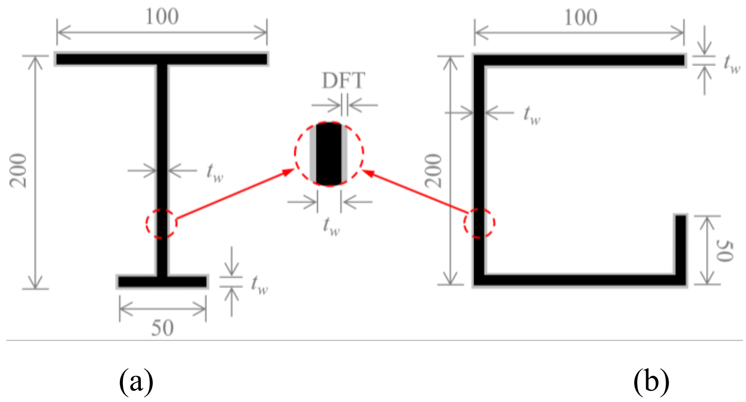

Figure 4-5 Dimensions (mm) of the cross-sections: (a) I-Section; (b) C-section.

To demonstrate the accuracy of the cross-section analysis method, a comparison is made with the SFEM in ABAQUS [152] using solid elements (C3D8R). In the sophisticated finite element model, the centroids of both ends are fixed with a coupling point that uses structural coupling to allow free warping, as the torsion constant must be obtained under Saint-Venant torsion conditions. Displacement loads are applied at the coupling points of both ends, and the cross-sectional properties ($E_r\bar{A}$, $E_r\bar{I}$, $G_r\bar{J}$) are determined by analyzing the relationship between the deformation and the reaction forces of the beam under compression, bending, and torsion. To ensure accurate results, the length L of the member is set to six times the section's height D to uphold assumption (2) and minimize the influence of the distortion of cross-section [153]. Mesh size tests have been carried out for better convergence. The IFC-protected members are subjected to a standard ISO 834 fire exposure [154]. The cross-sectional properties at various time points, calculated using the SFEM and the proposed method, are presented in Figure 4-6.

The results of the two methods exhibit strong consistency, confirming the accuracy of the present study. The minor error arises from the cross-sectional distortion in SFEM and the simplification in assumption (2). Moreover, the strain distribution across the section at 100 minutes, calculated using SFEM, is provided in **Appendix 4A** of this chapter. The proposed method is more efficient as it will use fewer elements, while the SFEM faces more complex modeling and coupling methods.

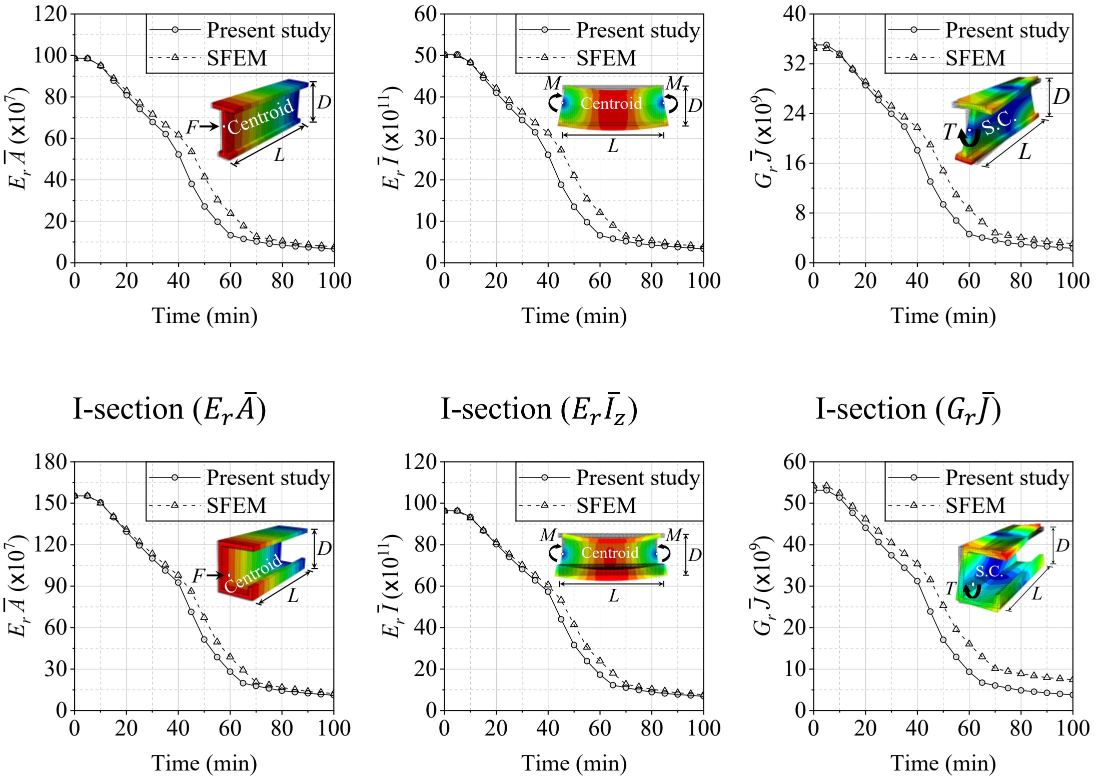

I-section ($E_r\bar{A}$) I-section ($E_r\bar{I}_z$) I-section ($G_r\bar{J}$)

C-section ($E_r\bar{A}$) C-section ($E_r\bar{I}_z$) C-section ($G_r\bar{J}$)

Figure 4-6 Cross-sectional properties at different time obtained by the present method and SFEM.

To illustrate the efficiency of the present study, the cross-sectional properties at the 40th minute calculated using CST and TDT elements are compared with the benchmark solutions derived from the SFEM. The number of elements used and the differences are recorded, as shown in Figure 4-7. With the same number of elements, the proposed method using TDT element can reduce the error in calculating the properties of I-section by up to 3.98% and C-section by 2.26%. It is evident that TDT elements can achieve better accuracy with fewer elements when calculating different cross-sectional properties, thereby demonstrating the efficiency of TDT elements.

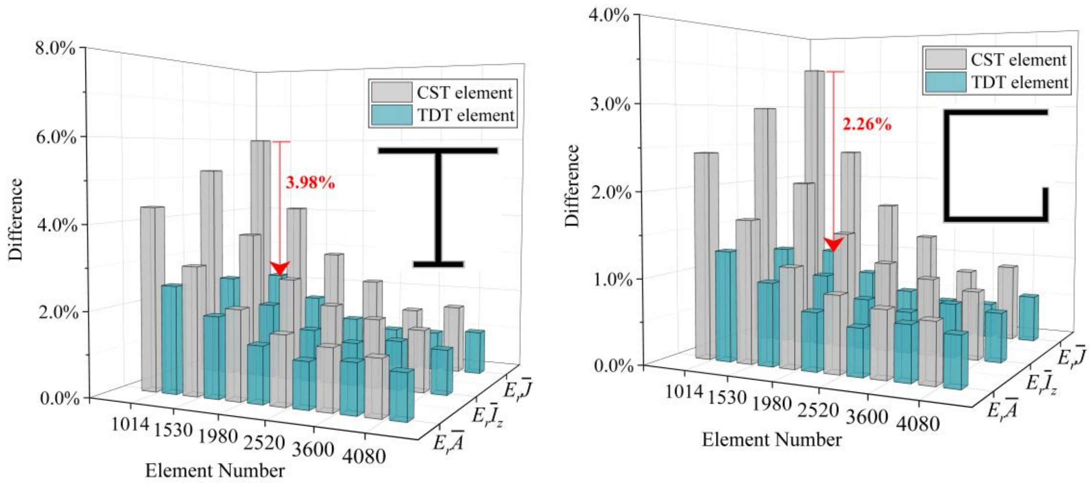

(a) I-section (b) C-section

Figure 4-7 Comparison of the efficiency between CST and TDT elements.

4.5.2 Global buckling analysis of IFC-protected steel members under fire

This example further validates the proposed buckling analysis method by comparing it with fire resistance tests of steel members protected with IFC. The fire resistance tests, reported by Mesquita et al. [155], involve simply supported IFC-protected steel members with varying cross-sections and DFTs. The span between the supports is 1210 mm, and the members are subjected to constant axial loads and fire exposure according to ISO 834 [154]. The temperature-dependent equivalent thermal conductivity is prescribed by the European standard [135]. Different cross-sections (IPE and LNP) and protection thicknesses are analyzed in this example, as shown in Figure 4-8. The reduction of the buckling capacity over fire exposure time is calculated using the proposed method, and the test results are presented. The results show good agreement, with only minor differences, which arise from the fire exposure length not being strictly equal to the length between the supports. Hence, the accuracy of the proposed approach is further confirmed.

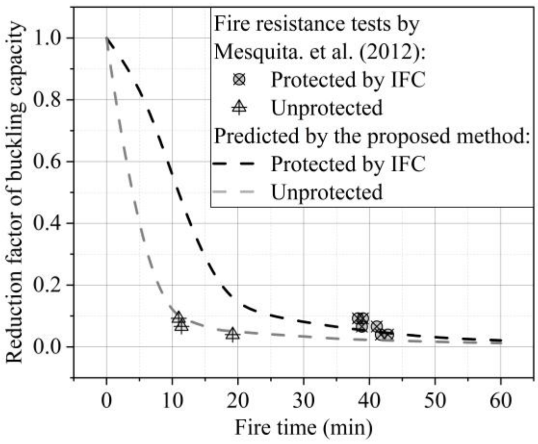

(a) IPE 100, Average DFT≈1 mm

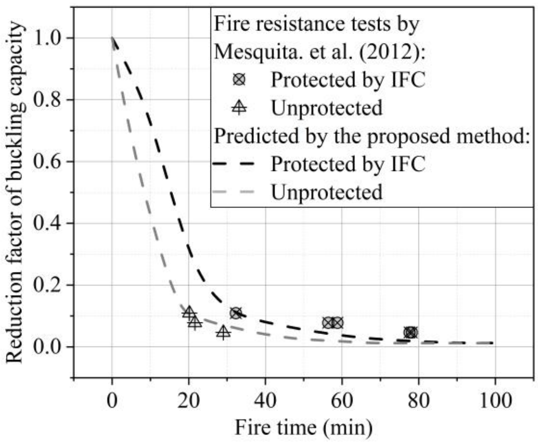

(b) LNP 100x50x8, Average DFT≈1.1 mm

Figure 4-8 Comparison between calculated results and fire resistance test outcomes.

4.6 Parametric Study

This section conducts a comprehensive parametric study on the global buckling behavior of steel members protected by IFC when exposed to fire conditions. Following the summary of results from the parametric study, a design method is proposed to estimate the required IFC thickness corresponding to the target fire resistance time. Several critical parameters are examined, including section shape, fire exposure time, slenderness ratio, DFT, section factor and load condition. For convenience, it is assumed that all steel members are simply supported, and the reduction factors for the buckling load under various parameters are evaluated. The equivalent thermal conductivity demonstrated by Li et al. [115] is applied. The cross-sections maintain the same dimensions as in the previous example, as shown in Figure 4-5.

4.6.1 Buckling load of axially loaded columns

The reduction factors (N_{cr}/N_{cr0}) for the axially loaded columns are shown in Figure 4-9 and Figure 4-10, where N_{cr0} represents the buckling load at ambient temperature. For clearer visualization, the data points are displayed in different colors based on their reduction factors. The 20% and 80% reductions in buckling load are indicated by blue and red lines, respectively. These lines correspond to the slenderness ratio and fire exposure time at the points of initial and near-total loss of buckling capacity, as typical fire resistance tests usually apply load ratios between 20% and 80% [156-158]. Generally, as time increases, the buckling load decreases significantly. Without IFC, the reduction factor rapidly decreases to 20% in 20 minutes, while a 5mm IFC can extend this time to over 70 minutes. The slenderness ratio has a more pronounced effect on C-sections, as shown in Figure 4-10 (b)-(f), because the transition from strength failure to buckling failure becomes more evident with changes in slenderness.

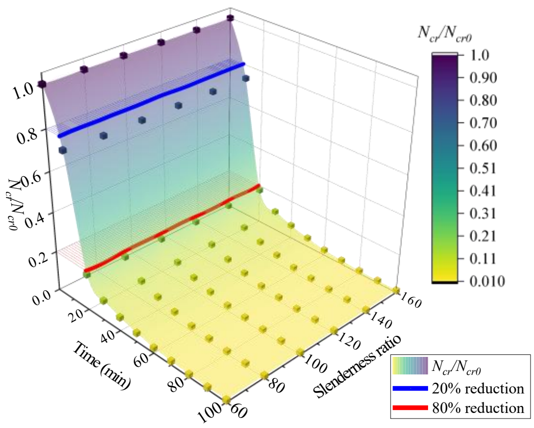

(a) Without IFC

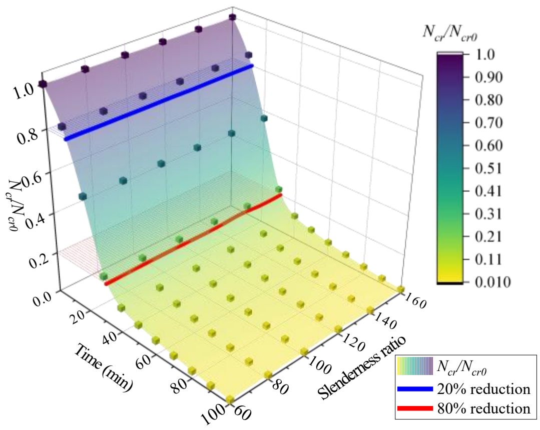

(b) DFT = 1 mm

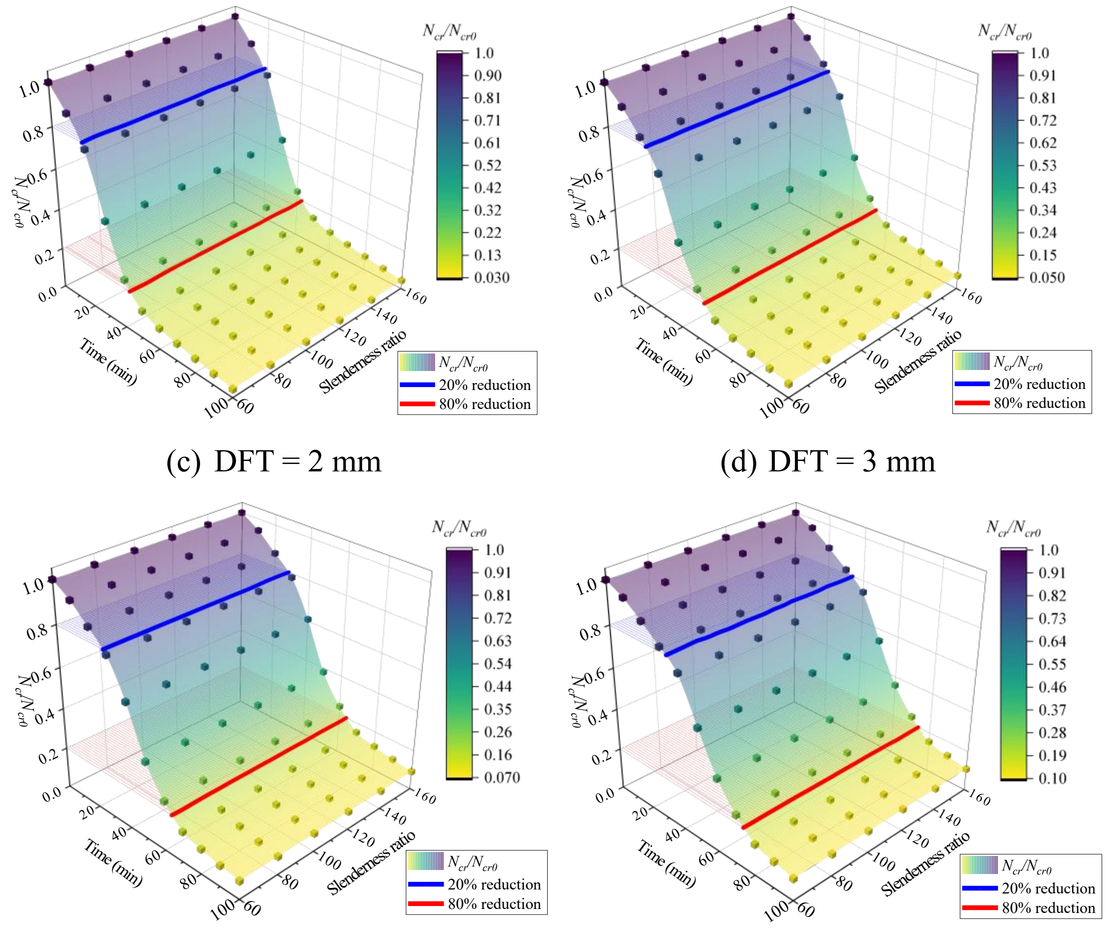

(c) DFT = 2 mm

(d) DFT = 3 mm

(e) DFT = 4 mm

(f) DFT = 5 mm

Figure 4-9 Reduction factors for the I-section members subjected to axial loads.

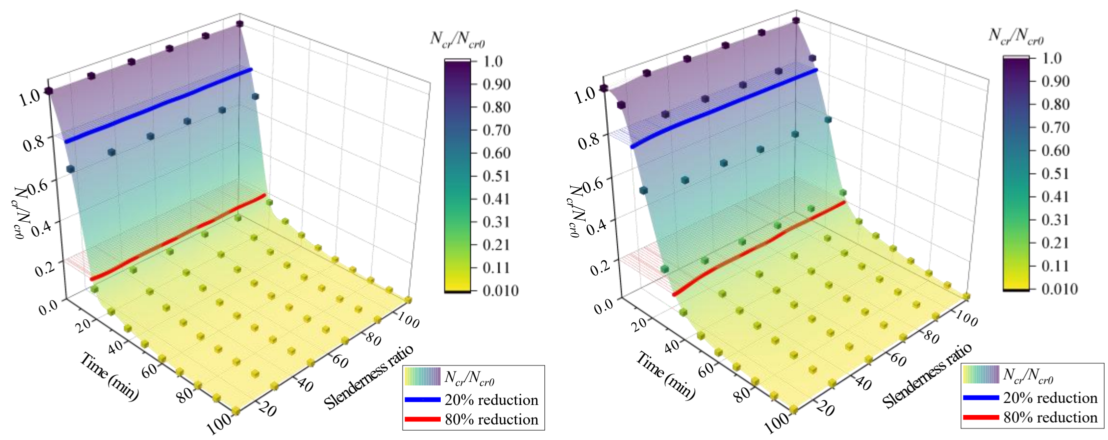

(a) Without IFC

(b) DFT = 1 mm

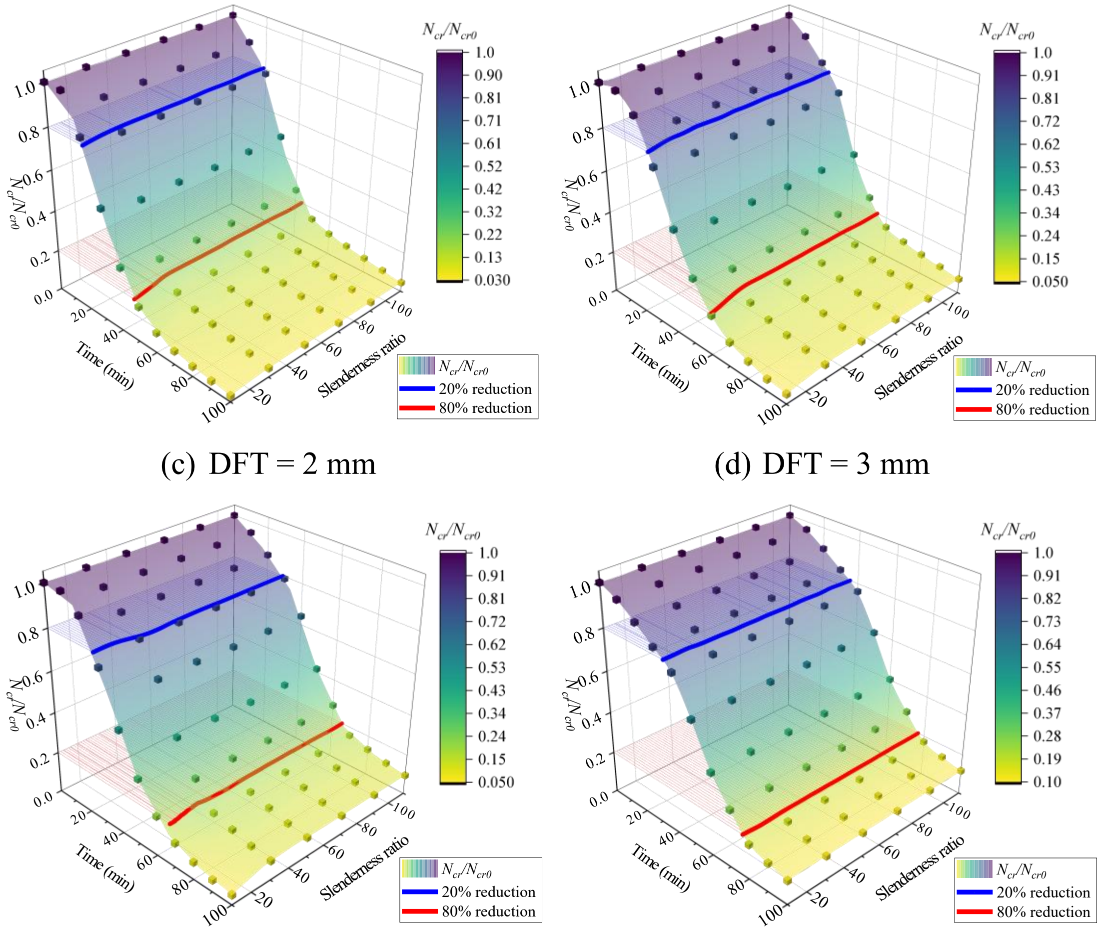

(c) DFT = 2 mm

(d) DFT = 3 mm

(e) DFT = 4 mm

(f) DFT = 5 mm

Figure 4-10 Reduction factors for the C-section members subjected to axial loads.

For each DFT, the projection areas between the curves corresponding to 20% and 80% reductions in the Time-Slenderness ratio plane are presented in Figure 4-11. The failure caused by stability and strength has also been marked in different areas according to Eqs.(4.34) and (4.35). As DFT increases from 0 to 5 mm, the time for an 80% reduction in buckling capacity increases from 20 minutes to 80 minutes, while the time for a 20% reduction in buckling capacity increases from 10 minutes to 35 minutes. It can be concluded that increasing the DFT significantly delays the loss of buckling capacity.

As the DFT increases, the boundary between strength failure and buckling failure of the C-section shifts toward a higher slenderness ratio, a phenomenon not observed in the I-section. This shift occurs because the buckling mode in C-section is more sensitive to variations in slenderness, as the Wagner effect is more pronounced in non-symmetric sections [139]. According to Eq. (4.31), the centroid and shear center of a C-section do not coincide (w_s and v_s are not zero), causing the smaller N_r to govern the load capacity at low slenderness ratios and N_w to govern it at high slenderness ratios. This shift leads the C-section column to transition from axial-torsional buckling to flexural buckling. For I-section members, the distance between the shear center and the centroid is very close, preventing axial-torsional buckling from governing the failure mode at low slenderness ratios. Within the slenderness ratios considered in this study, the buckling mode of I-section members remains unchanged. Consequently, the boundary between buckling failure and strength failure in I-section members also remains unchanged. Moreover, the reduction factor of buckling capacity demonstrates less sensitivity to variations in cross-sections, as indicated by the approximate similarity in their projected areas, as shown in Figure 4-11. This can be explained by the gradual decrease in most cross-sectional properties ($E_r\bar{I}$, $E_r\bar{A}$, $E_r\bar{I}_\omega$ and $G_r\bar{J}$) of both sections as the fire duration increases.

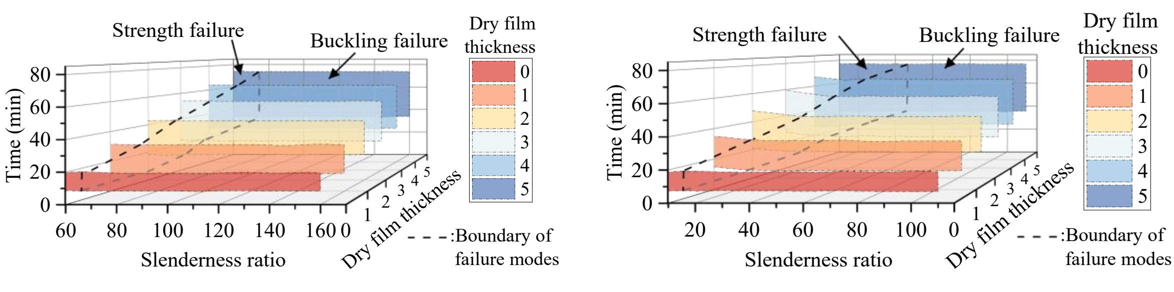

(a) I-section (b) C-section

Figure 4-11 Waterfall plot depicting the reduction in buckling load from 20% to 80% for axially loaded columns.

4.6.2 Buckling load of beams under pure bending

The reduction factors (M_{cr}/M_{cr0}) for the buckling load of beams subjected to pure bending are shown in Figure 4-12 and Figure 4-13 where M_{cr0} denotes the buckling load at ambient temperature. Similar to axially loaded columns, the reduction factor for beams subjected to pure bending decreases with increasing fire duration, while changes in slenderness ratio have minimal effect. With variations in DFT, the reduction coefficient for pure bending beams changes in a manner consistent with that of axially loaded columns.

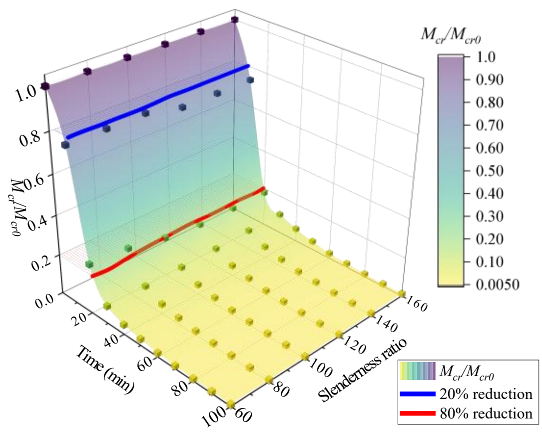

(a) Without IFC

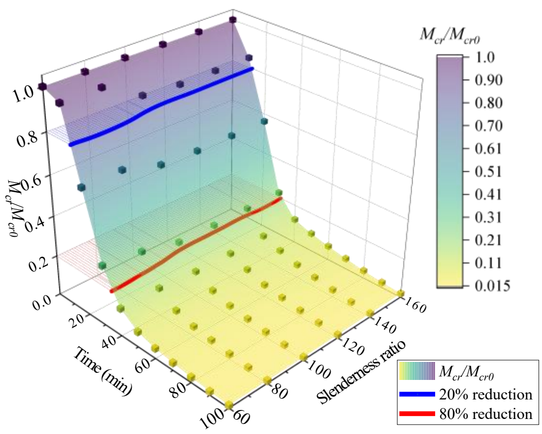

(b) DFT = 1 mm

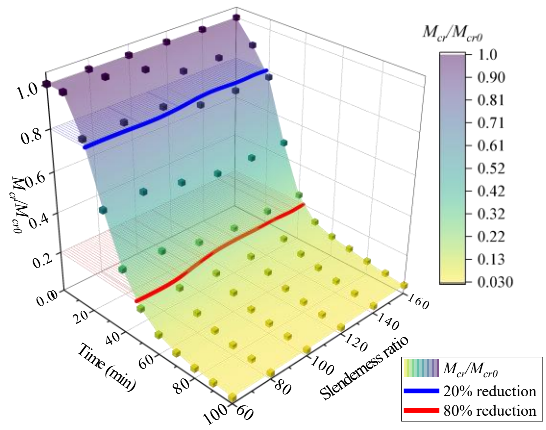

(c) DFT = 2 mm

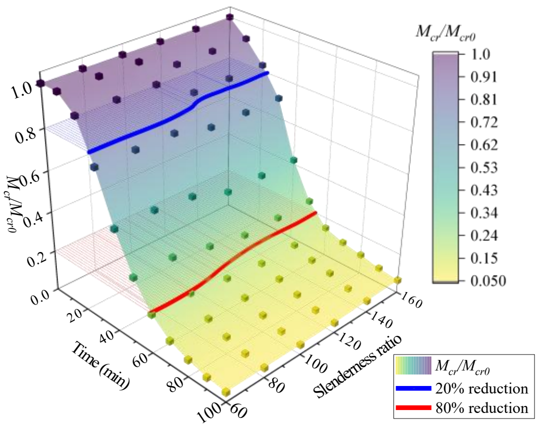

(d) DFT = 3 mm

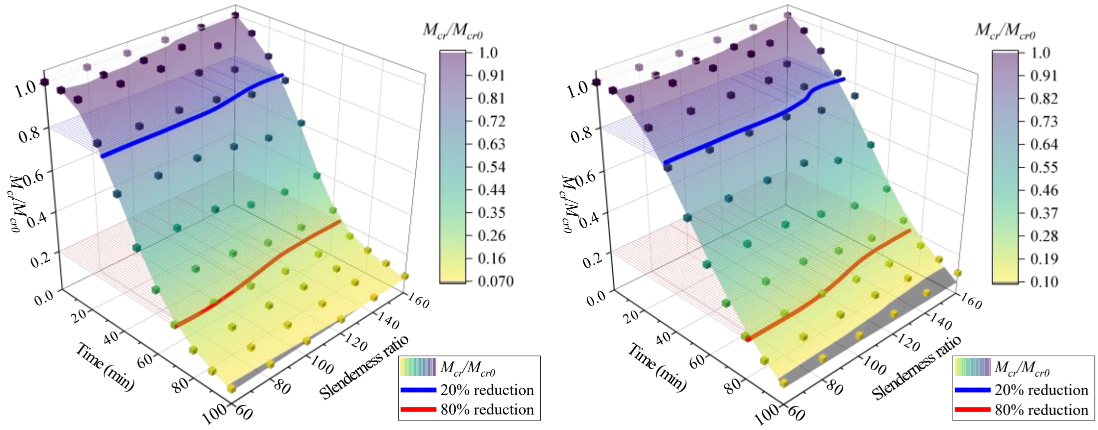

(e) DFT = 4 mm (f) DFT = 5 mm

Figure 4-12 Reduction factors for the I-section members subjected to bending moments.

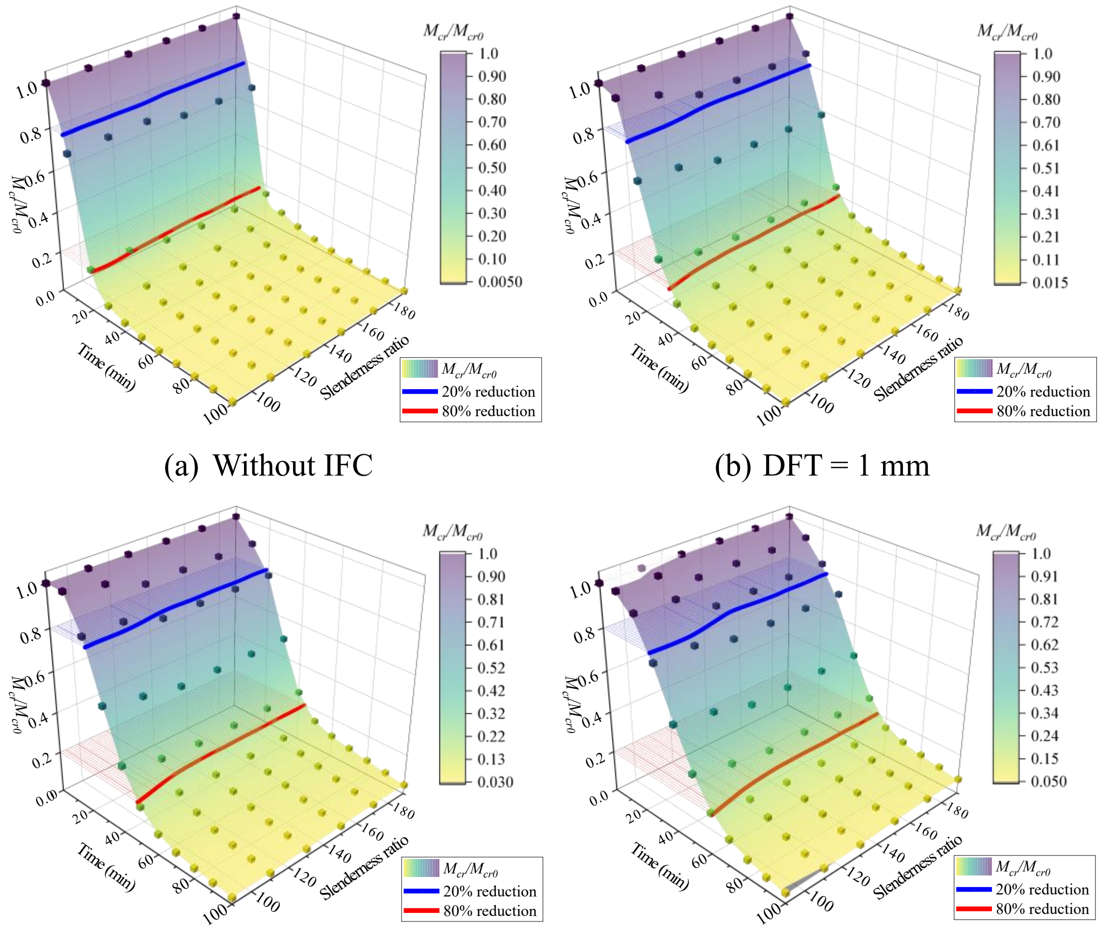

(a) Without IFC (b) DFT = 1 mm

(c) DFT = 2 mm (d) DFT = 3 mm

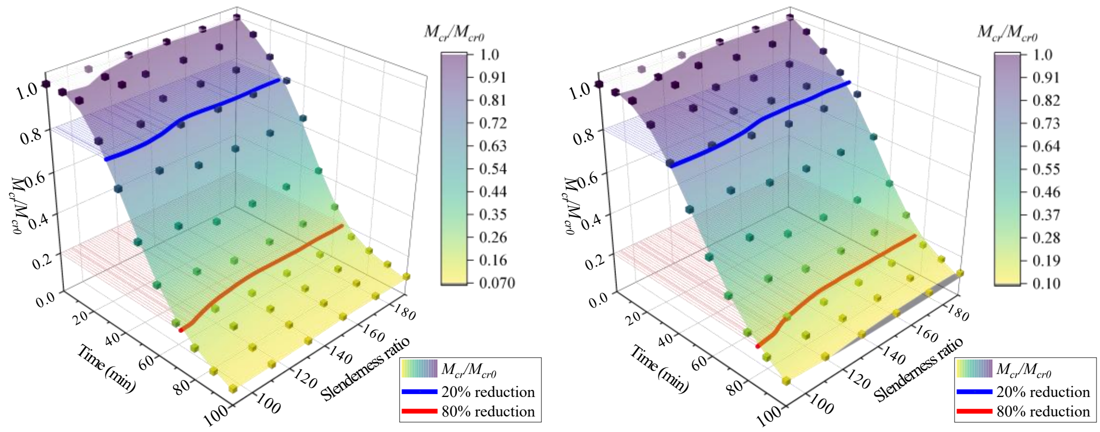

(e) DFT = 4 mm (f) DFT = 5 mm

Figure 4-13 Reduction factors for the C-section members subjected to bending moments.

The projection areas between the 20% and 80% reduction curves in the Time-Slenderness ratio plane are depicted in Figure 4-14. Compared to columns under axial compression, beams subjected to pure bending exhibit slightly higher buckling capacity at lower slenderness ratios than those with higher slenderness ratios. This occurs because the degradation in strength at lower slenderness ratios is more pronounced than the degradation in lateral-torsional buckling capacity. For both I-section and C-section, the boundary between strength failure and buckling failure shifts upward as the DFT increases. This indicates that DFT provides greater protection for lateral-torsional buckling capacity than for strength when the slenderness ratio is low. The C-section and I-section beams under bending exhibit similar patterns in failure boundary, as their global buckling mode is governed solely by lateral-torsional buckling, without transition in buckling mode. The variation in fire exposure time corresponding to the 20% and 80% reduction factor curves at different slenderness ratios is within 10%, which is significantly smaller than the effect of DFT. This behavior is consistent with that observed in the axially loaded columns.

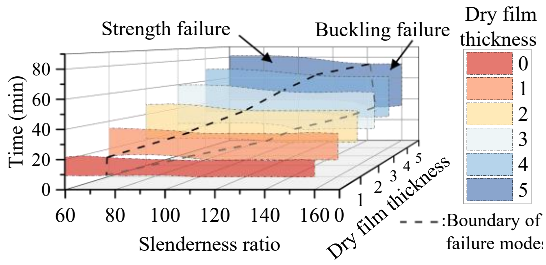

(a) I-section

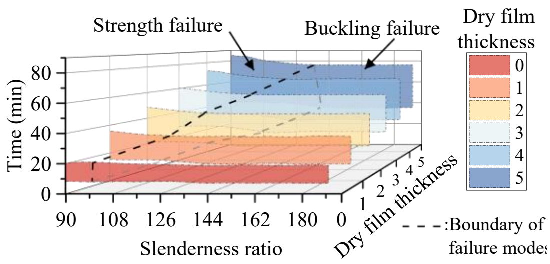

(b) C-section

Figure 4-14 Waterfall plot depicting the reduction in buckling load from 20% to 80% for beams subjected to bending moments.

4.6.3 Evaluation method for global buckling of IFC-protected steel members

This section extends the parametric analysis to various wall thicknesses (t_w), which can significantly influence the section factor, thereby affecting the temperature field and bucking capacity of the member [55, 110]. Given the minimal influence of the slenderness ratio on the reduction factor of buckling capacity, as previously discussed, the minimum fire exposure times for the 20% and 80% reduction curves are conservatively selected as the time points corresponding to the initial and near-total loss of buckling capacity in this study. The minimum time points corresponding to 20% and 80% reduction in buckling capacity for IFC-protected steel members with four different wall thicknesses (t_w = 5, 10, 15, and 20 mm) are calculated and summarized in theFigure 4-15 and Figure 4-16. It can be observed that, for the same wall thickness, the time to achieve a 20% or 80% reduction is approximately linearly related to the DFT. Therefore, a linear fitting is performed on the data as follows:

$$t = a \cdot \mathrm{DFT} + b \tag{4.36}$$

where a and b are the slope and intercept of the linear fitting, respectively. The coefficients of determination (R^2) for all fittings are no less than 0.979, indicating excellent fit. Furthermore, the slopes and intercepts are fitted with different section factors, and the results are shown in Figure 4-17. The section factor is defined as A_p/V [135, 154], where A_p represents the surface area of IFC per unit length of the member; V denotes the volume of the steel member per unit length. It is evident that the section coefficient, rather than the section shape, significantly influences the buckling load reduction coefficient. It is observed that the data patterns for bending and compression members are similar, allowing both types of members to share the same fitting. The optimal fittings of the slope and intercept with respect to the section factor are shown below:

$$a = \alpha + \beta \exp\left[\gamma\left(\frac{A_p}{V}\right)\right] \tag{4.37}$$

$$b = \eta + \xi\left(\frac{A_p}{V}\right) \tag{4.38}$$

in which, α, β, γ, η and ξ are the fitting coefficients listed in Table 4-1. The fittings of the slope and intercept also demonstrate excellent fit, as shown in Figure 4-17, with R^2 values close to 1 and narrow 95% confidence bands. Therefore, the time to achieve a 20% and 80% reduction in buckling capacity for IFC-protected steel members can be calculated by the following equation:

$$t = \left\{\alpha + \beta \exp\left[\gamma\left(\frac{A_p}{V}\right)\right]\right\} \cdot \mathrm{DFT} + \xi\left(\frac{A_p}{V}\right) + \eta \tag{4.39}$$

This proposed equation accounts for several key factors, including wall thickness, load conditions, section factor and DFT. Under ISO 834 standard fire conditions [154], it provides an approximate estimation of the fire duration corresponding to the initial and near-total loss of buckling capacity for simply supported IFC-protected steel members within the parameter ranges of this study. The fire exposure time corresponding to initial and near-total loss of buckling capacity provides engineers with a reference for prescriptive-based fire safety design and offers manufacturers insights into the performance of IFC.

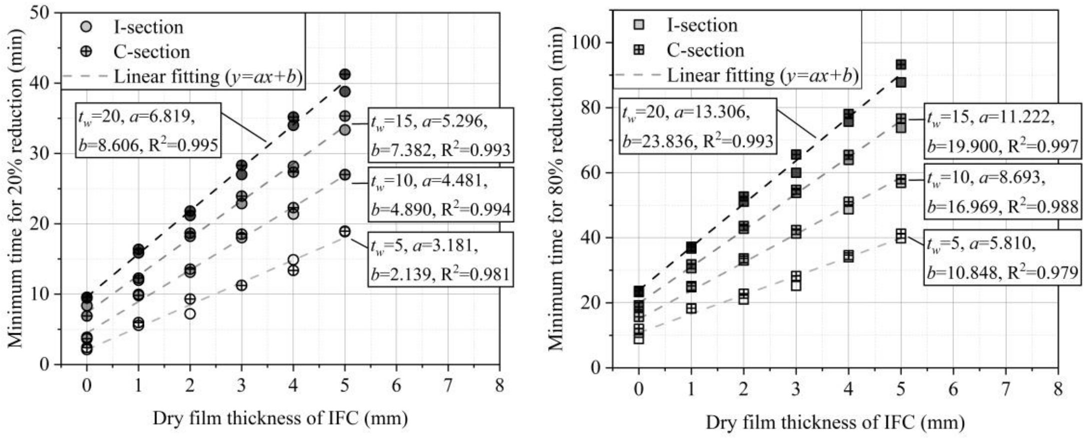

(a) 20% reduction (b) 80% reduction

Figure 4-15 The time points corresponding to the 20% and 80% reduction in buckling capacity for axially loaded IFC-protected steel columns.

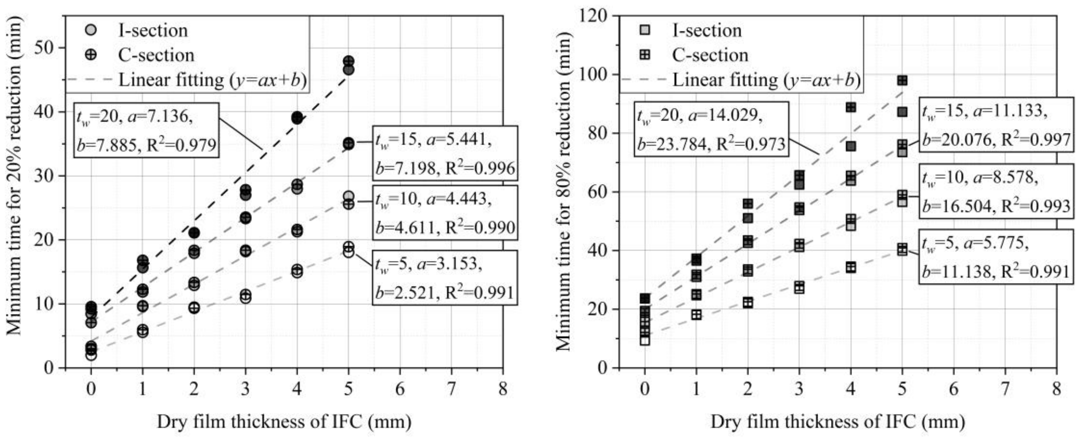

(a) 20% reduction (b) 80% reduction

Figure 4-16 The time points corresponding to the 20% and 80% reduction in buckling capacity for IFC-protected steel beams under pure bending.

Table 4-1 Fitting coefficients for the 20% and 80% reduction in buckling capacity for

Eq. (4.39).

Reduction factor	Fitting of the slope			Fitting of the intercept	
	α	β	γ	η	ξ
20% Reduction	3.127	13.344	-12.000	9.835	-19.277
80% Reduction	5.349	22.674	-9.541	26.387	-39.269

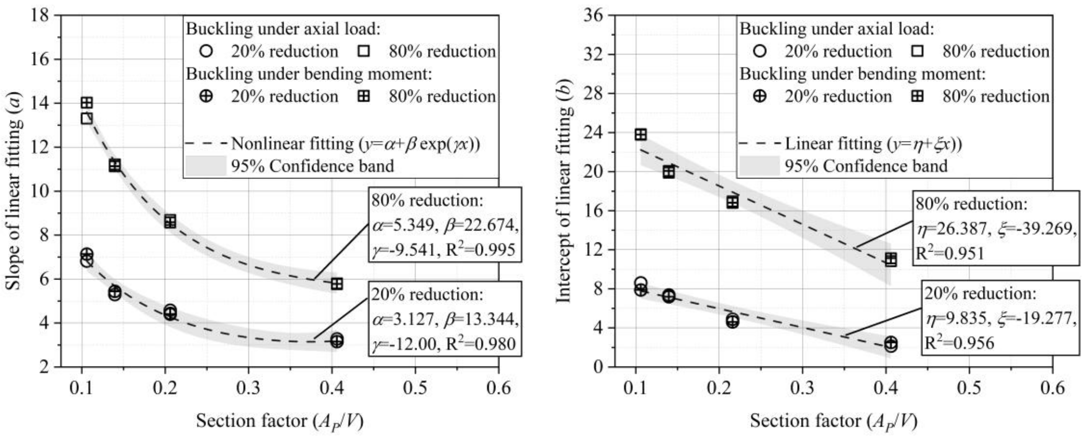

(a) Nonlinear fitting for the slope (b) Linear fitting for the intercept

Figure 4-17 Fitting for the slope and intercept.

Appendix 4A - Strain Distribution Across Section in Section 4.5.1

Although the plane-remains-plane assumption (Assumption (2)) may not be strictly accurate for steel members with a non-uniform thermal distribution, displacement changes caused by these differences are minimal compared to those caused by loads in slender members [153]. Figure 4-18 shows the strain distribution across the section at 100 minutes, calculated by SFEM in Section 7.2, indicating that the analysis method based on Assumption (2) is applicable.

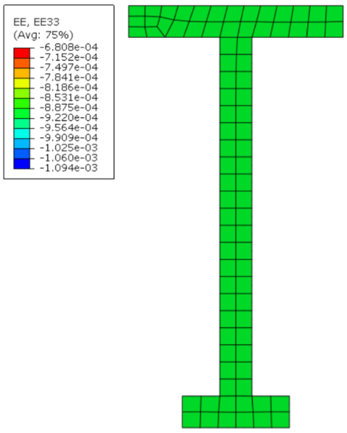

(a) I-section beam under compression

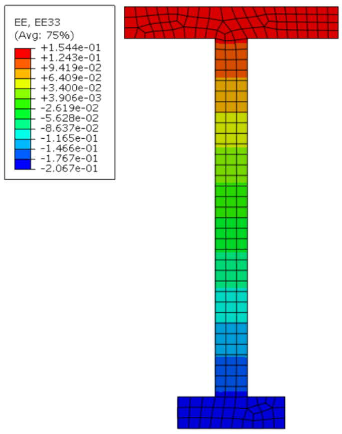

(b) I-section beam under bending

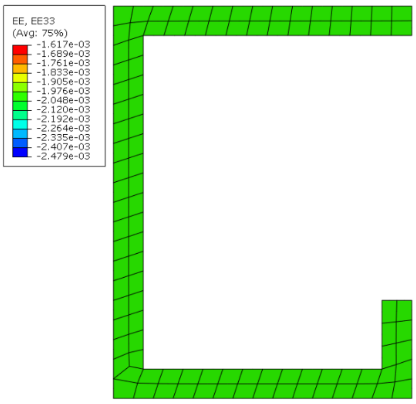

(c) C-section beam under compression

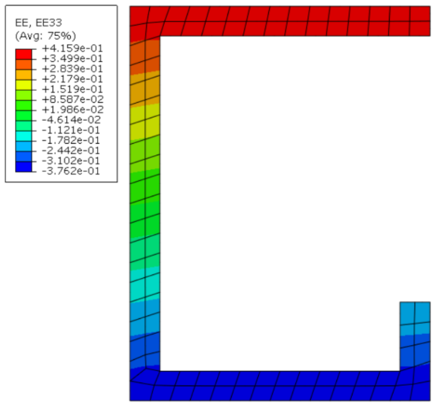

(d) C-section beam under bending

Figure 4-18 Strain distribution across the section at 100 min (from the SFEM).

CHAPTER 5.

SECOND-ORDER ANALYSIS OF STEEL MEMBERS UNDER FIRE BY ADVANCED LINE FINTE ELEMENT FORMULATION

5.1 Introduction

Traditional prescriptive fire resistance design approaches presume uniform fire exposure for steel members [135, 159, 160], which may result in a misestimation of the true capacity. As shown in Figure 5-1 (a) and (b), significant thermal gradients develop when perimeter columns [69, 161], bridges [162] and steel members connected to concrete [163] are exposed to natural fires. The thermal gradients cause non-uniform degradation of material properties within the cross-section, leading to an offset between the shear center and centroid of the cross-section, as shown in Figure 5-1(c). The offset may introduce additional torque in the member with large deflections, potentially causing early flexural-torsional or lateral-torsional buckling under external loads [56, 59, 139], as illustrated in Figure 5-1(d). This phenomenon highlights the necessity of considering twisting effects, as emphasized in the latest specification ANSI/AISC 360–22 [160].

Thermally induced twisting effects have also been observed in previous studies [164, 165], but most of these studies require sophisticated and detailed modeling to evaluate the impact. Although some numerical methods [100, 166] using beam-column elements are more appealing due to their higher efficiency and simpler modeling, their simplified assumptions expose limitations when encountering large deflections under non-uniform fire. Currently, there is a lack of accurate and efficient methods for second-order analysis of steel structures considering twisting effects under non-uniform fire. Furthermore, the mechanism of thermally induced twisting effects remains unexplored.

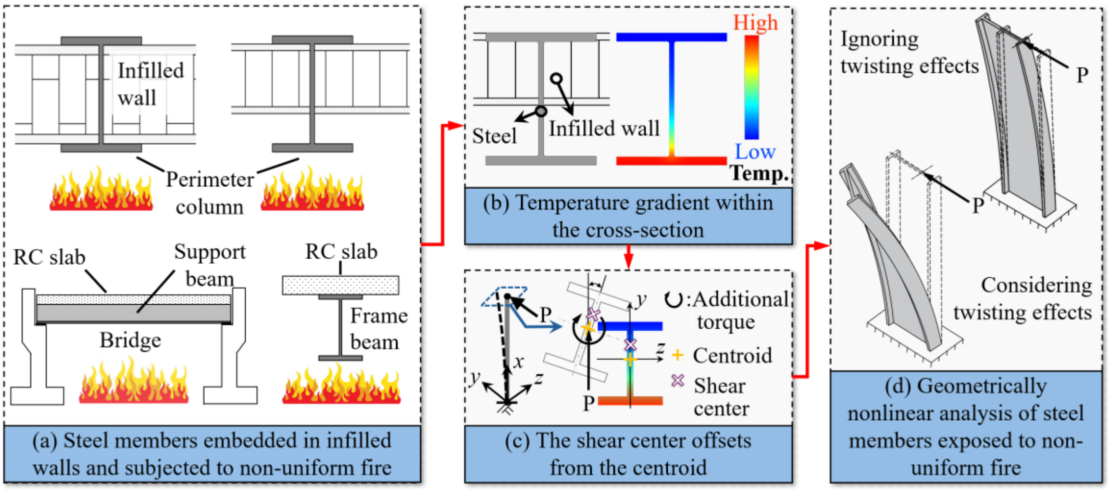

Figure 5-1 Mechanism of twisting effects in steel members subjected to natural fires.

Over the past few decades, substantial research has focused on the second-order analysis of steel members under non-uniform fire exposure. As early as 1988, Cooke [167] performed experimental research on steel members embedded in walls exposed to non-uniform fire and proposed corresponding design theories. Later, Usmani et al. [168] studied the curvature induced by thermal gradients in rotationally restrained members and provided an estimation method for thermal strains. Subsequently, Garlock and Quiel [136] analyzed the yield behavior of I-section steel members subjected to thermal gradients and proposed an evaluation method for determining the plastic neutral axis and stiffness center. Dwaikat et al. [169] carried out fire tests to investigate steel members subjected to fire-induced thermal gradients and introduced a finite element model to predict structural response and capacity. Moura et al. [161] conducted fire tests of steel columns embedded in walls under fire and found that current regulatory codes tend to be conservative in some cases. Their studies primarily focused on thermal bowing in the second-order behavior of steel members through experiments and qualitative analysis. However, calculating the structural responses of steel members under thermal gradients remains challenging, and the twisting effects are not examined.

To accurately evaluate the behavior of steel members under non-uniform fire conditions, several scholars have made significant efforts. Among these studies, the sophisticated finite element method (SFEM) is one of the most widely used approaches, typically employing shell or solid elements to develop detailed finite element models without relying on extensive simplified assumptions [170]. The SFEM can account for the detailed temperature distribution within a single component and its response to the combined effects of temperature variations and external forces, thereby robustly capturing the mechanical behavior of steel structures under non-uniform fire exposure. For instance, Agarwal et al. [69] investigated steel members subjected to thermal gradients using SFEM with shell elements. Lateral-torsional buckling due to cross-sectional asymmetry was observed, but the twisting effects underlying the buckling mode were not discussed. Chao et al. [171] developed a finite-element-based fire-structure model using shell and solid elements to predict the real response of a steel beam in localized fire tests, with the SFEM results showing good agreement with the test data. Recently, Nguyen et al. [172] conducted a parametric study on non-uniformly heated H-beams using the SFEM with shell elements. While SFEM offers detailed and accurate models for steel members subjected to non-uniform fire, this method requires significant computational resources, making it unsuitable for the engineering design of large-scale frame structures [173, 174].

Consequently, the line finite element method (LFEM) has emerged as an appealing solution for the second-order analysis of steel structures subjected to non-uniform fire. The LFEM refers to the finite element method using beam-column elements, offering enhanced computational efficiency and compatibility with large-scale frame structures [175, 176]. Some LFEMs incorporate various structural features, such as non-uniform expansion and thermally induced strain, making them suitable for the analysis of steel frames under fire conditions. For example, Li and Jiang [177] proposed a line element incorporating non-uniform temperature distribution to analyze large-scale steel frames. Franssen and Gernay [178] presented a line element based on the Bernoulli-type element and integrated it into SAFIR for implementation. Recently, Jiang et al. [98] reported a displacement-based line element that considered non-uniform thermal expansion, demonstrating good computational performance. However, these line elements neglect warping deformation and assume that the centroid and shear center coincide, which limits their ability to address large deflection problems involving twisting effects. Possidente et al. [179] presented a novel 3D beam element for addressing torsional problems, based on a corotational formulation and the assumption of small strains. However, their method did not account for the actual thermal gradients and expansion under non-uniform fire conditions. Against this background, Liu and his colleagues [62, 100, 150] developed a series of advanced line elements that account for the warping degree of freedom and have separate shear center and centroid axes. Although these line elements provide valuable insight into the second-order analysis of steel members, they assume a simplified distribution of temperature and thermal expansion and lack the ability to consider arbitrary cross-sections subjected to non-uniform fire.

Table 5-1 Characteristics of different finite element methods.

	SFEM [69, 164, 165, 172]	LFEM							
		ABQUS B31OS, B32OS [180]	Li & Jiang [177]	SAFIR beam [178]	Jiang et al. [98]	Liu et al. [62]	Chen et al. [100]	Possiden te et al. [179]	Present study
Second-order effect	✓	✓	✓	✓	✓	✓	✓	✓	✓

Twisting effects	✓	×	×	×	×	✓	✓	×	✓
Warping & torsion	✓	×	×	×	×	✓	✓	✓	✓
Real thermal gradient	✓	✓	✓	✓	✓	×	×	×	✓
Real thermal expansion	✓	✓	✓	✓	✓	×	×	×	✓
Arbitrary cross-section	✓	✓	×	✓	✓	✓	✓	✓	✓
Computing efficiency	*	***	***	**	***	***	***	***	***

Notes: A check (✓) means applicable, while a cross (×) means not applicable. The symbol (*) means the efficiency of the approach; for example, "*" for the lower efficiency and "***" for the higher.

To address these challenges, this study presents an advanced LFEM for the second-order analysis of steel members exposed to non-uniform fire, incorporating twisting effects induced by thermal gradients. This approach develops a refined line element based on the assumption that the shear center and centroid are offset due to non-uniform material degradation. The warping degree of freedom is also included, enabling the direct determination of lateral-torsional and flexural-torsional buckling in steel members subjected to non-uniform fire. A cross-section analysis approach is introduced to capture the cross-sectional properties considering non-uniform material degradation and parameters associated with twisting effects. A comparison with other methods, summarized in Table 5-1, highlights the novelty of the proposed approach. Several validation examples are provided to demonstrate the accuracy of the proposed LFEM, along with two case studies, which are carried out to discuss the impact of twisting effects on non-uniformly heated steel members and a single-story factory building, respectively. Additionally, the proposed method has been incorporated into a new structural analysis software, MSAsect2 [134], offering a practical tool for analyzing the geometrically nonlinear behavior of steel members under non-uniform fire conditions.

5.2 Assumptions

When a steel structure is subjected to non-uniform heating, significant thermal gradients develop. These gradients cause non-uniform degradation of material properties within the cross-section, resulting in an offset between the shear center and the centroid. This offset may introduce additional torque in members subjected to lateral loads. In some cases, the additional torque can lead to increased deformation and lateral–torsional buckling, potentially resulting in unsafe designs if twisting effects are neglected.

The following assumptions form the basis of this study: (1) The Timoshenko beam theory is applied to determine strain; (2) The member under investigation is sufficiently slender, therefore local buckling and cross-sectional distortion can be neglected; (3) Cross-sectional properties with non-uniform material degradation are represented by various products, such as axial stiffness $E_r\bar{A}$, bending stiffness $E_r\bar{I}$, and torsional stiffness $G_r\bar{J}$, where E_r and G_r are the reference material properties; (4) The variation of Poisson's ratio μ with temperature is neglected due to its minimal change [181, 182].

5.3 Advanced Line Element Formulation

To directly account for the twisting effects under fire, this section introduces a line element formulation that simultaneously considers non-uniform material degradation, second-order effects, thermal bowing, and twisting effects.

5.3.1 Definition of degrees of freedom and axes

The line element has two local axes and seven degrees of freedom (DOFs) at each node. The axes, nodal DOFs, and corresponding forces are depicted in Figure 5-2.

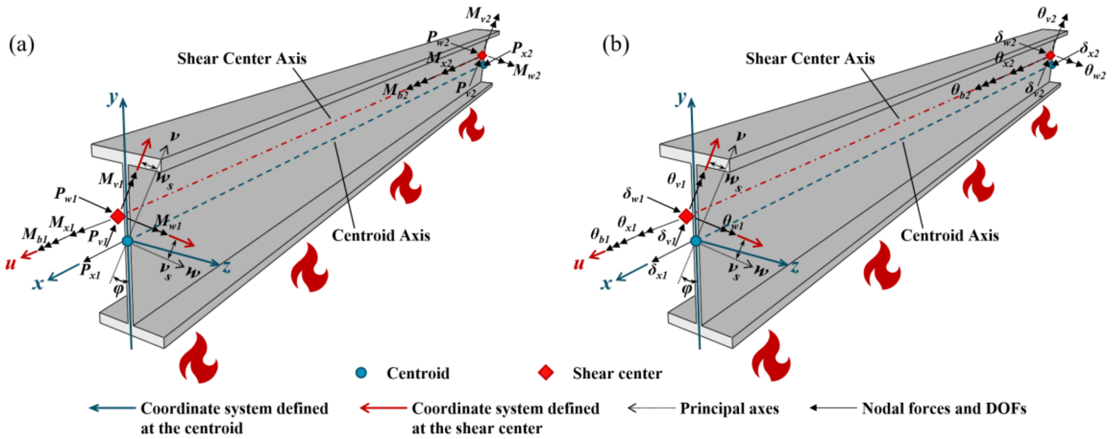

Figure 5-2 Definitions of local (a) nodal forces and (b) DOFs.

The shear center axis links the shear centers at both ends of the line element, whereas the centroid axis connects the centroids at each end. For clarity, only axial force P_{xi} and axial displacement δ_{xi} are aligned with the centroid axis, while all other forces and displacements are associated with the shear center axis. Due to non-uniform material degradation under fire, the shear center of the cross-section shifts, and the principal axis and shear center axis rotate by an angle φ. The nodal DOF vector is provided as follows:

$$\boldsymbol{u} = \begin{bmatrix} \delta_{xi} & \delta_{vi} & \delta_{wi} & \theta_{xi} & \theta_{vi} & \theta_{wi} & \theta_{bi} \end{bmatrix} \tag{5.1}$$

where i (i = 1, 2) is the number of the element nodes; δ_{xi}, δ_{vi}, and δ_{wi} are the nodal displacements along the shear center axis; θ_{xi}, θ_{vi}, and θ_{wi} are the nodal rotations along x-, v-, and w- axes, respectively; θ_{bi} represents the warping DOF. The corresponding force vector is

$$\boldsymbol{P} = \begin{bmatrix} P_{xi} & P_{vi} & P_{wi} & M_{xi} & M_{vi} & M_{wi} & M_{bi} \end{bmatrix} \tag{5.2}$$

in which P_{xi}, P_{vi}, and P_{wi} are the nodal forces along the shear center axis; M_{xi}, M_{vi}, and M_{wi} refer to the moments at the element node; M_{bi} represents the nodal bi-moment.

5.3.2 Interpolation functions

For the axial deformation, a linear interpolation function is employed, which can be easily derived from the nodal displacements:

$$\psi_x(\bar{x}) = (1-\bar{x})\delta_{x1} + \bar{x}\delta_{x2} \tag{5.3}$$

where $\bar{x} = x/L$ is the coordinate normalized by the length L of the line element. For lateral displacements of the Timoshenko line element, both shear distortion and bending deformations are taken into consideration. The interpolation functions are expressed as,

$$\psi_v(x) = \psi_{vb}(x) + \psi_{vs}(x) \tag{5.4}$$

$$\psi_w(x) = \psi_{wb}(x) + \psi_{ws}(x) \tag{5.5}$$

where $\psi_v(x)$ and $\psi_w(x)$ are the interpolation functions describing the lateral deflections along the v- and w- axes, respectively; $\psi_{vb}(x)$ and $\psi_{wb}(x)$ represent the bending deformations in v-w axes, while $\psi_{vs}(x)$ and $\psi_{ws}(x)$ represent the shear deformations. The rotation along the x-axis is divided into two components: shear and bending rotations, which are computed by,

$$\frac{d\psi_v(x)}{dx} = \theta_w(x) + \gamma_v(x) \tag{5.6}$$

$$\frac{d\psi_w(x)}{dx} = \theta_v(x) + \gamma_w(x) \tag{5.7}$$

in which $\gamma(x)$ and $\theta(x)$ denote the shear and bending rotations, respectively.

According to the relationship between shear forces and shear rotations [183],

$$P_v(x) = \frac{G_r \bar{A} \gamma_v(x)}{\alpha_{sv}} \tag{5.8}$$

$$P_w(x) = \frac{G_r \bar{A} \gamma_w(x)}{\alpha_{sw}} \tag{5.9}$$

the differential equations obtained from the equilibrium conditions are as follows:

$$\frac{G_r \bar{A}}{\alpha_{sw}} \left[\frac{\partial \psi_w(x)}{\partial x} - \theta_v(x) \right] - E_r \bar{I}_v \frac{\partial^2 \theta_v(x)}{\partial x^2} = 0 \tag{5.10}$$

$$\frac{G_r \bar{A}}{\alpha_{sv}} \left[\frac{\partial \psi_v(x)}{\partial x} - \theta_w(x) \right] - E_r \bar{I}_w \frac{\partial^2 \theta_w(x)}{\partial x^2} = 0 \tag{5.11}$$

where $G_r \bar{A}$, $E_r \bar{I}_v$, and $E_r \bar{I}_w$ are the degraded cross-sectional properties, which are detailed in Section 4.3; α_{sv} and α_{sw} denote the shear coefficients about *v*- and *w*-axes, respectively.

By substituting the Hermitian interpolation function [184] into Eqs. (5.10) and (5.11), the interpolation functions for shear rotations are derived, and the bending rotations are calculated as follows:

$$\theta_v(x) = a_0 + 2a_2 x + \left(3x^2 + \frac{\lambda_v L^2}{2} \right) a_3 \tag{5.12}$$

$$\theta_w(x) = a_0 + 2a_2 x + \left(3x^2 + \frac{\lambda_w L^2}{2} \right) a_3 \tag{5.13}$$

in which $\lambda_v = 12 E_r \bar{I}_v \alpha_{sv} / \left(G_r \bar{A} L^2 \right)$ and $\lambda_w = 12 E_r \bar{I}_w \alpha_{sw} / \left(G_r \bar{A} L^2 \right)$ are the coefficients corresponding to the shear deformation; a_0, a_2, and a_3 are the unknown coefficients in the Hermitian interpolation function, which remain to be determined.

Based on the values of nodal deformations and forces, the interpolation functions for the lateral displacements can be computed by,

$$\begin{aligned}\psi_v\left(\bar{x}\right) &= \left(1-\lambda_w b_w \bar{x}-3b_w\bar{x}^2+2b_w\bar{x}^3\right)\delta_{v1}+\left(\lambda_w b_w\bar{x}+3b_w\bar{x}^2-2b_w\bar{x}^3\right)\delta_{v2}\\ &+\left(\left(2+\lambda_w\right)\frac{b_w}{2}\bar{x}-\left(4+\lambda_w\right)\frac{b_w}{2}\bar{x}^2+b_w\bar{x}^3\right)L\theta_{w1}\\ &-\left(\lambda_w\frac{b_w}{2}\bar{x}+\left(2-\lambda_w\right)\frac{b_w}{2}\bar{x}^2-b_w\bar{x}^3\right)L\theta_{w2}\end{aligned} \tag{5.14}$$

$$\begin{aligned}\psi_w\left(\bar{x}\right) &= \left(1-\lambda_v b_v \bar{x}-3b_v\bar{x}^2+2b_v\bar{x}^3\right)\delta_{w1}+\left(\lambda_v b_v\bar{x}+3b_v\bar{x}^2-2b_v\bar{x}^3\right)\delta_{w2}\\ &+\left(\left(2+\lambda_v\right)\frac{b_v}{2}\bar{x}-\left(4+\lambda_v\right)\frac{b_v}{2}\bar{x}^2+b_v\bar{x}^3\right)L\theta_{v1}\\ &-\left(\lambda_v\frac{b_v}{2}\bar{x}+\left(2-\lambda_v\right)\frac{b_v}{2}\bar{x}^2-b_v\bar{x}^3\right)L\theta_{v2}\end{aligned} \tag{5.15}$$

where $b_v = 1/\left(1+\lambda_v\right)$ and $b_w = 1/\left(1+\lambda_w\right)$. For the rotational deformation along the element, a cubic Hermitian polynomial is recommended [58, 100] and it is assumed to be:

$$\psi_{\theta x}\left(x\right) = a_0 + a_1 x + a_2 x^2 + a_3 x^3 \tag{5.16}$$

Considering the boundary conditions,

$$\psi_{\theta x}\big|_{x=0} = \theta_{x1};\psi_{\theta x}\big|_{x=L} = \theta_{x2};\psi_{\theta x}'\Big|_{x=0} = \theta_{b1};\psi_{\theta x}'\Big|_{x=L} = \theta_{b2} \tag{5.17}$$

the interpolation function for rotational deformation can be obtained by solving for the unknown coefficients a_0, a_1, a_2 and a_3:

$$\begin{aligned}\psi_{\theta x}\left(\bar{x}\right) &= \left(\bar{x}-2\bar{x}^2+\bar{x}^3\right)\theta_{b1}L+\left(-\bar{x}^2+\bar{x}^3\right)\theta_{b2}L\\ &+\left(1-3\bar{x}^2+2\bar{x}^3\right)\theta_{x1}+\left(3\bar{x}^2-2\bar{x}^3\right)\theta_{x2}\end{aligned} \tag{5.18}$$

5.3.3 Total potential energy and element stiffness matrix

The stiffness matrix of the line element can be obtained through the second variation of the total potential energy Π, which consists of the work done by the external forces (V) and the strain energy stored in the element (U). The potential energy Π is given by,

$$\Pi = -V + U \tag{5.19}$$

where the strain energy can be computed by,

$$U = \frac{1}{2}\int_V \boldsymbol{\sigma}^T \boldsymbol{\varepsilon} dv = \frac{1}{2}\int_V \boldsymbol{\varepsilon}^T \boldsymbol{D}_0 \boldsymbol{\varepsilon} dv \tag{5.20}$$

where $\boldsymbol{\varepsilon}$ and $\boldsymbol{\sigma}$ denote the strain and stress vectors, as detailed by Liu et al. [58]; $\boldsymbol{D}_0$ represents the reference material constitutive matrix, and is expressed as,

$$\boldsymbol{D}_0 = \begin{bmatrix} E_0 & 0 & 0 \\ 0 & G_0 & 0 \\ 0 & 0 & G_0 \end{bmatrix} \tag{5.21}$$

The work done by the external forces is calculated as follows:

$$V = \sum \int_0^{u_i} \boldsymbol{P}_i \boldsymbol{u}_i \tag{5.22}$$

in which, $\boldsymbol{P}_i$ represents each possible external load on the element node in Eq. (5.2) and $\boldsymbol{u}_i$ represents the corresponding displacement along the load in Eq. (5.1). Considering the shear and normal stresses on the cross-section, along with the Green-Lagrange strain tensors given in [100], the total strain energy is calculated as follows after simplification:

$$
\begin{aligned}
U \approx & \frac{1}{2}\int_0^L E_0\left[\bar{A}\left(\frac{\partial \psi_x(x)}{\partial x}\right)^2+\bar{I}_w\left(\frac{\partial^2 \psi_v(x)}{\partial x^2}\right)^2+\bar{I}_v\left(\frac{\partial^2 \psi_w(x)}{\partial x^2}\right)^2+\bar{I}_\omega\left(\frac{\partial^2 \theta_x(x)}{\partial x^2}\right)^2\right]+G_0\bar{J}\left(\frac{\partial \theta_x(x)}{\partial x}\right)^2 dx \\
& +\frac{G_0\bar{A}}{\alpha_{sy}}\left[\left(\theta_w(x)\right)^2+\left(\frac{\partial \psi_v(x)}{\partial x}\right)^2-2\theta_w(x)\frac{\partial \psi_v(x)}{\partial x}\right]dx+\frac{G_0\bar{A}}{\alpha_{sz}}\left[\left(\theta_v(x)\right)^2+\left(\frac{\partial \psi_w(x)}{\partial x}\right)^2-2\theta_v(x)\frac{\partial \psi_w(x)}{\partial x}\right]dx \\
& +\int_0^L M_{v1}(1-\bar{x})\frac{\partial \theta_x(x)}{\partial x}\left[\frac{\partial \psi_v(x)}{\partial x}+\frac{1}{2}\beta_v\frac{\partial \theta_x(x)}{\partial x}\right]dx-\int_0^L M_{v2}\bar{x}\frac{\partial \theta_x(x)}{\partial x}\left[\frac{\partial \psi_v(x)}{\partial x}+\frac{1}{2}\beta_v\frac{\partial \theta_x(x)}{\partial x}\right]dx \\
& +\int_0^L M_{w1}(1-\bar{x})\frac{\partial \theta_x(x)}{\partial x}\left[\frac{\partial \psi_w(x)}{\partial x}+\frac{1}{2}\beta_w\frac{\partial \theta_x(x)}{\partial x}\right]dx-\int_0^L M_{w2}\bar{x}\frac{\partial \theta_x(x)}{\partial x}\left[\frac{\partial \psi_w(x)}{\partial x}+\frac{1}{2}\beta_w\frac{\partial \theta_x(x)}{\partial x}\right]dx \\
& +\int_0^L\left[P_v\left(\theta_x(x)\frac{\partial \psi_w(x)}{\partial x}-\frac{\partial \psi_x(x)}{\partial x}\frac{\partial \psi_v(x)}{\partial x}\right)-P_w\left(\theta_x(x)\frac{\partial \psi_v(x)}{\partial x}+\frac{\partial \psi_x(x)}{\partial x}\frac{\partial \psi_w(x)}{\partial x}\right)\right]dx \\
& +\frac{1}{2}\int_0^L P_x\left[\left(\frac{\partial \psi_v(x)}{\partial x}\right)^2+\left(\frac{\partial \psi_w(x)}{\partial x}\right)^2\right]dx+\frac{1}{2}\int_0^L P_x r^2\left(\frac{\partial \theta_x(x)}{\partial x}\right)^2 dx \\
& +\frac{1}{2}\int_0^L P_x\left[2v_s\frac{\partial \psi_w(x)}{\partial x}-2w_s\frac{\partial \psi_v(x)}{\partial x}\right]\frac{\partial \theta_x(x)}{\partial x}dx+\frac{1}{2}\int_0^L M_b\beta_\omega\left(\frac{\partial \theta_x(x)}{\partial x}\right)^2 dx
\end{aligned}
\tag{5.23}
$$

where β_v, β_w, and β_ω refer to the Wagner coefficients [185], which will be introduced in Section 4; $r^2=\left(\bar{I}_y+\bar{I}_z\right)/\bar{A}$. By incorporating the thermal-related energy [100] and performing the second variation, the tangent stiffness matrix $\boldsymbol{K}_{E,e}$ for the e^{th} line element is obtained:

$$
\boldsymbol{K}_{E,e}=\boldsymbol{T}\left(\boldsymbol{K}_{L,e}+\boldsymbol{K}_{G,e}+\boldsymbol{K}_{U,e}+\boldsymbol{K}_{T,e}\right)\boldsymbol{T}^T \tag{5.24}
$$

where $\boldsymbol{T}$ and $\boldsymbol{K}_{L,e}$ denote the transformation matrix from the shear center axis and the linear stiffness matrix considering the degraded cross-sectional properties, as detailed in **Appendix 5A**; $\boldsymbol{K}_{G,e}$ is the geometric stiffness matrix, as introduced by McGuire et al. [184]; $\boldsymbol{K}_{U,e}$ and $\boldsymbol{K}_{T,e}$ are the additional matrix accounting for the effects of non-symmetric cross-sections and thermal strain, which have been elaborated by Liu et al. [62, 100].

5.4 Key Properties under Non-uniform Fire

This section outlines the procedure for determining the cross-sectional properties of steel structures subject to non-uniform fire, providing the necessary calculation parameters for the aforementioned line elements, as shown in Figure 5-3.

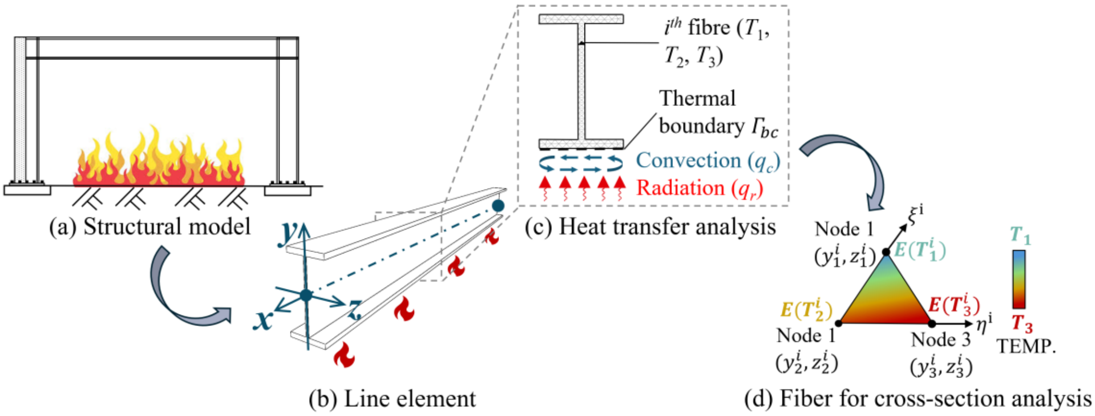

Figure 5-3 Sequentially coupled thermal-structural analysis process for cross-sectional properties.

This study adopts the sequentially coupled thermal-structural analysis approach, valued for its proven reliability and broad application [186, 187], to determine the cross-sectional properties of the structure shown in Figure 5-3(b). The temperature distribution is derived using the generalized Crank-Nicolson method illustrated in Section 3.3.

When the temperature across the cross-section is non-uniform, the material properties within the fibers become heterogeneous, as shown in Figure 5-3(d). To address this, reference material properties, which are positive constants that do not affect the calculations, are introduced to characterize the cross-sectional stiffnesses under non-uniform material degradation. These stiffnesses are a series of products, including reference material properties (E_r or G_r) and equivalent cross-sectional properties. By replacing the differential of the element area with its modulus-weighted counterpart, the area integrals can be computed. The details cross-section analysis method under non-uniform fire conditions is detailed in Secion 4.3. The derived cross-sectional properties provide a foundation for the implementation of LFEM.

5.5 Numerical Implementation

The numerical framework of the present study, as illustrated in Figure 5-4, comprises two main parts: cross-section analysis and structural analysis using the proposed line elements. First, a transient heat transfer analysis with s steps is conducted and the cross-sectional properties at different time steps are determined by accounting for non-uniform material degradation within each fiber, as shown in Figure 5-4(a). Key properties, including the shear center, centroid, and Wagner coefficient, which directly affect the twisting effects of the member, are calculated at each time step. Next, these cross-sectional properties are used in the LFEM for geometrically nonlinear analysis. An incremental-iterative procedure is applied at each time step, initializing the incremental forces as unbalanced forces, as depicted in Figure 5-4(b). At each load step of the incremental-iterative procedure, the element's tangent stiffness matrix is updated based on nodal displacements and forces. The Newton-Raphson technique is used for geometrically nonlinear analysis, maintaining equilibrium conditions at each load step. To ensure accurate results, incremental forces $\boldsymbol{U_F}$ should remain below 5% of the applied loads.

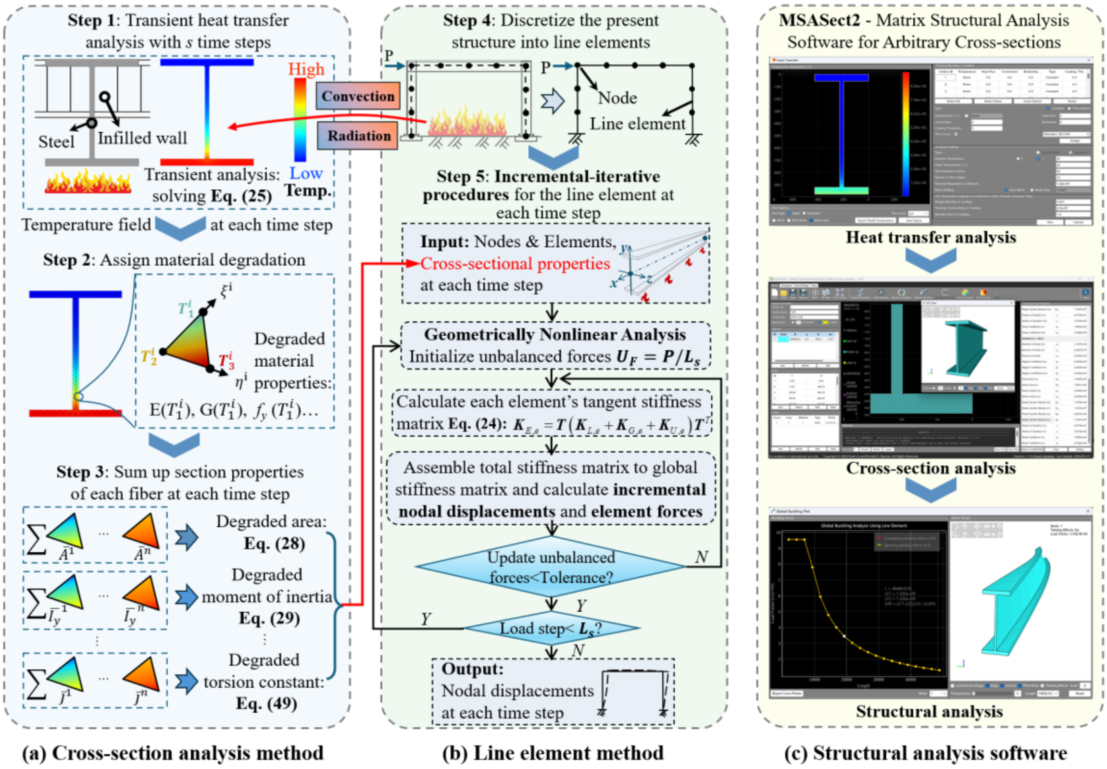

Figure 5-4 Numerical implementation of the proposed method.

Moreover, the proposed method is incorporated into the structural analysis software MSASect2 [134], as shown in Figure 5-4(c). The software, developed by the authors, has been publicly released and provides an efficient approach for analyzing steel structures with arbitrary cross-sections. The heat conduction module integrates the heat transfer and cross-section analysis methods presented in this study, enabling the analysis of the global buckling capacity of steel structures with fireproof coatings and arbitrary cross-sections under various thermal boundary conditions. This software aims to provide a user-friendly tool that enhances the reproducibility of this research.

5.6 Validation Examples

5.6.1 Cross-section analysis

The accuracy of the cross-section analysis is the base of the following geometric nonlinear analysis. To validate the proposed cross-section analysis method, this study compares its results with those from the SFEM. Specifically, the cross-sectional properties of H250×250×8×12 beams are examined under varying fire conditions. Figure 5-5 illustrates the different thermal boundary conditions, including the ISO 834 [154] standard fire exposure and adiabatic boundaries simulating surfaces protected by infilled walls. The infilled wall widths are D_1 = 100 mm and D_2 = 125 mm for cases (b) and (c), respectively.

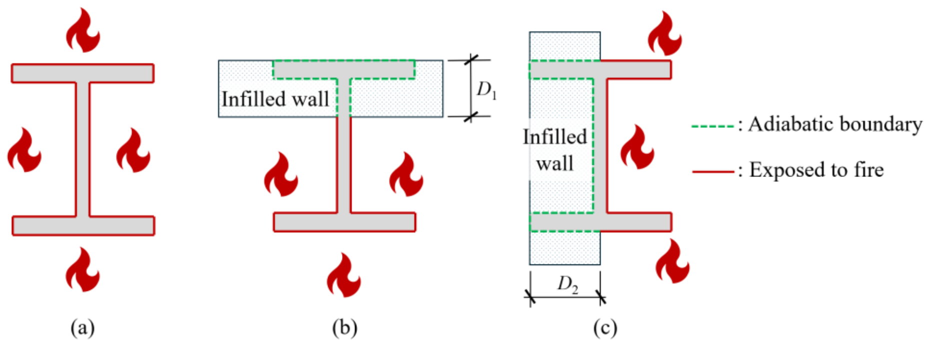

Figure 5-5 Thermal boundary conditions for the cross-sections in Example 2: (a) uniform fire exposure, (b) thermal gradients along the web, and (c) thermal gradients along the flanges.

The SFEM model is constructed in ABAQUS [180], employing 20-node solid elements (C3D20R). Both the web and flange of the model consist of two layers of elements, and the model has passed convergence tests. When calculating $E_r\bar{A}$ and $E_r\bar{I}$, the centroids at both ends are kinetically coupled via reference points, and equal and opposite axial forces or bending moments are applied at each reference point. The cross-sectional properties are determined by calculating the ratio of reaction forces to displacements. It is worth noting that when calculating the torsion constant $G_r\bar{J}$, the reference points are located at the shear centers, utilizing structural coupling to allow free warping, as the $G_r\bar{J}$ must be determined under Saint-Venant torsion conditions [188]. The length of the member is set to be more than 5 times the cross-section height to reduce the effects of cross-sectional distortion and local buckling [153, 189].

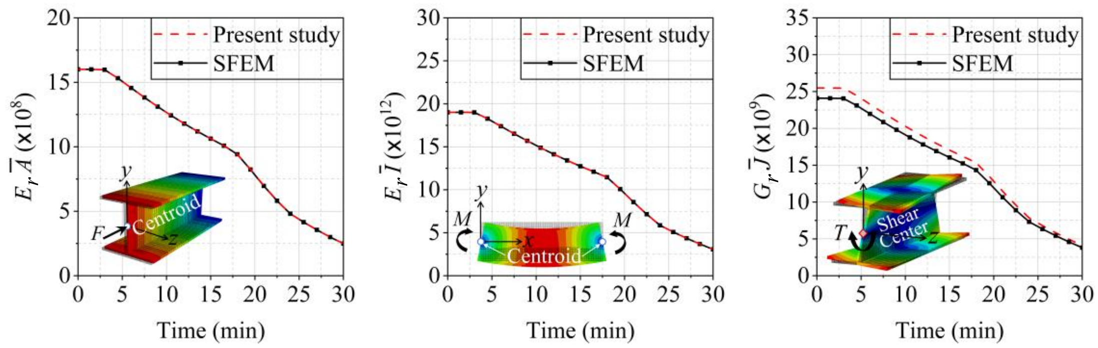

(a) $E_r\bar{A}$ (b) $E_r\bar{I}_z$ (c) $G_r\bar{J}$

Figure 5-6 Cross-sectional properties of steel members under thermal boundary (a).

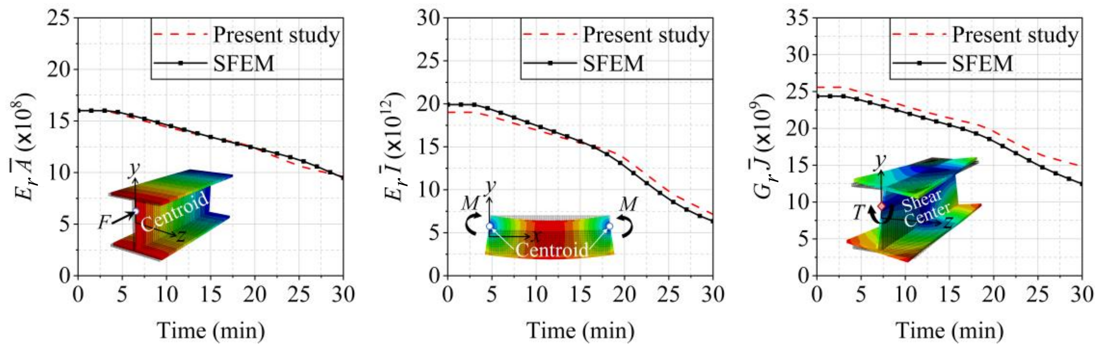

(a) $E_r\bar{A}$ (b) $E_r\bar{I}_z$ (c) $G_r\bar{J}$

Figure 5-7 Cross-sectional properties of steel members under thermal boundary (b).

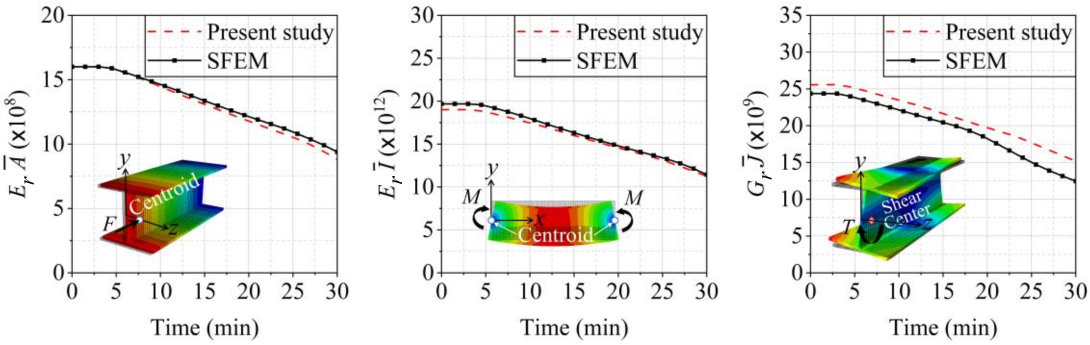

(a) $E_r\bar{A}$ (b) $E_r\bar{I}_z$ (c) $G_r\bar{J}$

Figure 5-8 Cross-sectional properties of steel members under thermal boundary (c).

The cross-sectional properties determined by the two methods under different fire exposure times are shown in Figure 5-6, Figure 5-7 and Figure 5-8, which demonstrates that the results predicted by the proposed method are almost identical to the SFEM. Minor discrepancies arise from the cross-sectional distortions in the SFEM model under load, which are neglected in the present study. Thus, it can be concluded that the proposed cross-section analysis method can robustly capture the degraded cross-sectional properties of the steel members subjected to non-uniform fire. The calculation times of both methods are provided in Table 5-2, demonstrating the efficiency of the proposed cross-section analysis method.

Table 5-2 The calculation time of the traditional SFEM and the proposed method.

Different fire conditions	Calculation time (s)				
	SFEM				Present study
	$E_r\bar{A}$	$E_r\bar{I}$	$G_r\bar{J}$	Total	$E_r\bar{A}$, $E_r\bar{I}$, $G_r\bar{J}$
Uniform fire exposure	124	128	1265	1517	12.2
Thermal gradients along the web	139	137	1392	1668	12.6

Thermal gradients along the flanges	172	191	1373	1736	12.5

5.6.2 Geometrically nonlinear analysis

In this example, originally reported by Li and Guo [130], a steel beam subjected to non-uniform fire and concentrated loads is studied. The beam has identical dimensions and thermal boundary conditions to those described in Example 1. The supports and loads are shown in Figure 5-9(a), where the stiffness of rotational and axial restrains are 1.09×10^{8} N·m/rad and 39.5 kN/mm, respectively, as calculated by Nguyen et al. [172]. The material degradation is presented in Section 4, and the thermal properties are derived from Eurocode 3, Part 1–2 [61]. The steel has a yield strength of 271 MPa, and a 1/1000 initial out-of-straightness is applied to the beam.

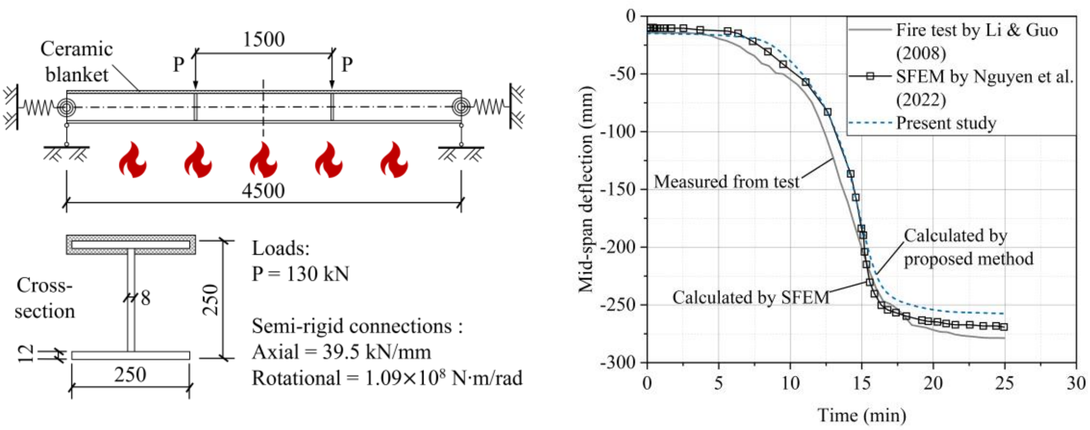

(a) Tested beam subjected to non-uniform fire

(b) Deflection at mid-span

Figure 5-9 Deflection of a non-uniformly heated steel beam obtained from different sources.

In the present study, a line element model with 20 elements is established to predict the mid-span deflection. The results from both the fire test and the present study are plotted in Figure 5-9(b). Additionally, the results from the SFEM by Nguyen et al. [172]

are also presented in the figure. Although the test beam was relatively slender, local buckling occurred due to rapid local heating, local loading from the oil jack and local initial imperfection. As a result, after 15 minutes of fire exposure, the predicted values deviated from both the SFEM-calculated and experimental values. Overall, the failure of the test beam is primarily governed by global buckling, and the predicted results of the proposed method are in good agreement with both the experimental values and SFEM calculation results. Therefore, the accuracy of the LFEM proposed in this study is further validated.

5.7 Case Studies

5.7.1 Steel members exposed to non-uniform fire

In this case study, different fire conditions and loading directions are investigated to analyze the mechanism and impact of twisting effects under non-uniform fires. A simply supported steel beam made of Q345 steel with a length of 8 m is subjected to the fire conditions shown in Figure 5-5 (D_1 = 100 mm, D_2 = 127 mm). The fire-exposed surface is subjected to ISO 834 standard fire [154] and is protected by a 4 mm layer of spray-applied fire resistive material (SFRM). The thermal conductivity, specific heat, and density of SFRM are assumed to be 0.02 W/(m·K), 1200 J/(kg·K), and 1000 kg/m^3, respectively. The beam, with a cross-section designated as W12×58, is subjected to a concentrated force of 132 kN at the mid-span in two directions: downward (-) and upward (+). The load ratio of concentrated force is approximately 60%. The beam is modeled using 10 proposed line elements, and a 1/1000 out-of-plane initial imperfection in the form of a sine curve is considered.

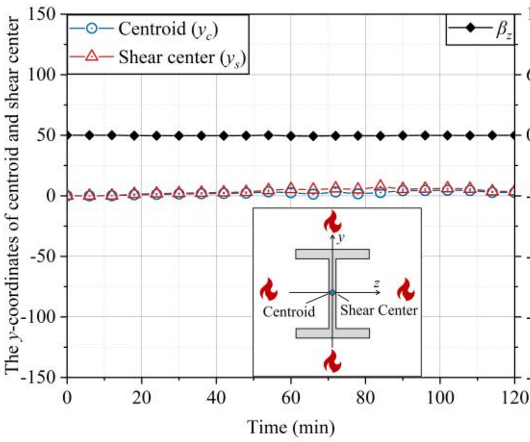

(a) Variation of centroid, shear center, and Wagner coefficient for steel members under uniform heating

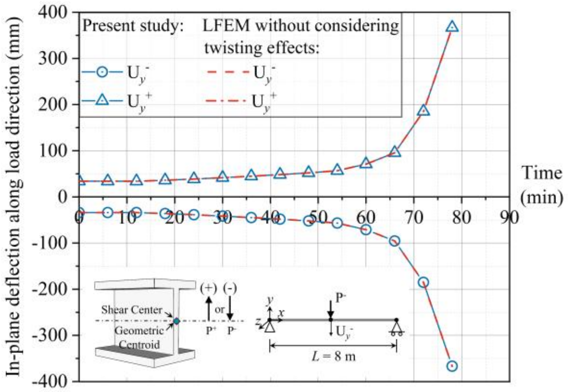

(b) Time-deflection curves for steel members under uniform heating

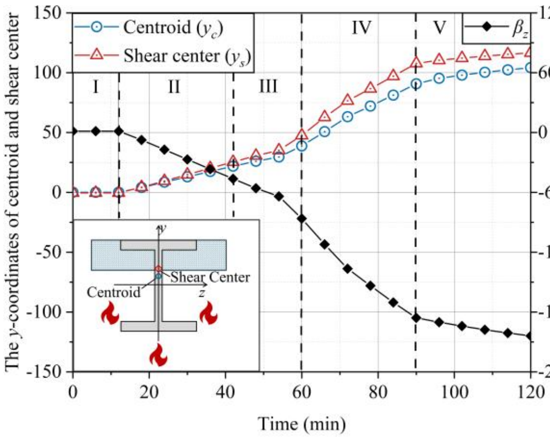

(c) Variation of cross-sectional properties for steel members with thermal gradients along the web

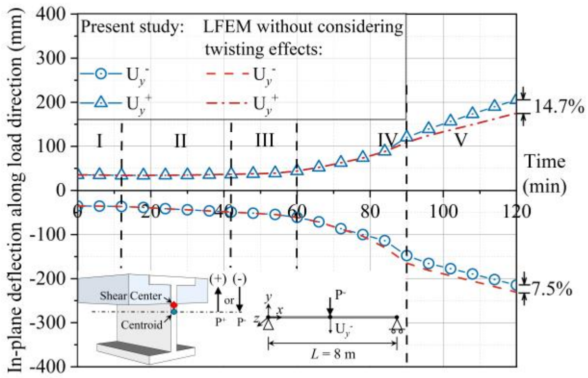

(d) Time-deflection curves for steel members with thermal gradients along the web

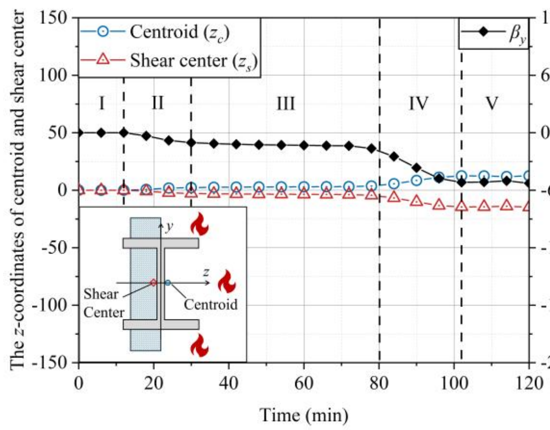

(e) Variation of cross-sectional properties for steel members

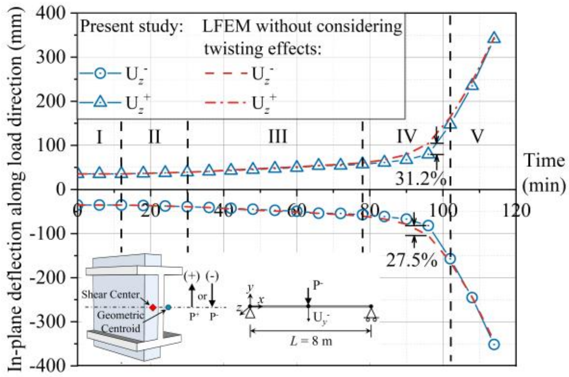

(f) Time-deflection curves for steel members with

with thermal gradients along the flanges thermal gradients along the flanges

Figure 5-10 Cross-sectional properties and time-deflection curves under different fire conditions.

The variations of cross-sectional properties, including Wagner coefficients and the coordinates of the centroid and shear center, are plotted in Figure 5-10. For sections with thermal gradients along the web, cross-sectional properties about the *y*-axis are provided, while for sections with thermal gradients along the flanges, the properties about *z*-axis are given. The fire exposure time-deflection curves calculated using the proposed method are also presented. For comparison, analysis results without considering twisting effects are provided, which employs the nonlinear LFEM proposed by Iu and Chan [93]. For the uniformly heated beam, the positions of the shear center and centroid remain unchanged, which results in β_z remaining zero, as shown in Figure 5-10(a). The temperature distribution across the cross-section is symmetrical. Thus, the time-deflection curves are the same under different load directions, as depicted in Figure 5-10(b).

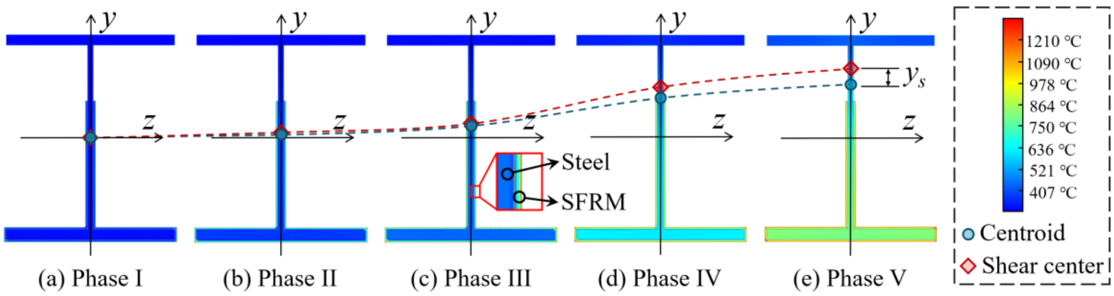

Figure 5-11 Temperature fields in different phases for the case of thermal gradients along the web.

For the beam with a thermal gradient along the web, the shear center and centroid move along the *y*-axis towards the unheated part. As the duration of exposure to fire increases, a clear distance gradually appears between the shear center and the centroid, and the absolute value of β_z also increases rapidly, as shown in Figure 5-10(c). Based on the cross-sectional properties, load-displacement curves (as shown in Figure 5-10(d)), and changes in temperature distribution (as shown in Figure 5-11), the entire process can be divided into five phases: (1) **Phase I** - Due to the protection provided by SFRM, there is no significant temperature change in the beam, the distance between the shear center and the centroid is zero, and the Wagner coefficient remains zero. Therefore, the deflection remains unchanged, and no twisting effects occur. (2) **Phase II** – As depicted in Figure 5-11, a thermal gradient begins to form, causing non-uniform thermal expansion that leads to thermal bowing towards the fire. The deflection of U_z^- increases, while U_z^+ experiences a slight decrease, as shown in Figure 5-10(d). (3) **Phase III** - As the highest temperature of the steel exceeds 300 °C, the material begins to degrade, the stiffness of the section decreases, and the displacement increases. (4) **Phase IV** - Due to non-uniform degradation of the material caused by thermal gradient shown in Figure 5-11, the absolute value of β_z increases rapidly, indicating that the cross-section becomes asymmetric as the material becomes increasingly uneven. The distance between the shear center and the centroid also increases rapidly, as shown in Figure 5-10(c). In the steel beam with torsional deformation, the load applied to the centroid generates an additional torque around the shear center, thereby increasing or decreasing the torsional deformation in a specific direction, as shown in Figure 5-12. Therefore, the twisting effect starts to appear. (5) **Phase V** - The distance between the shear center and the centroid reaches its maximum, and the difference between the two curves—one considering twisting effects and the other neglecting them—reaches as high as 14.7%.

When the thermal gradient is along the flanges, twisting effects still occur. However, **Phase V** exhibits a different behavior, as shown in Figure 5-10(f). Due to the faster heat flow in the double flanges compared to the single web, the stiffness of the beam decreases more rapidly, and the temperature gradient becomes less pronounced. The impact of twisting effects is much smaller than the decrease in stiffness. The deflection curves considering and ignoring twisting effects gradually approach each other.

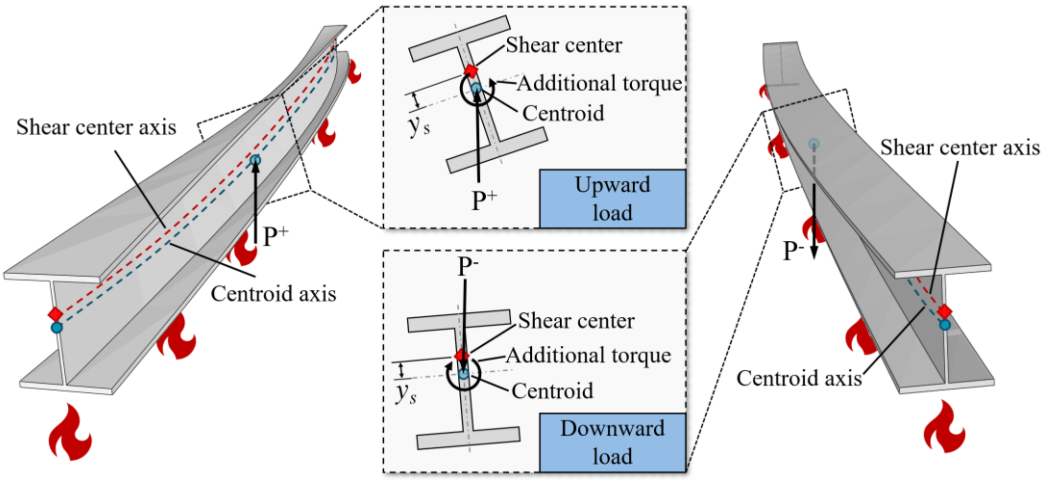

Figure 5-12 Mechanism of twisting effects in the beam under a thermal gradient along the web.

The mid-span torsion angle and out-of-plane deflection of the beam with a thermal gradient along the web are shown in Figure 5-13. The results of both methods indicate that the beam undergoes lateral-torsional buckling, characterized by a torsional angle and out-of-plane deflection. However, the method considering twisting effects predicts a larger torsional angle during lateral-torsional buckling, resulting in greater out-of-plane deflection. This occurs because, after lateral-torsional buckling, the load acting on the centroid generates additional torque at the shear center, as depicted in Figure 5-12. It can be observed that when the load direction aligns with the shear center offset, twisting effects cause greater deformation; conversely, when the directions oppose each other, the deformation is smaller.

This case study further investigates the impact of thermally induced twisting effects on non-symmetric I-section steel members. The upper flange of the I-section is narrower than that of the W12×58 section mentioned earlier, with a width of 190 mm, while all other dimensions remain unchanged. As shown in Figure 5-14, unlike double-symmetric I-section members, this member exhibits a non-coincidence of the centroid and shear center before fire exposure, making it prone to twisting effects at room temperature. Initially, the deformation under upward and downward loads differs, and the curves with and without considering twisting effects do not coincide. As the thermal gradient develops, the thermal expansion-induced bowing and the bending caused by the downward load act in the same direction, amplifying the twisting effects during **Phases I** to **III**. For upward loads, however, the thermal bowing opposes the applied load, thereby reducing twisting effects. From Figure 5-14(a), it is shown that the uneven material degradation during **Phase IV** causes the shear center and centroid to gradually approach each other. Consequently, the impact of twisting effects diminishes in **Phase V**, as illustrated in Figure 5-14(b). This analysis demonstrates that the presence of a thermal gradient can cause non-symmetric I-section members to behave similarly to double-symmetric I-sections at room temperature with respect to twisting effects.

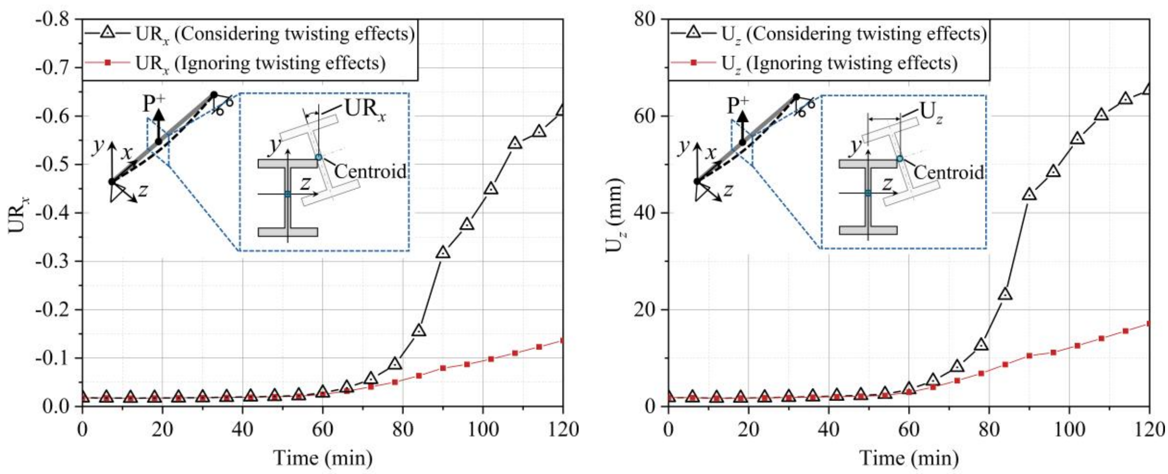

(a) Torsion angle (UR$_x$)

(b) Out-of-plane deflection (U$_z$)

Figure 5-13 Time-dependent variation of the torsion angle and out-of-plane deflection at the mid-span of the steel member with a thermal gradient along the web.

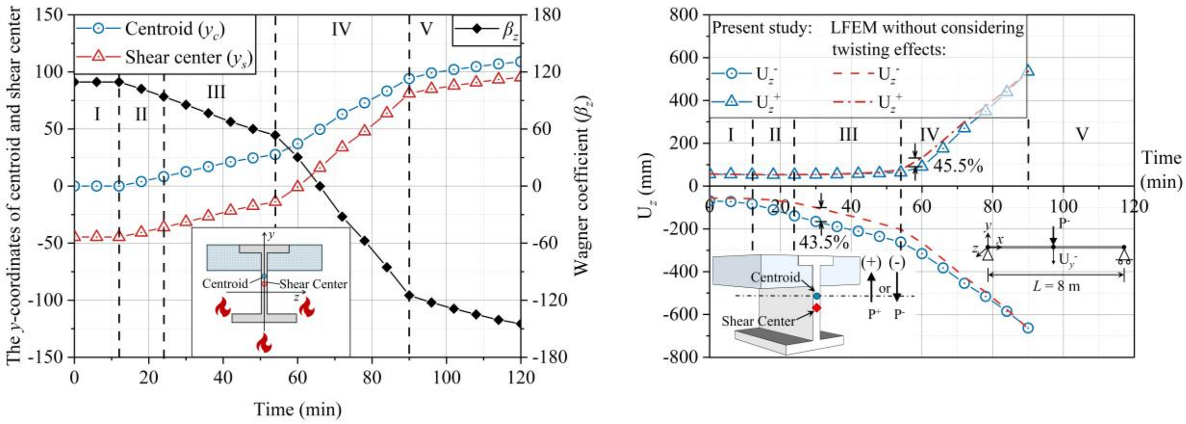

(a) Variation of cross-sectional properties for steel members with thermal gradients along the web

(b) Time-deflection curves for steel members with thermal gradients along the web

Figure 5-14 Cross-sectional properties and load-deflection curves for non-symmetric I-section steel members with thermal gradient.

5.7.2 Single-story factory building exposed to local fire

This case study investigates a single-story factory building under local fire to evaluate the influence of twisting effects on the frame structure. The plan and elevation views are shown in Figure 5-15. A typical local fire scenario on the rigid frame along grid line B is analyzed. The live and dead loads from the roof are applied to the floor slab and transmitted to the main beam web through the secondary beams. The columns are embedded in a 200 mm-thick infill wall, which does not contribute to the structural stiffness but serves as thermal insulation for the columns.

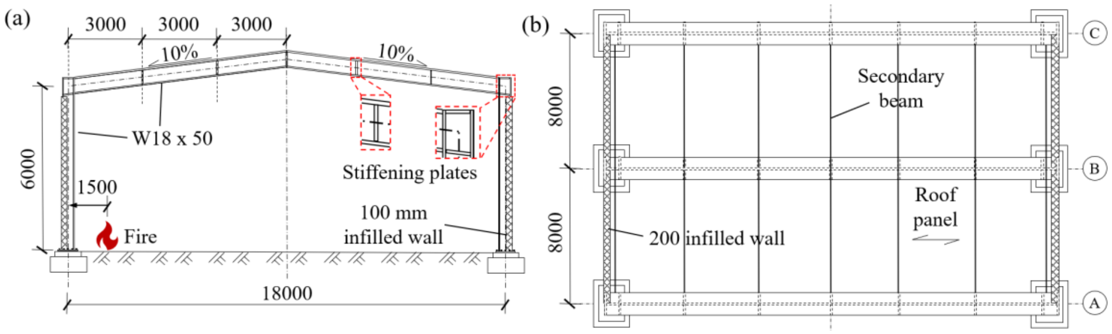

Figure 5-15 (a) Elevation view along Grid Line B and (b) plan view of a typical single-story factory building exposed to a local fire (unit: mm).

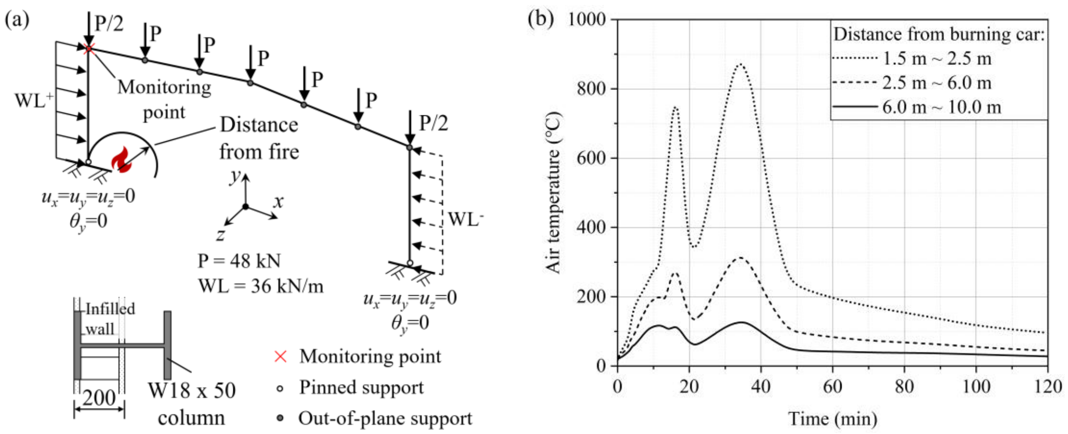

Figure 5-16 (a) Simplified mechanical model and loads of the factory building; (b) the air temperature depends on the distance from the local fire [45].

This frame structure is simplified into the model shown in Figure 5-16(a). The self-weight of roof panels and imposed load are modeled as vertical surface pressures of 0.5 kPa and 1.5 kPa, respectively. Therefore, a concentrated force of P = 48 kN, is transmitted by the secondary beam. The extreme wind load acts on the longitudinal infill wall and is transmitted to the columns. WL^+ and WL^- denote the wind loads acting on the column in two directions, each with a magnitude of 36 kN/m. The secondary beam provides out-of-plane support. All loads are assumed to be applied at the centroid of the cross-section, and each member is divided into 10 line elements, with a 1/1000 out-of-plane initial imperfection in the form of a sine curve. All beams and columns are

W18×50 sections made of Q345 steel, with the joints connected by welding. As shown in Fig(a), the local stiffness of the joints and the concentrated load application points on the primary beams are enhanced by adding 15 mm stiffening web plates to minimize the influence of local failure. The column base is connected to the foundation via a flange connection and is assumed to be pinned and free to warp. The maximum deflection of the members under service load conditions (including self-weight and imposed loads) is 49.3 mm, which is within the allowable limit (span/360 = 50 mm). The frame is designed to satisfy the serviceability limit states under ambient temperature conditions.

The fire is located at a vertical distance of 1.5 m from the left column. A typical local fire scenario is investigated to demonstrate the capability of the proposed method in handling non-uniform fires at the frame level. Figure 5-16(b) shows the air temperature as a function of fire duration and distance from the fire center, as reported in ECCS [45]. Under the local fire scenario, the joints reach a maximum temperature of below 300°C, and no significant yielding occurs in the joints, as shown in Figure 5-17. Therefore, the rigid joints are used in the LFEM calculations.

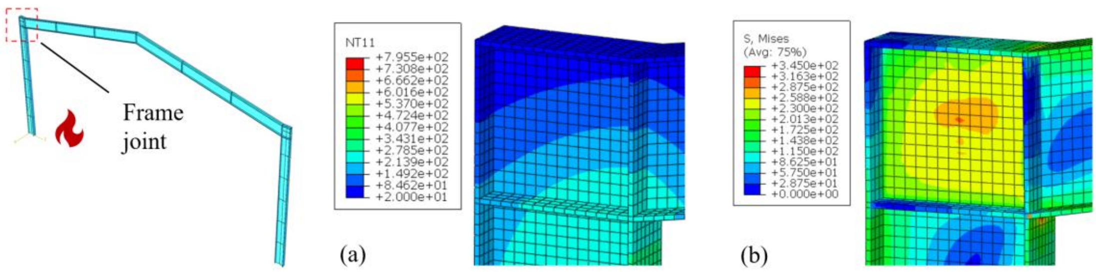

Figure 5-17 SFEM results of (a) temperature distribution and (b) Von Mises stress in the joints.

Under the applied load conditions, the steel frame does not collapse, and the horizontal displacements at the monitoring point, calculated using the proposed method, the SFEM described in Section 6.2 and another LFEM neglecting thermally induced twisting effects [100], are present in Figure 5-18. The proposed method shows closer agreement with the SFEM in capturing twisting effects. According to case study 1, the offset of the shear center from the centroid of the left column is in the negative *x*-axis direction. As shown in Figure 5-18, when the direction of the wind load is positive along the *x*-axis, twisting effects will cause a smaller displacement, whereas when the wind load is negative along the *x*-axis, twisting effects will cause a larger displacement. It can be concluded that when the bending of the member caused by external loads is towards the direction of the shear center offset, ignoring twisting effects results in conservative evaluation; conversely, when the bending is reversed, ignoring twisting effects leads to unsafe evaluation. Therefore, for structures subjected to non-uniform fire, it is essential to fully account for both fire and load conditions to assess the impact of twisting effects. Moreover, the proposed method is more efficient, requiring around 3 minutes for one load case compared to 19 minutes for the SFEM, with all computations performed on the same device.

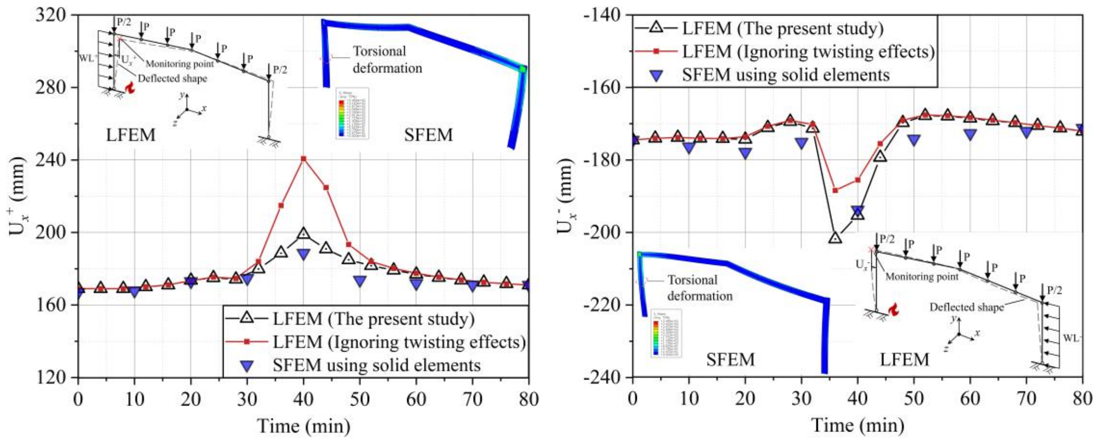

(a) Under WL$^+$ (b) Under WL$^-$

Figure 5-18 Horizontal displacement of the monitoring point.

Appendix 5A - Mathematical Expressions for Transformation Linear Stiffness Matrices

The transformation matrix and the linear stiffness matrix are expressed by,

$$\boldsymbol{T}=\begin{bmatrix}
1 & 0 & 0 & 0 & 0 & 0 & 0 & 1 & 0 & 0 & 0 & 0 & 0 & 0 \\
 & \vartheta_z & 0 & 0 & 0 & \vartheta_z & 0 & 0 & \vartheta_z & 0 & 0 & 0 & \vartheta_z & 0 \\
 & & \vartheta_y & 0 & \vartheta_y & 0 & 0 & 0 & 0 & \vartheta_y & 0 & \vartheta_y & 0 & 0 \\
 & & & 1 & 0 & 0 & 1 & 0 & 0 & 0 & 1 & 0 & 0 & 1 \\
 & & & & \vartheta_y & 0 & 0 & 0 & 0 & \vartheta_y & 0 & \vartheta_y & 0 & 0 \\
 & & & & & \vartheta_z & 0 & 0 & \vartheta_z & 0 & 0 & 0 & \vartheta_z & 0 \\
 & & & & & & 1 & 0 & 0 & 0 & 1 & 0 & 0 & 1 \\
 & & S. & & & & & 1 & 0 & 0 & 0 & 0 & 0 & 0 \\
 & & & Y. & & & & & \vartheta_z & 0 & 0 & 0 & \vartheta_z & 0 \\
 & & & & M. & & & & & \vartheta_y & 0 & \vartheta_y & 0 & 0 \\
 & & & & & & & & & & 1 & 0 & 0 & 1 \\
 & & & & & & & & & & & \vartheta_y & 0 & 0 \\
 & & & & & & & & & & & & \vartheta_z & 0 \\
 & & & & & & & & & & & & & 1
\end{bmatrix} \tag{5.25}$$

where $\vartheta_y=\dfrac{\overline{I}_y+\overline{I}_z+\left(\overline{I}_y-\overline{I}_z\right)cos2\varphi+2\overline{I}_{yz}sin2\varphi}{2\overline{I}_y}$, $\vartheta_z=\dfrac{\overline{I}_y+\overline{I}_z-\left(\overline{I}_y-\overline{I}_z\right)cos2\varphi-2\overline{I}_{yz}sin2\varphi}{2\overline{I}_z}$.

$$\boldsymbol{K}_{L,e}=\begin{bmatrix}
\frac{E_r\overline{A}}{L} & 0 & 0 & 0 & 0 & 0 & 0 & -\frac{E_r\overline{A}}{L} & 0 & 0 & 0 & 0 & 0 & 0 \\
 & \varsigma_z & 0 & 0 & 0 & \frac{L\varsigma_z}{2} & 0 & 0 & -\varsigma_z & 0 & 0 & 0 & \frac{L\varsigma_z}{2} & 0 \\
 & & \varsigma_y & 0 & -\frac{L\varsigma_y}{2} & 0 & 0 & 0 & 0 & -\varsigma_y & 0 & -\frac{L\varsigma_y}{2} & 0 & 0 \\
 & & & \frac{\kappa_1+6\kappa_2}{5L^3} & 0 & 0 & \frac{\kappa_1+\kappa_2}{10L^2} & 0 & 0 & 0 & -\frac{\kappa_1+6\kappa_2}{5L^3} & 0 & 0 & \frac{\kappa_1+\kappa_2}{10L^2} \\
 & & & & \varsigma_y\left(\frac{L^2}{3}+\varpi_z\right) & 0 & 0 & 0 & 0 & -\frac{L\varsigma_y}{2} & 0 & \varsigma_y\left(\frac{L^2}{6}-\varpi_z\right) & 0 & 0 \\
 & & & & & \varsigma_z\left(\frac{L^2}{3}+\varpi_y\right) & 0 & 0 & -\frac{\varsigma_z L}{2} & 0 & 0 & 0 & \varsigma_z\left(\frac{L^2}{6}-\varpi_y\right) & 0 \\
 & S. & & & & & \frac{\kappa_1+2\kappa_2}{15L} & 0 & 0 & 0 & -\frac{\kappa_1+\kappa_2}{15L^2} & 0 & 0 & \frac{\kappa_1-\kappa_2}{30L} \\
 & & & & & & & \frac{E_r\overline{A}}{L} & 0 & 0 & 0 & 0 & 0 & 0 \\
 & & Y. & & & & & & \varsigma_z & 0 & 0 & 0 & -\frac{\varsigma_z L}{2} & 0 \\
 & & & & & & & & & \varsigma_y & 0 & \frac{L\varsigma_y}{2} & 0 & 0 \\
 & & & & & M. & & & & & \frac{\kappa_1+6\kappa_2}{5L^3} & 0 & 0 & -\frac{\kappa_1+\kappa_2}{10L^2} \\
 & & & & & & & & & & & \varsigma_y\left(\frac{L^2}{3}+\varpi_z\right) & 0 & 0 \\
 & & & & & & & & & & & & \varsigma_z\left(\frac{L^2}{3}+\varpi_y\right) & 0 \\
 & & & & & & & & & & & & & \frac{\kappa_1+2\kappa_2}{15L}
\end{bmatrix}$$

(5.26)

in which $\varpi_y = \dfrac{E_r \bar{I}_y}{\alpha_{sy}} G_r \bar{A}$, $\varpi_z = \dfrac{E_r \bar{I}_z}{\alpha_{sz}} G_r \bar{A}$, $\zeta_z = \dfrac{12 E_r \bar{I}_z}{L^3 + 12\varpi_y L}$, $\zeta_y = \dfrac{12 E_r \bar{I}_y}{L^3 + 12\varpi_z L}$, $\kappa_1 = 60 E_r \bar{I}_\omega$ and $\kappa_2 = G_r \bar{J} L^2$; $\bar{I}_y$, $\bar{I}_z$, α_{sy} , α_{sz} , $\bar{I}_\omega$, and $\bar{J}$ are cross-sectional properties calculated in Section 4.3.

CHAPTER 6.

STRENGTH EVALUATION OF CONCRETE-ENCASED STEEL MEMBERS UNDER FIRE USING RIGOROUS CROSS-SECTIONAL YIELD SURFACES

6.1 Introduction

Concrete-encased steel columns exhibit exceptional fire resistance due to the low thermal conductivity and high specific heat capacity of the concrete within the concrete-encased steel cross-sections (see Figure 6-1(a)). In most cases, concrete reduces the overall thermal conductivity of the cross-sections and supports the steel profiles, thus mitigating local buckling and enhancing fire resistance [190-192]. After appropriate repairs, these columns can be reused after fire exposure and continue to carry loads [193-196]. Therefore, this chapter aims to provide a calculation method for the yield surfaces of these columns, serving as a foundational study for the plastic analysis of fire resistance design in the subsequent chapter.

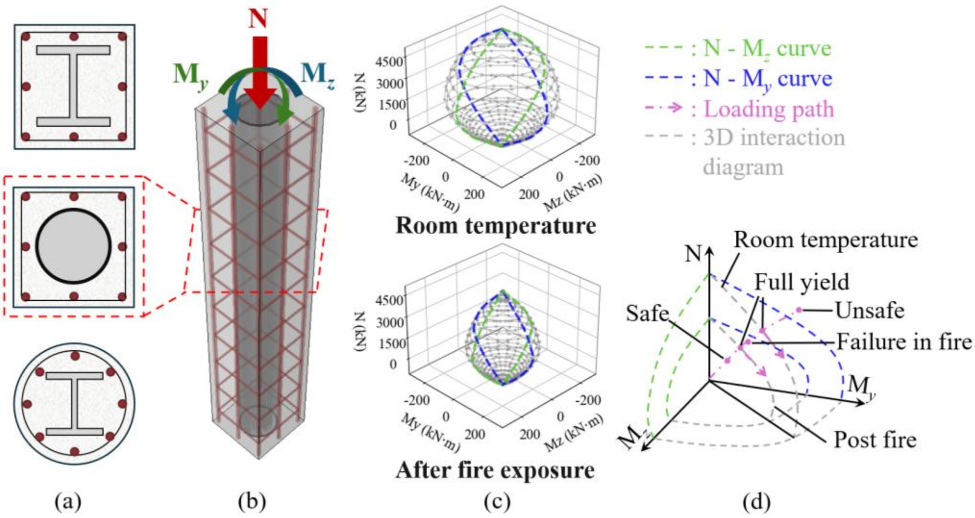

Figure 6-1 Analysis of interaction diagrams: (a) typical cross-sections; (b) concrete-encased steel column under biaxial bending; (c) 3D interaction diagrams; (d) Ultimate

capacity check.

Functional demands in real buildings often cause the columns to undergo combined compression and bending due to load transfer from adjacent beams and slabs. When a column is located at a corner or subjected to non-uniform fire effects, it experiences more complex loading conditions [197-199], including biaxial bending and compression, as shown in Figure 6-1(b). To evaluate and design these columns under biaxial bending and compression, 3D strength interaction diagrams (see Figure 6-1(c)) are commonly employed in structural analysis. These diagrams conveniently depict the ultimate axial-bending capacity within the loading domain. The safety of a column's strength capacity is assessed by determining whether the moment-axial load point lies inside or outside the interaction diagram, as shown Figure 6-1(d). However, existing research on interaction diagrams for these columns subjected to fire exposure is limited, especially for complex biaxial bending cases. Moreover, calculating interaction diagrams for concrete-encased steel sections under fire is challenging owing to non-uniform material degradation, which results in complex calculations, with the required incremental computations being impractical for routine structural design.

To develop a more practical calculation and design approach, several studies have contributed to the analysis of interaction diagrams for concrete-encased steel columns subjected to standard fire [128]. For example, Caldas et al. [73] proposed a procedure to calculate the axial force-moment interaction curves of concrete-encased steel columns and extended this technique to other composite columns with general cross-sections. Law and Gillie [74] developed a numerical method to generate 2D interaction diagrams at high temperatures based on the tangent stiffness matrix of the cross-sections. Pham et al. [77] reported a yield design approach for directly computing 2D Interaction diagrams of reinforced concrete sections under fire. Albero et al. [78]

addressed the challenge of uneven temperature distribution across different components by assigning equivalent uniform temperatures to each component, thereby proposing a simplified design method. Li et al. [191] conducted experimental investigation on high-strength concrete-encased steel columns, and proposed a design method based on steel contribution ratio. Xiong and Liew [200] proposed a refined axial force-moment interaction curve model for concrete-filled steel tubes under fire, based on the plastic design principles. While these studies offer valuable insights for developing interaction diagrams of concrete-encased steel columns under fire, they primarily focus on behavior at elevated temperatures and are not applicable to biaxial bending and compression. Additionally, some simplifications in these methods, such as assuming uniform temperature distribution within components and representing the interaction curve as a polyline, may lead to overly conservative outcomes.

Research works on the interaction diagrams of concrete-encased steel columns after fire exposure remains limited. Han et al. [201] employed a sophisticated finite element model to simulate the behavior of steel-reinforced concrete columns after fire exposure and calculated their interaction curves under various parameters. Liu et al. [202] integrated experimental data and finite element simulations to develop a simplified polylinear model for predicting the axial force-moment interaction curves of concrete filled steel tubes (CFSTs) after fire exposure. Hwang and Kwak [203] carried out numerical study on post-fire interaction diagrams of RC columns and compared the proposed design method with several design codes. Demir et al. [204] investigated the post-fire 2D interaction diagrams of concrete-encased steel columns experimentally and evaluated their residual bearing capacity to resist seismic loads. More recently, Zhong et al. [205] conducted experimental and numerical studies on the eccentric compression performance of high-strength steel-reinforced concrete columns after fire exposure, proposing a simplified model for post-fire interaction curves. These studies have contributed to methods for calculating interaction diagrams of concrete-encased steel columns after fire exposure. However, the high cost of fire testing and the computational demands of sophisticated finite element models limit the practical applicability of these methods in design.

Therefore, this study aims to develop a simplified model to calculate the 3D interaction diagrams of concrete-encased steel columns after fire exposure. The model offers a practical tool to evaluate the post-fire ultimate strength of typical concrete-encased steel columns subjected to biaxial bending moments and axial compression. To establish this model, a fiber-based cross-section analysis method is developed to compute the 3D interaction diagrams and validated against fire test data as well as other numerical methods. The cross-section analysis method demonstrates good accuracy and is employed in a parametric study comprising 162,000 cases, revealing the influence of various parameters. The results form a comprehensive database used to derive the simplified model for concrete-encased steel columns, which achieves a mean error of 5.3%. Furthermore, the cross-section analysis method has been integrated into the novel software, MSASect2 [134], to facilitate calculation of residual section capacity of concrete-encased steel columns after fire exposure and to enhance the reproducibility of this study.

6.2 Rigorous Cross-sectional Yield Surfaces

6.2.1 Assumptions

The present study is based on the following assumptions: (1) Plane cross-sections remain plane after deformation, indicating that strain is linearly distributed across the entire cross-section; (2) Tensile strength of concrete is neglected after cracking; (3) Steel profiles are assumed to be embedded in the concrete without bond-slip; (4) Thermal creep strain is neglected due to its minimal contribution to the total strain in post-fire analysis [206-208].

6.2.2 Heat transfer analysis

This study adopts the sequentially coupled thermal–stress analysis framework, as illustrated in Figure 6-2, which is widely used in post-fire assessments and is recognized for its robustness and accuracy [131, 209, 210]. The temperature distribution across the cross-section is calculated using a transient finite element method with n time steps, employing the generalized Crank–Nicolson scheme [117]. The governing equation of the (s+1)-th step is expressed as:

$$\left(\frac{1}{\Delta t}\boldsymbol{M}^{i}+\boldsymbol{K}^{i}\right)\left\{\boldsymbol{T}^{i}\right\}^{s+1}=\frac{1}{\Delta t}\boldsymbol{M}^{i}\left\{\boldsymbol{T}^{i}\right\}^{s}+\left\{\boldsymbol{q}^{i}\right\}^{s+1} \tag{6.1}$$

where Δt represents the step length; $\boldsymbol{M}^{i}$ and $\boldsymbol{K}^{i}$ are the element capacitance matrix and element conductivity matrix of the i-th fiber, respectively; $\boldsymbol{T}^{i}$ is the vector of nodal temperatures obtained by solving the governing equation; $\boldsymbol{q}^{i}$ denotes the load vector accounting for heat convection and radiation. As shown in Figure 6-2(b), both thermal radiation and convection are taken into account. The convective heat transfer coefficient adopts the recommended value 25 W/(m^2·°C) from EN 1991-1-2 [211]. The emissivity coefficient has been investigated by many researchers. In this study, a value of 0.7 is adopted, as it falls within the range commonly reported in previous studies and has demonstrated reliability [212-215].

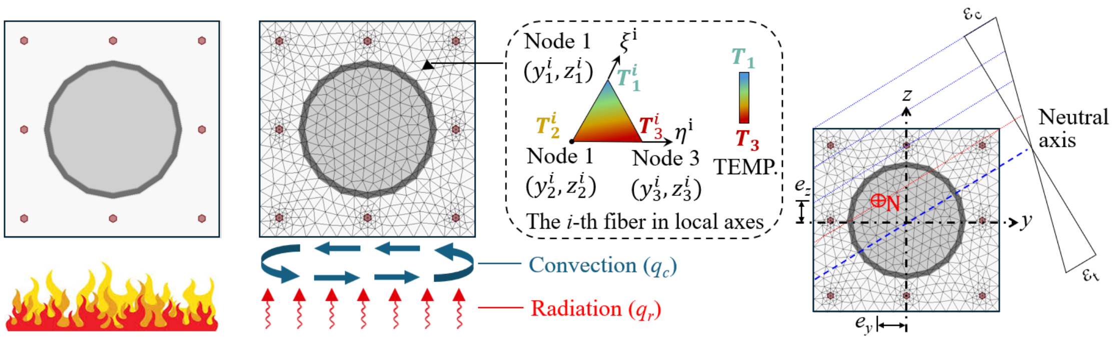

(a) Fire scenario (b) Heat transfer analysis (c) Fiber of cross-section (d) Cross-section analysis

Figure 6-2 Sequentially coupled thermal–stress analysis.

To ensure reasonable and sufficient cooling of the members after a fire, this study adopts the heating and cooling fire curve [128], which encompasses both ascending and descending stages of the temperature evolution. The temperature–time relationship is defined as follows:

$$\text{Ascending stage:}\quad T = T_0 + 345\log_{10}\left(8t+1\right) \tag{6.2}$$

$$\text{Descending stage:}\quad T = \begin{cases} T_h - 10.417\left(t-t_h\right), t_h \le 30 \\ T_h - 4.167\left(3-t_h/60\right)\left(t-t_h\right), 30 < t_h < 120 \\ T_h - 4.167\left(t-t_h\right), t_h \ge 120 \end{cases} \tag{6.3}$$

where T denotes the fire temperature (in °C, above T_0); T_0 and T_h represent the room temperature and the maximum fire temperature, respectively; t (min) is the elapsed time from the start of the fire; t_h (min) is the duration of the ascending stage. After the temperature returns to room temperature, the heat transfer analysis continues for a sufficient duration to ensure complete cooling of the cross-section. Although various models exist for temperature rise and cooling, this study focuses on calculating the 3D interaction diagrams after fire. The present study is expected to remain valid when applied to other fire models.

The transient temperature field distribution is obtained by solving Eq.(6.1), using the solution proposed in Section 3.3. To improve applicability to arbitrary cross-sections, triangular finite elements are employed to compute the temperature distribution within the cross-section. As shown in Figure 6-2(d), a mesh size of 1/20 of the cross-section width is recommended to balance computational efficiency and accuracy. Mesh refinement is applied only near the steel bars and steel profiles.

6.2.3 Stress resultants

As shown in Figure 6-3, three different coordinate systems are used in the numerical implementation: Y-C-Z, *y*-o-*z* and *u*-o-*v*. The Y-C-Z system represents the global axes of the cross-section and is set according to the preferences of designers. The *y*-o-*z* and *u*-o-*v* systems are derived from the global axes, with their origins located at the geometric centroid. The *u*- axis of *u*-o-*v* system is parallel to the neutral axis and rotated by an angle of α_n from the *y*-o-*z* system. The coordinates in the *u*-o-*v* system can be obtained by a double transformation from the coordinates in the Y-C-Z system. The transformation procedure is outlined as follows:

$$y = \mathrm{Y} - \mathrm{Y}_{gc}, z = \mathrm{Z} - \mathrm{Z}_{gc} \tag{6.4}$$

$$u = y\sin\alpha_n + z\cos\alpha_n, v = y\cos\alpha_n - z\sin\alpha_n \tag{6.5}$$

in which, Y and Z, *y* and *z*, *u* and *v* denote the coordinates in the Y-C-Z, *y*-o-*z* and *u*-o-*v* systems, respectively. The geometric centroid is computed as,

$$\mathrm{Y}_{gc} = \frac{A_c\mathrm{Y}_c + A_s\mathrm{Y}_s + A_r\mathrm{Y}_r - A_o\mathrm{Y}_o}{A_c + A_s + A_r - A_o}, \mathrm{Z}_{gc} = \frac{A_c\mathrm{Z}_c + A_s\mathrm{Z}_s + A_r\mathrm{Z}_r - A_o\mathrm{Z}_o}{A_c + A_s + A_r - A_o} \tag{6.6}$$

where A_c, A_s, A_r and A_o are the area of concrete encasement, steel profiles, rebars and opening, respectively; (Y_c, Z_c), (Y_s, Z_s), (Y_r, Z_r) and (Y_o, Z_o) are the coordinates of the centroids of these components.

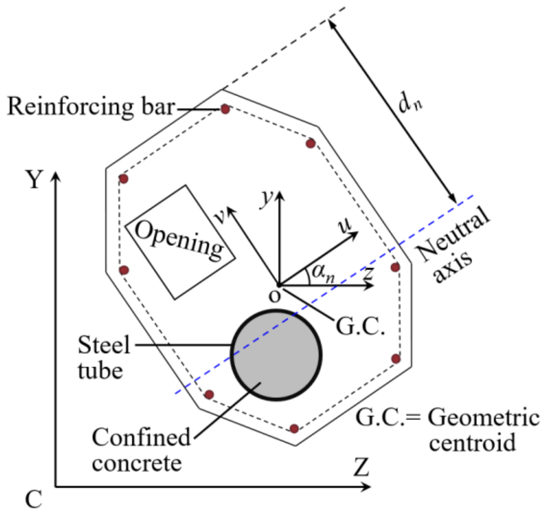

Figure 6-3 Arbitrary concrete-encased steel cross-section and the coordinate systems.

For convenience, the cross-section calculation uses the same mesh as the heat transfer analysis shown in Figure 6-2(b). Based on the linearly distributed strain derived from assumption (1), the stress resultants are obtained by summing the stresses of the fibers:

$$\mathrm{N} = \sum_{i=1}^{n} A_i \sigma_i \tag{6.7}$$

$$\mathrm{M}_u = \sum_{i=1}^{n} A_i \sigma_i v_i \tag{6.8}$$

$$\mathrm{M}_v = \sum_{i=1}^{n} A_i \sigma_i u_i \tag{6.9}$$

where M_u and M_v are the resultant moments about the u- and v- axes, respectively; A_i is the area of the i-th fiber; n is the total number of the fibers; (u_i, v_i) denote the coordinates the geometric centroid of the i-th fiber; σ_i represents the stress, which is a function of the total strain ε_i of the i-th fiber:

$$\sigma_i = f\left(\varepsilon_i\right) \tag{6.10}$$

in which, the function $y = f(x)$ describes the stress-strain curves of the materials after fire exposure, highly dependent on the highest temperature experienced. For the post-fire stress-strain relationship of steel, this study adopts the bilinear model proposed by Han et al. [216]. For concrete, two scenarios are considered: unconfined and confined by steel profiles. The former uses the model proposed by Lie [217], while the latter employs the widely accepted model proposed by Han et al. [218, 219]. The reliability and accuracy of these modes have been validated in numerous previous studies on the post-fire behavior of concrete-encased steel structures [201, 220-222]. The total moments about the Y- and Z- axes can be calculated as:

$$\mathrm{M_Y} = \mathrm{M}_u \sin\alpha_n + \mathrm{M}_v \cos\alpha_n = -\sum_{i=1}^{n} A_i\sigma_i v_i \cdot \sin\alpha_n + \sum_{i=1}^{n} A_i\sigma_i u_i \cdot \cos\alpha_n \tag{6.11}$$

$$\mathrm{M_Z} = \mathrm{M}_u \cos\alpha_n - \mathrm{M}_v \sin\alpha_n = -\left(\sum_{i=1}^{n} A_i\sigma_i v_i \cdot \cos\alpha_n + \sum_{i=1}^{n} A_i\sigma_i u_i \cdot \sin\alpha_n\right) \tag{6.12}$$

6.2.4 Iteration strategy

By rotating the neutral axis orientation α_n from 0° to 360° and varying the depth d_n, the section capacity is determined. The Regula-Falsi method [75, 76] is adopted to ensure equilibrium, compatibility, and stress-strain relationships are satisfied. The axial force capacity N is iterated with respect to d_n, while α_n remains constant under a given direction. The update method of the iterative strategy is given as follows:

$$d_{n,p} = d_n + \frac{\tilde{d}_n - d_n}{\tilde{\mathrm{N}} - \mathrm{N}}\left(\mathrm{N}_d - \mathrm{N}\right) \tag{6.13}$$

where $d_{n,p}$ refers to the updated depth of the neutral axis; while N and $\tilde{\mathrm{N}}$ correspond to the axial forces obtained at d_n and $\tilde{d}_n$, respectively; N_d denotes the present design axial load; d_n and $\tilde{d}_n$ represent the neutral axis depths at which the axial capacities are less than and greater than the design axial load.

6.2.5 Numerical procedure

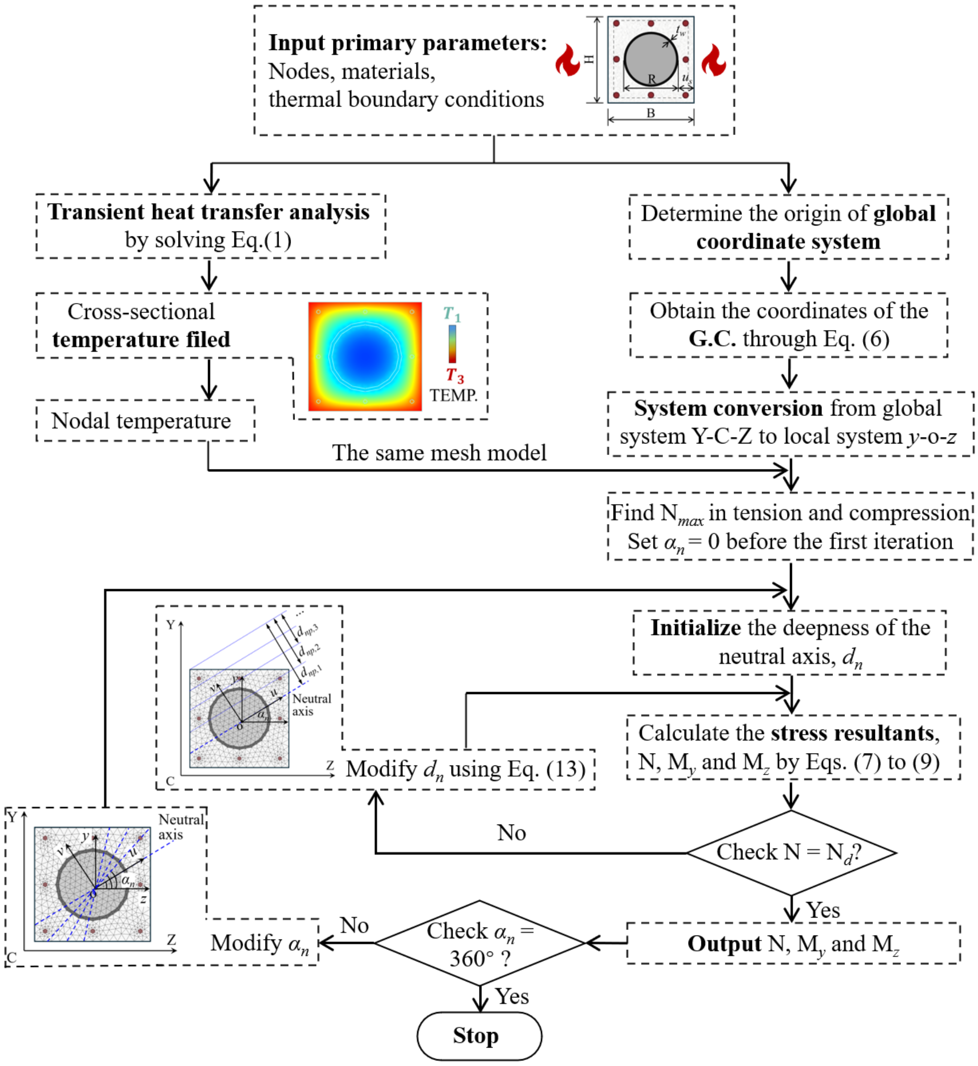

Figure 6-4 Numerical framework for the generation of the 3D interaction diagram.

The detailed numerical implementation is presented in Figure 6-4. After obtaining the temperature filed, the triangular mesh model and nodal temperatures are transferred to the cross-section analysis algorithm. The coordinates of the geometric centroid and the maximum axial force N_{max} of tension and compression are then calculated. Subsequently, α_n and d_n are initialized for the first iteration. Based on assumption (1), the curvature of the entire cross-section is determined from the linear strain distribution.

The ultimate curvature limit state is reached when any nodal strain attains its post-fire ultimate strain. The stress resultants are calculated by considering the stress-strain relationships of different materials at the corresponding highest historical temperatures. Finally, by updating the depth of d_n and increasing α_n from 0° to 360°, the complete interaction surface is captured.

The proposed numerical framework has been integrated into the free structural analysis software, MSASect2 [134], to facilitate its application for designers and to enhance the reproducibility of this research. As shown in Figure 6-5Figure 6-4, the software includes both a heat transfer analysis module and a cross-sectional analysis module, all developed and publicly released by the authors. The software covers the analysis process and iterative procedure to calculate the 3D interaction diagrams, accounting for material plasticity and degradation after fire.

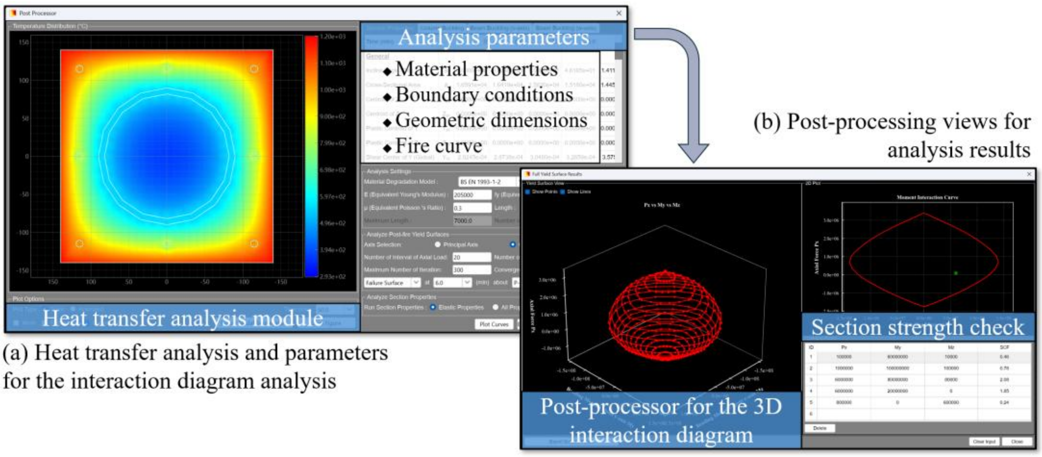

Figure 6-5 The graphical user interface of MSASect2 [134].

6.3 Mechanical Tests

To verify the accuracy of the numerical method presented in this study, mechanical tests were conducted on eccentrically loaded concrete-encased steel columns after fire exposure. Several columns underwent a full-range fire, including heating and cooling phases. After cooling to room temperature, eccentric loading tests were performed to determine the residual capacities of these columns. This section presents the test design and results, which will provide benchmark data for the validation in Section 6.4.

Table 6-1 Summary of the test parameters for each specimen.

Specimen	Eccentricity ratio e_r	Encased material	Heating-up time t_h (min)	Peak vertical load N_c (kN)
CC-0.4	0.4	Concrete	45	1396
EC-0.2	0.2	ECC	45	2799
EC-0.4	0.4	ECC	45	1896
EC-0.6	0.6	ECC	45	1319

Notes: Eccentricity ratio e_r represents the ratio of load eccentricity to column section height; ECC denotes the concrete encasement of the column has PVA fibers.

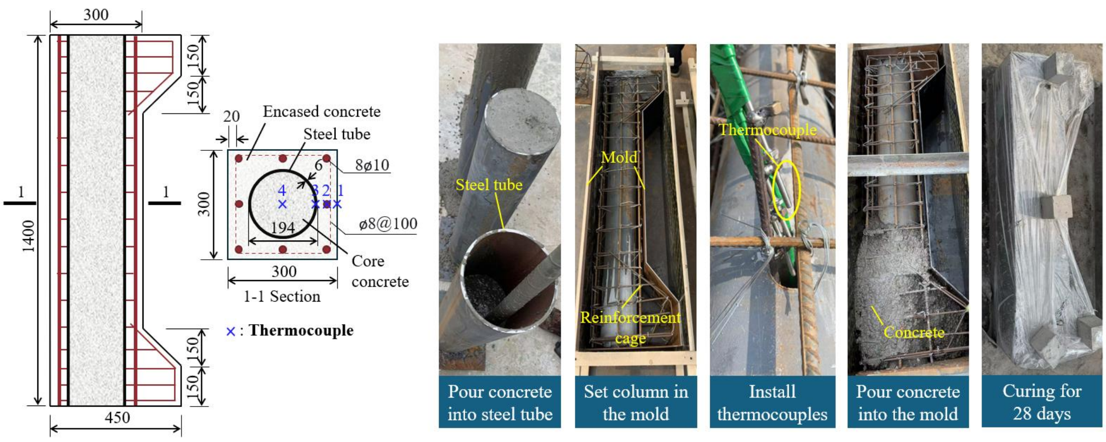

(a) Dimensions (unit: mm)

(b) Preparation processes of the specimens

Figure 6-6 Dimensions and preparation of the concrete-encased CFST columns.

6.3.1 Test specimens and material characteristics

The tests focus on a typical type of concrete-encased column, the concrete-encased concrete-filled steel tube (CFST). This type of column, which consists of reinforced concrete encasing the steel tube, is recognized for its excellent fire resistance and ability to survive fire exposure [122, 223, 224]. Therefore, investigating its residual bearing capacity after fire holds significant engineering value. A total of four columns were tested, with different parameters considered, including eccentricity ratio and encased material. The dimensions are shown in Figure 6-6(a), and the parameters of the specimens are summarized in Figure 6-6.

The columns were designed and prepared in accordance with ACI 318-05 [225], and the preparation process are presented in Figure 6-6(b). Thermocouples were installed and fixed inside the columns to record the temperature across the cross-sections during the fire test. Polyvinyl alcohol (PVA) fibers are added to effectively prevent explosive spalling of the outer layer material [122, 226]. This spalling mitigation measurement enhances the rigor of validating numerical method that neglects concrete spalling. Uniaxial compressive tests were conducted on the concrete in accordance with ASTM C39 [227], and the average compressive strengths of concrete and fiber-reinforced concrete were 34.6 MPa and 35.2 MPa, respectively. As per ASTM E8M [228] and ASTM A615 [229], the average yield strengths of the steel specimens (extracted from the steel tube) and steel rebars were 346 MPa and 330 MPa, respectively.

6.3.2 Test procedure and setup

Fire exposure tests were conducted on all columns in a gas fire furnace with automatic temperature control device, as shown in Figure 6-7(a). During the test, the temperature inside the furnace was controlled by high-precision thermocouples and an electronic temperature control system. The heating and cooling temperatures followed the fire described in Eqs. (6.2) and (6.3) After all test specimens cooled to room temperature, the eccentric loading tests were performed, with the test setup shown in Figure 6-7(b) and (c). Eccentric loading was applied through knife plates at both ends of the specimen, and the axial displacement was recorded by linear variable differential transducers (LVDTs). A hydraulic testing machine with a bearing capacity of 10,000 kN applied a load that increased by 50 kN per minute, and the total applied load was monitored by a force sensor. The test was terminated when the axial load dropped to 80% of the peak load or when severe cracking and spalling occurred.

There are three main reasons for not applying preloading to the columns. First, preloading under fire conditions may reduce expansion cracking and material degradation in the concrete encasement. As a result, preloaded columns tend to exhibit greater residual load-bearing capacity than columns without preloading. In this study, the columns were therefore tested without preloading to obtain more conservative results. Second, omitting preloading helps protect the thermocouples installed inside the columns during the fire test. Finally, this measure also reduces the risk associated with the fire test, as hydraulic jacks operating at high temperatures may pose safety hazards.

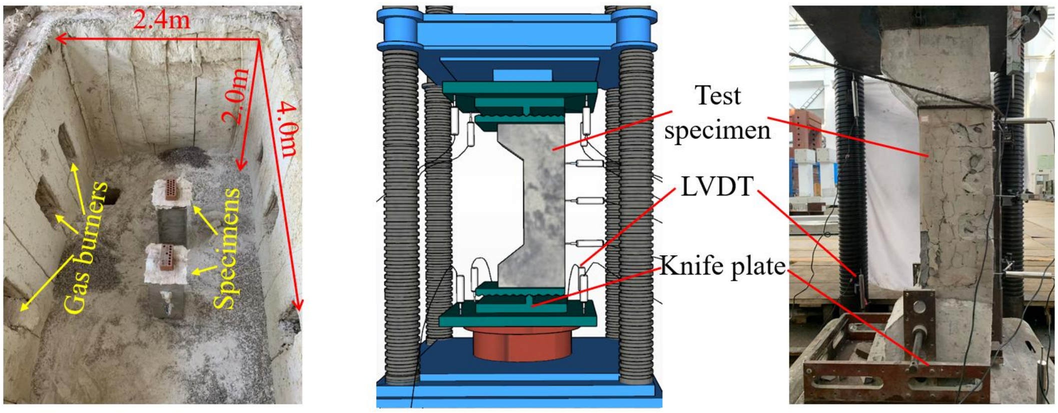

(a) Fire furnace (b) Diagrammatic view (c) Test photograph

Figure 6-7 Test setup.

6.3.3 Test outcomes

The test results, including the typical failure modes and load-displacement curves, are shown in Figure 6-8. It can be observed that as the eccentricity gradually increases from 0.2 to 0.6, the main failure zone shifts from the compression side to the tension side, and the ultimate load-bearing capacity gradually decreases. The post-fire material properties, provided in the authors' previous work [131], will be used for validation in the following section.

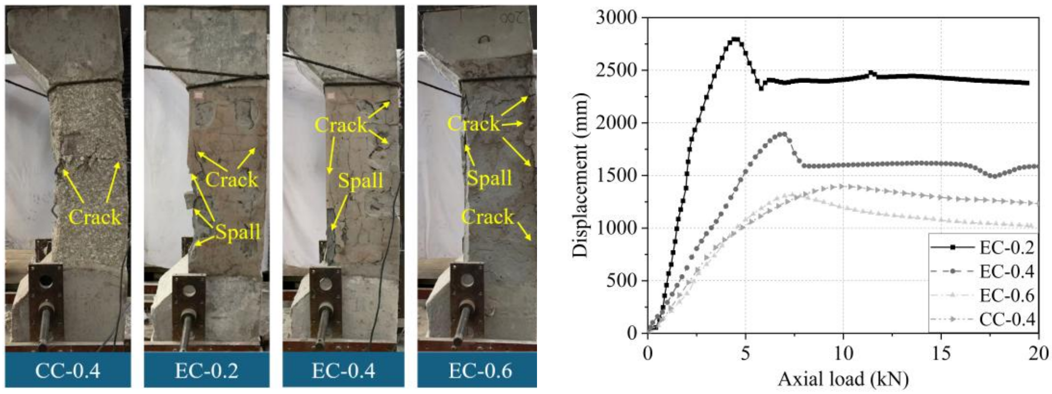

(a) Failure modes (b) Load-displacement curves

Figure 6-8 Failure modes and corresponding load-displacement curves of the specimens.

6.4 Validation of the Numerical Method

Given the limited number of previous studies on the interaction diagrams of concrete-encased CFST columns after fire exposure and the complexity of biaxial bending test, the mechanical model is validated not only against the test results presented in this study but also against the numerical results for columns reported by other researchers.

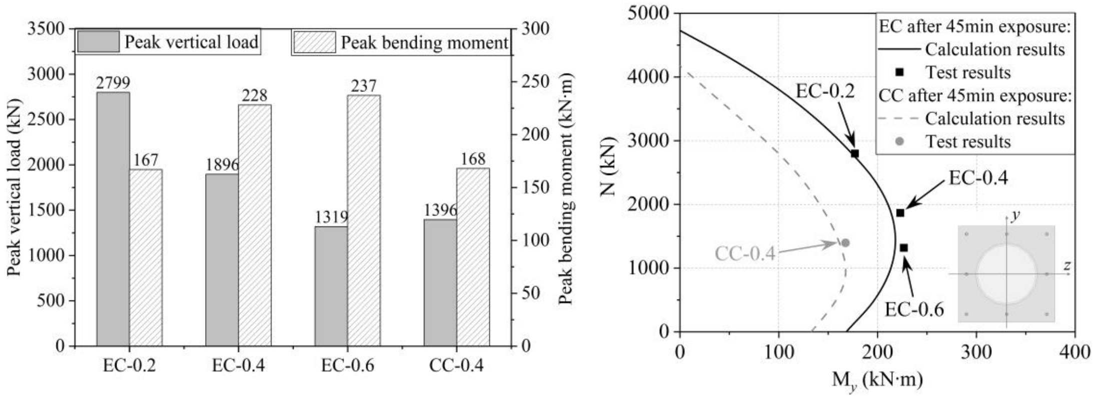

(a) Test results (b) Comparison results

Figure 6-9 Comparison of test results and proposed analysis method.

The peak vertical loads and corresponding bending moments from the tests are summarized in Figure 6-9(a). The interaction diagrams of the tested concrete-encased CFST columns are calculated, and their comparison with the test results are illustrated in Figure 6-9(b). The comparison reveals that the predicted results closely align with the test results, although the test results are consistently slightly higher. This discrepancy arises because the concrete material model developed by Han et al. [216], used in the analysis, accounts only for the confinement provided by the steel tube on the core concrete in CFST, while neglecting the additional confinement effects from the outermost concrete encasement layers. These results indicate that the proposed numerical method provides accurate predictions of the interaction diagrams for concrete-encased CFST columns after fire exposure.

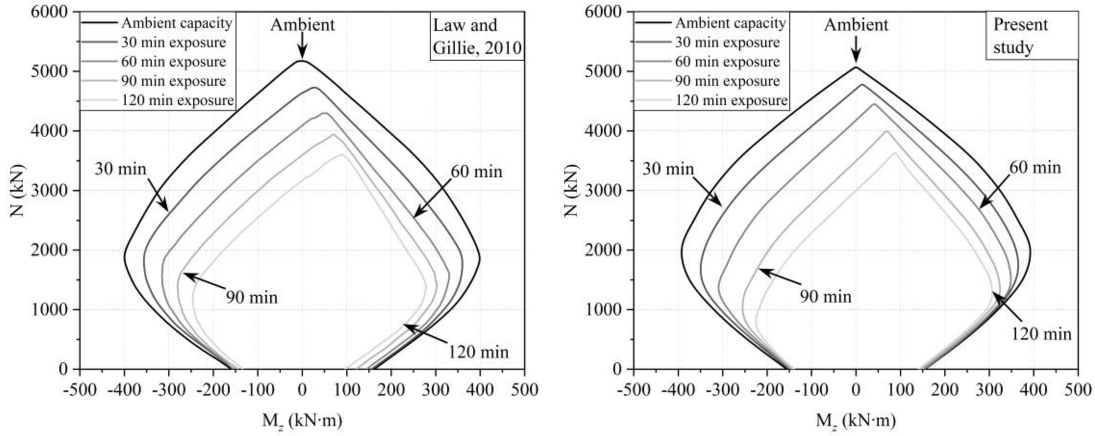

(a) Predictions from the previous study [74]   (b) Results obtained from the present study

Figure 6-10. Interaction diagrams of columns under various fire exposure times.

In another validation example, the predictions from the tangent modulus method reported by Law and Gillie [74] are compared with those obtained from the present approach. This validation example involves a reinforced concrete column with a cross-section of 300 mm × 500 mm, exposed to the ISO 834 standard fire [128] on three sides. The interaction diagrams at various fire exposure times are calculated and compared with the results from the previous study, as shown in Figure 6-10. The results obtained using the present method show good agreement with those reported in the literature, further validating the proposed approach.

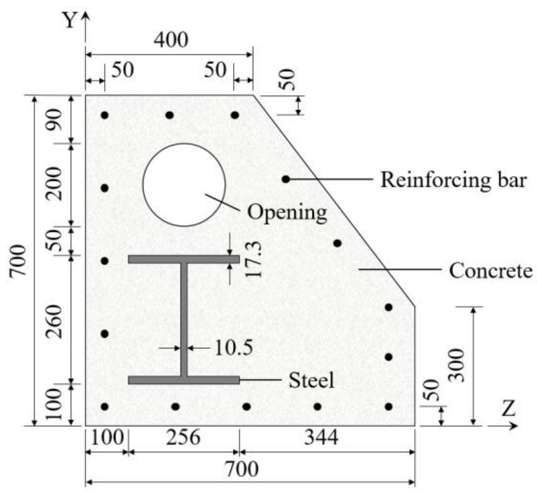

Figure 6-11. Cross-section of a general concrete-encased steel column from [230] (unit: mm).

For more general concrete-encased steel cross-sections under biaxial bending and compression, the proposed method is validated using previous studies conducted by Chen et al. [230] and Caldas et al. [73]. A general cross-section is studied, with detailed dimensions provided in Figure 6-11. The concrete has a compressive strength of 20 MPa and contains siliceous aggregates, while the steel profile has a yield strength of 323 MPa. Reinforcement is provided by steel bars with a diameter of 18 mm and a yield strength of 400 MPa. The elastic modulus and Poisson's ratio of the steel are taken as 2×10^5 MPa and 0.3, respectively, consistent with values used in prior studies. Each steel bar is positioned 50 mm from the concrete surface. This section is subjected to an axial force of 4,120 kN, and the proposed method is employed to calculate the biaxial bending interaction diagrams under both ambient and standard fire conditions [211].

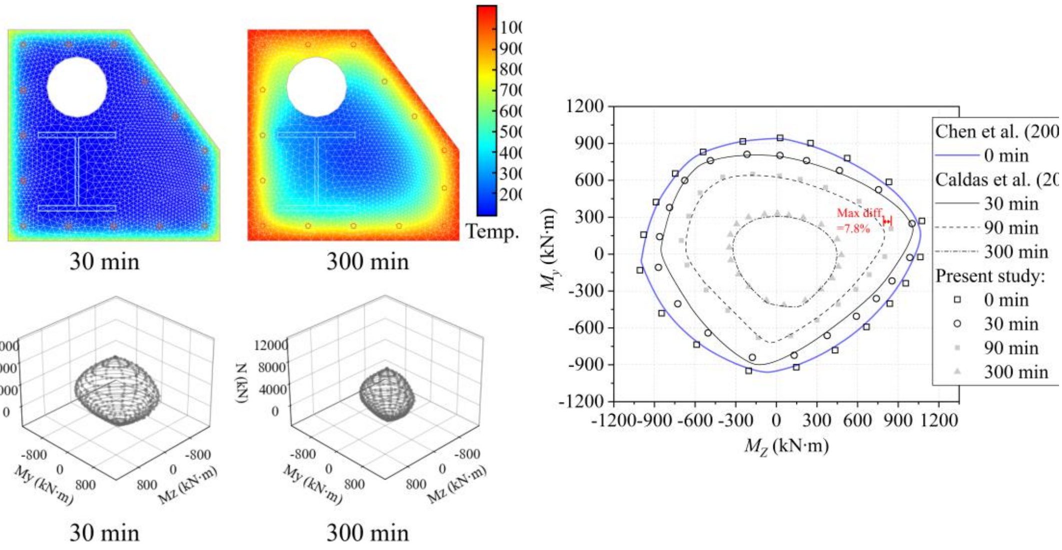

(a) Temperature fields and 3D interaction diagrams at various fire exposure times

(b) Interaction diagrams under biaxial bending (axial force 4,120 kN)

Figure 6-12. Analysis results of a general concrete-encased steel section subjected to biaxial bending.

The temperature field and corresponding 3D interaction diagrams at various fire exposure times are shown in Figure 6-12(a). As the temperature increases, the cross-section experiences significant degradation. Owing to the asymmetry of the section, both the temperature field and interaction diagram become increasingly asymmetric after 300 minutes of fire exposure, and the proposed method can capture this characteristic. The biaxial bending diagrams are extracted from the 3D interaction diagram at an axial load of N = 4,120 kN, as shown in Figure 6-12(b), and compared with different benchmark solutions. The maximum deviation is 7.8%, further verifying the accuracy of the proposed numerical method in handling biaxial bending cases.

6.5 Parametric Study

6.5.1 Study description

After validation, the proposed numerical approach is employed to conduct a parametric study that comprehensively investigates the post-fire interaction diagrams of concrete-encased CFST columns subjected to four-sided ISO 834 standard fire [128], including heating and cooling stages. It should be noted that, due to space limitations of this paper, the parameter analysis is specific to this typical concrete-encased column type under standard fire. The proposed framework is still applicable to other column types and fire conditions.

Table 6-2 List of parameters.

Parameters	Values	Dimension description
Fire exposure time (T, min)	0, 30, 60, 90, 120	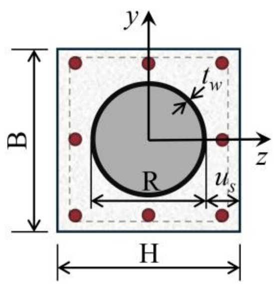
Aspect ratio (H / B)	1, 1.2, 1.5	
Concrete compressive strength (f_c, MPa)	30, 40, 50	
Wall thickness of steel tube (t_w, mm)	6, 8, 10	
Thickness of concrete cover (u_s, mm)	35, 50, 80	
Confinement factor ($\xi = \alpha f_y / f_c$)	$1.02 \leq \xi \leq 3.05$	
Reinforcement ratio (ρ)	$0.037 \leq \rho \leq 0.243$	

Notes: α represents the area ratio between the steel tube and core concrete; f_y and f_c are the strengths of the steel and concrete, respectively.

The parameters considered in the study are summarized in Table 6-2. A total of seven parameters are examined, and the concrete-encased CFST columns are analyzed. The diameters of the CFST and the reinforcing bars are 180 mm and 10 mm, respectively, while the overall cross-sectional dimensions (H × B) vary from 250 × 250 mm to 510 × 340 mm, indirectly affecting the reinforcement ratio (ρ) of the encased concrete layer. The concrete strength in both the inner and outer regions of the steel tube is identical and ranges from 30 MPa to 50 MPa. The yield strength of both reinforcing bars and steel tube is 345 MPa. The wall thickness of the steel tube (t_w) increases from 6 mm to 8 mm, thereby altering the confinement coefficient (ξ) of the

CFST [206, 218]. The fire exposure duration ranges from 0 min to 120 min. Additionally, the cross-sectional aspect ratio (H / B) varies from 1.0 to 1.5.

The selected parameter ranges define a configuration space comprising 405 distinct column cross-sections. To generate accurate 3D interaction diagrams of these columns, the numerical framework described in Section 2 is applied to each cross-section considering 20 rotation angles (α_n). The axial load (N) is divided into 20 intervals, ranging from the maximum compressive load ($N_{c,max}$) to the maximum tensile load ($N_{t,max}$). Therefore, the combination of various cross-sections, rotation angles, and axial load levels generates a total of 162,000 distinct calculation cases. The results from the extensive exploration of the configuration space have led to the development of a comprehensive database to support further analysis of the compressive-bending behavior of concrete-encased CFST columns after fire exposure

6.5.2 Results and discussion

Partial results of the parametric study are presented in To objectively assess the influence of each parameter on the post-fire behavior of concrete-encased CFST columns, all other parameters are held constant when evaluating the effect of a specific parameter. For example, the results presented in Figure 6-13(b) correspond to the columns with cross-sectional dimensions of 280 × 280 mm and 420 × 280 mm, respectively, while all other parameters are kept constant: the fire exposure duration (T) is 90 minutes, the concrete compressive strength (f_c) is 40 MPa, the steel tube wall thickness (t_w) is 8 mm, the yield strength of both reinforcing bars and steel tube is 345 MPa, and the concrete cover thickness (u_s) is 50 mm.

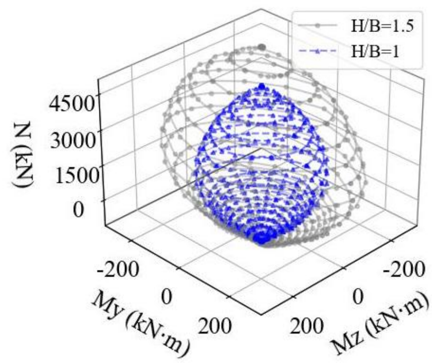

(a) Ambient temperature

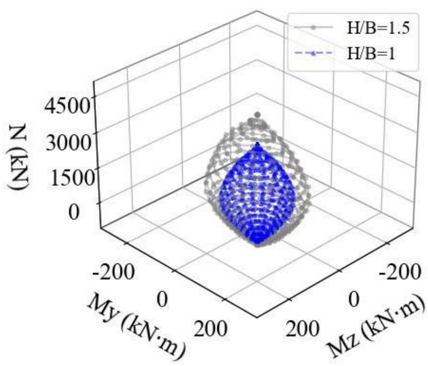

(b) After 90 min fire exposure

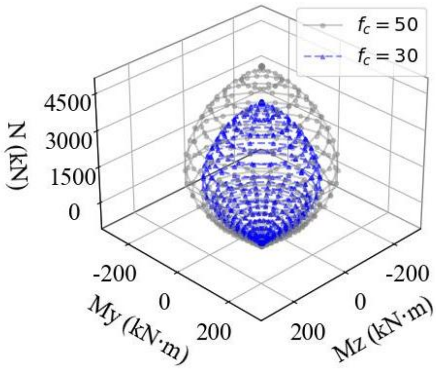

(c) Ambient temperature

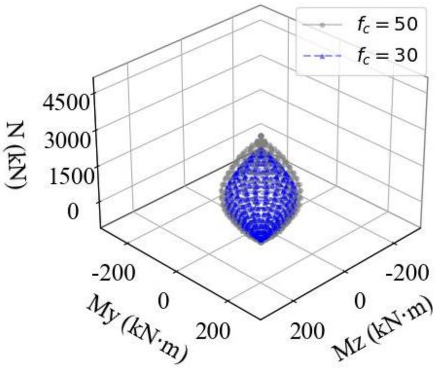

(d) After 90 min fire exposure

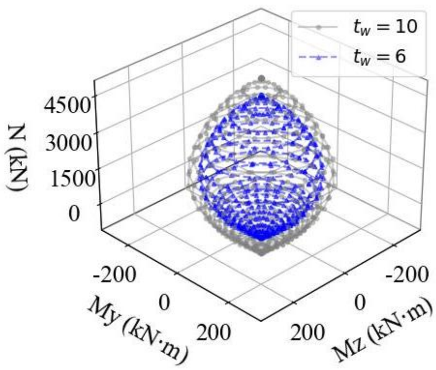

(e) Ambient temperature

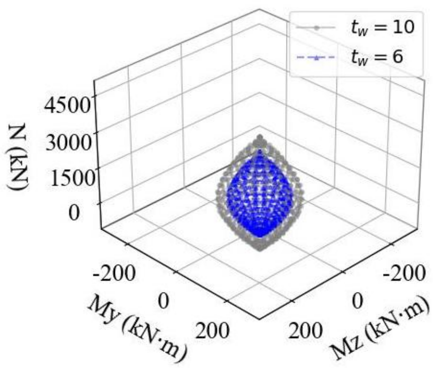

(f) After 90 min fire exposure

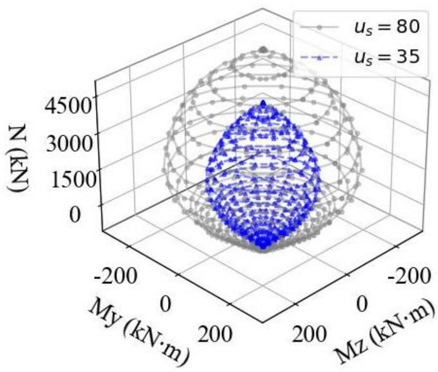

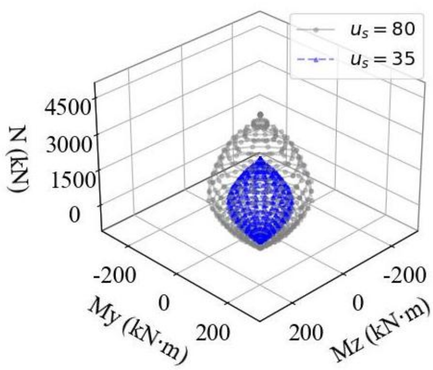

(g) Ambient temperature (h) After 90 min fire exposure

Figure 6-13 Partial results from parametric study.

To quantify the impact of each parameter, this study evaluates the volumetric change of 3D interaction diagrams defined in the N–M_y–M_z space. Specifically, it compares the ratios of the interaction diagram envelope volumes at different parameter values before and after fire exposure to quantitatively assess each parameter's effect on the residual bearing capacity.

1) Aspect ratio (H / B)

Figure 6-13(a) and (b) present the results of concrete-encased CFST columns with varying aspect ratios. The volumetric ratio changes of the interaction diagrams are calculated as follows:

$$\frac{V_0\big|_{\mathrm{H/B=1.5}}}{V_0\big|_{\mathrm{H/B=1}}} = 2.874 \tag{6.14}$$

$$\frac{V_{90}\big|_{\mathrm{H/B=1.5}}}{V_{90}\big|_{\mathrm{H/B=1}}} = 2.683 \tag{6.15}$$

where V_0 represents the envelope volume of the interaction diagram of the column at ambient temperature, while V_{90} denotes the envelope volume of the interaction diagram after the column has cooled following 90 minutes of standard fire exposure.

These volume changes indicate that increasing the aspect ratio can significantly enhance the compressive-bending performance when the cross-sectional width remains constant. Specifically, increasing the aspect ratio from 1.0 to 1.5 leads to an increase in the envelope volume of over 260%. However, this improvement does not differ significantly between ambient and post-fire conditions. This observation suggests that the benefit of increasing the aspect ratio does not improve after fire exposure, as the larger aspect ratio also increases the fire-exposed surface area, resulting in greater heat flux and more severe material degradation.

2) Concrete compressive strength (f_c)

This case examines concrete-encased CFST sections with concrete compressive strengths of 30 MPa and 50MPa, respectively. All other parameters are held constant: H × B = 250 × 250 mm, t_w = 8 mm, u_s = 50 mm. The results are illustrated in Figure 6-13(c) and (d), and the corresponding volumetric ratio changes of the interaction diagrams are presented below:

$$\frac{V_0\big|_{f_c=50}}{V_0\big|_{f_c=30}} = 2.155 \tag{6.16}$$

$$\frac{V_{90}\big|_{f_c=50}}{V_{90}\big|_{f_c=30}} = 1.520 \tag{6.17}$$

The calculation results indicate that increasing the concrete strength significantly enhances the biaxial bending performance. However, this benefit is substantially reduced 29% after fire exposure. This reduction can be attributed to the temperature-dependent material properties of concrete used in the analysis model. As temperature rises, the strain corresponding to the peak compressive stress in concrete increases [217]. Under the assumption of a linear strain distribution, a portion of the concrete becomes underutilized, and failure occurs due to the ultimate strain limit being reached in the fire-degraded outer concrete. Therefore, increasing concrete strength does not offer a more beneficial approach to enhancing the residual bearing capacity of concrete-encased CFST columns after fire exposure.

3) Wall thickness of steel tube (t_w)

Two concrete-encased CFST columns with wall thicknesses of 6 mm and 10 mm are selected for analysis. The columns have a cross-section of 280 mm × 280 mm, a concrete compressive strength of 40 MPa, a steel tube diameter of 180 mm, and a concrete cover thickness of 50 mm. The yield strength of both reinforcing bars and steel tube is 345 MPa. The volumetric ratio changes of the interaction diagrams (see Figure 6-13(e) and (f)) are:

$$\frac{V_0\big|_{t_w=10}}{V_0\big|_{t_w=6}} = 1.670 \tag{6.18}$$

$$\frac{V_{90}\big|_{t_w=10}}{V_{90}\big|_{t_w=6}} = 2.418 \tag{6.19}$$

This outcome indicates that increasing the steel tube wall thickness contributes more significantly to enhancing the residual bearing capacity after fire exposure, yielding a 48% improvement. This can be attributed to two primary reasons. First, the outer concrete layer provides thermal protection, allowing the steel tube to retain most of its material properties after fire exposure. A thicker steel tube wall results in less overall degradation of the cross-section. Second, a thicker steel tube wall results in a higher confinement coefficient (ξ). According to Han's confined concrete model [219], a higher confinement coefficient corresponds to a higher residual strength. Therefore, for concrete-encased CFST column sections containing steel restrained concrete, thicker wall thickness will be more favorable for the improvement of residual bearing capacity after a fire.

4) Thickness of concrete cover (u_s)

The final parameter studied is the concrete cover thickness, as defined in Table 6-2. Two columns with an aspect ratio of 1.0, a concrete compressive strength of 40 MPa, and a steel tube wall thickness of 8 mm are analyzed. The results for these columns are shown in Figure 6-13(g) and (h). The volumetric ratio changes are as follows:

$$\frac{V_0\big|_{u_s=80}}{V_0\big|_{u_s=35}} = 4.414 \tag{6.20}$$

$$\frac{V_{90}\big|_{u_s=80}}{V_{90}\big|_{u_s=35}} = 4.343 \tag{6.21}$$

It can be observed that in both cases, at room temperature and after fire exposure, increasing the concrete cover thickness significantly improves the compressive-bending behavior of the columns. However, the magnitude of this improvement remains unchanged after fire exposure. This is because, although a thicker concrete cover provides better protection for the internal steel profile, it also increases the fire-affected area and the associated heat flux, leading to greater degradation of the outer layer of the concrete cover.

6.6 Simplified Design Model

This section aims to develop an analytical solution for the 3D strength interaction diagrams of concrete-encased CFST columns. Although several analytical expressions have been proposed for reinforced concrete columns [77, 231], they primarily focus on 2D interaction curves and are not applicable to columns under biaxial bending. Hence, this study proposes a simplified analytical model based on Bresler's equation [232], which has been proven reliable and robust for reinforced concrete columns under fire conditions [197, 233].

6.6.1 Derivation of the model

The skeleton curves of the simplified analytical model are constructed using the generatrix and directrix lines, as shown in Figure 6-14. The generatrix line is divided into two parts by the directrix line. For the descending branch, the expression is calculated as follows:

$$\left(\frac{N_{c,max}-N}{N_{c,max}-N_{b1}}\right)^{\psi}-\left(\frac{M}{M_{b1}}\right)=0, N_{b1}\leq N\leq N_{c,max} \tag{6.22}$$

For the ascending branch, the expression is presented as follows:

$$\left(\frac{N_{t,max}-N}{N_{t,max}-N_{b1}}\right)^{\varphi}-\left(\frac{M}{M_{b1}}\right)=0, N_{t,max}\leq N\leq N_{b1} \tag{6.23}$$

where ψ and φ are the parameters controlling the shape of the generatrix line; $N_{c,max}$ and $N_{t,max}$ are the maximum compression and tension capacities of the cross-section, respectively; M_{b1} denotes the maximum moment capacity in the direction of α_n; N_{b1} refers to the axial load corresponding to the maximum moment capacity.

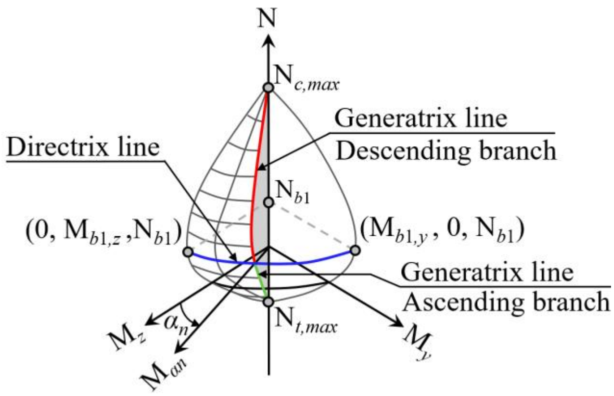

Figure 6-14 Simplified analytical model of the 3D strength interaction diagram.

To calculate M_{b1} on the generatrix line in the direction of α_n, the following equation is used:

$$\left(\frac{M_{b1}\cos\alpha_n}{M_{b1,z}}\right)^{\tau}+\left(\frac{M_{b1}\sin\alpha_n}{M_{b1,y}}\right)^{\tau}=1 \tag{6.24}$$

in which, τ is the parameter controlling the shape of the directrix line; $M_{b1,z}$ and $M_{b1,y}$ are the maximum moment capacities in the direction of M_z- and M_y- axes, respectively.

These equations construct the complete 3D strength interaction diagram, in which the parameters ψ, φ and τ control the shape. The parameters can be computed using the database built previously, with the equation presented as follows:

$$\psi = ln\left(\frac{M}{M_{b1}}\right) \Big/ ln\left(\frac{N_{c,max}-N}{N_{c,max}-N_{b1}}\right), N_{b1} \le N \le N_{c,max} \tag{6.25}$$

$$\varphi = ln\left(\frac{M}{M_{b1}}\right) \Big/ ln\left(\frac{N_{t,max}-N}{N_{t,max}-N_{b1}}\right), N_{t,max} \le N \le N_{b1} \tag{6.26}$$

A total of 162,000 samples in parametric analysis are used to calculate these two parameters. The calculated results are shown in Figure 6-15 and Figure 6-16. By performing nonlinear and linear fittings on the calculation results respectively, the regression model can be obtained as,

$$\psi = -0.28P_c^2 - 0.42P_c + 1.10 \tag{6.27}$$

$$\varphi = -0.535P_t + 0.910 \tag{6.28}$$

in which, P_c and P_t are the normalized axial loads for compression and tension, respectively, and are expressed by the following equations:

$$P_c = \frac{N_{c,max}-N}{N_{c,max}-N_{b1}}, N_{b1} \le N \le N_{c,max} \tag{6.29}$$

$$P_t = \frac{N_{t,max}-N}{N_{t,max}-N_{b1}}, N_{t,max} \le N \le N_{b1} \tag{6.30}$$

Due to the high degree of dispersion in the original calculation results, a conservative regression model is selected to ensure that only approximately 2% of unsafe predictions exceed the 15% error border. The regression model is conservatively adopted as the simplified model to calculate the values of ψ and φ.

Similarly, by substituting the values from the database into Eq.(6.24) and solving for τ, the regression model for the directrix line can be obtained. Through parameter analysis and correlation coefficient regression, fire exposure time (T), aspect ratio (H / B), confinement factor (ξ) and thickness of concrete cover (u_s) are selected as independent variables. The regression results and the corresponding standard deviation (DEV) are presented in Figure 6-17, demonstrating a good fit for τ. The regression model is summarized as follows:

$$\text{Room temperature:}\quad \tau = 1.6867 + \left(-0.48\frac{\mathrm{H}}{\mathrm{B}} + 0.39\xi - 0.97u_s\right)\times 10^{-2} \tag{6.31}$$

$$\text{After fire:}\quad \tau = 1.6197 + \left(-3.39\frac{\mathrm{H}}{\mathrm{B}} + 2.15\xi - 8.06u_s + 5.76\mathrm{T}\right)\times 10^{-2} \tag{6.32}$$

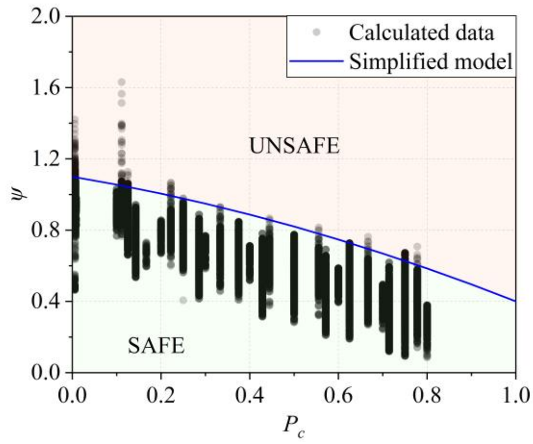

(a) ψ vs. P_c

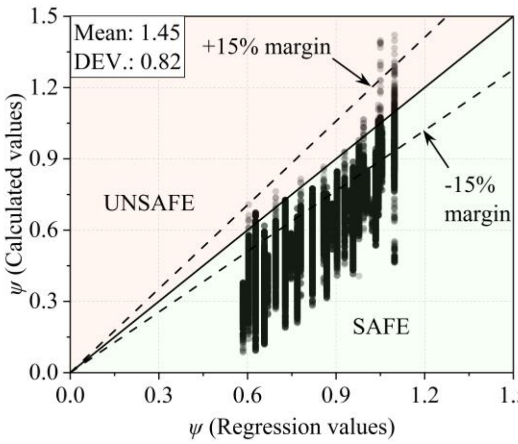

(b) Calculated values vs. regression values

Figure 6-15 Calculation results and nonlinear fitting of ψ.

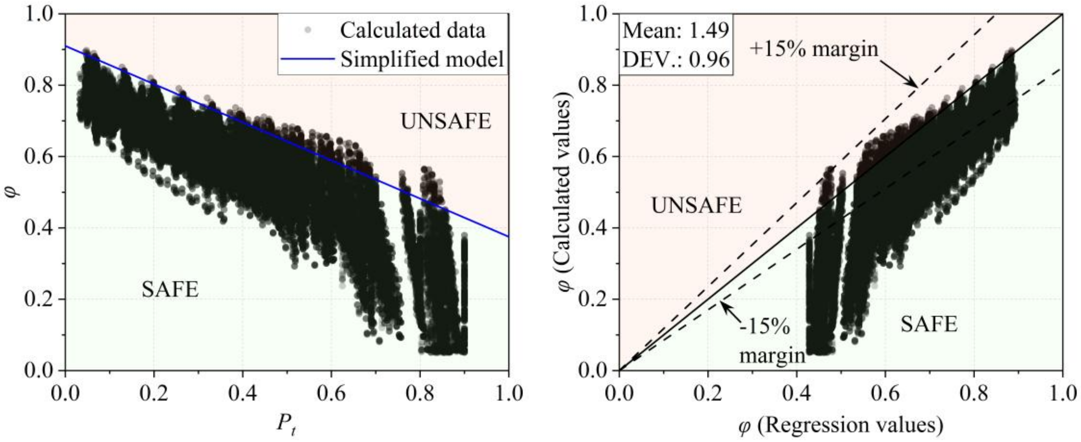

(a) φ vs. P_t

(b) Calculated values vs. regression values

Figure 6-16 Calculation results and linear fitting of φ.

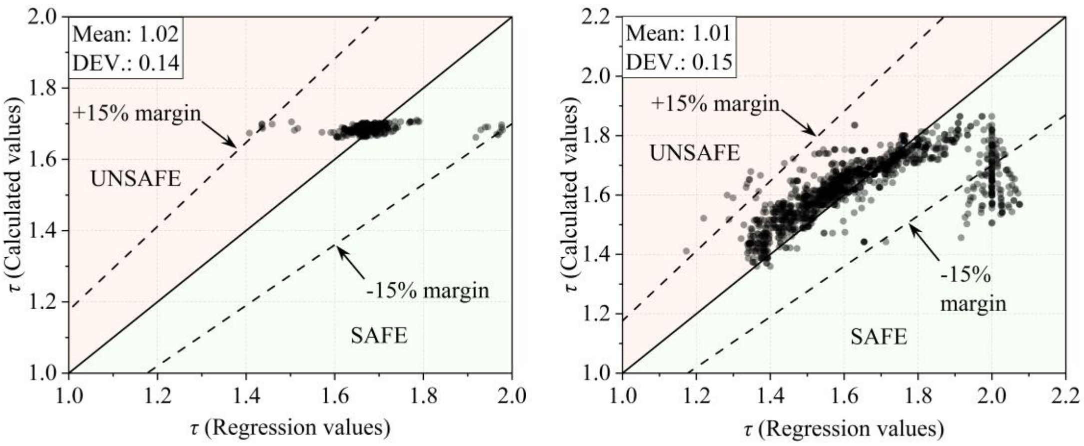

(a) Room temperature

(b) After fire exposure

Figure 6-17 Regression results of τ.

6.6.2 Workflow of the simplified design model

The workflow of the simplified design model for evaluating the post-fire biaxial bending behavior of the concrete-encased CFST column is shown in Figure 6-18. First, input the cross-section information and design loads of the column. Then, compute the post-fire axial compressive and uniaxial bending capacities for parameter set A using either the cross-section analysis method proposed in Section 2, alternative simplified design approaches [122, 131], or sophisticated finite element methods [193, 201, 234]. Next, identify the part of generatrix line of the interaction diagram corresponding to the current design axial load. Calculate the shape coefficients of the generatrix line using Eq.(6.27) or (6.28), and determine the shape coefficient of the directrix line using Eq.(6.31) or (6.32). Based on the established 3D interaction curve, compute the bending moment M under the given axial force and rotation angle α_n. Finally, compare the design bending moment with the calculated value to assess whether the cross-section satisfies the design requirements or has failed.

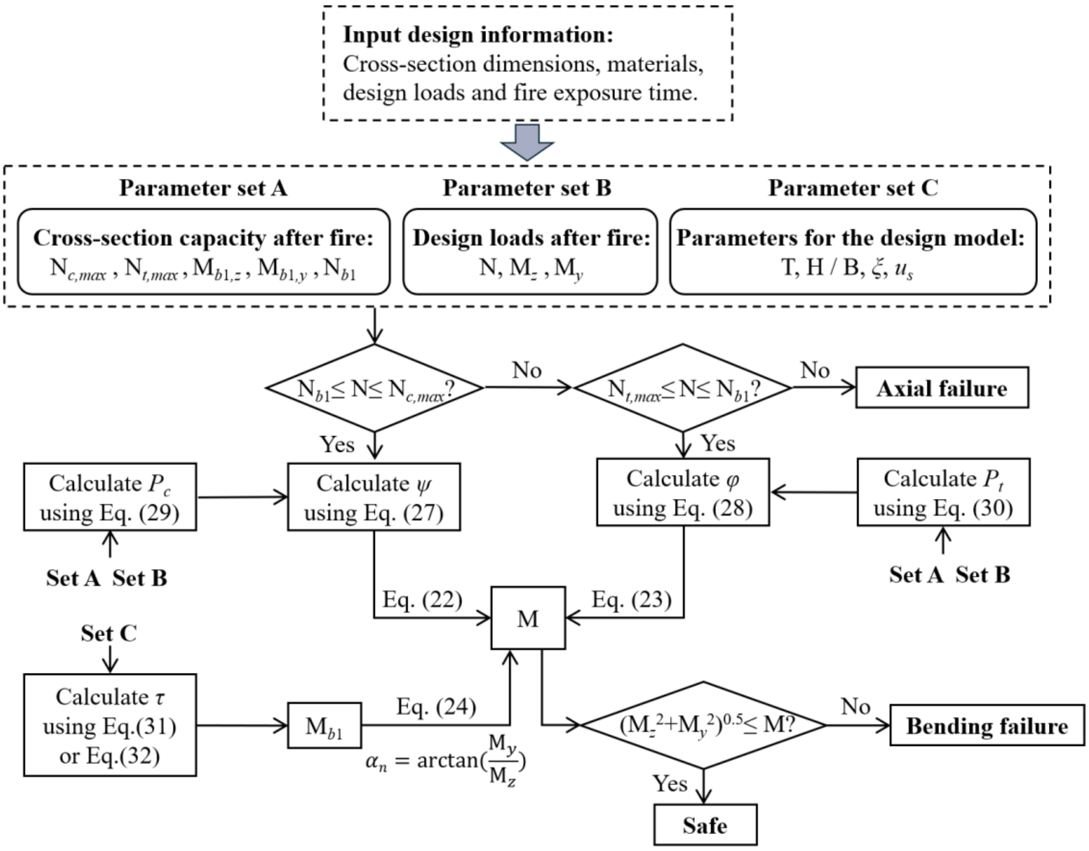

Figure 6-18 Workflow of the simplified design model.

6.6.3 Verification of design model

This section validates the simplified design model proposed in this study. A total of 540 calculation cases, including 108 cases for each fire exposure time, are randomly selected. These cases are distinct from the cross-sections defined by the parameters in Table 6-2 but remain within the studied parameter range. The simplified design model and the numerical method introduced in Section 6.2 are employed to compute the points on the 3D interaction diagram.

Figure 6-19 illustrates the deviations between the simplified design method and the numerical method results. Due to the conservative fitting adopted in the simplified method, its results are smaller than those obtained from the numerical method. The histogram shows that most deviations cluster around 5%, with a maximum deviation below 15% and a mean error of 5.3%. The violin plot further demonstrates that, across all fire exposure times, deviations remain below 15%, with peak probability densities centered around 5%. Results at room temperature exhibit slightly larger deviations, though they remain within an acceptable range. These results confirm the accuracy and reliability of the proposed simplified design method.

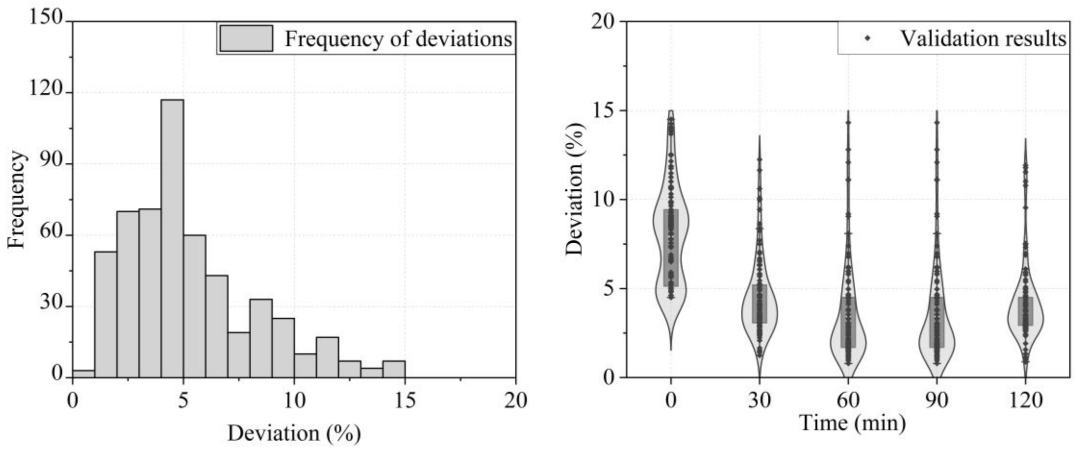

(a) Histogram of deviations (b) Violin plot with validation results

Figure 6-19 Validation against the numerical method.

CHAPTER 7.

REFINED SECOND-ORDER DIRECT ANALYSIS METHOD FOR FIRE RESISTANCE DESIGN OF STEEL STRUCTURES

7.1 Introduction

Prescriptive methods have long dominated the structural fire design of steel structures [7, 235, 236]. In these approaches, structural response is evaluated using code-specified procedures under standard fire conditions, making them straightforward to apply because engineers follow established rules and formulas. However, such checks can be inadequate for real fire scenarios [237, 238]. In many natural fires, some members are exposed to elevated temperatures while others remain near ambient [22, 53], as shown in Figure 7-1. It is inaccurate for traditional fire resistance design methods to assume uniform heating of the structure during analysis, as this assumption deviates significantly from real fire conditions and leads to overly conservative evaluations [239, 240].

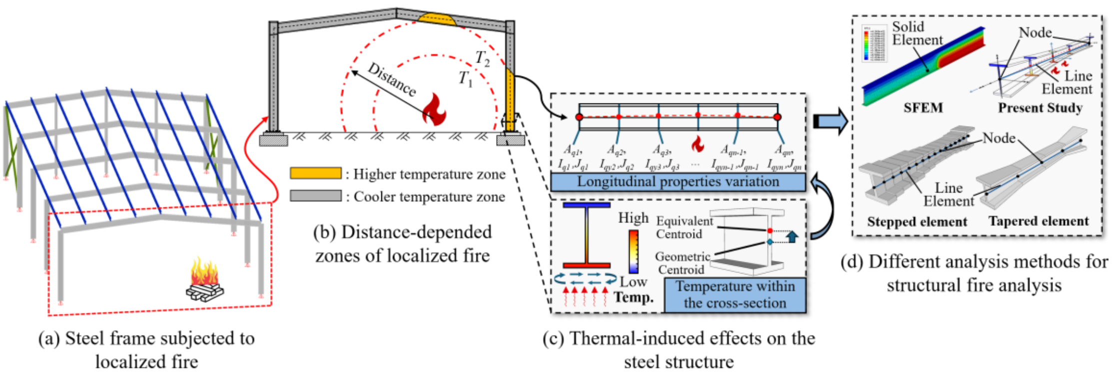

Figure 7-1 Challenges of structural fire analysis considering localized fire.

In contrast, modern performance-based fire resistance analysis involves advanced simulation methods to address the limitations of traditional approaches. Rather than relying on uniform-heating assumptions and pre-defined codes, it evaluates the real response of steel structures under credible, scenario-specific fire exposures. By considering the location of the fire and non-uniform heating, advanced computational methods can accurately simulate the thermal response, mechanical degradation, and structural deformation throughout the fire duration [49, 241].

Among these approaches, the sophisticated finite element method (SFEM), which typically employs solid or shell elements, is one of the most widely adopted methods. This is because it can simultaneously capture thermally induced effects such as non-uniform stiffness and strength degradation, second-order effects and centroid eccentricity under localized fire exposure (see Figure 7-1(c)). For example, Kolšek and Češarek [242] employed solid elements to develop a detailed numerical model for the fire resistance analysis of intumescent-coated steel structures. Dwaikat and Kodur [243] proposed a performance-based approach for the fire design of steel beams based on results obtained from a finite element model using shell elements. Silva et al. [244] introduced a one-way coupled finite element model combining shell and solid elements to analyze the global behavior of frame structures. Ye et al. [245] developed a finite element model using shell elements to accurately predict the anti-collapse performance of a single-story steel frame structure under fire conditions. More recently, Kim et al. [246] proposed a coupled computational fluid dynamics–finite element method to evaluate the fire behavior of modular steel buildings, in which the steel frame was modeled using eight-node linear solid elements. Although SFEM can provide detailed and accurate modeling capabilities, its computational demands are substantial. The complexity of the modeling process and high computational cost in frame structural analysis render it inefficient and impractical for routine design applications.

Hence, the line finite element method (LFEM) emerges as an efficient and appealing option for modern fire resistance design. The LFEM is a simplified form of the finite element method in which structural members, such as beams, columns, trusses, and frames, are modeled as one-dimensional line elements (e.g., beam-column elements) rather than full continuum elements (e.g., solid and shell elements), as shown in Figure 7-1Figure(d). Several LFEMs have been developed for fire resistance design, including those by Li et al. [177], Liew et al. [22], Iu et al. [151], Jiang and Usmani [247],Ying et al. [248] and Tang et al. [249]. In these studies, the thermal distribution across the cross-section was assumed to be either uniform, linearly varying, or obtained through fiber-based cross-section analysis. Along the member length, the members were discretized into numerous beam–column elements, ensuring that each thermal zone contained at least one element.

To further simplify the LFEM, Jiang and Usmani [98] implemented a force-based element in OpenSees, considering longitudinal thermal distribution through the *ThermalActionWrapper* and cross-sectional thermal variation via linear interpolation of fibers. Although this approach reduced the number of elements required, section-specific thermal modifiers and modifications to the element's internal iteration were still necessary to ensure computational accuracy. Additionally, Luu et al. [250] introduced an advanced line element that incorporates stability functions and the distributed plasticity model to account for non-uniform temperature distributions. The study provided valuable insights, though the ability to capture the offset of the centroid resulting from temperature gradients could be further improved.

Notably, when modeling members exposed to localized fires, the previously mentioned LFEMs adopted two primary strategies. The first approach, known as the stepped element method [251], divides the member into multiple short segments, each assigned different thermal conditions. The second approach adopts interpolation techniques to represent predefined variations in cross-sectional degradation, also referred to as tapered elements [252]. However, both methods have their limitations. The stepped element method requires a large number of elements to achieve convergence, since both temperature and cross-sectional properties are assumed to be constant within each segment. Similarly, tapered beam–column elements can only accommodate specific forms of cross-sectional variation, thus necessitating a sufficiently fine mesh to maintain computational accuracy.

In addition to the variation in cross-sectional properties, another challenge in traditional line element modeling lies in capturing the eccentricity of the cross-sectional centroid. Under non-uniform heating, the centroid shifts away from the geometric center, as shown in Figure 7-1(c). To account for this, current modeling practices typically offset nodal connections to reflect the displacement of the centroid. However, conventional line elements lack a generalized capability to automatically accommodate arbitrary centroid paths in steel members exposed to localized fires.

To develop a more efficient and accurate second-order analysis method for fire resistance design, this study proposes a novel line element to capture thermally induced effects under localized fires. The proposed method comprehensively accounts for several key thermal effects, including stiffness and strength degradation, centroidal offsets, thermal expansion, and second-order behaviors, thereby enabling accurate and efficient evaluation of the nonlinear response of steel structures subjected to localized fires. The line element formulation incorporates cross-section varying factors to model the non-uniform degradation of the member properties and enhance computational efficiency. A dedicated cross-section analysis method is developed to capture the spatial variation of material degradation and the corresponding moment–curvature relationships. The equivalent centroid axis is derived based on the principle of complementary virtual work and equilibrium equations to accommodate arbitrary centroid paths. The Updated Lagrangian formulation is employed to perform nonlinear analysis using the proposed line element. Finally, the proposed method is verified through several validation examples, demonstrating both its accuracy and efficiency.

7.2 Assumptions and Definitions

As shown in Figure 7-2, this study proposes a novel line finite element for fire resistance design. The element is assumed to be subjected to a localized fire, which induces temperature gradients across both the cross-section and the longitudinal axis. The non-uniform degradation of steel properties at elevated temperatures is represented as cross-sectional "shrinkage". Equivalent cross-sectional properties are introduced in the element formulation, including equivalent axial rigidity $E_r A_q$, flexural rigidity $E_r I_q$ and torsional rigidity $G_r J_q$, where E_r and G_r are the reference elastic modulus and shear modulus, respectively. A_q, I_q and J_q denote the equivalent geometric properties, which facilitate the derivation of the line element. The procedure for obtaining equivalent cross-sectional properties through the reduction factor is presented in Section 4.1. The uneven thermal gradient along the length produces a varying eccentricity of the centroid, and the connection of these centroids defines the equivalent centroidal axis. The co-rotational (CR) method is employed to describe pure deformational motions in the local coordinate system, thereby reducing the number of degrees of freedom (DOFs) and improving computational efficiency.

The proposed line element is based on the following assumptions: (1) deformations and rotations can be large, but strains remain small; (2) the applied loads are conservative; (3) the members are sufficiently slender, ; therefore, local buckling is neglected, and the heat flux on the surface of the member is much greater than the heat flux along the longitudinal direction; (4) warping and shear deformations are disregarded due to their minor contributions, consistent with the empirical design equations for slender members in Eurocode 3 [61] and AISC 360-10 [253]; (5) An elastic–perfectly plastic model, incorporating the reduction factor (λ) recommended by Eurocode 3 [61] and illustrated in Figure 7-3, is employed to balance computational efficiency and accuracy [249]. The reduction factor λ is defined as $\sigma_{y,T}/\sigma_y$ for yield strength and $E_{y,T}/E_y$ for elastic modulus, where $\sigma_{y,T}$ and $E_{y,T}$ are the yield strength and elastic modulus at T °C, respectively.

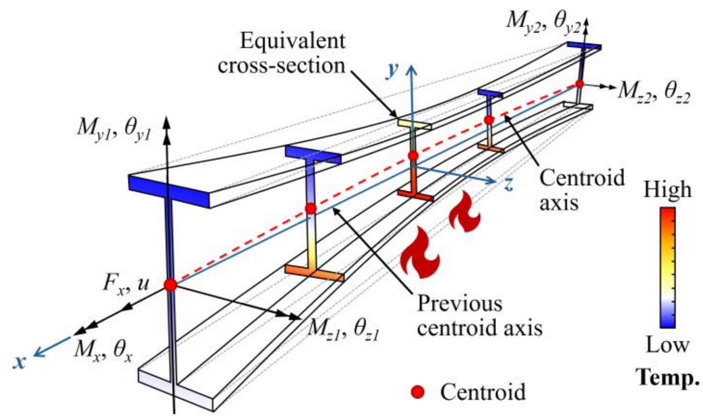

Figure 7-2 DOFs and nodal forces of the proposed line element.

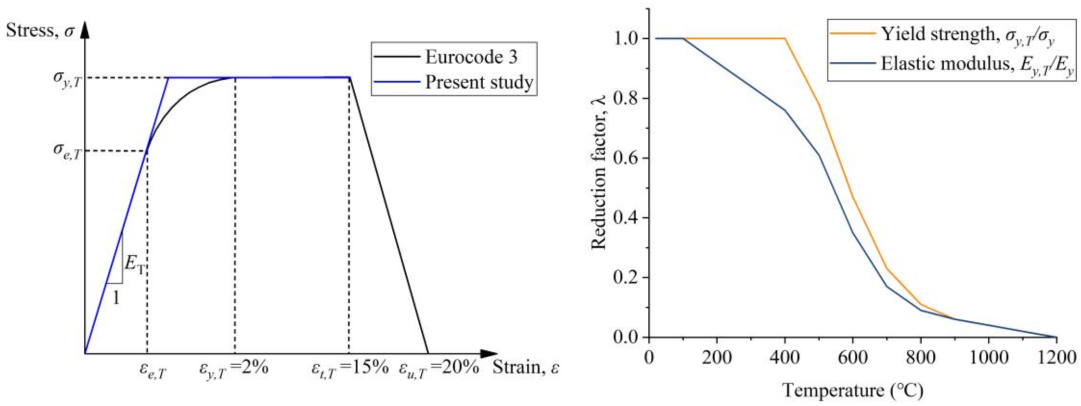

(a) Stress-strain curves at elevated temperature

(b) Reduction factor from Eurocode 3

Figure 7-3 Elastic–perfectly plastic model for steel at elevated temperature.

7.3 Formulations of Line Element

This section provides the derivation of the proposed line element, which simultaneously accounts for stiffness and strength degradation, second-order effects, thermal strains, and non-uniform thermal gradients.

7.3.1 Shape functions

According to Figure 7-2, the local axes are positioned at the mid-span of the line element. The element displacements are described by six DOFs, as given by

$$\boldsymbol{u}_e = [u \quad \theta_{y1} \quad \theta_{z1} \quad \theta_x \quad \theta_{y2} \quad \theta_{z2}]^T \tag{7.1}$$

where u is the displacement along x-axis; θ_{y1} and θ_{y2} are the rotations at nodes 1 and 2 around y-axis, respectively; while θ_{z1} and θ_{z2} are the rotations at nodes 1 and 2 around z-axis, respectively; θ_x represents the total torsional angle of the line element.

$$\boldsymbol{F}_e = [F_x \quad M_{y1} \quad M_{z1} \quad M_x \quad M_{y2} \quad M_{z2}]^T \tag{7.2}$$

where F_x is the axial load; M_{y1} and M_{y2} are the nodal bending moments about y-axis; M_{z1} and M_{z2} refer to the nodal bending moments about z-axis; M_x denotes the nodal torque. Given the nodal displacements and employing Hermite interpolation matrix, the shape functions of the element can be obtained by

$$\boldsymbol{f}_e(\eta) = \left[f_x(\eta) \quad f_y(\eta) \quad f_t(\eta) \quad f_z(\eta) \right]^T = \boldsymbol{N}_e(\eta)\boldsymbol{u}_e \tag{7.3}$$

$$\boldsymbol{N}_e(\eta) = \begin{bmatrix} N_1 & 0 & 0 & 0 & 0 & 0 \\ 0 & 0 & N_2 & 0 & 0 & N_3 \\ 0 & 0 & 0 & N_1 & 0 & 0 \\ 0 & N_2 & 0 & 0 & N_3 & 0 \end{bmatrix} \tag{7.4}$$

in which, $\eta = x/L$; L denotes the length of the element; $f_x(\eta)$ refers to the axial deformation; $f_y(\eta)$ and $f_z(\eta)$ are the lateral deflection along y- and z- axes, respectively; $f_t(\eta)$ denotes the torsional deformation; N_1, N_2 and N_3 are expressed as

$$N_1 = (1+2\eta)/2;$$

$$N_2 = L(1-2\eta)^2(1+2\eta)/8; \quad N_3 = -L(1-2\eta)(1+2\eta)^2/8 \tag{7.5}$$

7.3.2 Second-order effects

The second-order effects, also known as bowing effects [251], which account for the axial shortening due to bending deformation of the element, are considered. The deformation induced by the second-order effects is calculated by

$$f_b = \frac{1}{2}\int_0^L \left[\dot{f}_y^{\,2} + \dot{f}_z^{\,2}\right] dx \tag{7.6}$$

By substituting the components from Eq.(7.3) into Eq.(7.6), the expression for the second-order deformation is obtained as

$$f_b = \frac{L}{30}\left(2\theta_{y1}^{\ 2} - \theta_{y1}\theta_{y2} + 2\theta_{y2}^{\ 2}\right) + \frac{L}{30}\left(2\theta_{z1}^{\ 2} - \theta_{z1}\theta_{z2} + 2\theta_{z2}^{\ 2}\right) \tag{7.7}$$

7.3.3 Total potential energy function

The element stiffness matrix is derived from the second variation of the total potential energy, while the secant relationships are obtained from the first variation of the total potential energy. The total potential energy is expressed as

$$\Pi = -V + U \tag{7.8}$$

where V is the work done by external forces, and U denotes the strain energy within the element, including stress-related energy U_σ and thermal-related U_T, as given by following equation:

$$U = U_\sigma + U_T = \frac{1}{2}\int_V \left([\boldsymbol{\varepsilon}_L]^T \boldsymbol{D}\boldsymbol{\varepsilon}_L + 2[\boldsymbol{\sigma}]^T \boldsymbol{\varepsilon}_{NL} \right) dV + \int_V [\boldsymbol{\varepsilon}_T]^T \boldsymbol{D}\left(\boldsymbol{\varepsilon}_L + \boldsymbol{\varepsilon}_{NL}\right) dV \tag{7.9}$$

in which, $\boldsymbol{\varepsilon}_L$ and $\boldsymbol{\varepsilon}_{NL}$ refer to the linear and nonlinear strain vectors, respectively; $\boldsymbol{\varepsilon}_T$ is the thermal-related strain vector; $\boldsymbol{\sigma}$ is the stress vector. The vectors are calculated as below,

$$\boldsymbol{\varepsilon}_L = \left[\dot{f}_x - \ddot{f}_y y - \ddot{f}_z z \quad -\dot{f}_t z/2 \quad \dot{f}_t y/2 \right]^T; \ \boldsymbol{\varepsilon}_{NL} = \left[\left(\dot{f}_y^2 + \dot{f}_z^2 \right)/2 \quad 0 \quad 0 \right]^T \tag{7.10}$$

$$\boldsymbol{\varepsilon}_T = \left[\alpha \left(\Delta T + \frac{\partial T}{\partial y} y + \frac{\partial T}{\partial z} z \right) \quad 0 \quad 0 \right]^T \tag{7.11}$$

$$\boldsymbol{\sigma} = \left[F_x/\overline{A} + \left[M_{z1}(1-\eta) - M_{z2}\eta \right] y/I_{qz,i} + \left[M_{y1}(1-\eta) - M_{y2}\eta \right] z/I_{qy,i} \quad 0 \quad 0 \right]^T \tag{7.12}$$

where α represents the thermal expansion coefficient and taken as 1.2×10^{-5}/°C; T is the temperature along the cross-section; $\overline{A} = \sum_{i=1}^{n} A_{q,i}/n$ is the average area of the element, in which, n is the number of the integration points. $\boldsymbol{D}$ denotes the constitutive matrix containing reference material properties, given by

$$\boldsymbol{D} = \begin{bmatrix} E_r & 0 & 0 \\ 0 & G_r & 0 \\ 0 & 0 & G_r \end{bmatrix} \tag{7.13}$$

The degradation of material properties at elevated temperatures is represented by changes in the cross-sectional properties, which are introduced in Section 4.1. The strain energy is calculated by substituting Eqs.(7.10)-(7.13) into Eq.(7.9), followed by discarding some high-order terms:

$$U_\sigma \approx \frac{1}{2}\int_L E_r \bar{A} \dot{f}_x^2 dx + \frac{1}{2}\int_L E_r I_{qy}(x)\ddot{f}_z^2 dx + \frac{1}{2}\int_L E_r I_{qz}(x)\ddot{f}_y^2 dx + \frac{1}{2}\int_L G_r J_{qy}(x)\dot{f}_t^2 dx + \frac{1}{2}\int_L F_x\left(\dot{f}_y^2 + \dot{f}_z^2\right)dx \tag{7.14}$$

$$U_T \approx \int_L \alpha E_r \Delta T \bar{A}\left[\dot{f}_x + \left(\dot{f}_y^2 + \dot{f}_x^2\right)/2\right]dx - \int_L \alpha E_r I_{qz}(x)\frac{\partial T}{\partial y}\ddot{f}_y dx - \int_L \alpha E_r I_{qy}(x)\frac{\partial T}{\partial z}\ddot{f}_z dx \tag{7.15}$$

The work done by external forces is calculated by

$$V = \sum F_i u_i \tag{7.16}$$

in which, F_i denotes any possible external force acting on the element, and u_i is the corresponding displacement associated with that force.

7.3.4 Tangent stiffness matrix

The tangent stiffness matrix of the proposed element is derived from the second variation of Eq.(7.8), and the formulation is given by

$$\delta^2 \Pi = \frac{\delta^2 \Pi}{\delta u_i \delta u_j}\delta u_i \delta u_j = \boldsymbol{k}\Delta\boldsymbol{u} - \Delta\boldsymbol{F} = 0, (i, j = 1 \sim 6) \tag{7.17}$$

where $\boldsymbol{k}$ is the tangent stiffness matrix, which contains three components:

$$\boldsymbol{k} = \boldsymbol{k}_L + \boldsymbol{k}_G + \boldsymbol{k}_T \tag{7.18}$$

in which, $\boldsymbol{k}_L$ is the linear matrix, and $\boldsymbol{k}_G$ is the nonlinear matrix; $\boldsymbol{k}_T$ denotes the thermal-related stiffness matrix. The expressions of these matrices are given by

$$\boldsymbol{k}_L = \begin{bmatrix} E_r\bar{A}/L & 0 & 0 & 0 & 0 & 0 \\ & 4E_r\alpha_1/L & 0 & 0 & 2E_r\alpha_2/L & 0 \\ & & 4E_r\beta_1/L & 0 & 0 & 2E_r\beta_2/L \\ S. & & & G_r\bar{J}/L & 0 & 0 \\ & Y. & & & 4E_r\alpha_4/L & 0 \\ & & M. & & & 2E_r\beta_4/L \end{bmatrix} \tag{7.19}$$

$$\boldsymbol{k}_G = \begin{bmatrix} 0 & k_{G,12} & k_{G,13} & 0 & k_{G,15} & k_{G,16} \\ & k_{G,22} & k_{G,23} & 0 & k_{G,25} & k_{G,26} \\ & & k_{G,33} & 0 & k_{G,35} & k_{G,36} \\ S. & & & 0 & 0 & 0 \\ & Y. & & & k_{G,55} & k_{G,56} \\ & & M. & & & k_{G,66} \end{bmatrix} \tag{7.20}$$

$$\boldsymbol{k}_T = \begin{bmatrix} 0 & 0 & 0 & 0 & 0 & 0 \\ & k_{T,22} & 0 & k_{T,24} & k_{T,25} & 0 \\ & & k_{T,33} & k_{T,34} & 0 & k_{T,36} \\ S. & & & k_{T,44} & k_{T,45} & k_{T,46} \\ & Y. & & & k_{T,55} & 0 \\ & & M. & & & k_{T,66} \end{bmatrix} \tag{7.21}$$

where α_i and β_i are the cross-section varying factors to simplify the formulation, which will be illustrated in Section 4.2. The explicit expressions for $\boldsymbol{k}_G$ and $\boldsymbol{k}_T$ are provided in **Appendix 7A**. The element stiffness matrix $\boldsymbol{K}$ in the global axes is calculated as follows:

$$\boldsymbol{K} = \boldsymbol{L}\left(\boldsymbol{T}_E\boldsymbol{k}\left[\boldsymbol{T}_E\right]^T + \boldsymbol{H}\right)\boldsymbol{L}^T \tag{7.22}$$

where $\boldsymbol{L}$ and $\boldsymbol{T}_E$ are the transformation matrices; $\boldsymbol{H}$ denotes the rigid-body movement matrix. These matrices for the CR method can be found in Ref. [252, 254].

7.4 Thermally Induced Effects

The exposure of a member to localized fire can induce a series of thermally induced effects. A thermal gradient across the cross-section not only causes uneven material degradation but also results in an offset of the sectional centroid. A thermal gradient in the longitudinal direction requires traditional methods to employ a larger number of elements to satisfy accuracy requirements. In this section, a new solution is proposed to account for these effects.

7.4.1 Heat transfer analysis and cross-sectional properties

This study adopts the sequential coupling method, a well-established and robust approach for thermal-stress analysis coupling analysis [255, 256]. Since steel structural members are typically partially heated in natural fires, the “multi-zone” fire model proposed by Liew et al. [22] is employed to simulate the non-uniform temperature development. As illustrated in Figure 7-4(a), different temperature–time relationships occur at varying distances from the fire. The thermal gradient across each cross-section at the integration points of the line element is calculated by solving the transient heat-transfer governing equation for the cross-section fibers:

$$\left(\frac{1}{\Delta t}\boldsymbol{M}^i + \boldsymbol{K}_T{}^i\right)\left\{\boldsymbol{T}^i\right\}^{s+1} = \frac{1}{\Delta t}\boldsymbol{M}^i\left\{\boldsymbol{T}^i\right\}^s + \left\{\boldsymbol{f}^i\right\}^{s+1} \tag{7.23}$$

where $\boldsymbol{M}^i$ and $\boldsymbol{K}_T{}^i$ are the capacitance matrix and stiffness matrix for the i^{th} fiber, respectively; $\boldsymbol{T}^i = \begin{bmatrix} T_1^i & T_2^i & T_3^i \end{bmatrix}^T$ contains the nodal temperature; Δt and s represent the time step and number of the iteration step, respectively; $\boldsymbol{f}^i$ denotes the thermal condition vector, accounting for thermal convection and thermal radiation, as shown in Figure 7-4(b). The recommended values for thermal convection coefficient and thermal radiation coefficient are 25 $W/\left(m^2 \cdot ℃\right)$ [211] and 0.7 [187], respectively. The explicit forms of the matrices and the solution method have been introduced in previous work [56].

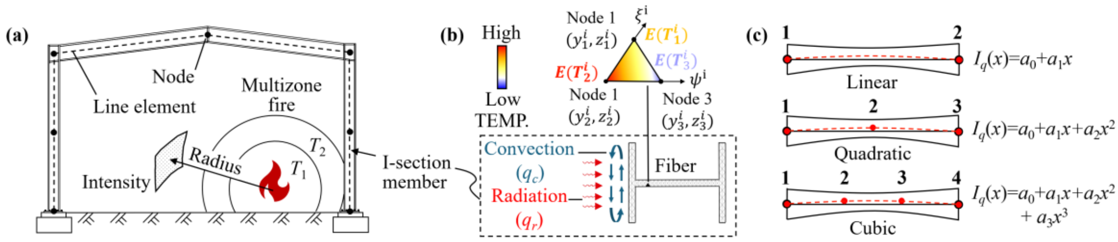

Figure 7-4 Varying cross-section properties of the proposed element exposed to fire.

After obtaining the temperature distribution of the cross-section at different integration points of the element, the equivalent cross-sectional properties are calculated using the material reduction factors shown in Figure 7-3(b). The equivalent properties are determined as follows:

$$A_q = \sum_{i=1}^{n} \int d\widehat{A} = \sum_{i=1}^{n} \int_{-1}^{1}\int_{-1}^{1} \boldsymbol{N}^i \boldsymbol{E}^i \left|\boldsymbol{J}^i\right| / E_r d\psi^i d\xi^i \tag{7.24}$$

$$I_{qy} = \sum_{i=1}^{n} \int z^2 d\widehat{A} = \sum_{i=1}^{n} \int_{-1}^{1}\int_{-1}^{1} \boldsymbol{N}^i \boldsymbol{E}^i \left(\boldsymbol{N}^i \boldsymbol{z}^i\right)^2 \left|\boldsymbol{J}^i\right| / E_r d\psi^i d\xi^i \tag{7.25}$$

$$I_{qz} = \sum_{i=1}^{n} \int y^2 d\widehat{A} = \sum_{i=1}^{n} \int_{-1}^{1}\int_{-1}^{1} \boldsymbol{N}^i \boldsymbol{E}^i \left(\boldsymbol{N}^i \boldsymbol{y}^i\right)^2 \left|\boldsymbol{J}^i\right| / E_r d\psi^i d\xi^i \tag{7.26}$$

where $d\widehat{A} = \boldsymbol{N}^i \boldsymbol{E}^i / E_r dA$ is the modulus-weighted area differential for fibers with non-uniform material degradation; $\boldsymbol{E}^i = \left[E(T_1^i), E(T_2^i), E(T_3^i)\right]^{\mathrm{T}}$ contains the degraded nodal elastic modulus at elevated temperatures T_1, T_2 and T_3; n is the number of the fibers; ψ^i and ξ^i denote the natural local coordinates of the i^{th} fiber (see Figure 7-4(b)), which range from 0 to 1; $\boldsymbol{N}^i$ is the shape function of the fiber, and can be formulated as:

$$\boldsymbol{N}^i(\psi^i, \xi^i) = \begin{bmatrix} \psi^i & \xi^i & 1-\psi^i-\xi^i \end{bmatrix} \tag{7.27}$$

$\boldsymbol{J}^i$ is the Jacobian matrix, which maps the global coordinate system to the natural coordinate system for integration, and is calculated as follows:

$$\boldsymbol{J}^i = \begin{bmatrix} \dfrac{\partial z}{\partial \psi^i} & \dfrac{\partial y}{\partial \psi^i} \\ \dfrac{\partial z}{\partial \xi^i} & \dfrac{\partial y}{\partial \xi^i} \end{bmatrix} = \begin{bmatrix} \dfrac{\partial \boldsymbol{N}^i}{\partial \psi^i} \\ \dfrac{\partial \boldsymbol{N}^i}{\partial \xi^i} \end{bmatrix} \begin{bmatrix} \boldsymbol{z}^i & \boldsymbol{y}^i \end{bmatrix} = \begin{bmatrix} z_1^{\,i} - z_3^{\,i} & y_1^{\,i} - y_3^{\,i} \\ z_2^{\,i} - z_3^{\,i} & y_2^{\,i} - y_3^{\,i} \end{bmatrix} \tag{7.28}$$

The coordinate of the cross-section centroid is calculated as below:

$$y_c = \sum_{i=1}^{n} \int y d\widehat{A} \Big/ A_q = \sum_{i=1}^{n} \int_{-1}^{1}\int_{-1}^{1} \left(\boldsymbol{N}^i \boldsymbol{y}^i\right) \boldsymbol{N}^i \boldsymbol{E}^i \left|\boldsymbol{J}^i\right| / \left(E_r A_q\right) d\psi^i d\xi^i \tag{7.29}$$

$$z_c = \sum_{i=1}^{n} \int z d\widehat{A} \Big/ A_q = \sum_{i=1}^{n} \int_{-1}^{1}\int_{-1}^{1} \left(\boldsymbol{N}^i z^i\right) \boldsymbol{N}^i \boldsymbol{E}^i \left|\boldsymbol{J}^i\right| / \left(E_r A_q\right) d\psi^i d\xi^i \tag{7.30}$$

The equivalent torsion constant is given by

$$\begin{aligned} J_q = & \sum_{i=1}^{n} \int_{-1}^{1}\int_{-1}^{1} \left\{ \left[\frac{\partial \boldsymbol{N}^i}{\partial y} \boldsymbol{\omega}_s^{\,i} \left(\boldsymbol{N}^i \boldsymbol{z}^i - z_s \right) + \left(\boldsymbol{N}^i \boldsymbol{z}^i - z_s \right)^2 \right] \right\} \left|\boldsymbol{J}^i\right| \boldsymbol{N}^i \boldsymbol{G}^i / G_r d\eta^i d\xi^i \\ & - \sum_{i=1}^{n} \int_{-1}^{1}\int_{-1}^{1} \left\{ \left[\frac{\partial \boldsymbol{N}^i}{\partial z} \boldsymbol{\omega}_s^{\,i} \left(\boldsymbol{N}^i \boldsymbol{y}^i - y_s \right) - \left(\boldsymbol{N}^i \boldsymbol{y}^i - y_s \right)^2 \right] \right\} \left|\boldsymbol{J}^i\right| \boldsymbol{N}^i \boldsymbol{G}^i / G_r d\eta^i d\xi^i \end{aligned} \tag{7.31}$$

in which, $\boldsymbol{\omega}_s^{\,i}$ denotes the nodal warping values, obtained by solving the torsional equilibrium equation of the cross-section [198]; $\boldsymbol{y}^i$ and $\boldsymbol{z}^i$ are the nodal coordinates vectors; $\boldsymbol{G}^i = \boldsymbol{E}^i \big/ \left[2\left(1+\mu\right)\right]$ is the shear modulus vector; $\left(y_s, z_s\right)$ are the coordinates of shear center.

7.4.2 Cross-section varying factors

From Eqs.(7.17) and (7.19), the cross-section varying factors α_i and β_i can be computed from the variation of cross-sectional properties along the x-axis. As shown in

Figure 7-4(c), these variations are approximated by polynomials whose order is determined by the number of sampling positions. The analytical expressions for the cross-sectional varying factors α_i and β_i are described by different polynomial orders (linear, quadratic, cubic, and quartic), which are provided in **Appendix 7B**.

Table 7-1. Maximum lateral displacements with different modelling approaches (Unit: mm).

	Nonlinear analysis of steel members under localized fires	
	Localized fire scenario 1	Localized fire scenario 2
Propose line element		
Linear	54.32 (-12.76%)	64.09 (-6.99%)
Quadratic	58.90 (-5.41%)	65.09(-5.54%)
Cubic	62.43 (0.27%)	68.76 (-0.22%)
Quartic	62.11 (-0.26%)	68.88 (-0.04%)
Benchmark solution		
40 stepped elements	62.27	68.91

To balance the number of sapling points and computational accuracy, a test involving different modelling approaches is carried out. A steel cantilever column with a 250 × 250 × 8 mm square hollow section is subjected to the localized fire scenarios described in Example 3 of this paper. The length of the column is 4 m. Transverse forces of 25 kN are applied at the free end in both the *y*- and *z*- directions. The steel has a yield strength of 345 MPa and a Poisson's ratio of 0.30. Linear, quadratic, cubic and quartic polynomials are used to fit the cross-sectional properties at the sampling points, which are uniformly distributed in each element. Two proposed line elements are employed to model the column, while a traditional method with 40 stepped elements is set as the benchmark solution. The adequacy of 40 elements in achieving accurate and convergent results is verified in the subsequent examples.

The comparative results of the maximum lateral displacements at the free end obtained from the two approaches are presented in Table 7-1. It is observed that the use of linear and quadratic polynomials leads to errors greater than 5%, whereas cubic and quartic polynomials yield errors below 1%. These results indicate that elements with cubic polynomials provide sufficiently accurate predictions and increasing the polynomial order beyond this yields only marginal improvements in accuracy. Therefore, in the subsequent analysis, the cubic polynomial is adopted to represent the cross-section varying factors for accuracy and efficiency.

7.4.3 Eccentricity of centroid

Previous studies [69, 136] has revealed that steel structures under localized fires can experience offsets of the cross-section centroid, which is caused by non-uniform degradation of steel. Thess offsets can cause additional bending moments to be generated by the axial pressure acting on the member. To account for the centroid offset, the present study introduces an equivalent centroidal axis, which differs from element axis and centroid axis, as shown in Figure 7-5. For each element, the equivalent centroid offsets in the y- direction are denoted as e_{yL} and e_{yR} at the element's beginning and end, respectively, while those in the z- direction are denoted as e_{zL} and e_{zR}. The straight line connecting these offset positions defines the equivalent centroidal axis of the element. To obtain the equivalent centroid offsets, the offsets $e_{y,i}$ and $e_{z,i}$ along the element's centroid axis are first calculated using Eqs.(7.29) and (7.30).

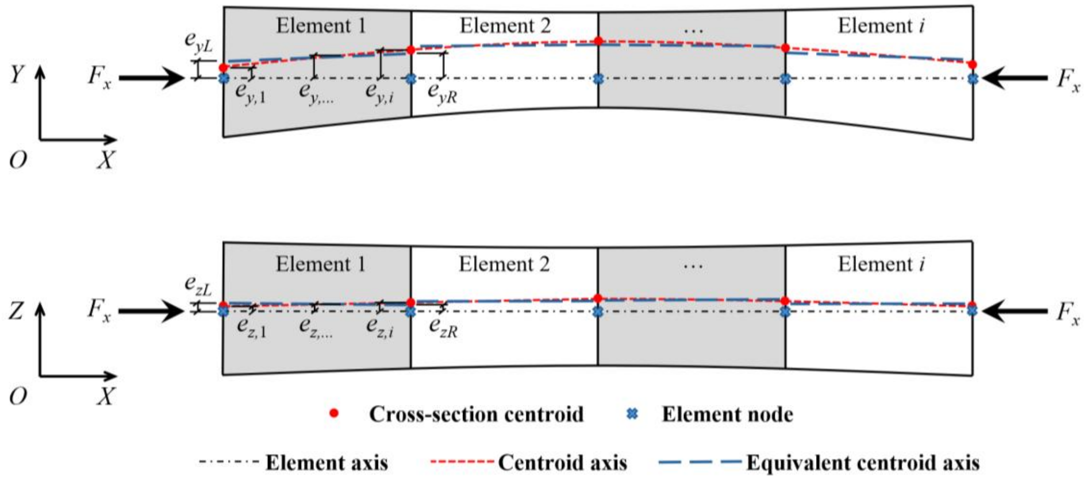

Figure 7-5 Centroid offsets and definition of axes.

The equivalent centroid offset of an element with cubic polynomial is derived as follows. Assuming that the sampling points are uniformly distributed along the element length, the centroid axis curves $e_y(\eta)$ and $e_z(\eta)$ are derived under the following boundary conditions: $e_y(-L/2) = e_{y,1}$, $e_y(-L/6) = e_{y,2}$, $e_y(L/6) = e_{y,3}$, $e_y(L/2) = e_{y,4}$, $e_z(-L/2) = e_{z,1}$, $e_z(-L/6) = e_{z,2}$, $e_z(L/6) = e_{z,3}$, $e_z(L/2) = e_{z,4}$. It can be solved that $e_y(x)$ and $e_z(x)$ are

$$\begin{aligned}e_y(x) &= \left(-e_{y,1}+9e_{y,2}+9e_{y,3}-e_{y,4}\right)/16-\left(-e_{y,1}+27e_{y,2}-27e_{y,3}+e_{y,4}\right)x/(8L) \\ &+9\left(e_{y,1}-e_{y,2}-e_{y,3}+e_{y,4}\right)x^2/\left(4L^2\right)-9\left(e_{y,1}-3e_{y,2}+3e_{y,3}-e_{y,4}\right)x^3/\left(2L^3\right)\end{aligned} \tag{7.32}$$

$$\begin{aligned}e_z(x) &= \left(-e_{z,1}+9e_{z,2}+9e_{z,3}-e_{z,4}\right)/16-\left(-e_{z,1}+27e_{z,2}-27e_{z,3}+e_{z,4}\right)x/(8L) \\ &+9\left(e_{z,1}-e_{z,2}-e_{z,3}+e_{z,4}\right)x^2/\left(4L^2\right)-9\left(e_{z,1}-3e_{z,2}+3e_{z,3}-e_{z,4}\right)x^3/\left(2L^3\right)\end{aligned} \tag{7.33}$$

The principle of complementary virtual work is employed, that is, the work done by the additional moments induced by the centroid offset equals the internal work, as expressed by

$$F_x\left[e_{zL} \quad -e_{zR}\right]\delta\begin{bmatrix}\theta_{y1}\\ \theta_{y2}\end{bmatrix}=\int_{-L/2}^{L/2}F_x e_z(x)\begin{bmatrix}\dfrac{\partial^2 N_2}{\partial x^2} & \dfrac{\partial^2 N_3}{\partial x^2}\end{bmatrix}\delta\begin{bmatrix}\theta_{y1}\\ \theta_{y2}\end{bmatrix}dx \tag{7.34}$$

$$F_x\begin{bmatrix} e_{yL} & -e_{yR} \end{bmatrix}\delta\begin{bmatrix}\theta_{z1}\\ \theta_{z2}\end{bmatrix} = \int_{-L/2}^{L/2} F_x e_y\left(x\right)\begin{bmatrix}\dfrac{\partial^2 N_2}{\partial x^2} & \dfrac{\partial^2 N_3}{\partial x^2}\end{bmatrix}\delta\begin{bmatrix}\theta_{z1}\\ \theta_{z2}\end{bmatrix}dx \tag{7.35}$$

By solving Eqs.(7.34) and (7.35), the solutions for the equivalent centroid offsets are

$$e_{yL} = \left(-8e_{y,1} - 21e_{y,2} + 6e_{y,3} + 3e_{y,4}\right)/20;\, e_{yR} = \left(3e_{y,1} + 6e_{y,2} - 21e_{y,3} - 8e_{y,4}\right)/20 \tag{7.36}$$

$$e_{zL} = \left(-8e_{z,1} - 21e_{z,2} + 6e_{z,3} + 3e_{z,4}\right)/20;\, e_{zR} = \left(3e_{z,1} + 6e_{z,2} - 21e_{z,3} - 8e_{z,4}\right)/20 \tag{7.37}$$

Equivalent centroid offsets derived from higher-order polynomials can be calculated using a similar procedure. Based on the geometric relationship between the displacement at the centroid and that at the equivalent centroid, the nodal displacements follow that

$$\Delta v_y = L\cos\left(\theta_0 + \theta_x\right) - e_y;\, \Delta v_z = L\cos\left(\theta_0 + \theta_x\right) - e_z \tag{7.38}$$

where θ_0 denote the rotation of the element node without offset; Δv_y and Δv_z are the nodal displacements due to offset of centroid in local axis. Given the deformation relationships in CR method [252], Eq. (7.38) can also be expressed by

$$\Delta v_y \approx -e_z\theta_x - e_y\theta_x^{\,2}/2;\, \Delta v_z \approx e_y\theta_x - e_z\theta_x^{\,2}/2 \tag{7.39}$$

Therefore, the relationship between the displacement vector at the equivalent centroid and that at the element node is given by

$$\hat{\boldsymbol{u}} = \boldsymbol{u}_E + \Delta\hat{\boldsymbol{u}} \tag{7.40}$$

in which, $\hat{\boldsymbol{u}}$ is the displacement vector at the equivalent centroid; $\Delta\hat{\boldsymbol{u}}$ is the additional displacement vector induced by the nodal rotations. $\boldsymbol{u}_E = \begin{bmatrix} u & v_y & v_z & \theta_x & \theta_y & \theta_z \end{bmatrix}^T$

denotes the converted displacement vector from CR method. By variation, Eq.(7.40) takes the form:

$$\delta\hat{\boldsymbol{u}} = \boldsymbol{T}_d \delta \boldsymbol{u}_E \tag{7.41}$$

where $\boldsymbol{T}_d$ is the offset matrix for nodal displacement vector and expressed as

$$\boldsymbol{T}_d = \begin{bmatrix} 1 & 0 & 0 & T_{d,14} & T_{d,15} & T_{d,16} \\ 0 & 1 & 0 & T_{d,24} & T_{d,25} & T_{d,26} \\ 0 & 0 & 1 & T_{d,34} & T_{d,35} & 0 \\ 0 & 0 & 0 & 1 & 0 & 0 \\ 0 & 0 & 0 & 0 & 1 & 0 \\ 0 & 0 & 0 & 0 & 0 & 1 \end{bmatrix} \tag{7.42}$$

The explicit expressions of $\boldsymbol{T}_d$ for tapered elements have been presented by Bai et al. [252]. By substituting Eqs.(7.36) and (7.37) derived in the present study into these expressions, the $\boldsymbol{T}_d$ for the proposed line element can be obtained. Similarly, the transformation for load vector is given by

$$\hat{\boldsymbol{F}} = \boldsymbol{T}_d^{\ T} \boldsymbol{F}_E = \boldsymbol{T}_f \boldsymbol{F}_E \tag{7.43}$$

in which, $\boldsymbol{F}_E = \begin{bmatrix} F_x & F_y & F_z & M_x & M_y & M_z \end{bmatrix}^T$ is the converted load vector at a node. The transformation matrices for the displacement and force vectors are

$$\boldsymbol{T}_D = \begin{bmatrix} \boldsymbol{T}_{d,L} & 0 \\ 0 & \boldsymbol{T}_{d,R} \end{bmatrix}; \ \boldsymbol{T}_F = \begin{bmatrix} \boldsymbol{T}_{f,L} & 0 \\ 0 & \boldsymbol{T}_{f,R} \end{bmatrix} = \begin{bmatrix} \boldsymbol{T}_{d,L}^{\ T} & 0 \\ 0 & \boldsymbol{T}_{d,R}^{\ T} \end{bmatrix} \tag{7.44}$$

where the subscript L and R represent the matrices and vectors at the element's beginning and end, respectively. The element equilibrium equation is rewritten as

$$\boldsymbol{T}_F \boldsymbol{K} \boldsymbol{T}_D \begin{bmatrix} \boldsymbol{u}_{E,L} & 0 \\ 0 & \boldsymbol{u}_{E,R} \end{bmatrix} = \begin{bmatrix} \boldsymbol{F}_{E,L} & 0 \\ 0 & \boldsymbol{F}_{E,R} \end{bmatrix} \tag{7.45}$$

Therefore, the element stiffness matrix considering centroid offset is calculated by

$$\boldsymbol{K}_E = \boldsymbol{T}_F \boldsymbol{K} \boldsymbol{T}_D \tag{7.46}$$

7.4.4 Moment-curvature relationships

The yield strength of steel under fire decreases rapidly with the increase of temperature, thus the development of plasticity of steel structures under fire must be considered. In this study, a concentrated plasticity model is incorporated into the line element, building on its implementation in several previous studies [59, 257, 258], which have demonstrated both accuracy and robustness. The concentrated plasticity model is a zero-length hinge located at the end of the element, as shown in Figure 7-6. As the member temperature increases, plastic strain develops across the cross-section until it reaches full yield. The application of the concentrated plasticity model efficiently captures material nonlinearity and avoids the need for complex and tedious stress-resultant formulations.

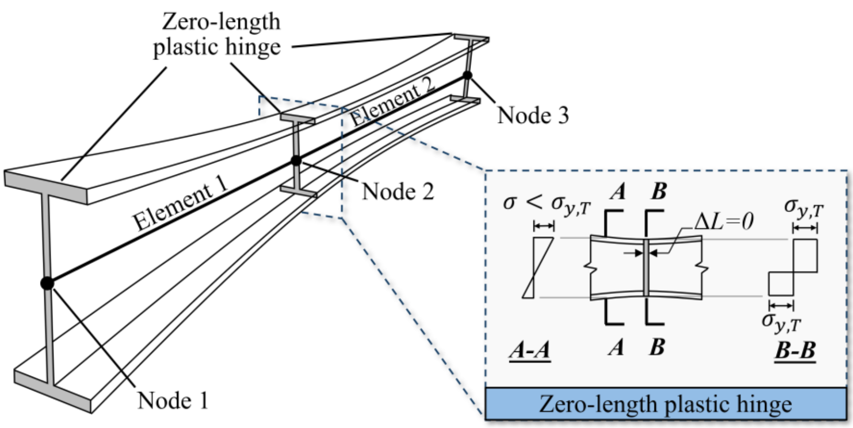

Figure 7-6 Illustration of concentrated plasticity model.

The bending rigidity at the plastic hinge is quantified by the moment-thrust-curvature relationship which is obtained from the thermally degraded cross-sections after heat transfer analysis. The moment-thrust-curvature analysis employs the same fiber model used in the heat transfer analysis (see Figure 7-7 (a) and (d)) to reduce numerical interpolation and thereby improve accuracy. The moment-thrust-curvature characterizes the strength under combined axial and bending loads (see Figure 7-7 (b) and (e)). Its derivation has been presented in numerous studies [259-261] and is also outlined in Chapter 6. Given that the tangent slope along the curvature (κ) direction represents the flexural rigidity of the section, the stiffness variation of the concentrated plasticity model under axial load and bending moment is calculated from the gradient ($\partial\Phi/\partial\kappa$) of the moment–thrust–curvature surface, as shown in Figure 7-7 (c) and (f). It is observed that the cross-section exposed to fire experienced a significant decrease in both strength and stiffness.

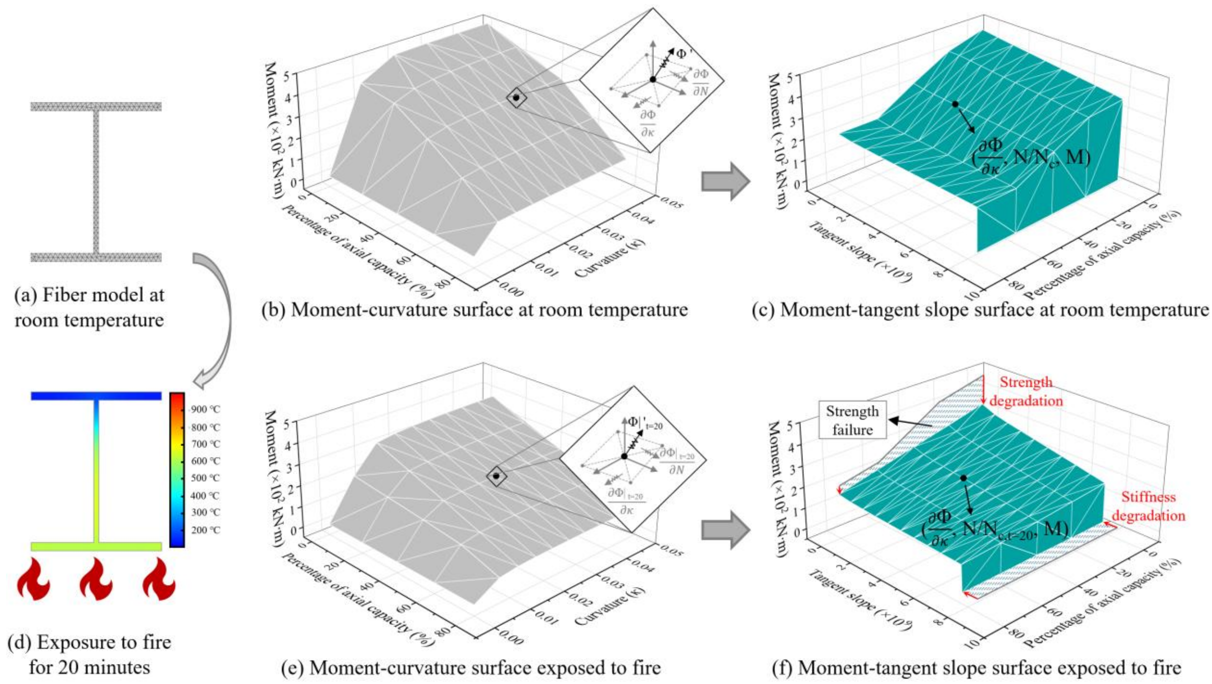

Figure 7-7 Moment-thrust-curvature analysis under fire.

During the iteration process of the LFEM, once the nodal internal forces from the $(i\text{-}1)^{th}$ step are obtained, the plastic cross-sectional properties in the i^{th} step are determined based on the moment-tangent slope surface of the cross-section. The cross-section varying factors α_i and β_i are then calculated based on these properties, followed by an update of the tangent stiffness matrix of the line element. Finally, the load step is also updated to calculate the node forces for the $(i+1)^{th}$ step.

7.5 Numerical Implementation

7.5.1 Adaptive mesh technique

To strike a balance between computational efficiency and accuracy, it is essential to determine both the quantity and positioning of elements for the members. This study introduces an adaptive mesh algorithm that removes the need for trial-and-error discretization of members. The implementation of the procedure is depicted in Figure 7-8(a).

Initially, the geometric properties $I_{qy}(x)$ and $I_{qz}(x)$ are approximated using the available data. For example, when cubic polynomials are used, at least $3n_E+1$ data points are required for both $I_{qy}(x)$ and $I_{qz}(x)$, where n_E represents the number of elements. Next, the error is determined by comparing the predicted value I_{pre} obtained from the fitting curve with the reference values I_{mid} at the midpoints. The region where the error exceeds the predefined tolerance (set to 0.05 in the present study) will be subdivided into two elements, and the fitting and convergence checking procedures are repeated for these parts. This iterative process continues until the error tolerance is met for each element.

Adaptive mesh algorithm

Choose the order of $I_{qy}(x)$ and $I_{qz}(x)$
Initialize the element number $n_E = 1$
Input data points for cross-sectional properties I_{qy}, I_{qz} (Num. > $3n_E$ +1)
Calculate the fitting curves for $I_{qy}(x)$ and $I_{qz}(x)$
IF $|I_{pre} - I_{mid}| / I_{pre}$ > tolerance **THEN**
    Divide the divergent parts by half
    Update element number based on divergent (n_D) and convergent number (n_C): $n_E = 2 \times n_D + n_C$
    Record element nodal coordinates
    IF Num. is enough **THEN**
        Calculate the fitting curves
    ELSE Input data points
    END IF
ELSE Output meshing results
END IF

(a) Pseudocode

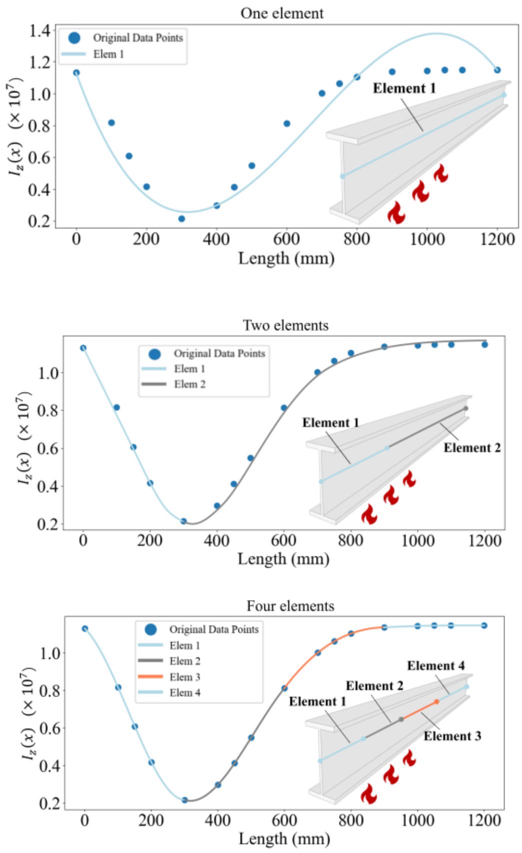

(b) Results in each iteration

Figure 7-8 Workflow for adaptive mesh generation.

Figure 7-8(b) illustrates an example of the mesh generation process for a typical I-section member under localized fire, where four proposed elements are created for the entire member. Elements 2 and 3 are associated with regions exhibiting greater errors, owing to abrupt changes in their cross-sectional properties. In addition, since the final mesh generally divides the member into elements at the extremum points of $I_{qy}(x)$ and $I_{qz}(x)$, which are also the first locations where plastic hinges appear, this ensures that the aforementioned concentrated plasticity model accurately simulates plastic hinges with fewer elements.

7.5.2 Incremental stiffness procedure

To account for 3D element motions under large deflections, the incremental stiffness method is applied, with equilibrium conditions referenced from the previous configuration using the Updated Lagrangian approach. The incremental nodal deformation $\Delta \boldsymbol{u}_{e,i}$ at the i^{th} step is expressed as

$$\Delta \boldsymbol{u}_{e,i} = [\Delta u_i \quad \Delta\theta_{y1,i} \quad \Delta\theta_{z1,i} \quad \Delta\theta_{x,i} \quad \Delta\theta_{y2,i} \quad \Delta\theta_{z2,i}]^T \tag{7.47}$$

According to the kinematic description shown in Figure 7-9, the element rotation at the i^{th} step can be calculated as:

$$\Delta\theta_{y1,i+1} = \Delta\beta_{y1,i} + \left(\Delta w_{z2,i} - \Delta w_{z1,i}\right)/L_i \,;\Delta\theta_{y2,i+1} = \Delta\beta_{y2,i} + \left(\Delta w_{z2,i} - \Delta w_{z1,i}\right)/L_i \tag{7.48}$$

$$\Delta\theta_{z1,i+1} = \Delta\beta_{z1,i} + \left(\Delta v_{y2,i} - \Delta v_{y1,i}\right)/L_i \,;\Delta\theta_{z2,i+1} = \Delta\beta_{z2,i} + \left(\Delta v_{y2,i} - \Delta v_{y1,i}\right)/L_i \tag{7.49}$$

where $\Delta\beta_{y1,i}$ and $\Delta\beta_{y2,i}$ denote the nodal incremental rotations at element nodes 1 and 2 along the local y- axis relative to the last configuration, while $\Delta\beta_{z1,i}$ and $\Delta\beta_{z2,i}$ are those along the local z- axis. The incremental axial lengthening and rotation around x- axis are

$$\Delta\theta_{x,i+1} = \Delta\theta_{x2,i} - \Delta\theta_{x1,i}; \Delta u_{i+1} = L_{i+1} - L_i \tag{7.50}$$

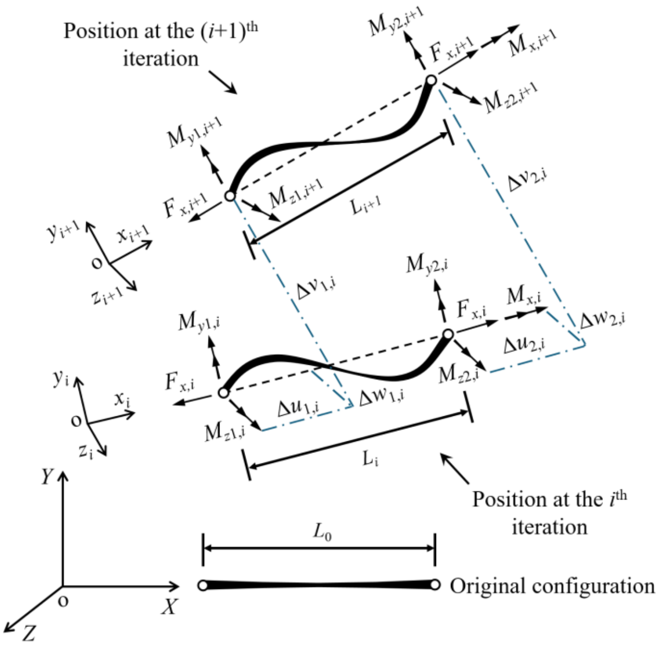

Figure 7-9 Kinematic description of incremental stiffness procedure.

Based on the nodal deformation, the incremental forces and resistance forces can be calculated as follows:

$$\Delta \boldsymbol{R}_{E,i+1} = \boldsymbol{K}\Delta \boldsymbol{u}_{e,i+1}; \boldsymbol{R}_{E,i+1} = \boldsymbol{R}_{E,i} + \Delta \boldsymbol{R}_{E,i+1} \tag{7.51}$$

The numerical implementation of the proposed LFEM is depicted in Figure 7-10. As described in the preceding sections, the framework simultaneously accounts for cross-sectional analysis under fire, adaptive mesh generation, and the determination of the equivalent centroid considering cross-sectional variation and strength degradation. The critical parameters obtained from these analyses are then used as input for the incremental stiffness procedure in the nonlinear analysis through LFEM (Step 5).

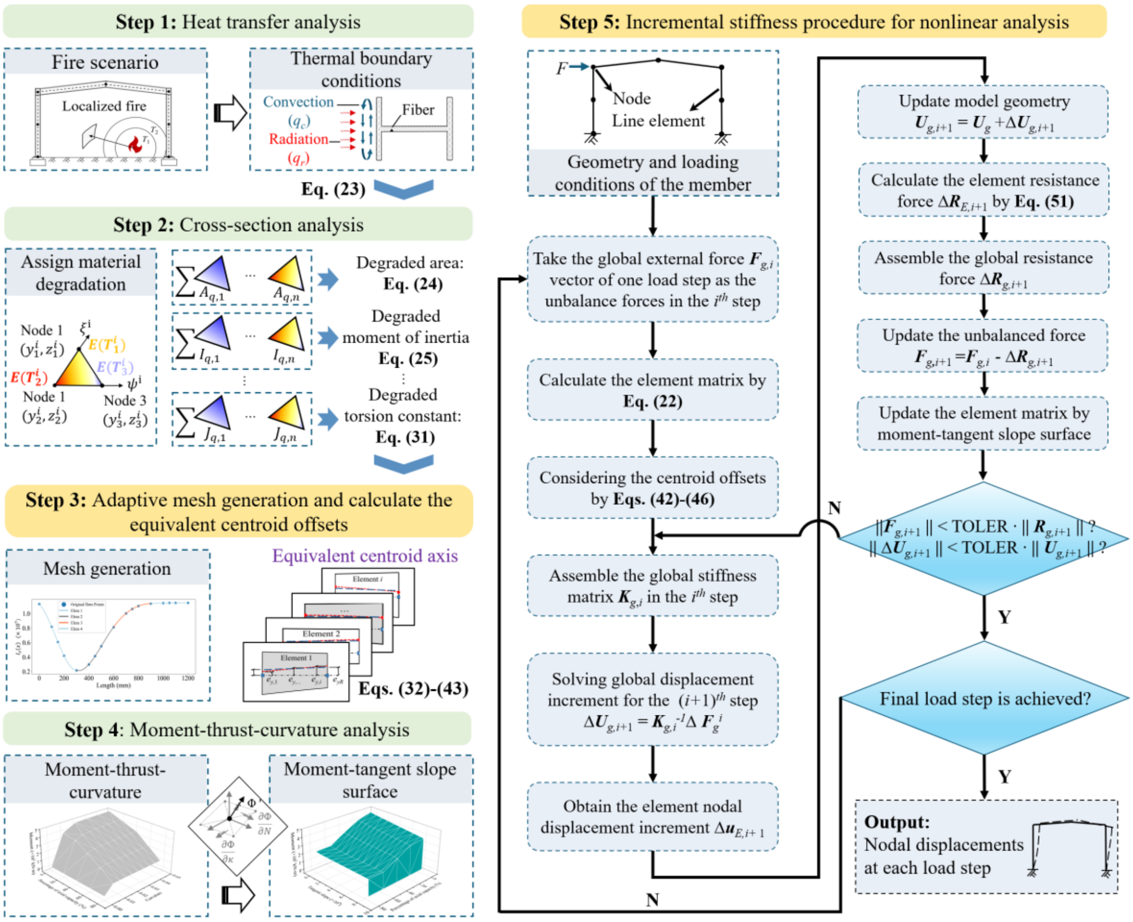

Figure 7-10 Numerical implementation of the proposed method.

7.6 Validation Examples

This section presents various validation examples to assess the accuracy and efficiency of the proposed LFEM. The examples encompass a series of cross-sectional geometries and localized fire scenarios, as summarized in Table 7-2. The parameters for different cross-sections are depicted in Figure 7-11. Stability and large deflection performances of the members and structures are analyzed using the proposed method. All examples are conducted under localized-fire conditions and capture thermally induced material degradation and centroid offsets, thereby providing sufficient validation of the proposed method.

Table 7-2 Cross-sections dimensions (mm) and localized fire scenarios in each example.

Example	Section type	B	D	t_f	t_w	Fire scenario
6.1	T, L	165(T), 205(L)	155(T), 305(L)	12(T), 35(L)	6(T), 35(L)	Non-uniformly heated across section
6.2	HR, SI, T	250	250	8(HR), 10(SI, T)	8	Pool fire
6.3	HR	250	250	8	8	Pool fire
6.4	T	100	100	11	11	Uniformly heated, Typical localized fire

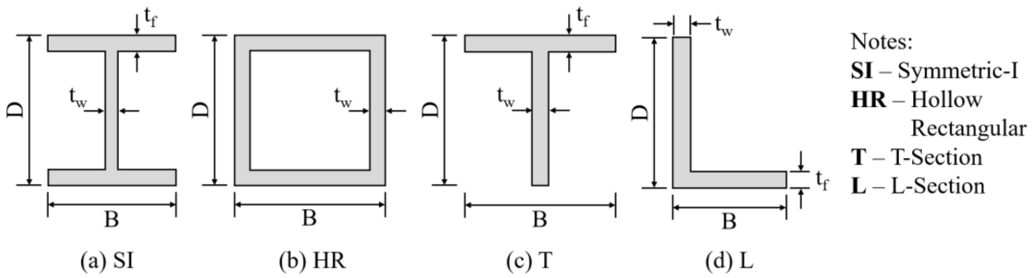

Figure 7-11 Parameters for cross-sections.

7.6.1 Cross-sectional degradation under fire

Under localized fires, temperature gradients occur across the cross-section, and the material degrade non-uniformly. Obtaining accurate properties of these cross-sections is the basis for LFEM. To verify the accuracy of the cross-section analysis method presented in this study, T- and L-shaped sections under localized fire conditions are selected as examples. The surfaces of the web and lower flange of the T-shaped section are exposed to the ISO 834 standard fire [128], and the long limb of the L-shaped section was subjected to the same fire. It is notable that, although the standard fire is used in this example for illustration, the cross-section analysis method is applicable to other localized fire scenarios.

Both the SFEM and the proposed cross-section analysis method are employed to calculate the cross-sectional properties at different fire durations. The SFEM model is constructed by ABAQUS [180], using C3D20R solid elements for the entire member under various loading conditions: axial compression at both ends to obtain axial rigidity $E_r A_q$, bending at both ends to obtain flexural rigidity $E_r I_q$, and torsion at both ends to obtain torsional rigidity $G_r J_q$. The flange and web are discretized with three or more layers of mesh to ensure accurate capture of temperature gradients. Both ends of the member are coupled to a reference point for the application of forces and boundary conditions. For compression and bending specimens, the reference point is located at the centroid, whereas for torsion specimens, it is positioned at the shear center. A slenderness ratio of 5 or greater is required to minimize the effects of cross-sectional distortion and local buckling on the members.

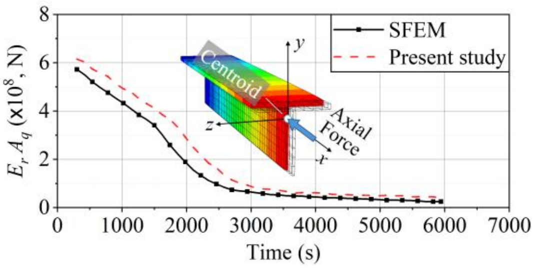

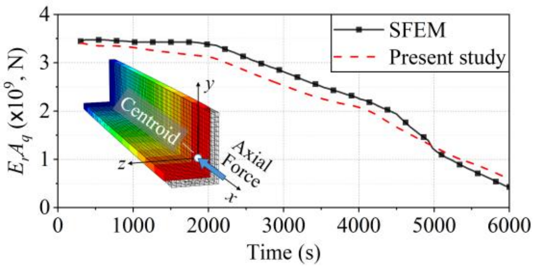

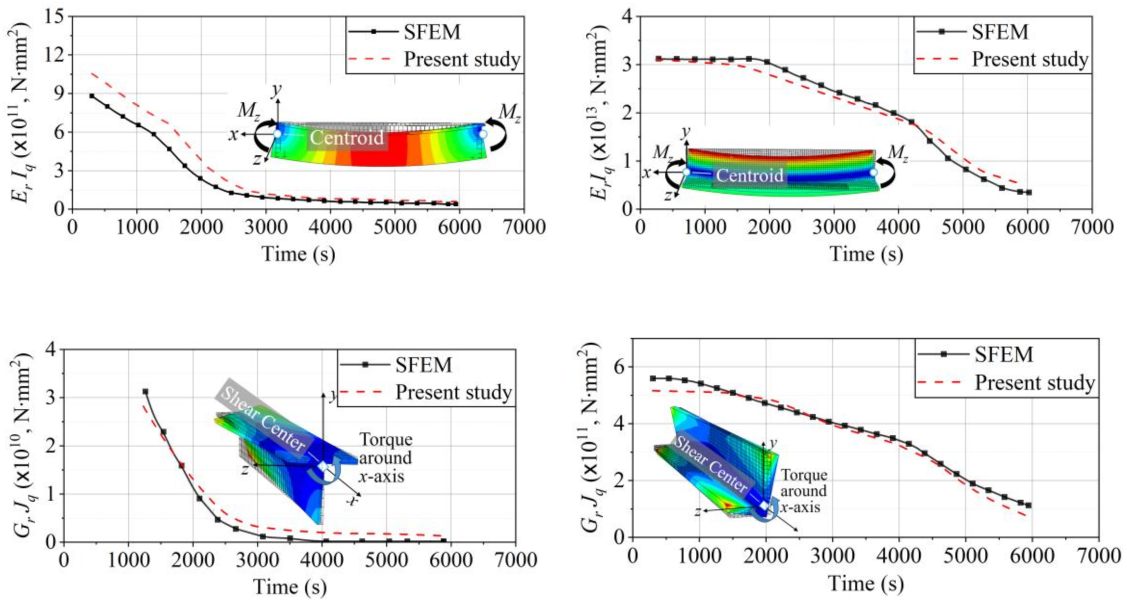

(a) T-Section (b) L-Section

Figure 7-12 Cross-section analysis under non-uniform heating.

The cross-sectional properties are obtained by calculating the ratio of reaction forces to displacements in SFEM. The results of the two methods are plotted in Figure 7-12, which shows that the results obtained by the proposed method are in good agreement with those from SFEM. The slight differences arise from the inevitable cross-sectional distortion in SFEM. Therefore, the cross-section analysis under non-uniform heating is validated.

7.6.2 Global buckling analyses under localized fires

In this example, the accuracy of stiffness matrices incorporating cross-section variation factors is validated through global buckling analysis of steel beams subjected to localized pool fires. The fire scenario is taken from the report of Qing X. and Li G. Q. [262], which involves a 5 m horizontal specimen protected with intumescent coating in a pool fire. The yield strength of steel is 345MPa. Temperatures along the specimen length at 700 s and 1600 s were recorded and are presented in Figure 7-13. The temperature difference across the cross-section was modest due to the exposure conditions around the steel member; therefore, the cross-sectional temperature distribution can be computed using the well-established lumped mass method [263]. Three boundary conditions, including simply supported, cantilever, and one end pinned with the other end clamped, are considered in this example. The global buckling loads computed using LFEM (with proposed and stepped elements) and SFEM are shown in Figure 7-14 and Figure 7-15.

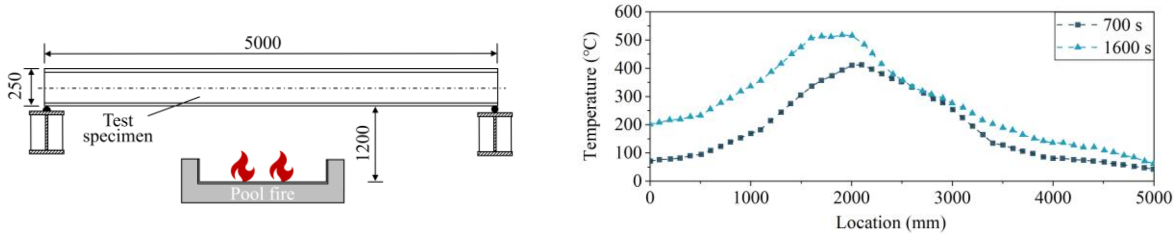

(a) Fire test setup (b) Average temperature along specimen length

Figure 7-13 Temperature distribution of a beam exposed to localized pool fire [262].

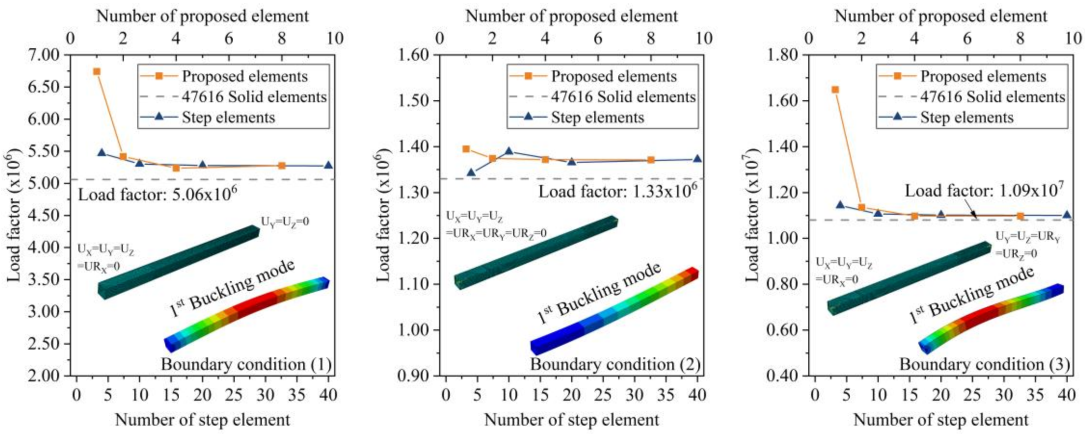

(a) Simply supported (HR) (b) Cantilever (HR) (c) Pinned-clamped (HR)

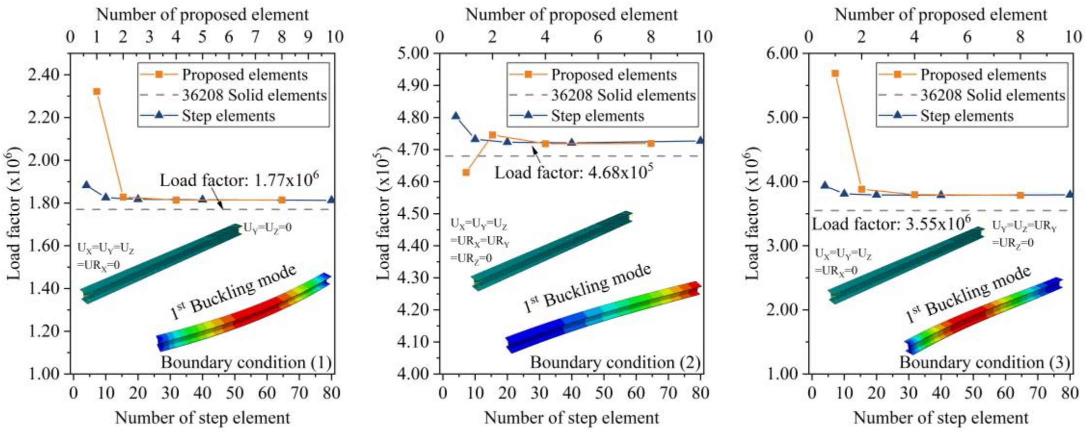

(d) Simply supported (SI) (e) Cantilever (SI) (f) Pinned-clamped (SI)

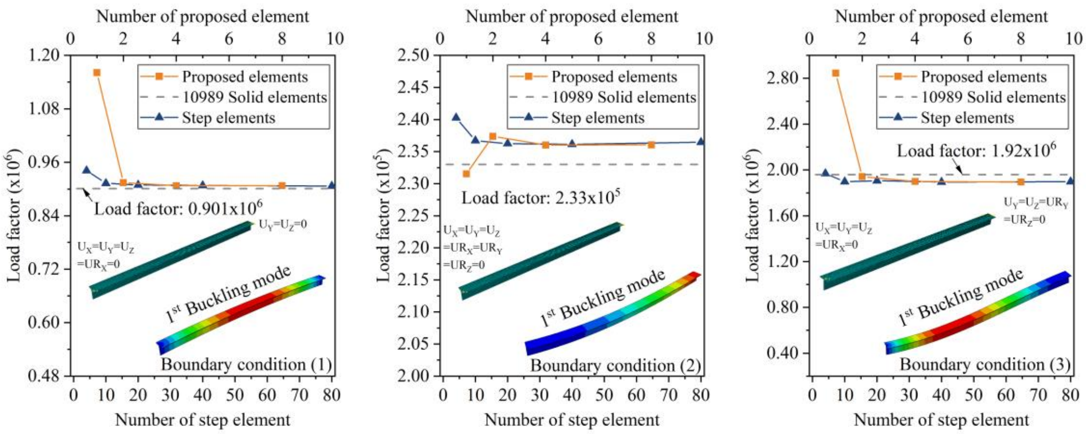

(g) Simply supported (T) (h) Cantilever (T) (i) Pinned-clamped (T)

Figure 7-14 Comparisons of buckling loads between different approaches (fire duration = 700s).

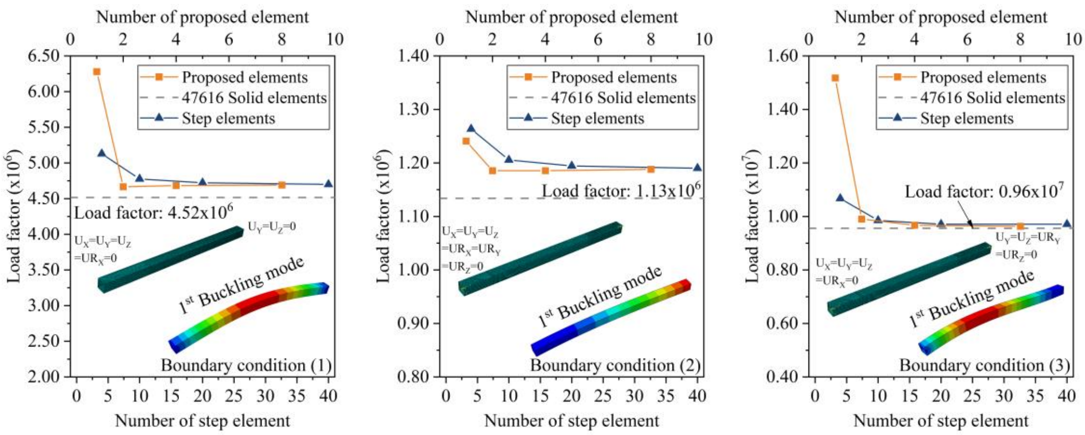

(a) Simply supported (HR) (b) Cantilever (HR) (c) Pinned-clamped (HR)

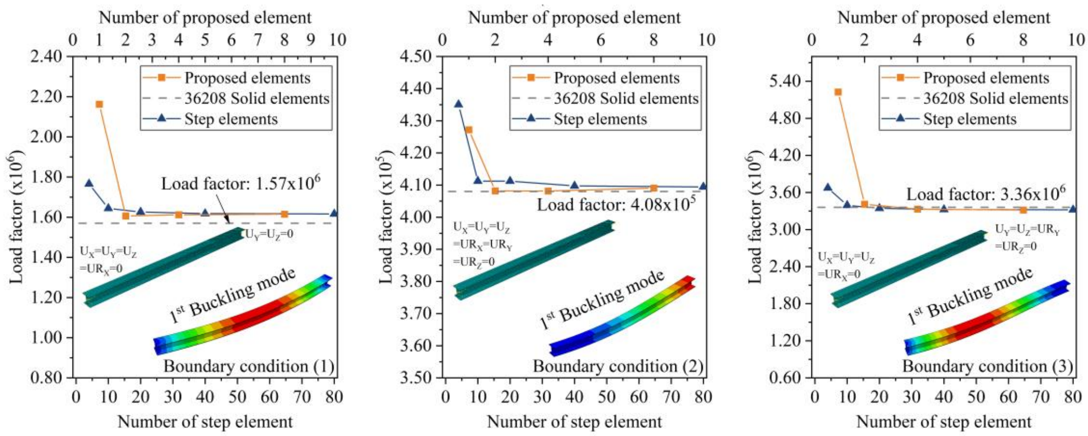

(d) Simply supported (SI) (e) Cantilever (SI) (f) Pinned-clamped (SI)

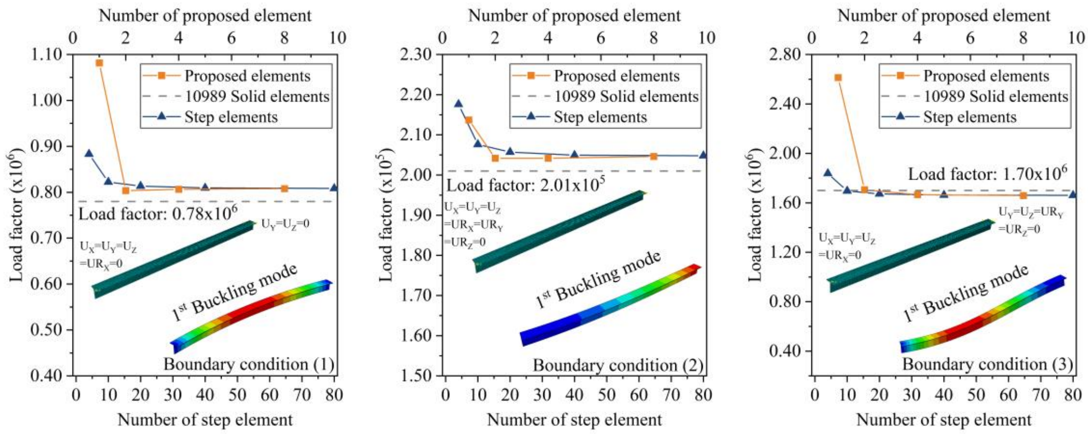

(g) Simply supported (T) (h) Cantilever (T) (i) Pinned-clamped (T)

Figure 7-15 Comparisons of buckling loads between different approaches (fire duration = 1600s).

Compared with SFEM, which uses a large number of solid elements, LFEM can achieve satisfactory results when the number of elements is sufficient. Using 10 stepped elements and one proposed line element results in a considerable difference between the two methods. However, when the number of proposed elements is increased to two, the results closely approach the converged LFEM solution, with an error within 3%. With two proposed elements, the performance is comparable to that obtained using 20 stepped elements, highlighting the significant efficiency of the method proposed in this study.

7.6.3 Second-order analyses under localized fires

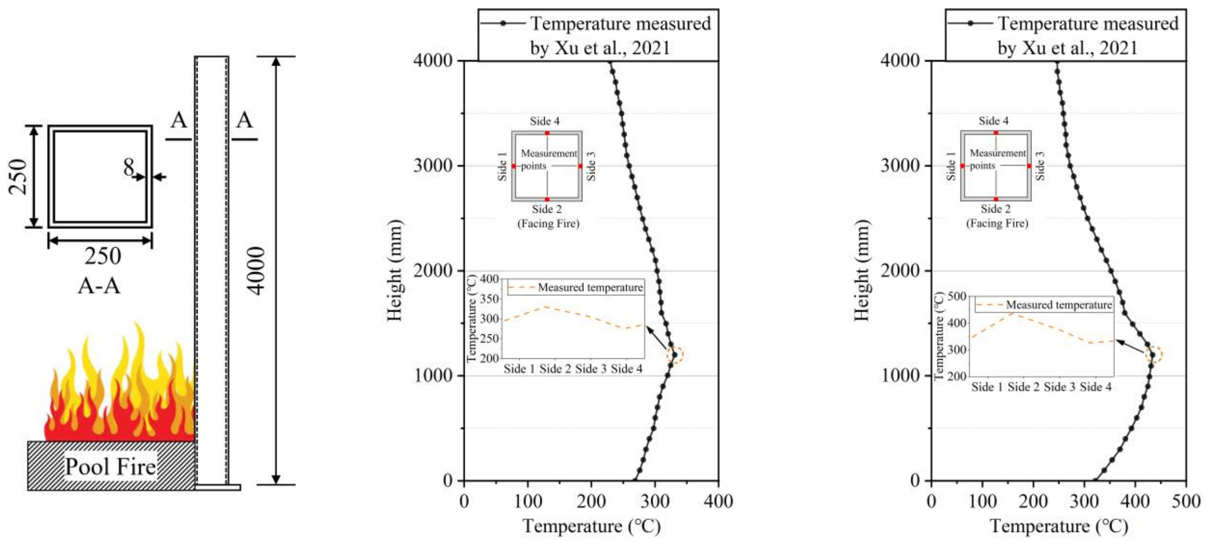

(a) Fire test layout (b) Temperature distribution (700 s) (c) Temperature distribution (1500 s)

Figure 7-16 Measured temperature distribution during the pool fire test [264].

The accuracy of the proposed method in predicting the nonlinear structural behavior of steel members under localized fire is validated in this example. A pool fire scenario reported by Xu et al. [264] is adopted, and the temperature distributions across the cross-section and along the longitudinal direction are shown in Figure 7-16. This temperature filed is used for the nonlinear sequential coupling analysis. The yield strength and Young' modular of steel are 345MPa and 205 GPa, respectively. Three typical loading conditions are applied: compression only, lateral concentrated forces, and combining compression with biaxial bending. The first two cases employ cantilever boundary conditions, whereas the third is simply supported. The number of proposed elements is determined using the adaptive mesh generation illustrated in Section 7.5.1.

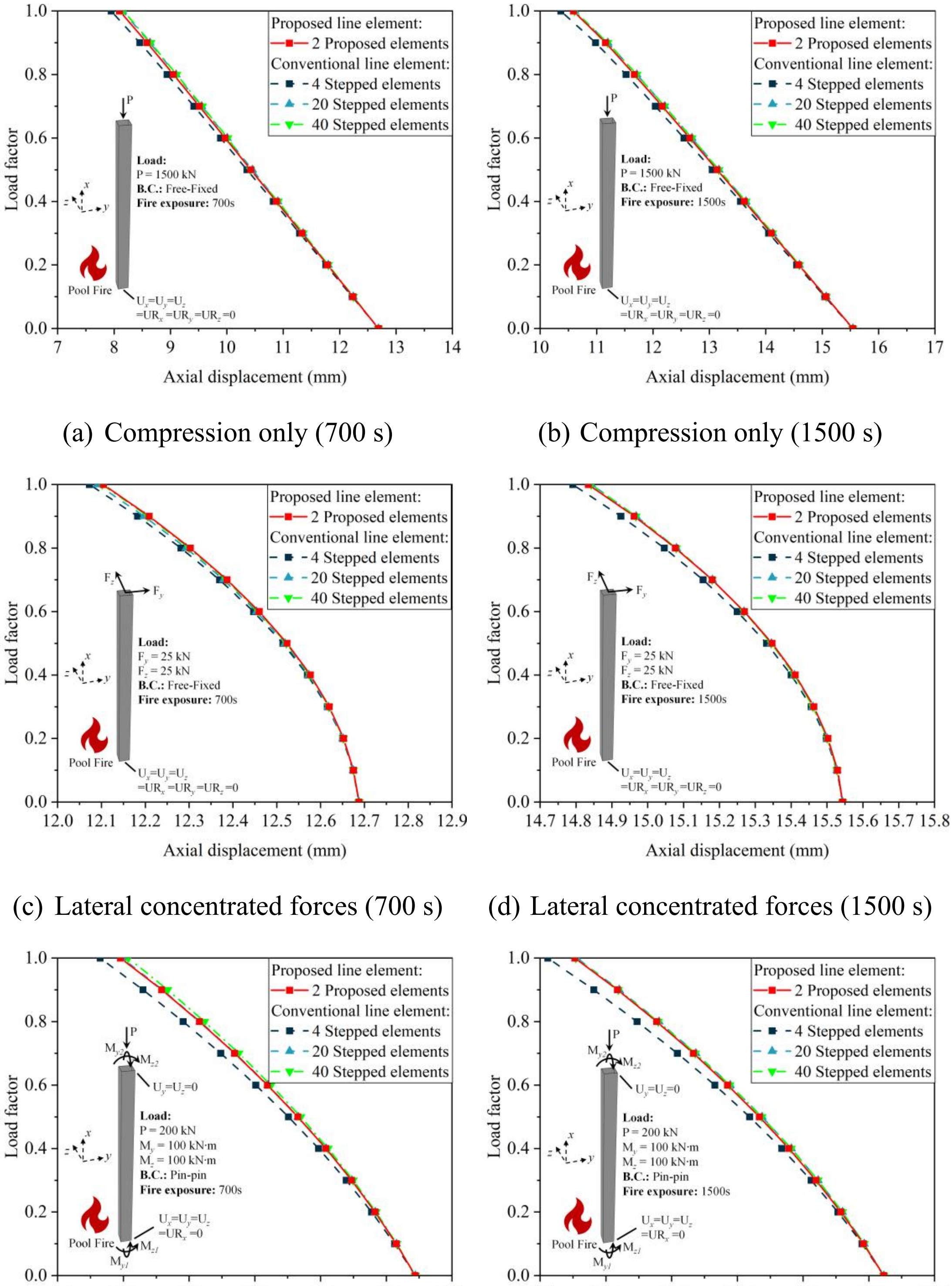

(a) Compression only (700 s)

(b) Compression only (1500 s)

(c) Lateral concentrated forces (700 s)

(d) Lateral concentrated forces (1500 s)

(e) Compression and biaxial bending (700 s)

(f) Compression and biaxial bending (1500 s)

Figure 7-17 Nonlinear analysis of steel members subjected to pool fire.

The axial displacements at the top end of the members, obtained from the proposed and stepped elements, are compared in

Figure 7-17. When the load factor is 0, only thermal expansion occurs. As the applied load on the member increases, the discrepancy among the results obtained from different methods becomes more pronounced. Only two proposed elements are required to achieve results comparable to 20 stepped elements. The results are compared with line finite element models using 20 and 40 stepped elements. These comparisons indicate that, to accurately capture the nonlinear behavior of a member under localized fires, at least 20 stepped elements are needed per member. In contrast, two proposed elements per member are sufficient. The difference between the proposed approach and the fine meshed stepped element model is within 2%, allowing the total stiffness matrix to be reduced dramatically from 126 × 126 to 30 × 30.

7.6.4 Second-order Analysis of a star shaped dome roof under localized fire

This example investigates a star shaped dome roof and examines its large-deflection performance under different fire scenarios. All structural members are modeled with a Young's modulus of 205 GPa and a yield strength of 345 MPa. The frame has six pinned supports and a concentrated force of 3 kN applied at the center. The span of the frame is 8 m with a slope of 1:10, and the cross-section is T-section, as shown in Figure 7-18.

The first fire scenario is based on the research of Chen et al. [100] on the roof under elevated temperatures. Their study assumes that the roof either heats up uniformly or exhibits a linear 5% temperature gradient along the cross-section. This scenario is reproduced in the present study, and the results are compared with their benchmark solutions. The comparison is presented in Figure 7-19. As the temperature rises, the cross-sectional properties degrade rapidly, leading to increasing displacement. The temperature gradient contributes to an additional increase in deformation due to the thermal-induced moments. The results from the two methods are consistent, indicating the accuracy of the proposed method in modeling this fire scenario.

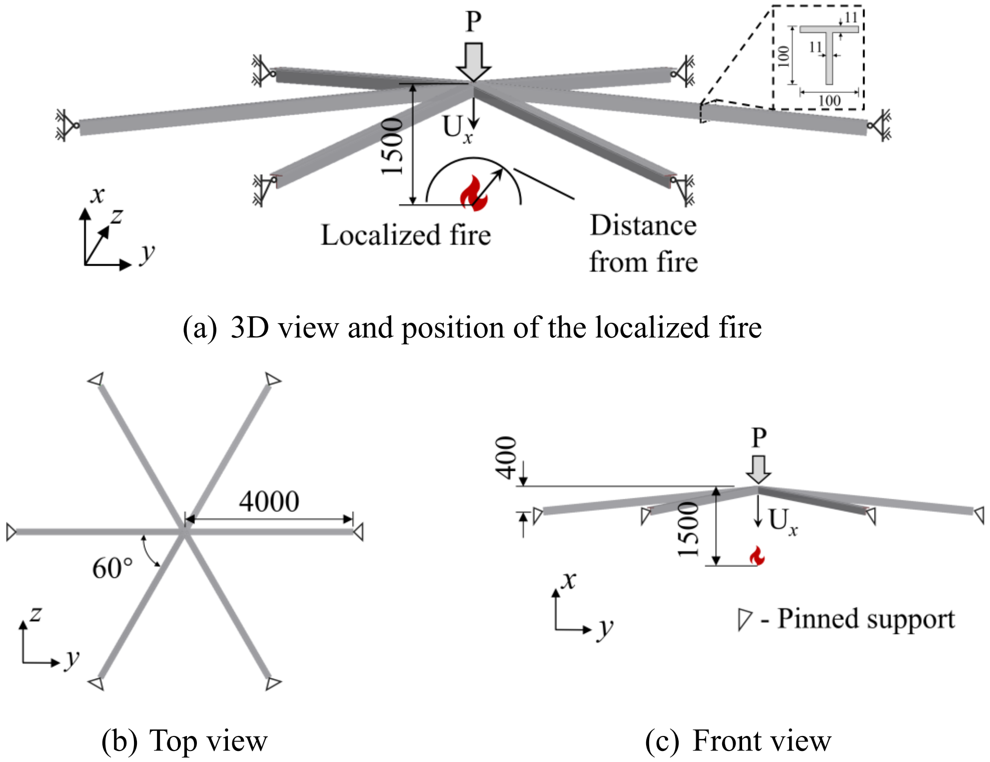

Figure 7-18 Layout and dimensions of the star shaped dome roof (unit: mm).

However, the previous fire scenario did not reflect real fire conditions. In practice, heated individual members are part of an entire structure, while other portions remain cool. The intact parts of the structure can support weakened fire-exposed members and limit their thermal expansion. To assess structural real performance under realistic fire conditions, this study adopts a typical localized fire scenario from ECCS [265], which has been used in several studies [22, 266], as shown in Figure 7-20(a). The fire is located 1.5 meters below the midspan of the roof, causing various members to experience significant temperature gradients along both the cross-section and the length, depending on their positions relative to the fire. The LFEMs using proposed elements and stepped elements are applied to analyze this fire scenario, and the results are shown in Figure 7-20(b). To obtain an accuracy solution under a larger temperature gradient, 90 stepped elements are used, yielding results almost identical to those of a more finely meshed model (268 elements), indicating convergence. The proposed method requires only 30 elements to achieve results with an error of 1.21%. This example further demonstrates the efficiency and robustness of the proposed method for conducting a structural fire analysis under localized fire.

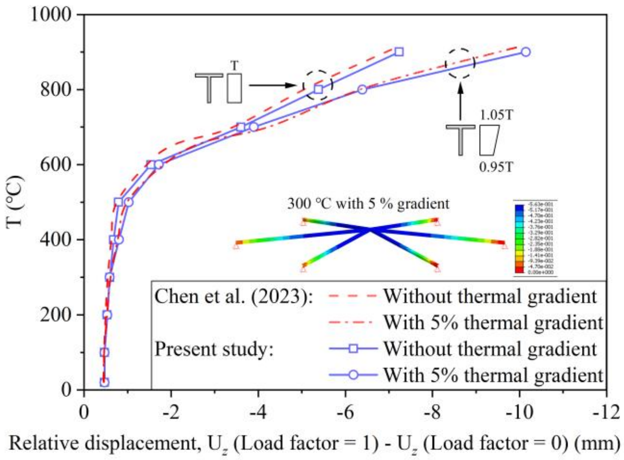

Figure 7-19 Temperature-displacement curves of the mid-span using different approaches.

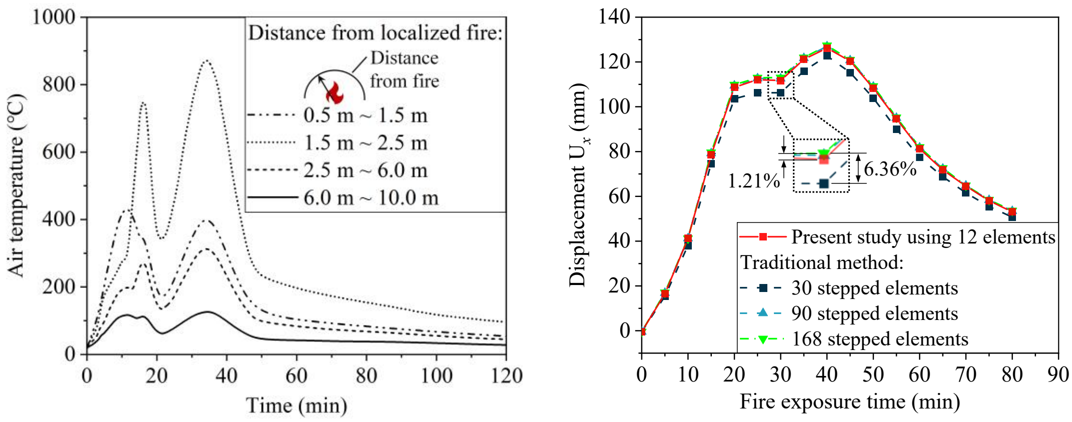

(a) Multizone model for localized fire (b) Mid-span displacement

Figure 7-20 Typical localized fire and structural behaviors.

Appendix 7A. Explicit Expressions for Stiffness Matrices.

The expressions for $k_{G,ij}$ $(i, j = 1\sim6)$ are given by,

$$k_{G,12} = k_{G,21} = \frac{2E_r A_q \theta_{y1}}{15} - \frac{E_r A_q \theta_{y2}}{30}, k_{G,13} = k_{G,31} = \frac{2E_r A_q \theta_{z1}}{15} - \frac{E_r A_q \theta_{z2}}{30}, \quad (7.52)$$

$$k_{G,15} = k_{G,51} = -\frac{E_r A_q \theta_{y1}}{30} + \frac{2E_r A_q \theta_{y2}}{15}, k_{G,16} = k_{G,61} = -\frac{E_r A_q \theta_{z1}}{30} + \frac{2E_r A_q \theta_{z2}}{15}, \quad (7.53)$$

$$k_{G,22} = \frac{2F_x L}{15} + \frac{E_r A_q L}{900}\left(\theta_{y2} - 4\theta_{y1}\right)^2, k_{G,33} = \frac{2F_x L}{15} + \frac{E_r A_q L}{900}\left(-4\theta_{z2} + \theta_{z2}\right)^2, \quad (7.54)$$

$$k_{G,23} = k_{G,32} = \frac{E_r A_q L}{900}\left(4\theta_{y1} - \theta_{y2}\right)\left(4\theta_{z1} - \theta_{z2}\right), \quad (7.55)$$

$$k_{G,25} = k_{G,52} = -\frac{F_x L}{30} - \frac{E_r A_q L}{900}\left(\theta_{y1} - 4\theta_{y2}\right)\left(4\theta_{y1} - \theta_{y2}\right), \quad (7.56)$$

$$\begin{aligned} k_{G,26} = k_{G,62} &= -\frac{E_r A_q L}{900}\left(4\theta_{y1} - \theta_{y2}\right)\left(\theta_{z1} - 4\theta_{z2}\right), \\ k_{G,35} = k_{G,53} &= -\frac{E_r A_q L}{900}\left(\theta_{y1} - 4\theta_{y2}\right)\left(4\theta_{z1} - \theta_{z2}\right), \end{aligned} \quad (7.57)$$

$$k_{G,36} = k_{G,63} = -\frac{F_x L}{30} - \frac{E_r A_q L}{900}\left(\theta_{z1} - 4\theta_{z2}\right)\left(4\theta_{z1} - \theta_{z2}\right), \quad (7.58)$$

$$k_{G,55} = \frac{2F_x L}{15} + \frac{E_r A_q L}{900}\left(\theta_{y1} - 4\theta_{y2}\right)^2, k_{G,66} = \frac{2F_x L}{15} + \frac{E_r A_q L}{900}\left(\theta_{z1} - 4\theta_{z2}\right)^2, \quad (7.59)$$

$$k_{G,56} = k_{G,65} = \frac{E_r A_q L}{900}\left(\theta_{y1} - 4\theta_{y2}\right)\left(\theta_{z1} - 4\theta_{z2}\right) \quad (7.60)$$

The expressions for $k_{T,ij}$ $(i, j = 1\sim6)$ are given by,

$$k_{T,22} = \frac{-2\alpha E_r \bar{A}_q L\Delta T}{15L},\ \ k_{T,24} = k_{T,42} = \frac{\alpha\left[E_r \bar{I}_{qz}\left(dT/dy\right) - E_r \bar{A}_q \Delta T e_y\right]}{10} \quad (7.61)$$

$$k_{T,25} = k_{T,52} = \frac{\alpha E_r \bar{A}_q L\Delta T}{30}, k_{T,33} = \frac{-2\alpha E_r \bar{A}_q L\Delta T}{15L}, \quad (7.62)$$

$$k_{T,34} = k_{T,43} = \frac{\alpha E_r\left[-\bar{I}_{qy}\left(dT/dz\right) - \bar{A}_q \Delta T e_z\right]}{10}, k_{T,36} = k_{T,63} = \frac{\alpha E_r \bar{A}_q L\Delta T}{30}, \quad (7.63)$$

$$k_{T,44} = \frac{\alpha\left[-12\Delta T E_r\left(\bar{I}_{qy} + \bar{I}_{qz}\right) - 24E_r \bar{I}_{qz}\left(dT/dy\right)e_y - 24E_r \bar{I}_{qy}\left(dT/dz\right)e_z - 12\Delta T E_r \bar{A}_q\left(e_y^{\ 2} + e_z^{\ 2}\right)\right]}{15L}, (7.64)$$

$$\begin{aligned} k_{T,45} = k_{T,54} &= \frac{\alpha E_r\left[\bar{I}_{qz}\left(dT/dy\right) + \bar{A}_q \Delta T e_y\right]}{10L}, \\ k_{T,46} = k_{T,64} &= \frac{\alpha E_r\left[-\bar{I}_{qy}\left(dT/dz\right) - \bar{A}_q \Delta T e_z\right]}{10L}, \end{aligned} \quad (7.65)$$

$$k_{T,55} = \frac{-2\alpha E_r \bar{A}_q L\Delta T}{15}, k_{T,66} = \frac{-2\alpha E_r \bar{A}_q L\Delta T}{15} \quad (7.66)$$

where $\bar{A}_q = \sum_{i=1}^{i=n} A_{q,i} \big/ n$, $\bar{I}_{qy} = \sum_{i=1}^{i=n} I_{qy,i} \big/ n$, $\bar{I}_{qz} = \sum_{i=1}^{i=n} I_{qz,i} \big/ n$.

Appendix 7B. Determination of Cross-section Varying Factors.

The cross-section varying factors are calculated by following expressions:

Linear:

$$\alpha_1 = \left(3I_{qz,1} + I_{qz,2}\right)\big/4, \alpha_2 = \alpha_3 = \left(I_{qz,1} + I_{qz,2}\right)\big/2, \alpha_4 = \left(I_{qz,1} + 3I_{qz,2}\right)\big/4 \quad (7.67)$$

$$\beta_1 = \left(3I_{qy,1} + I_{qz,2}\right)\big/4, \beta_2 = \beta_3 = \left(I_{qy,1} + I_{qy,2}\right)\big/2, \beta_4 = \left(I_{qy,1} + 3I_{qy,2}\right)\big/4 \quad (7.68)$$

Quadratic:

$$\alpha_1 = \left(31I_{qz,1} + 28I_{qz,2} + I_{qz,3}\right)/60, \alpha_2 = \alpha_3 = \left(11I_{qz,1} + 8I_{qz,2} + 11I_{qz,3}\right)/30, \quad (7.69)$$

$$\alpha_4 = \left(I_{qz,1} + 28I_{qz,2} + 31I_{qz,3}\right)/60, \beta_1 = \left(31I_{qy,1} + 28I_{qy,2} + I_{qy,3}\right)/60, \quad (7.70)$$

$$\beta_2 = \beta_3 = \left(11I_{qy,1} + 8I_{qy,2} + 11I_{qy,3}\right)/30, \beta_4 = \left(I_{qy,1} + 28I_{qy,2} + 31I_{qy,3}\right)/60 \quad (7.71)$$

Cubic:

$$\begin{aligned} \alpha_1 &= \left(15I_{qz,1} + 24I_{qz,2} - 3I_{qz,3} + 4I_{qz,4}\right)/40, \\ \alpha_2 = \alpha_3 &= \left(7I_{qz,1} + 3I_{qz,2} + 3I_{qz,3} + 7I_{qz,4}\right)/20, \end{aligned} \quad (7.72)$$

$$\begin{aligned} \alpha_4 &= \left(4I_{qz,1} - 3I_{qz,2} + 24I_{qz,3} + 15I_{qz,4}\right)/40, \\ \beta_1 &= \left(15I_{qy,1} + 24I_{qy,2} - 3I_{qy,3} + 4I_{qy,4}\right)/40, \end{aligned} \quad (7.73)$$

$$\begin{aligned} \beta_2 = \beta_3 &= \left(7I_{qy,1} + 3I_{qy,2} + 3I_{qy,3} + 7I_{qy,4}\right)/20, \\ \beta_4 &= \left(4I_{qy,1} - 3I_{qy,2} + 24I_{qy,3} + 15I_{qy,4}\right)/40 \end{aligned} \quad (7.74)$$

Quartic:

$$\alpha_1 = \left(347I_{qz,1} + 880I_{qz,2} - 228I_{qz,3} + 208I_{qz,4} + 53I_{qz,5}\right)/1260, \quad (7.75)$$

$$\alpha_2 = \alpha_3 = \left(151I_{qz,1} + 320I_{qz,2} - 312I_{qz,3} + 320I_{qz,4} + 151I_{qz,5}\right)/630, \quad (7.76)$$

$$\alpha_4 = \left(53I_{qz,1} + 208I_{qz,2} - 228I_{qz,3} + 880I_{qz,4} + 347I_{qz,5}\right)/1260, \quad (7.77)$$

$$\beta_1 = \left(347I_{qy,1} + 880I_{qy,2} - 228I_{qy,3} + 208I_{qy,4} + 53I_{qy,5}\right)/1260, \quad (7.78)$$

$$\beta_2 = \beta_3 = \left(151I_{qy,1} + 320I_{qy,2} - 312I_{qy,3} + 320I_{qy,4} + 151I_{qy,5}\right)/630, \quad (7.79)$$

$$\beta_4 = \left(53I_{qy,1} + 208I_{qy,2} - 228I_{qy,3} + 880I_{qy,4} + 347I_{qy,5}\right)\Big/1260 \qquad (7.80)$$

CHAPTER 8.

CONCLUSIONS AND FUTURE WORK

8.1 Conclusions

In this thesis, a numerical framework is developed for the Second-Order Direct Analysis (SODA) of fire resistance design. First, a refined heat-transfer analysis procedure for steel members protected with intumescent fire coatings (IFCs) is introduced, which incorporates various thermal boundary conditions and alternative thermal conductivity models. Next, a cross-sectional analysis method based on thermal deterioration triangle (TDT) elements is proposed to account for the non-uniform degradation of the cross-section. On the basis of the derived cross-sectional properties, an advanced line finite element is formulated for the geometrically nonlinear analysis of steel structures subjected to non-uniform fire exposure. Subsequently, a rigorous cross-sectional analysis approach is developed to capture the yield surfaces and moment–curvature relationships. Finally, the heat-transfer and cross-sectional analysis procedures are synergistically integrated into an efficient line-element formulation for analyzing steel structures exposed to non-uniform heating along both the cross-sectional and longitudinal directions.

The main findings and key contributions of the thesis are summarized as follows:

1) A refined transient heat-transfer analysis method for arbitrary IFC-protected cross-sections is developed. The generalized Crank–Nicolson scheme is employed to enhance numerical stability and convergence. The method accommodates thermal boundary conditions defined by fire curves, heat flux, convection, and radiation. Moreover, it has been integrated into the user-friendly software MSASect2 to assist engineers in structural fire design.
2) A cross-section analysis method for IFC-protected members with irregular

sections under fire is developed, employing improved TDT elements to capture non-uniform material degradation. The proposed approach is validated through comparisons with experimental results and with the SFEM using solid elements. Based on this method, a parametric study involving 3,168 analyses of the global buckling performance of IFC-protected steel members under fire is conducted. A design recommendation is proposed to estimate the target thickness of IFCs required to satisfy specified performance criteria.

3) A novel line finite element method (LFEM) is proposed for the geometrically nonlinear analysis of steel members exposed to non-uniform fire, explicitly accounting for thermally induced twisting effects. A line element formulation is derived that accounts for the additional torque arising from the non-coincidence of the shear center and centroid of the cross-section, thereby enabling the handling of large deflection cases with twisting effects. Several validation examples are conducted to assess the accuracy of the proposed LFEM, followed by two case studies investigating the influence of thermally induced twisting effects and analyzing the underlying mechanisms behind these effects.
4) To provide cross-sectional strength for the LFEM, a fiber-based cross-sectional analysis method is developed for constructing the interaction diagrams of concrete-encased steel columns under fire. The proposed method is validated through comparisons with both test results and prior studies, demonstrating its accuracy and robustness. A parametric study involving 162,000 cases is performed to evaluate the influence of key design parameters. Based on the resulting database, a simplified design method is developed, exhibiting good accuracy.
5) A more efficient LFEM is established for fire resistance design of steel members and frames under localized fires. The proposed line element features

a "shrunk" cross-section that varies longitudinally, accompanied by continuously changing cross-sectional eccentricity. The degradation of cross-sectional stiffness and strength is evaluated using a refined cross-section analysis method and the moment–thrust–curvature analysis, respectively, while variations in eccentricity and cross-sectional properties along the member length are considered through the equivalent centroid axis and cross-section varying factors, respectively. The examples demonstrate that the proposed method achieves accuracy results while requiring significantly fewer line elements and reducing the stiffness matrix size by approximately 17 times.

8.2 Future Work

This thesis develops a numerical framework combining heat transfer analysis, cross-section analysis and line finite element formulations for fire resistance design of steel structures. However, there still remain some studies that need to be carried out in the future:

i. Computational fluid dynamics (CFD) can provide high-resolution thermal boundary conditions. Extending the current numerical framework to achieve full coupling between CFD and LFEM would enable more accurate and realistic simulation of fire and structural responses, thereby facilitating more advanced performance-based design.
ii. Proposing higher-order planar elements could improve the efficiency of cross-sectional analysis and enable accurate capture of cross-sectional properties with steep material gradients using fewer elements.
iii. Local buckling and cross-sectional distortion of steel members under fire will be considered in the future work. The LFEM formulation assumes that members are sufficiently slender, which is not always valid in practical steel structures. Incorporating these local behaviors into the analysis would

improve the accuracy of the structural response prediction.

iv. The effects of steel creep at elevated temperatures and residual stress after fire will be considered, as both can significantly influence the stability, load-bearing capacity, and overall performance of structural members.

v. Extending the proposed numerical framework to time-dependent problems: Structural dynamic analysis is crucial in engineering applications. Extending the current SODA framework from static analysis to dynamic, time-dependent problems is essential for broader applicability.

REFERENCES

[1] Engelhardt MD, Morovat MA. Directions in structural-fire safety design for steel buildingsa. Japan Architectural Review. 2022;5:20-31.

[2] Hurley MJ, Rosenbaum ER. Performance-based fire safety design: CRC Press Boca Raton; 2015.

[3] Nelson H. Performance Based Fire Safety. Fire Science and Technology. 1997;17:49-54.

[4] Hurley MJ, Gottuk DT, Hall Jr JR, Harada K, Kuligowski ED, Puchovsky M et al. SFPE handbook of fire protection engineering: Springer; 2015.

[5] Johann MA, Albano LD, Fitzgerald RW, Meacham BJ. Performance-Based Structural Fire Safety. Journal of performance of constructed facilities. 2006;20:45-53.

[6] Alvarez A, Meacham B, Dembsey N, Thomas J. Twenty years of performance-based fire protection design: challenges faced and a look ahead. Journal of Fire Protection Engineering. 2013;23:249-76.

[7] Gernay T. Performance-based design for structures in fire: Advances, challenges, and perspectives. Fire Safety Journal. 2024;142:104036.

[8] Buchanan AH. Fire engineering for a performance based code. Fire safety journal. 1994;23:1-16.

[9] Mowrer F. Methods of quantitative fire hazard analysis. Final report. Electric Power Research Inst., Palo Alto, CA (United States); Mowrer …; 1992.

[10] FCRCL. Fire Code Reform Centre Limited, Promotional Literature. Sydney, Australia1994.

[11] CCBFC. Canadian Commission on Building and Fire Codes, Draft Strategic Plan, CCBFC Strategic Planning Task Grounp. Ontario, Canada: National Research Council; 1995.

[12] Meacham BJ. Assessment of the Technological Requirements for the Realization of Performance-Based Fire Safety Design in the United States. Final Report. 1998.

[13] Koffel WE. A Review of Life Safety Codes in USA. Proceedings of the Korea Institute of Fire Science and Engineering Conference: Korean Institute of Fire Science and Engineering; 2000. p. 142-6.

[14] Custer R, Meacham B. Engineering guide to performance based fire protection analysis and design. SFPE (Society of Fire Protection Engineers), Handbook of Fire Protection Engineering. 2000.

[15] ICC. Performance code for buildings and facilities. International Conference of Building Officials; 2001.

[16] Ghosh S. Provisions related to structural design and concrete of the 2003 IBC and NFPA Building code. PCI journal. 2003;48:108-13.

[17] Saab HA, Nethercot DA. Modelling steel frame behaviour under fire conditions. Engineering structures. 1991;13:371-82.

[18] El-Rimawi JA, Burgess IW, Plank RJ. The analysis of semi-rigid frames in fire—a secant approach. Journal of Constructional Steel Research. 1995;33:125-46.

[19] Lennon T, Moore D, Bailey C. The behaviour of full-scale steel-framed buildings subjected to compartment fires. The Structural Engineer. 1999;77:15-21.

[20] Tang L, Liew J, Choo Y. Advanced analysis of localised fires in a large-span arched framework. Proc, 6th Int Conf on Steel and Space Structures1999. p. 163-70.

[21] Huang Z, Burgess IW, Plank RJ. Three-Dimensional Analysis of Composite Steel-Framed Buildings in Fire. Journal of structural engineering (New York, NY). 2000;126:389-97.

[22] Liew JR, Tang L, Choo Y. Advanced analysis for performance-based design of steel structures exposed to fires. Journal of Structural Engineering. 2002;128:1584-93.

[23] Usmani AS, Chung Y, Torero JL. How did the WTC towers collapse: a new theory. Fire Safety Journal. 2003;38:501-33.

[24] Lamont S, Lane B, Flint G, Usmani A. Behavior of Structures in Fire and Real Design - A Case Study. Society for Fire Protection Engineers; 2006.

[25] Block F, Yu C, Butterworth N. The Practical Application of Structural Fire Engineering on a Retail Development in the UK. Journal of structural fire engineering. 2010;1:205-18.

[26] Tonicello E, Desanghere S, Vassart O, Franssen J-M. Fire analysis of a new steel bridge. 7th International conference on Structures in Fire: ETH Zürich, Zürich, Switzerland; 2012.

[27] Mohan AT, Van Coile R, Hopkin D, Jomaas G, Caspeele R. Risk Tolerability Limits for Fire Engineering Design: Methodology and Reference Case Study. Fire technology. 2021;57:2235-67.

[28] Guo Q, Quiel SE, Naito CJ. Traffic-based quantitative risk analysis of structural fire damage to roadway tunnel linings. Structure and infrastructure engineering. 2023;19:932-48.

[29] Hopkin D, Anastasov S, Illingworth D, McColl B, Loughlin EO, Taylor A. A

structural fire strategy for an exposed weathering steel-framed building. The Structural Engineer: Journal of the Institution of Structural Engineer. 2018;96:60-6.

[30] Meacham BJ. Fire performance and regulatory considerations with modern methods of construction. Buildings & Cities. 2022;3.

[31] Molkens T, Van Coile R, Gernay T. Assessment of damage and residual load bearing capacity of a concrete slab after fire: Applied reliability-based methodology. Engineering Structures. 2017;150:969-85.

[32] Taler J, Duda P. Solving direct and inverse heat conduction problems. Berlin ;: Springer; 2006.

[33] Lewis RW, Nithiarasu P, Seetharamu KN. Fundamentals of the finite element method for heat and fluid flow. Hoboken, N.J: John Wiley & Sons; 2004.

[34] Taler J, Ocłoń P. Finite element method in steady-state and transient heat conduction. Encyclopedia of thermal stresses: Springer; 2014. p. 1604-33.

[35] Reddy JN, Gartling DK. The finite element method in heat transfer and fluid dynamics. 3rd ed. ed. Boca Raton, FL: CRC Press; 2010.

[36] Nithiarasu P, Seetharamu KN, Lewis RW. Fundamentals of the finite element method for heat and mass transfer. Second edition ed. Chichester, West Sussex: John Wiley & Sons, Ltd.; 2016.

[37] Özişik M,Orlande, Helcio RB, Colaço MJ, Cotta, RM. Finite difference methods in heat transfer. CRC press.; 2017.

[38] Sheikholeslami M. Application of Control Volume Based Finite Element Method (CVFEM) for nanofluid flow and heat transfer. Amsterdam: Elsevier; 2019.

[39] Özışık MN, Orlande HRB, Colaco MJ, Cotta RM. Finite difference methods in heat transfer. Second edition. ed. Boca Raton: CRC Press; 2017.

[40] Xue H, Ho JC, Cheng YM. Comparison of different combustion models in enclosure fire simulation. Fire Safety Journal. 2001;36:37-54.

[41] Yu FB, Wang XT, Zhou M, Wang WZ. Research on Fire Resistance Performance of Pre-stressed Suspended Steel Reticulated Shell. Advanced Materials Research. 2011;163:790-4.

[42] Fan S-G, Shu G-P, She G-J, Liew JR. Computational method and numerical simulation of temperature field for large-space steel structures in fire. Advanced Steel Construction. 2014;10:151-78.

[43] Jiang L, Chen S, Usmani A. Feasibility of dimensionally reduced heat transfer analysis for structural members subjected to localised fire. Advances in Structural Engineering. 2018;21:1708-22.

[44] Wang YC, Lennon T, Moore DB. The behaviour of steel frames subject to fire. Journal of Constructional Steel Research. 1995;35:291-322.

[45] ECCS. (European Convention for Constructional Steelwork). Fire safety in open car parks. Brussels, Belgium: Modern Fire Engineering, Technical Committee 3, European Convention for Constructional Steelwork; 1993.

[46] Liew JR. Performance based fire safety design of structures—a multi-dimensional integration. Advances in Structural Engineering. 2004;7:311-33.

[47] Parkinson DL, Kodur V. Performance Based Design of Structural Steel for Fire Conditions: A Calculation Methodology. Structures Congress 2006: Structural Engineering and Public Safety2006. p. 1-10.

[48] Hamilton SR. Performance-based fire engineering for steel framed structures: a probabilistic methodology: Stanford University Stanford; 2011.

[49] Gernay T, Khorasani NE. Recommendations for performance-based fire design of composite steel buildings using computational analysis. Journal of Constructional Steel Research. 2020;166:105906.

[50] Wickström U, Duthinh D, McGrattan K. Adiabatic surface temperature for calculating heat transfer to fire exposed structures. Proceedings of the Eleventh International Interflam Conference Interscience Communications, London2007. p. 943-53.

[51] Zhang C, Silva JG, Weinschenk C, Kamikawa D, Hasemi Y. Simulation methodology for coupled fire-structure analysis: modeling localized fire tests on a steel column. Fire Technology. 2016;52:239-62.

[52] Choe L, Choe L, Ramesh S, Hoehler M, Seif M, Gross J et al. National fire research laboratory commissioning project: testing steel beams under localized fire exposure: US Department of Commerce, National Institute of Standards and Technology; 2018.

[53] Yan X, Gernay T. Numerical modeling of localized fire exposures on structures using FDS-FEM and simple models. Engineering Structures. 2021;246:112997.

[54] Yang Y-F, Fu F. Fire resistance of steel beam to square CFST column composite joints using RC slabs: Experiments and numerical studies. Fire Safety Journal. 2019;104:90-108.

[55] Wang J, Song Q-Y, Han L-H. Temperature field of intumescent coating protected concrete-filled steel tubular columns under fire. Journal of constructional steel research. 2023;201:107695.

[56] Li G, Gu Z-Z, Du E, Liu S-W, Liu Y-P, Chan S-L. Global buckling analysis of IFC-protected steel members with irregular sections under fire. Journal of constructional steel research. 2025;224:109158.

[57] Chen W-F, Atsuta T. Theory of beam-columns, volume 2: space behavior and design: J. Ross Publishing; 2007.

[58] Liu S-W, Gao W-L, Ziemian RD. Improved line-element formulations for the stability analysis of arbitrarily-shaped open-section beam-columns. Thin-walled structures. 2019;144:106290.

[59] Chen L, Gao W-L, Liu S-W, Ziemian RD, Chan S-L. Geometric and material nonlinear analysis of steel members with nonsymmetric sections. Journal of Constructional Steel Research. 2022;198:107537.

[60] ASCE. ANSI/AISC 360–10: specification for structural steel buildings. Chicago, IL: American Institute of Steel Construction, Inc; 2010.

[61] EN1993-1-2. Eurocode 3: Design of Steel Structures– Part 1–2: General Rules– Structural Fire Design. European Committee for Standardisation, Brussels. 2005.

[62] Liu S-W, Ziemian RD, Chen L, Chan S-L. Bifurcation and large-deflection analyses of thin-walled beam-columns with non-symmetric open-sections. Thin-walled structures. 2018;132:287-301.

[63] Chen L, Zhang H-Y, Liu S-W, Ziemian RD. Efficient line-element method for the second-order analysis of steel members with nonsymmetric thick-walled cross sections. Journal of Structural Engineering. 2024;150:04023226.

[64] Chen S, Teng J, Chan S-L. Design of biaxially loaded short composite columns of arbitrary section. Journal of Structural Engineering. 2001;127:678-85.

[65] Pilkey WD. Analysis and Design of Elastic Beams: Computational Methods. 1. Aufl. ed. Newark: Wiley; 2002.

[66] Anwar N, Najam FA. Structural cross sections: analysis and design: Butterworth-Heinemann; 2016.

[67] Li G, Gu Z-Z, Ouyang W, Liu S-W, Abdelrahman A. Finite-element-based cross-section analysis method for functionally graded sandwich members with arbitrary shapes and gradients. Journal of Sandwich Structures & Materials. 2024;26:1182-208.

[68] Garlock ME, Quiel SE. Plastic axial load and moment interaction curves for fire-exposed steel sections with thermal gradients. Journal of structural engineering. 2008;134:874-80.

[69] Agarwal A, Choe L, Varma AH. Fire design of steel columns: Effects of thermal gradients. Journal of constructional steel research. 2014;93:107-18.

[70] Maria EMG, Spencer EQ. Mechanics of Wide-flanged Steel Sections that Develope Thermal Gradients Due to Fire Exposure. International journal of steel structures. 2007:153-62.

[71] Ziemian RD. Guide to stability design criteria for metal structures. 6th ed. ed. Hoboken, N.J: John Wiley & Sons; 2010.

[72] Chan S-L, Liu Y-P, Liu S-W. A new codified design theory of second-order direct analysis for steel and composite structures–From research to practice. Structures: Elsevier; 2017. p. 105-11.

[73] Caldas RB, Sousa JBM, Fakury RH. Interaction diagrams for reinforced concrete sections subjected to fire. Engineering Structures. 2010;32:2832-8.

[74] Law A, Gillie M. Interaction diagrams for ambient and heated concrete sections. Engineering Structures. 2010;32:1641-9.

[75] Liu S-W, Liu Y-P, Chan S-L. Advanced analysis of hybrid steel and concrete frames: Part 1: Cross-section analysis technique and second-order analysis. Journal of Constructional Steel Research. 2012;70:326-36.

[76] Li T-J, Liu S-W, Chan S-L. Cross-sectional analysis of arbitrary sections allowing for residual stresses. Steel & Composite Structures. 2015;18:985-1000.

[77] Pham DT, de Buhan P, Florence C, Heck J-V, Nguyen HH. Interaction diagrams of reinforced concrete sections in fire: A yield design approach. Engineering Structures. 2015;90:38-47.

[78] Albero V, Espinós A, Romero ML, Wang YC, Renaud C, Schaumann P et al. Interaction diagram based method for fire resistance design of eccentrically loaded concrete-filled steel tubular columns. Thin-Walled Structures. 2018;130:641-51.

[79] Code HKS. Code of Practice for the Structural Use of Steel. Buildings Department, Hong Kong Special Administrative Region. 2023.

[80] Mabsout ME, Tarhini KM, Frederick GR, Tayar C. Finite-Element Analysis of Steel Girder Highway Bridges. Journal of bridge engineering. 1997;2:83-7.

[81] Naceur H, Shiri S, Coutellier D, Batoz J-L. On the modeling and design of composite multilayered structures using solid-shell finite element model. Finite Elements in Analysis and Design. 2013;70:1-14.

[82] Ellobody E. Nonlinear analysis of cellular steel beams under combined buckling modes. Thin-Walled Structures. 2012;52:66-79.

[83] Schafer B. Local, distortional, and Euler buckling of thin-walled columns. Journal

of structural engineering. 2002;128:289-99.

[84] Schafer BW. Designing cold-formed steel using the direct strength method. 2006.

[85] Bian G, Peterman KD, Torabian S, Schafer BW. Torsion of cold-formed steel lipped channels dominated by warping response. Thin-Walled Structures. 2016;98:565-77.

[86] Chan SL, Cho SH. Second-order analysis and design of angle trusses Part I: Elastic analysis and design. Engineering Structures. 2008;30:616-25.

[87] Liu S-W, Liu Y-P, Chan S-L. Advanced analysis of hybrid steel and concrete frames: Part 2: Refined plastic hinge and advanced analysis. Journal of Constructional Steel Research. 2012;70:337-49.

[88] Chen L. Second-order direct analysis for design of modern steel structures with nonsymmetric cross-sections. Hong Kong: The Hong Kong Polytechnic University; 2023.

[89] Liu S-W, Bai R, Chan S-L. Dynamic time-history elastic analysis of steel frames using one element per member. Structures: Elsevier; 2016. p. 300-9.

[90] Bai R, Liu S-W, Liu Y-P, Chan S-L. Direct analysis of tapered-I-section columns by one-element-per-member models with the appropriate geometric-imperfections. Engineering Structures. 2019;183:907-21.

[91] Chan SL, Chan B. Refined plastic hinge analysis of steel frames under fire. Steel and Composite Structures, An International Journal. 2001;1:111-30.

[92] El-Tawil S, Deierlein GG. Nonlinear analysis of mixed steel-concrete frames. I: Element formulation. Journal of Structural engineering. 2001;127:647-55.

[93] Iu CK, Chan SL. A simulation-based large deflection and inelastic analysis of steel frames under fire. Journal of constructional steel research. 2004;60:1495-524.

[94] Landesmann A, de M. Batista E, Drummond Alves JL. Implementation of advanced analysis method for steel-framed structures under fire conditions. Fire Safety Journal. 2005;40:339-66.

[95] Li G, Wang P, Shouchao J. Non-linear finite element analysis of axially restrained steel beams at elevated temperatures in a fire. Journal of Constructional Steel Research. 2007;63:1175-83.

[96] Heidarpour A, Bradford MA. Beam–column element for non-linear dynamic analysis of steel members subjected to blast loading. Engineering Structures. 2011;33:1259-66.

[97] Sun R, Huang Z, Burgess IW. Progressive collapse analysis of steel structures under fire conditions. Engineering Structures. 2012;34:400-13.

[98] Jiang L, Usmani A. Computational performance of beam-column elements in modelling structural members subjected to localised fire. Engineering structures. 2018;156:490-502.

[99] Possidente L, Tondini N, Battini J-M. 3D beam element for the analysis of torsional problems of steel-structures in fire. Journal of Structural Engineering. 2020;146:04020125.

[100] Chen L, Liu S-W, Chan S-L. Geometrically nonlinear analysis of steel structures with nonsymmetric sections under elevated temperatures. Journal of Constructional Steel Research. 2023;211:108205.

[101] Lange D, Torero JL, Spinardi G, Law A, Johnson P, Brinson A et al. A competency

framework for fire safety engineering. Fire safety journal. 2022;127:103511.

[102] Salminen M, Hietaniemi J. Performance-Based Fire Design of Steel Structures of Helsinki Olympic Stadium. Applications of Structural Fire Engineering. 2015.

[103] Khan AA, Usmani A, Torero JL. Evolution of fire models for estimating structural fire-resistance. Fire safety journal. 2021;124:103367.

[104] Kuehnen R, Youssef M, El-Fitiany S. Performance-based design of RC beams using an equivalent standard fire. Journal of Structural Fire Engineering. 2021;12:98-109.

[105] Wickström U, Robbins A, Baker G. The use of adiabatic surface temperature to design structures for fire exposure. Journal of structural fire engineering. 2011;2:21-8.

[106] Andreozzi A, Bianco N, Musto M, Rotondo G. Adiabatic surface temperature as thermal/structural parameter in fire modeling: thermal analysis for different wall conductivities. Applied thermal engineering. 2014;65:422-32.

[107] Malendowski M. Analytical solution for adiabatic surface temperature (AST). Fire technology. 2017;53:413-20.

[108] Mostofi S, Altunişik AC. Surrogate Model-Driven Estimation of Adiabatic Surface Temperature of Fire Exposed Suspension Bridge Towers. Fire Technology. 2025;61:603-30.

[109] Jafarian M, Wang YC, Yuan J. Temperature Attained in Intumescent Coating–Protected Concrete-Filled Circular Steel Tubular Sections under the Standard Fire Condition. Journal of structural engineering (New York, NY). 2022;148.

[110] Song Q-Y, Han L-H, Yuan F, Zhou K. Temperature rise distribution of circular

concrete-filled steel tubular cross-sections with intumescent coating. Journal of constructional steel research. 2020;168:105869.

[111] de Silva D, Bilotta A, Nigro E. Approach for modelling thermal properties of intumescent coating applied on steel members. Fire safety journal. 2020;116:103200.

[112] Lucherini A, Maluk C. Intumescent coatings used for the fire-safe design of steel structures: A review. Journal of constructional steel research. 2019;162:105712.

[113] Li G-Q, Han J, Lou G-B, Wang YC. Predicting intumescent coating protected steel temperature in fire using constant thermal conductivity. Thin-walled structures. 2016;98:177-84.

[114] de Normalization CEJB, Belgium. EN 13381-8: 2013 Test methods for determining the contribution to the fire resistance of structural members-Part 8: Applied reactive protection to steel members. 2013.

[115] Li G-Q, Zhang C, Lou G-B, Wang Y-C, Wang L-L. Assess the Fire Resistance of Intumescent Coatings by Equivalent Constant Thermal Resistance. Fire technology. 2012;48:529-46.

[116] Han J, Li G-Q, Wang YC, Xu Q. An experimental study to assess the feasibility of a three stage thermal conductivity model for intumescent coatings in large space fires. Fire safety journal. 2019;109:102860.

[117] Taler J, Ocłoń P. Finite Element Method in Steady-State and Transient Heat Conduction. Dordrecht: Springer Netherlands. p. 1604-33.

[118] Jamet P. Stability and Convergence of a Generalized Crank-Nicolson Scheme on a Variable Mesh for the Heat Equation. SIAM journal on numerical analysis.

1980;17:530-9.

[119] Guilin S, Trueman CW. Efficient implementations of the Crank-Nicolson scheme for the finite-difference time-domain method. IEEE transactions on microwave theory and techniques. 2006;54:2275-84.

[120] Kakaç S, Yener Y, Naveira-Cotta CP. Heat conduction. Fifth edition. ed. Boca Raton, FL: CRC Press; 2018.

[121] Hahn DW, Özışık MN. Heat conduction. 3rd ed. ed. Hoboken, N.J: John Wiley; 2012.

[122] Cai J, Pan J, Li G, Elchalakani M. Behaviors of eccentrically loaded ECC-encased CFST columns after fire exposure. Engineering structures. 2023;289:116258.

[123] Song Q-Y, Han L-H, Zhou K, Feng Y. Fire resistance of circular concrete-filled steel tubular (CFST) column protected by intumescent coating. Journal of constructional steel research. 2018;147:154-70.

[124] EN 1991-1-2: 2002-Eurocode 1: Actions on structures-Part 1-2: General actions-Actions on structures exposed to fire. 2002.

[125] Wang Y, Goransson U, Holmstedt G, Omrane AJFSS. A model for prediction of temperature in steel structure protected by intumescent coating, based on tests in the cone calorimeter. 2005;8:235-46.

[126] Cess R. The interaction of thermal radiation with conduction and convection heat transfer. Advances in heat transfer: Elsevier; 1964. p. 1-50.

[127] Frei S, Singh MK. An Implicitly Extended Crank–Nicolson Scheme for the Heat Equation on a Time-Dependent Domain. Journal of scientific computing. 2024;99:64.

[128] ISO/CD834-11. Fire resistance tests—elements of building construction, specific requirements for the assessment of fire protection to structural steel elements. International Organization for Standardization; 2014.

[129] Lie T. Fire resistance of circular steel columns filled with bar-reinforced concrete. Journal of structural engineering. 1994;120:1489-509.

[130] Li G-Q, Guo S-X. Experiment on restrained steel beams subjected to heating and cooling. Journal of constructional steel research. 2008;64:268-74.

[131] Pan J, Li G, Cai J, Tao Z. Axial compressive behaviors of engineered cementitious composites-encased concrete filled steel tube columns after fire exposure. Engineering Structures. 2022;273:115127.

[132] Zhang H, Jiang W, Wu B, Wen B, Qi C, Yuan L. Model fire test and similarity relationship development of RC columns subjected to uneven fire exposure. Engineering Structures. 2023;295:116858.

[133] Du T, Yang H, Liu F. Eccentrically loaded high-strength concrete filled high-strength steel tubular columns subjected to fire: Modelling, full-scale testing and design. Engineering Structures. 2025;343:121194.

[134] Liu S-W, Ziemian RD. MSASect2 - Matrix Structural Analysis Software for Arbitrary Cross-sections. Retrieved from http://www.msasect.com. 2023.

[135] EN1991-1-2. Eurocode 1: Actions on structures– Part 1–2: General actions actions on structures exposed to fire, CEN (European Committee for Standardisation). Brussels2002.

[136] Garlock ME, Quiel SE. Plastic Axial Load and Moment Interaction Curves for Fire-Exposed Steel Sections with Thermal Gradients. Journal of structural

engineering (New York, NY). 2008;134:874-80.

[137] Kucukler M, Xing Z, Gardner L. Behaviour and design of stainless steel I-section columns in fire. Journal of constructional steel research. 2020;165:105890.

[138] Jin B, Xu X. Machine learning price index forecasts of flat steel products. Mineral economics : raw materials report. 2024.

[139] Chen L, Zhang H-Y, Liu S-W, Ziemian RD. Efficient Line-Element Method for the Second-Order Analysis of Steel Members with Nonsymmetric Thick-Walled Cross Sections. Journal of structural engineering (New York, NY). 2024;150.

[140] Chen W-F, Atsuta T. Theory of beam-columns, space behavior, and design: Lauderdale, Fla.: J. Ross Pub; 2008.

[141] Tao Z, Ghannam M, Song T-Y, Han L-H. Experimental and numerical investigation of concrete-filled stainless steel columns exposed to fire. Journal of Constructional Steel Research. 2016;118:120-34.

[142] Fan S, Liu M, Sun W, Guo Y, Han YL. Experimental investigation of eccentrically compressed stainless steel columns with constraints in fire. Fire safety journal. 2018;99:49-62.

[143] Wu Y, Fan S, He B, Liu M, Zhou H. Research on the fire resistance design of high-strength steel hollow columns under axial compression. Engineering structures. 2021;234:111943.

[144] Fan S, Du L, Li S, Zhang L, Shi K. Fire-resistance of RHS stainless steel beams with three faces exposed to fire. Journal of constructional steel research. 2019;152:284-95.

[145] Wang Y. Performance-based fire engineering of structures. Boca Raton, Fla: CRC

Press; 2013.

[146] Lange D, Devaney S, Usmani A. An application of the PEER performance based earthquake engineering framework to structures in fire. Engineering structures. 2014;66:100-15.

[147] Herrmann LR. Elastic Torsional Analysis of Irregular Shapes. Journal of the Engineering Mechanics Division. 1965;91:11-9.

[148] ASCE. ASCE 29-05: Standard calculation methods for structural fire protection. Reston, VA.: AISC/SFPE; 2008.

[149] Galambos TV. Structural members and frames. Englewood Cliffs, N.J: Prentice-Hall; 1968.

[150] Li G, Gu Z-Z, Zhang H-Y, Ouyang W, Liu S-W. Line finite element method for geometrically nonlinear analysis of functionally graded members accounting for twisting effects. Composite structures. 2024;343:118268.

[151] Iu CK, Chan SL, Zha XX. Nonlinear pre-fire and post-fire analysis of steel frames. Engineering structures. 2005;27:1689-702.

[152] Systèmes D. ABAQUS 6.14 User's Guide. Providence, USA: ABAQUS Documentation; 2014.

[153] Wu Y-F. The conditions for plane sections remaining plane. Engineering Structures. 2022;263:114387.

[154] ISO/CD834-11. Fire resistance tests—elements of building construction, specific requirements for the assessment of fire protection to structural steel elements. International Organization for Standardization; 2014.

[155] Mesquita L, Piloto P, Roque S, Vaz M. Fire resistance of steel members protected with intumescent coatings. YIC2012-First ECCOMAS Young Investigators Conference2012. p. 1-12.

[156] Wu M, Fan S, Zhou H, Han Y, Liang D. Experimental and numerical research on fire resistance of stainless steel-concrete composite beam. Journal of constructional steel research. 2022;194:107342.

[157] Liu M, Fan S, Ding R, Chen G, Du E, Wang K. Experimental investigation on the fire resistance of restrained stainless steel H-section columns. Journal of constructional steel research. 2019;163:105770.

[158] Xiong M-X, Liew JYR. Fire resistance of high-strength steel tubes infilled with ultra-high-strength concrete under compression. Journal of constructional steel research. 2021;176:106410.

[159] Agarwal A, Varma AH. Design of steel columns at elevated temperatures due to fire: Effects of rotational. Engineering Journal AISC. 2011;48:297-314.

[160] AISC. Specification for structural steel buildings. ANSI/AISC 360-22. Chicago: AISC.2022.

[161] Moura Correia AJP, Rodrigues JPC, Real PV. Thermal bowing on steel columns embedded on walls under fire conditions. Fire safety journal. 2014;67:53-69.

[162] Alos-Moya J, Paya-Zaforteza I, Hospitaler A, Rinaudo P. Valencia bridge fire tests: Experimental study of a composite bridge under fire. Journal of Constructional Steel Research. 2017;138:538-54.

[163] Davidson MT, Harik IE, Davis DB. Fire Impact and Passive Fire Protection of Infrastructure: State of the Art. Journal of performance of constructed facilities.

2013;27:135-43.

[164] Suman S, Samanta A. Behavior of laterally unsupported monosymmetric steel I-section beams at elevated temperature under non-uniform moments. Structures. 2021;33:3324-56.

[165] Yin YZ, Wang YC. Numerical simulations of the effects of non-uniform temperature distributions on lateral torsional buckling resistance of steel I-beams. Journal of Constructional Steel Research. 2003;59:1009-33.

[166] Pallares-Muñoz MR, Paya-Zaforteza I, Hospitaler A. A new methodology using beam elements for the analysis of steel frames subjected to non-uniform temperatures due to fires. Structures. 2021;31:462-83.

[167] Cooke GME. Thermal bowing and how it affects the design of fire separating construction. Fire and materials. 1988;13:230-6.

[168] Usmani AS, Rotter JM, Lamont S, Sanad AM, Gillie M. Fundamental principles of structural behaviour under thermal effects. Fire safety journal. 2001;36:721-44.

[169] Dwaikat MMS, Kodur VKR, Quiel SE, Garlock MEM. Experimental behavior of steel beam–columns subjected to fire-induced thermal gradients. Journal of constructional steel research. 2011;67:30-8.

[170] Vishal J, Aman Preet Singh S, Khushmeet K. Finite Element Method: An Overview. Walailak journal of science and technology. 2013;10.

[171] Zhang C, Yu H-X, Choe L, Gross J, Li G-H. Simulating the fire-thermal-structural behavior in a localized fire test on a bare steel beam. Engineering structures. 2018;163:61-70.

[172] Nguyen TQ, Nguyen XT, Nguyen TNM, Bui-Tien T, Park JS. Numerical study

on buckling capacity of steel H-beams under non-uniform temperature distribution. Journal of structural fire engineering. 2023;14:254-68.

[173] Zhang C, Li GQ. Fire dynamic simulation on thermal actions in localized fires in large enclosure. Advanced Steel Construction. 2012;8:124-36.

[174] Yu HX, Richard Liew JY. Steel framed structures subjected to the combined effects of blast and fire - Part 1: State-of-the-art review. Advanced Steel Construction. 2005;1:79-96.

[175] Song Y, Huang Z, Burgess IW, Plank RJ. The behaviour of single-storey industrial steel frames in fire. Advanced Steel Construction. 2009;5:289-302.

[176] Fan SG, Shu GP, She GJ, Richard Liew JY. Computational method and numerical simulation of temperature field for large-space steel structures in fire. Advanced Steel Construction. 2014;10:151-78.

[177] Li G-Q, Jiang S-C. Prediction to nonlinear behavior of steel frames subjected to fire. Fire Safety Journal. 1999;32:347-68.

[178] Franssen J-M, Gernay T. Modeling structures in fire with SAFIR®: theoretical background and capabilities. Journal of structural fire engineering. 2017;8:300-23.

[179] Possidente L, Tondini N, Battini J-M. 3D Beam Element for the Analysis of Torsional Problems of Steel-Structures in Fire. Journal of structural engineering (New York, NY). 2020;146.

[180] Systèmes D. ABAQUS 6.14, User’s Guide. ABAQUS Documentation. Providence, USA: ABAQUS Documentation; 2014.

[181] Han L-H, Tan Q-H, Song T-Y. Fire Performance of Steel Reinforced Concrete Columns. Journal of structural engineering (New York, NY). 2015;141.

[182] Lu H, Zhao X-L, Han L-H. Fire behaviour of high strength self-consolidating concrete filled steel tubular stub columns. Journal of Constructional Steel Research. 2009;65:1995-2010.

[183] Ouyang W, Li G, Chen L, Liu SW. Physics-informed neural networks for large deflection analysis of slender piles incorporating non-differentiable soil-structure interaction. International journal for numerical and analytical methods in geomechanics. 2024;48:1278-308.

[184] McGuire W, Gallagher RH, Ziemian RD. Matrix structural analysis. 2nd ed. ed. New York: John Wiley; 2000.

[185] Attard MM. Lateral buckling analysis of beams by the fem. Computers & Structures. 1986;23:217-31.

[186] Jawdhari A, Fam A, Kadhim MMA. Thermal bowing of reinforced concrete sandwich panels using time-domain coupled-field finite element analysis. Engineering structures. 2022;252:113592.

[187] Qiu J, Jiang L, Anwar Orabi M, Usmani A, Li G. A computational approach for modelling composite slabs in fire within OpenSees framework. Engineering Structures. 2022;255:113909.

[188] Pezeshky P, Sahraei A, Rong F, Sasibut S, Mohareb M. Generalization of the Vlasov theory for lateral torsional buckling analysis of built-up monosymmetric assemblies. Engineering structures. 2020;221:111055.

[189] Ng KT, Gardner L. Buckling of stainless steel columns and beams in fire. Engineering Structures. 2007;29:717-30.

[190] Fang C, Izzuddin B, Elghazouli A, Nethercot D. Robustness of steel-composite

building structures subject to localised fire. Fire Safety Journal. 2011;46:348-63.

[191] Li S, Liew JR, Xiong M-X, Lai B-L. Experimental investigation on fire resistance of high-strength concrete encased steel composite columns. Fire Safety Journal. 2021;121:103273.

[192] Lee C-H, Park MJ. Integrated Fire Resistance Analysis of Concrete-Filled Steel Tube Columns Under Standard Fire: Design Standards, Simulations, and Experimental Validation. Fire Safety Journal. 2025:104508.

[193] Han L-H, Zhou K, Tan Q-H, Song T-Y. Performance of Steel-Reinforced Concrete Column after Exposure to Fire: FEA Model and Experiments. Journal of structural engineering (New York, NY). 2016;142.

[194] Long-fei HOU, Ming LI, Wu-yuan CUI, Yu-chen LIU. Numerical Simulation and Analysis of On-building High-rise Building Fires. Procedia engineering. 2011;11:127-34.

[195] Zheng L, Wang W, Zhou C, Li J. Numerical study on the residual performance of partially encased composite frames after being subjected to full-range fire. Structures. 2025;74:108450.

[196] Khalaf S, Abed F, El Refai A, Roshan N, Hajiloo H. Circular RC columns wrapped with PBO-FRCM and CFRP strengthening systems in a standard fire. Fire Safety Journal. 2025;155:104424.

[197] Peña DL, Albero V, Ibáñez C, Hospitaler A. Sectional model for the fire evaluation of reinforced concrete columns subjected to biaxial bending. Engineering Structures. 2021;247:113094.

[198] Li G, Gu Z-Z, Chen L, Liu S-W. Geometrically nonlinear analysis of steel

members under non-uniform fire considering twisting effects. Journal of Constructional Steel Research. 2025;231:109596.

[199] Kumar R, Alam N, Nadjai A. Structural response of a column under eccentric loading in a travelling fire scenario with open ventilation conditions. Fire Safety Journal. 2025:104474.

[200] Xiong M-X, Liew JYR. Discussion on the applicability of the M-N interaction curve for the fire resistance design of CFT members. Thin-Walled Structures. 2018;125:172-86.

[201] Han L-H, Zhou K, Tan Q-H, Song T-Y. Performance of steel reinforced concrete columns after exposure to fire: Numerical analysis and application. Engineering Structures. 2020;211:110421.

[202] Liu F, Yang H, Gardner L. Post-fire behaviour of eccentrically loaded reinforced concrete columns confined by circular steel tubes. Journal of Constructional Steel Research. 2016;122:495-510.

[203] Hwang J-y, Kwak H-G. Evaluation of post-fire residual resistance of RC columns considering non-mechanical deformations. Fire Safety Journal. 2018;100:128-39.

[204] Demir U, Goksu C, Binbir E, Ilki A. Impact of time after fire on post-fire seismic behavior of RC columns. Structures. 2020;26:537-48.

[205] Zhong Y, Jiang K, Zhao O. Post-fire behaviour and capacity of high strength concrete-filled high strength steel tube (HCFHST) stub columns under combined compression and bending. Engineering Structures. 2022;253:113837.

[206] Yang H, Han L-H, Wang Y-C. Effects of heating and loading histories on post-fire cooling behaviour of concrete-filled steel tubular columns. Journal of

Constructional Steel Research. 2008;64:556-70.

[207] Lapuebla-Ferri A, Pons D, Romero ML. Load and temperature influence on the post-fire mechanical properties of steel reinforcements. Journal of Constructional Steel Research. 2021;185:106866.

[208] Wang Y, Bu Y, Huang Z, Gu A, Han G, Zhang X et al. Experimental and numerical investigation on reinforced-concrete slab-beam assemblies exposed to extended and travelling fires. Engineering Structures. 2022;264:114430.

[209] Wang F, Liu F, Hai Tan K, Yang H, Peng K. Post-fire performance of circular steel tube confined steel-reinforced concrete slender columns: Testing, simulation and design. Engineering Structures. 2024;298:117084.

[210] Peng K, Yang H, Liu F, Wang F. Post-fire residual behavior of square steel tube confined steel-reinforced concrete slender columns under axial compression: Tests, numerical simulation, and calculation methods. Engineering Structures. 2025;333:120125.

[211] EN1991-1-2. Eurocode 1: Actions on structures– Part 1–2: General actions actions on structures exposed to fire, CEN (European Committee for Standardisation). Brussels2002.

[212] Shakil S, Lu W, Puttonen J. Behaviour of vertically loaded steel beams under a travelling fire. Structures. 2022;44:1-17.

[213] Heo I, Haam S, Lee S, Darkhanbat K, Kim KS, Choi S-H. Analytical study on fire resistance performance of precast concrete hollow-core slabs for electric vehicle fire in parking structures. Structures. 2024;70:107766.

[214] Kamalvand M, Massumi A, Homami P. Prediction of post-fire seismic

performance of reinforced concrete frames. Structures. 2023;56:104874.

[215] Zhou J, Zhou X, Cong B, Wang W. Numerical study of the convective heat transfer coefficient for steel column surrounded by localized fires. Fire Safety Journal. 2023;141:103987.

[216] Han L-H, Yang H, Cheng S-L. Residual Strength of Concrete Filled RHS Stub Columns after Exposure to High Temperatures. Advances in structural engineering. 2002;5:123-34.

[217] Lie TT. Fire Resistance of Circular Steel Columns Filled with Bar-Reinforced Concrete. Journal of structural engineering (New York, NY). 1994;120:1489-509.

[218] Han L-H, Yang Y-F, Yang H, Huo J-s. Residual strength of concrete-filled RHS columns after exposure to the ISO-834 standard fire. Thin-walled structures. 2002;40:991-1012.

[219] Han L-H. Fire performance of concrete filled steel tubular beam-columns. Journal of Constructional Steel Research. 2001;57:697-711.

[220] Zhong Y, Zhao O. Concrete-filled high strength steel tube stub columns after exposure to fire: Testing, numerical modelling and design. Thin-Walled Structures. 2022;177:109428.

[221] Moradi M, Daneshvar K, Ghazi-Nader D, Hajiloo H. The prediction of fire performance of concrete-filled steel tubes (CFST) using artificial neural network. Thin-Walled Structures. 2021;161:107499.

[222] Ji S-H, Wang W-D, Chen W, Shi Y-L, Xian W. Lateral impact behaviour of post-fire steel-reinforced concrete-filled steel tubular members: Experiment and evaluation method. Engineering Structures. 2023;293:116612.

[223] Zhou K, Han L-H. Modelling the behaviour of concrete-encased concrete-filled steel tube (CFST) columns subjected to full-range fire. Engineering Structures. 2019;183:265-80.

[224] Ma Y-X, Zhao O, Tan KH. Experimental and numerical studies of concrete-encased concrete-filled steel tube stub columns under uniaxial and biaxial eccentric compression. Engineering Structures. 2021;232:111796.

[225] ACI. Building Code Requirements for Structural Concrete, ACI 318-05. American Concrete Institute, Farmington Hills2005.

[226] Li S, Liew JYR, Xiong M-X. Fire performance of composite columns made of high strength steel and concrete. Journal of Constructional Steel Research. 2021;181:106640.

[227] ASTM C39. Standard test method for compressive strength of cylindrical concrete specimens. ASTM International, West Conshohocken, PA2014.

[228] ASTM E8M. Standard test methods for tension testing of metallic materials. ASTM International, West Conshohocken, PA2016.

[229] ASTM A615. Standard specification for deformed and plain carbon-steel bars for concrete reinforcement. ASTM International, West Conshohocken, PA2009.

[230] Chen SF, Teng JG, Chan SL. Design of Biaxially Loaded Short Composite Columns of Arbitrary Section. Journal of structural engineering (New York, NY). 2001;127:678-85.

[231] El-Fitiany SF, Youssef MA. Interaction diagrams for fire-exposed reinforced concrete sections. Engineering Structures. 2014;70:246-59.

[232] Bonet JL, Miguel PF, Fernandez MA, Romero ML. Analytical Approach to

Failure Surfaces in Reinforced Concrete Sections Subjected to Axial Loads and Biaxial Bending. Journal of structural engineering (New York, NY). 2004;130:2006-15.

[233] Wang L, Van Coile R, Caspeele R, Taerwe L. Simplified method for evaluating the biaxial capacity of rectangular reinforced concrete columns during fire. Materials and Structures. 2017;50:1-13.

[234] Du Y, Qi H-h, Jiang J, Richard Liew JY, Li S. Thermo-mechanical behaviour of ultra-high strength concrete encased steel columns in standard fires. Engineering Structures. 2021;231:111757.

[235] Hadjisophocleous GV, Benichou N. Performance criteria used in fire safety design. Automation in construction. 1999;8:489-501.

[236] Ma C, Van Coile R, Gernay T. Fire protection costs in composite buildings for cost-benefit analysis of fire designs. Journal of Constructional Steel Research. 2024;215:108517.

[237] Usmani AS, Rotter JM, Lamont S, Sanad A, Gillie M. Fundamental principles of structural behaviour under thermal effects. Fire safety journal. 2001;36:721-44.

[238] Bisby L, Gales J, Maluk C. A contemporary review of large-scale non-standard structural fire testing. Fire science reviews. 2013;2:1.

[239] Zhang C, Choe L, Seif M, Zhang Z. Behavior of axially loaded steel short columns subjected to a localized fire. Journal of Constructional Steel Research. 2015;111:103-11.

[240] Zhang C, Li G-Q. Thermal response of steel columns exposed to localized fires-numerical simulation and comparison with experimental results. Journal of

Structural fire engineering. 2011;2:311-8.

[241] Fischer EC, Varma AH, Agarwal A. Performance-Based Structural Fire Engineering of Steel Building Structures: Design-Basis Compartment Fires. Journal of structural engineering (New York, NY). 2019;145.

[242] Kolšek J, Češarek P. Performance-based fire modelling of intumescent painted steel structures and comparison to EC3. Journal of Constructional Steel Research. 2015;104:91-103.

[243] Dwaikat MMS, Kodur VKR. A performance based methodology for fire design of restrained steel beams. Journal of Constructional Steel Research. 2011;67:510-24.

[244] Silva JCG, Landesmann A, Ribeiro FLB. Fire-thermomechanical interface model for performance-based analysis of structures exposed to fire. Fire Safety Journal. 2016;83:66-78.

[245] Ye Z, Hsu S-C, Wei H-H. Real-time prediction of structural fire responses: A finite element-based machine-learning approach. Automation in Construction. 2022;136:104165.

[246] Kim H, Lee C-H, Choi J-H, Han K-H, Ha T, Park MJ. Computational methodology for investigating the fire behavior of modular steel buildings using full-scale testing and coupled CFD-FEM analysis. Fire Safety Journal. 2025;156:104476.

[247] Jiang J, Usmani A. Modeling of steel frame structures in fire using OpenSees. Computers & Structures. 2013;118:90-9.

[248] Hua Y, Duan L, Zhao J. Performance-based fire protection of clustered individual

members within a steel frame structure. Journal of Constructional Steel Research. 2024;218:108691.

[249] Tang Y-Q, Xu F, Liu Y-P, Du E-F, Chan S-L. A hybrid beam-column element for second-order inelastic analysis of fire-exposed steel frames. Journal of Constructional Steel Research. 2025;235:109912.

[250] Luu V-T, Bui V-T, Kim S-E. An advanced computational method for nonlinear inelastic thermo-mechanical analysis of spatial steel frames in fires. Engineering Structures. 2023;275:115329.

[251] Liu S-W, Bai R, Chan S-L. Second-order analysis of non-prismatic steel members by tapered beam–column elements. Structures. 2016;6:108-18.

[252] Bai R, Liu S-W, Chan S-L. Finite-element implementation for nonlinear static and dynamic frame analysis of tapered members. Engineering Structures. 2018;172:358-81.

[253] ASCE. ANSI/AISC 360–10: specification for structural steel buildings. Chicago, IL: American Institute of Steel Construction, Inc; 2010.

[254] Liu S-W, Bai R, Chan S-L. Second-order analysis of non-prismatic steel members by tapered beam–column elements. Structures: Elsevier; 2016. p. 108-18.

[255] Ding R, Fan S, Jia L, Zhou H. Fire-Resistance Design Method for Stainless Steel Tubular X-Joints. Journal of structural engineering (New York, NY). 2022;148.

[256] Tao Z, Ghannam M. Heat transfer in concrete-filled carbon and stainless steel tubes exposed to fire. Fire safety journal. 2013;61:1-11.

[257] Ziemian RD, McGuire W. Modified tangent modulus approach, a contribution to plastic hinge analysis. Journal of Structural Engineering. 2002;128:1301-7.

[258] Bruschi E, Calvi PM, Quaglini V. Concentrated plasticity modelling of RC frames in time-history analyses. Engineering Structures. 2021;243:112716.

[259] Chen L, Liu S-W, Chan S-L. Divergence-free algorithms for moment-thrust-curvature analysis of arbitrary sections. Steel and Composite Structures, An International Journal. 2017;25:557-69.

[260] Chadwell C, Imbsen R. XTRACT: a tool for axial force-ultimate curvature interactions, structures. Building on the Past, Securing the Future. 2004.

[261] Rodriguez-Gutierrez JA, Dario Aristizabal-Ochoa J. Bending Moment-Axial Force-Curvature Interactions for Metal Beam-Column Sections. Structures. 2017;10:139-46.

[262] Xu Q, Li G-Q, Wang YC. A simplified method for calculating non-uniform temperature distributions in thin-walled steel members protected by intumescent coatings under localized fires. Thin-Walled Structures. 2021;162:107580.

[263] EN13381-8 B. Test Methods for Determining the Contribution to the Fire

Resistance of Structural Members, Applied Reactive Protection to Steel Members. London2013.

[264] Xu Q, Li G-Q, Wang YC, Bisby L. An experimental study of the behavior of intumescent coatings under localized fires. Fire Safety Journal. 2020;115:103003.

[265] ECCS. (European Convention for Constructional Steelwork). Fire safety in open car parks. Brussels, Belgium: Modern Fire Engineering, Technical Committee 3, European Convention for Constructional Steelwork; 1993.

[266] Haremza C, Santiago A, Da Silva LS. Design of steel and composite open car parks under fire. International Journal of Advanced Steel Construction.

2013;9:350-68.